CATION TUNABLE REACTIVITY AND CATALYSIS WITH IRIDIUM PINCER-CROWN ETHER COMPLEXES

Matthew R. Kita

A dissertation submitted to the faculty at the University of North Carolina at Chapel Hill in partial fulfillment of the requirements for the degree of Doctor of Philosophy in the Department of Chemistry.

Chapel Hill
2017

Approved by:

Alexander J. M. Miller

Cynthia K. Schauer

Maurice S. Brookhart

Frank A. Leibfarth

Simon J. Meek

ABSTRACT

Matthew R. Kita: Cation Tunable Reactivity and Catalysis with
Iridium Pincer-Crown Ether Complexes
(Under the direction of Alexander J. M. Miller)

Iridium complexes of a new multidentate ligand combining a rigid, strongly donating pincer scaffold with a flexible, weakly donating aza-crown ether moiety are reported. The "pincer-crown ether ligand" exhibits tridentate, tetradentate, and pentadentate coordination modes. The coordination mode can be changed by Lewis base displacement of the chelating ethers, with binding equilibria dramatically altered through cation–macrocycle interactions. Cation-promoted hydrogen activation was accomplished by an iridium monohydride cation ligated in a pentadentate fashion by the pincer-crown ether ligand. The rate can be controlled on the basis of the choice of cation, and the concentration of cation.

Using the same complex, rapid, selective, and highly controllable iridium-catalyzed allylbenzene isomerization is described, enabled by tunable hemilability based on alkali metal cation binding with the macrocyclic pincer-crown ether ligand. An inactive chloride-ligated complex can be activated by halide abstraction with sodium salts, with the resulting catalyst [κ^5-(^{15c5}NCOPi^{Pr})Ir(H)]$^+$ exhibiting modest activity. Addition of Li^+ provides a further boost in activity, with up to 1000-fold rate enhancement. Ethers and chloride salts dampen or turn off reactivity, leading to three distinct catalyst states with activity spanning several orders of magnitude. Mechanistic studies suggest that the large rate enhancement and high degree of tunability stem from control over substrate binding.

Methods to convert CO_2 to formate using iridium pincer-crown ether complexes are discussed. The synthesis of iridium dihydride pincer-crown ether complexes is attempted. Electrochemistry of pincer-crown ether complexes reveal very negative iridium reduction potentials. Lastly, CO_2 hydrogenation to formate is accomplished in bicarbonate solutions with turn over numbers up to 1000.

ACKNOWLEDGEMENTS

To my advisor Alexander J. M. Miller, the past five years have been an incredible scientific experience. I remember meeting you during visitation weekend and hearing about your crazy idea to synthesize new transition metal complexes that could interact with cations, and do weird new reactivity. The project seemed a bit out there, it was an unproven, but I thought the project looked coo, and wanted to go to school to do some traditional organometallic chemistry. So, I made the jump, and in July of 2012, the Miller Group inhabited the humble dwellings known as the 6th floor of Kenan. In my first year, you trained me how to do synthesis, air free techniques, NMR spectral interpretation, and never seem phased whenever I was up to something bizarre. It was awesome experience getting hands on training from you, and building this project from the ground up. After a few months, we had synthesized the ligands and complexes that this thesis is largely based on. In the summer of 2013, the lab moved to the newly renovated 4th floor, the lab rapidly grew in size, and the project continued to evolve. At the end of 2013, I ran the first HD exchange experiment, and we finally had proof that cations could do something! During the development of this project, you were consistently an amazing advisor and mentor to me. I can't thank you enough for believing in me, pushing me, and being patient with me. It has been immensely satisfying to help grow this project from a proposal, to a major project within the lab over 5 years.

To the professors at UNC that were always around to give me scientific help, and advice. Brookhart, thank you for always giving friendly help with the interpretation of NMR spectra. Joe

Templeton, thank you for your continued professional advice, and friendly jests. Cindy Schauer, thank you for helping me with my 550L renovation project, and for all the advice during EFRC meetings. Simon Meek, thank you for your assistance with organic synthesis. Jillian Dempsey, thank you for being another Jersey native, and for always being available for miscellaneous scientific and pedagogical discussion. Tom Meyer, thank you for allowing me to participate in the EFRC and learn more about solar fuels. Nita Eskew, thank you for your assistance when I was a teaching assistant, and helping me organize the changes made to 550L.

Mom and Dad, thank you so much for helping me move down here, your continued love and support, and always being available to talk on the phone to give me advice. I wish I could have come home more often to visit. Amanda, thank you for all of your chemistry help during college, and for being an amazing sister. To nick, thank you for always keeping it real, and reminding me to focus on my goals, but also to learn how to laugh at life.

Lastly to my friends and colleagues at UNC. To the miller Lab, Andrew W, Kate, Jacob, Seth, Kelsey, Javier, Lauren, Ali, Brian, Matt, Andrew C, Bethany, and Ann Marie, you have all been amazing to work with. To the 6th floor Dempsey crew, I'll always remember the weird and wonderful times. To Gish, it's been amazing to have a friend capable of discussions that mix scientific progress, and pop culture in a blender. Oh, and to Mike, thanks for keeping me sane for the past 3 years.

TABLE OF CONTENTS

LIST OF FIGURES

LIST OF SCHEMES

LIST OF ABBREVIATIONS AND SYMBOLS

°	degree(s)
α	Greek alpha: crystallographic angle
β	Greek beta: crystallographic angle
γ	Greek gamma: crystallographic angle
δ	Greek delta: denotes chemical shift reference scale
η	Greek eta: ligand hapticity
κ	Greek kappa: denotes coordination to metal by x atoms
ν	Greek mu: IR absorption band frequency
π	Greek pi: denotes bond
θ	Greek theta: general angle
σ	Greek sigma: denotes coordination to a metal via a single atom
Δ	Greek capital delta: denotes separation between values or applied heat
a,b,c	crystallographic unit cell parameters
Å	angstrom(s)
aq	Aqueous
atm	Atmosphere
Ar	general aromatic
BAr^F_4	tetrakis(3,5-trifluoromethylphenyl)borate
^{13}C	Carbon NMR
C	Celsius
cm^{-1}	wavenumber
CV	Cyclic voltammetry

C-X	Carbon-halide bond
^{o}	Degree
D	Deuterium
d	doublet
e^-	Electron
$\Delta G°$	standard Gibbs energy
eq	equation
equiv	equivalents
E^o	Formal potential
Et	ethyl, $-CH_2CH_3$
HCO_2^-	Formate
HCO_2H	Formic acid
g	Gram
h	hour(s)
Hz	Hertz
PF_6^-	Hexafluorophosphate
IR	infrared
Ir-H	Iridium-hydrogen bond
Ir-O	Iridium-oxygen bond
$^{x}J_{YZ}$	magnetic coupling between atoms X and Y through a distance of x bonds
K	Kelvin
kcal	kilocalorie
KIE	Kinetic isotope effect

L	general ligand, usually 2 e^- donor
M	Molar
M	general metal atom
µL	Microliter
mg	Milligram
mL	Milliliter
mM	Millimolar
mmol	Millimole
min	Minute
m	multiplet
m	meta
Me	methyl, $-CH_3$
min	minute(s)
mol	mole
*n*Bu	*n*-butyl, $-C_4H_9$
NMR	nuclear magnetic resonance
o	ortho
OTf	triflate, trifluoromethane sulfonate: $CF_3SO_3^-$
^{31}P	Phosphorous NMR
p	para
Ph	phenyl, $-C_6H_5$
ppm	parts per million
^{1}H	Proton NMR

q	quartet
R	general alkyl group
R, R_W	crystallographic refinement quality indicators
s	singlet (NMR data)
s	second
t	triplet
^{t}Bu	tertiary butyl, -C(CH_3)$_3$
THF	tetrahydrofuran
TMS	trimethylsilyl, -Si(CH_3)$_3$
TOF	Turnover frequency
TON	Turnover number
X	general halogen atom

Chapter 1 : METHODS TO CONTROL SUBSTRATE BINDING TO TRANSITION METAL COMPLEXES

1.1 Electronic and Steric Ligand Tuning Methods

Transition metal catalysis is fundamental to the production of commodity chemicals, polymers, pharmaceuticals, and the discovery of new organic and inorganic transformations.[1,2] Since the inception of the field, organometallic chemists have honed the art of synthesizing organotransition metal complexes, studying their reactivity, and formulating trends to enable new reactivity. Substrate binding lies at the heart of transition metal reactivity: in nearly every catalytic cycle, the substrate must initially bind to the metal center in order to undergo activation and subsequent functionalization. An ideal catalyst balances the demands of 1) allowing substrate binding, 2) avoiding decomposition, 3) activating substrates in the proper geometry, and 4) maintaining rapid activity for many cycles. Over time, chemists have conducted many detailed mechanistic studies of these individual processes. These studies have led to the development of different tools to control catalysis, and have increased the knowledge base needed to develop better catalysts.

A watershed moment for understanding reactivity in transition metal complexes was ushered in by Tolman through a comprehensive study of the electronic and steric properties of various phosphine ligands (PR_3) in $(PR_3)Ni(CO)_3$ complexes.[3,4] By measuring the CO stretching frequency (υ_{CO}), and cone angle (θ), of the $(PR_3)Ni(CO)_3$ complexes, Tolman was able to quantify how various phosphine ligands affected electronics at the nickel center. Phosphines with

electron-releasing groups like $P(CH_3)_3$ were found to provide the metal center with higher electron density than phosphines with electron-withdrawing groups like $P(OCH_3)_3$ and PCl_3. Bulky phosphines like P^tBu_3 (^{t}Bu = *tert*-butyl) crowded the metal center with their steric bulk compared to $P(CH_3)_3$. Since the landmark report, numerous studies have been conducted to determine the steric and electronic effects of phosphine ligands in different transition metal carbonyl systems.[5–9] This knowledge base acts as a general guide to help control various substitution reactions. In associative ligand substitution reactions, a substrate binds the metal first, so smaller ligands will allow for easier substrate access. Conversely, in dissociative ligand substitution mechanisms, larger phosphines, or more donating phosphines can help drive ligand dissociation, and allow substrate binding.[10]

Suppose the six-coordinate complex $L_5M(PR_3)$ could undergo catalysis via ligand dissociation (–L), and substrate binding (+L') as shown in scheme 1.1. Ligand dissociation forms the five-coordinate species $L_4M(PR_3)$ in a concentration governed by the ligand dissociation equilibrium. Fast substrate binding of L' then forms a precursor ready to undergo catalysis. Combining all of these steps leads to rate equation 1.1.

Scheme 1.1

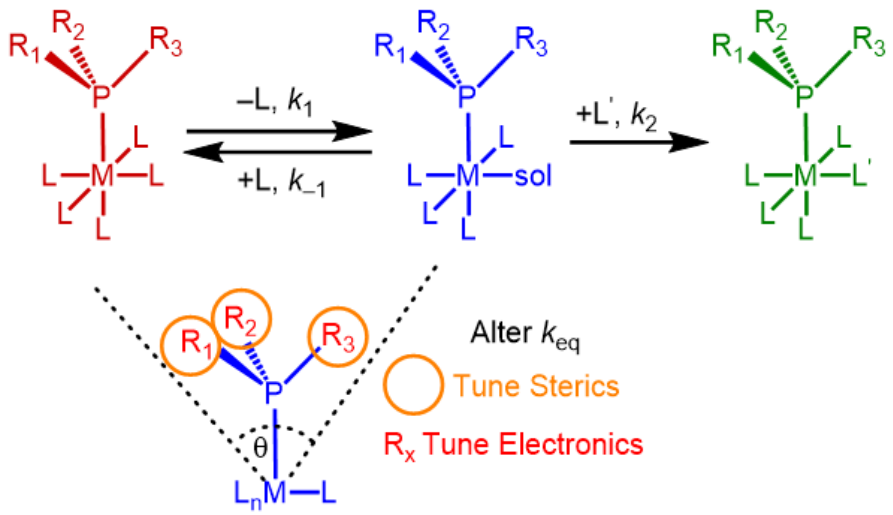

$$\text{Rate} = \frac{k_1 k_2 [L'][L_5M(PR_3)]}{k_{-1}[L]+k_2[L']} \qquad \text{(Equation 1.1)}$$

$$\text{Rate} = k_1[L_5M(PR_3)] \qquad \text{(Equation 1.2)}$$

To tune the binding of L', chemists can alter the concentration of L. If dissociation of the ligand L is the rate-determining step, the rate will only depend on the properties of the transition metal complex. Thus equation 1.1 simplifies to equation 1.2. Limited by k_1, chemists can only tune the dissociation of L (k_1) by altering the PR_3 ligand. By increasing steric bulk of PR_3, or increasing the electron donor ability, chemists can alter the dissociation equilibrium and favor L labilization, thus altering the binding of L'. The method to tune ligand substitution reactions through phosphine substitution alteration (PR_3) has been studied in a number of model systems including $Cr(CO)_5PR_3$,[11] *trans*-$Cr(CO)_4(PR_3)_2$,[12] and $Mo(CO)_5(PR_3)$.[10] Chemists have successfully utilized iterative phosphine design to produce desired reactivity in many cases.[13–15] It is important to note that iterative ligand design requires synthetic effort, and often alters more than substrate binding. Key catalytic steps like oxidative addition, migratory insertion, and

reductive elimination are often affected as well, and it is not obvious which steps will be impacted.[16]

An exemplary case for tuning reactivity using iterative ligand design is the development of Grubbs-type catalysts for olefin metathesis.[17–19] The first-generation Grubbs metathesis catalyst contains a ruthenium alkylidene fragment, two neutral ligands, and two anionic ligands. Through countless synthetic modifications to the catalyst (selected examples in Scheme 1.2), substitution at all sites has been studied — but the biggest strides have come from changing the axial neutral donors. The first-generation Grubbs catalyst featured two phosphine ligands in a *trans* geometry. Using phosphine chemistry, it was possible to alter the activity and stability of metathesis catalysis, but major reactivity changes were observed upon swapping one PR_3 ligand for a N-heterocyclic carbene (NHC) ligand.[20] NHC ligands are known to have improved electron-donating abilities, and different steric properties than PR_3 ligands.[21] These NHC-containing second-generation catalysts significantly altered the properties for ligand dissociation and substrate binding, and accounted for the improved activity.

Scheme 1.2

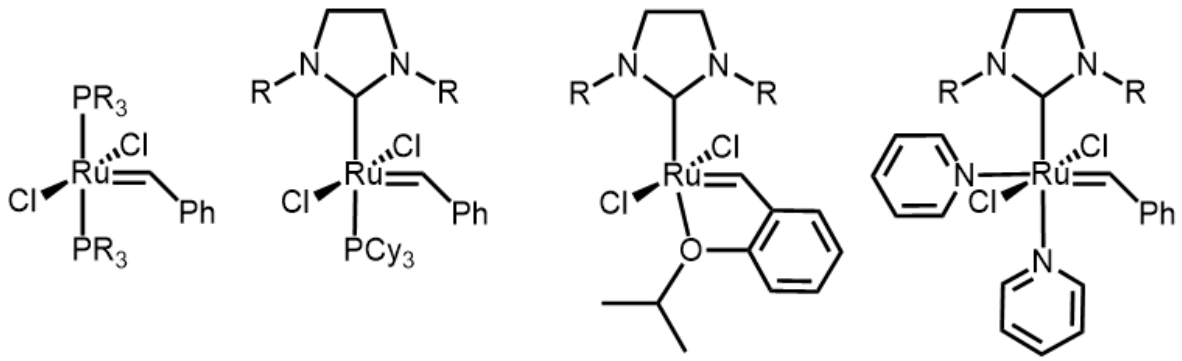

A general mechanism[22] for olefin metathesis with the first and second-generation type catalysts is shown in scheme 1.3. Starting from the 5-coordinate species **(A)**, dissociation of PR_3 via k_1 produces 4-coordinate intermediate **(B)**. Intermediate **(B)** can then bind olefin (k_2) or rebind PR_3 (k_{-1}). The bis-phosphine first generation catalysts have large values for k_1, but small values for olefin binding ($k_{-1} >> k_2$). In comparison, NHC containing catalysts have small values for k_1 but much higher affinity for olefin binding ($k_{-1}/k_2 \sim 1$). Accordingly, even though the NHC-containing catalyst produces less 4-coordinate intermediate, it binds more substrate when activated, performing more metathesis events. The more electron-releasing NHC ligands facilitate olefin binding by promoting π-backbonding.[23]

Scheme 1.3

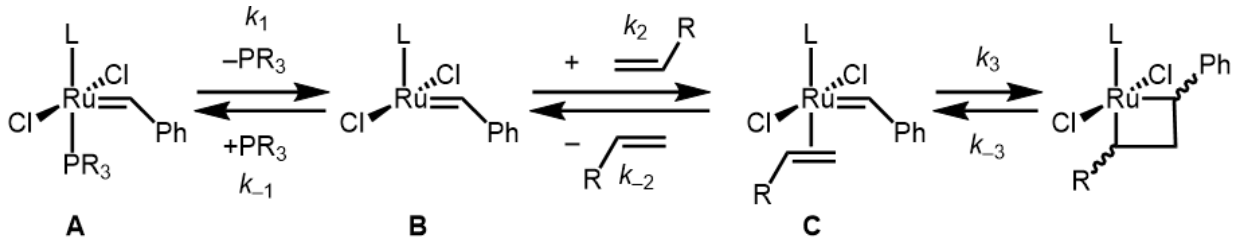

Further developments of the Grubbs metathesis catalysts have addressed the issues of slow PR_3 release (k_1), competitive PR_3 binding ($k_{-1}/k_2 \sim 1$), and catalyst stability. Initiation times were improved by substituting the PR_3 ligand, with a pyridine ligand[24] in the third generation. The pyridine ligands are highly labile relative to PR_3, leading to rapid initiation,[25] and enabling the metathesis of substrates not previously possible.[26]

The stability of the second-generation catalyst was improved by completely removing the PR_3 ligand, and replacing it with a chelating alkylidene group (the Hoveyda-Grubbs catalyst, Scheme 1.2).[27] The chelating alkylidene group features an ether group that reversibly binds the ruthenium center *trans* to the NHC ligand. Dissociation of the ether group initiates catalysis.

When catalysis stops, the ether donor can ligate the ruthenium center again. This reversible ligand binding provides increased thermal stability, and allows for catalyst recycling.[18]

In the development of these ruthenium metathesis catalysts, hundreds of ligand modifications were done to achieve the desired reactivity, stability, and kinetics. By and large, the changes were informed by altering the steric and electronic properties of the ligands to understand how they affected the generation of an active site, the binding of substrates, and catalytic activity. This method of iterative ligand design employed by Robert Grubbs contributed so much to the understanding of olefin metathesis, that the work was awarded the 2005 Nobel Prize in Chemistry.

1.2 New Ligand Tuning Methods

The reversible alkylidene ligand binding featured in the Hoveyda-Grubbs catalyst is part of a larger trend in new ligand design for applications in catalysis.[28–32] Through strategic planning, chemists have developed different ligands that can feature:

- dynamic hemilabile reversible binding
- Lewis acid responsive functional groups
- Photo-switchable groups
- Supramolecular scaffolds that control substrate access

When applied properly, these methods can provide increased stability, new reactivity, and even switchable catalytic behavior.[33–35]

Dynamic Hemilabile Ligands

In pursuit of new methods to control reactivity, chemists have investigated transition metal complexes with *hemilabile ligands*,[36–39] which chelate a metal and feature a donor that reversibly binds the metal. As shown in scheme 1.4, hemilabile ligands featuring rapid reversible binding are classified as having *dynamic hemilabile* behavior. Partial dissociation of the hemilabile chelate into the secondary coordination sphere generates an open site in the primary coordination sphere. The propensity to generate an open site in dynamic hemilabile systems is limited by ligand dissociation equilibria, which can be altered based on solvent polarity.[40] In ideal cases, a rapid equilibrium exists between the two coordination modes to provide good catalyst activity and stability.

Scheme 1.4

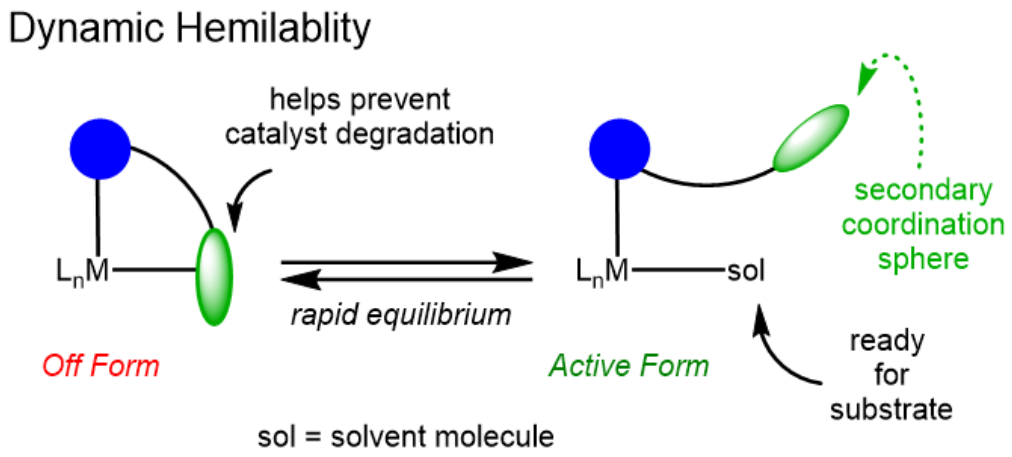

The Hoveyda-Grubbs metathesis catalyst is an excellent example of a complex with a dynamic hemilabile ligand. The tethered ether group of the alkylidine fragment can dissociate to generate an active catalytic site, but chelate to protect the catalyst. The ether dissociation equilibrium was found to be unfavorable. So, ligand alteration was done to make dissociation of

the Ru–O bond faster, like adding steric bulk and/or electron-withdrawing groups to the alkylidene fragment.[18,41–43]

Dissociation of dynamic hemilabile ligands can also serve to assist in the activation of substrates via secondary coordination sphere effects. The octahedral Fe(II) complex shown in scheme 1.5 contains the dynamic hemilabile bis(diphenylphosphino)amine ligand.[44] The dynamic hemilabile behavior observed in this complex is attributed to the small bite angle of the ligand, and steric repulsion. In the open form, hydrogen can bind the metal center, and the amine functional group can be properly positioned within the secondary coordination sphere to act as an internal base to activate H_2. During this process, the Fe center accepts H^- and the bis(diphenylphosphino)amine ligand gets protonated.

Scheme 1.5

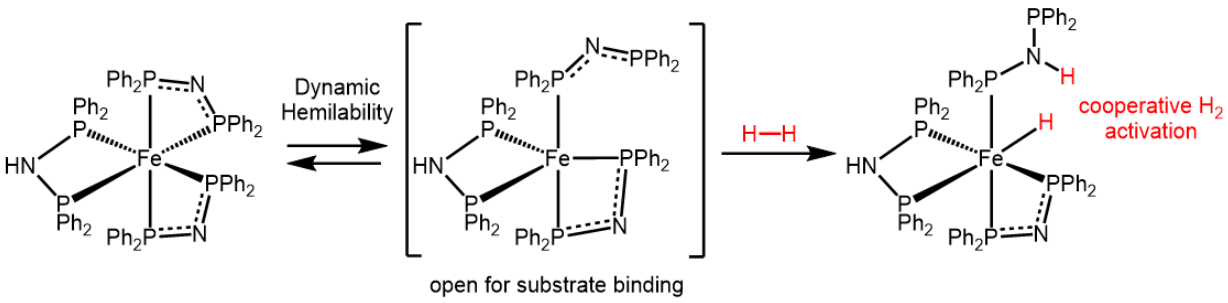

The design of ligands containing dynamic hemilabile behavior remains a difficult task. Methods to alter the hemilabile behavior include typical steric and electronic methods, but also consist of new ligand synthesis to change the chelate length[45,46] or donor strength.[47] These synthetic methods often drastically change reactivity in ways hard to rationalize. For example, Milstein investigated how arm length affects hemilability of platinum carbonyl complexes containing PCN pincer ligands as shown in scheme 1.6.

Scheme 1.6

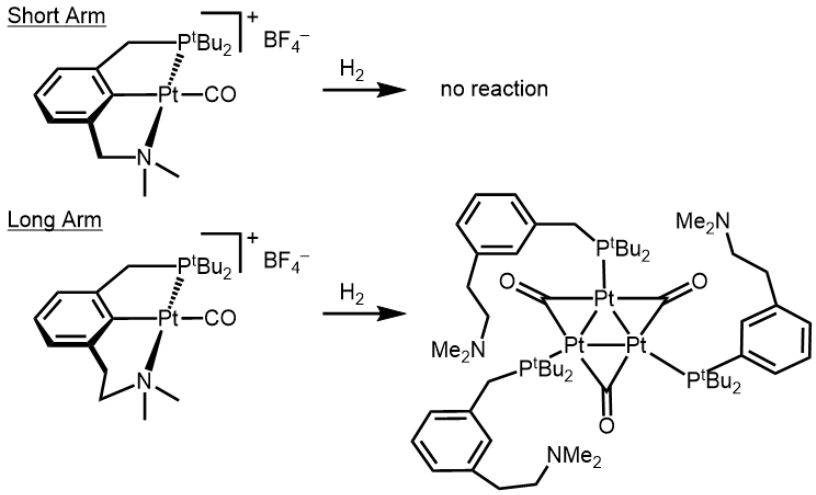

The short arm complex shows no reactivity when the substrate H_2 is added.[46] Conversely, the long arm complex reacts with H_2 to form a trinuclear platinum cluster. This striking difference is explained by the increased hemilabile behavior of the long arm complex. Amine arm dissociation allows for H_2 binding and H_2 activation. Acting as an internal base, the amine arm helps split the H_2 to form a Pt–H. From here, the Pt center can undergo C–H reductive elimination of the arene backbone, leading to cluster formation.

Tuning with Lewis Acids

Ligands that interact with external additives like Lewis acids or protons, represent a method that chemists have used to alter electronic properties and ligand substitution. The electronic properties of such complexes shift upon Lewis acid addition, providing possible switchable properties. This technique was employed by adding a proton responsive tertiary amine group to the NHC ligand of a Hoveyda-Grubbs catalyst as shown in scheme 1.6.[48]

Strong acids like HCl readily protonate the amine groups. In low polarity solvents, protonation reduces the solubility of the complex, causing the catalyst to precipitate from the

reaction mixture, allowing for catalyst recycling.[48] In more polar solvents, the complex maintains solubility after protonation, but decreases the donor ability of the NHC ligand. This results in decreased activity for ring-opening metathesis polymerization of exo-7-oxanorbornene.[49] Alternatively, protonation can alter the stereoselectivity for ring-opening metathesis polymerization as shown in scheme 1.7. When the basic form of the ligand is used, norbornene is catalyzed to *cis*-enriched polynorbornene. Protonation of the amine causes the electronics to shift such that *trans*-enriched polynorbornene is produced.

Scheme 1.7

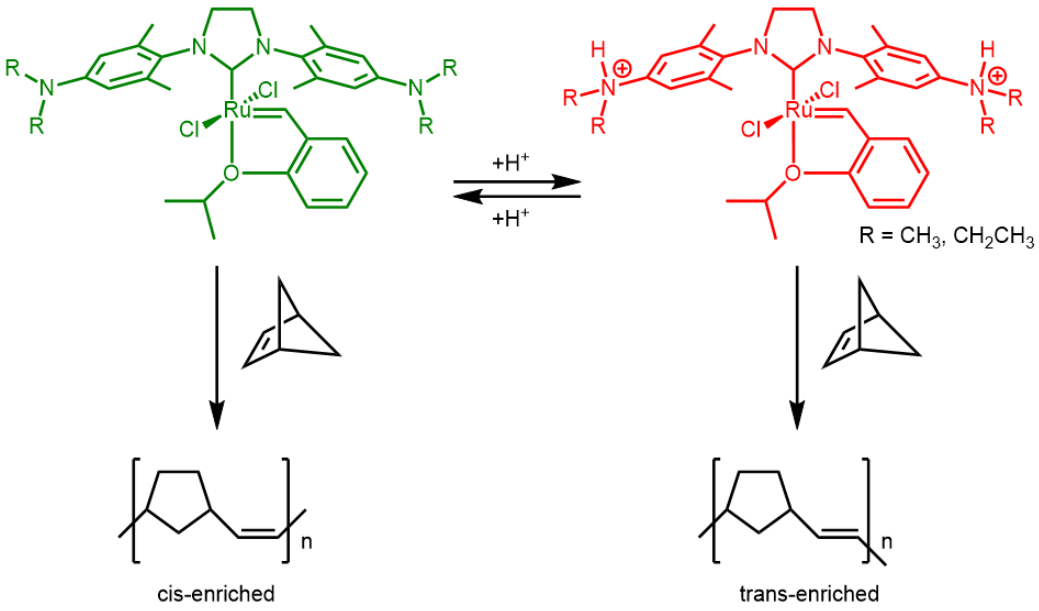

Redox Switchable Ligands

The principle of changing ligand electronics with additives applies to ligands featuring redox switchable groups. By using a redox active group in a ligand, the relative electron-donor ability of the ligand can be increased via reduction or decreased with oxidation. This strategy was demonstrated by adding a ferrocene group to the NHC unit of a Grubbs-Hoveyda catalyst (Scheme 1.8). When the ferrocene unit is in the reduced Fe^{2+} form, diethyl diallylmalonate ring-

closing metathesis activity proceeds with good activity. Oxidation of the ferrocene to Fe^{3+} reduces the activity of the catalyst by almost an order of magnitude on the basis of decreased electron donation.[50]

Scheme 1.8

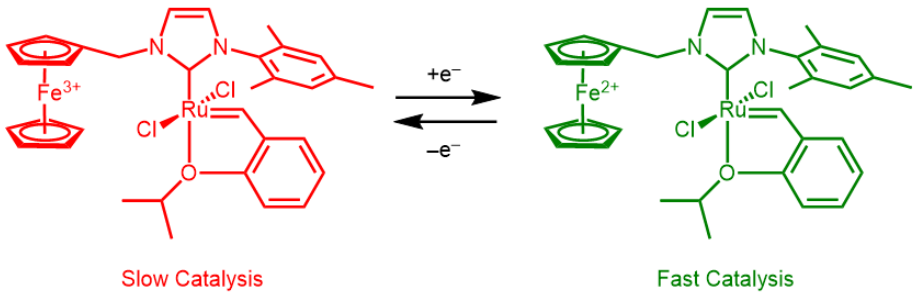

Photo Switchable Ligands

Light absorption has also been explored as a method to prompt reactivity of transition metal complexes. In some cases excitation of a transition metal complex via irradiation leads to weakening of metal—ligand bonds, and subsequent ligand dissociation to generate an open site.[51,52] Alternatively, ligands have been designed that change their donor properties upon photon absorption. Such ligands have been designed to perform photon-initiated pericyclic reactions, which changes the ligand connectivity and electronic properties. For example, the Rh(I) complex shown in scheme 1.9 contains a photo-switchable NHC ligand. Irradiating the complex with 315 nm light causes the NHC ligand to cyclize, forming a lower energy conjugated ring system. This cyclized form is less electron-donating, and shows slow catalytic activity in the hydroboration of styrene.[53] Irradiation of the complex with visible light >500 nm reverses the cyclization, and catalysis proceeds faster by an order of magnitude!

Scheme 1.9

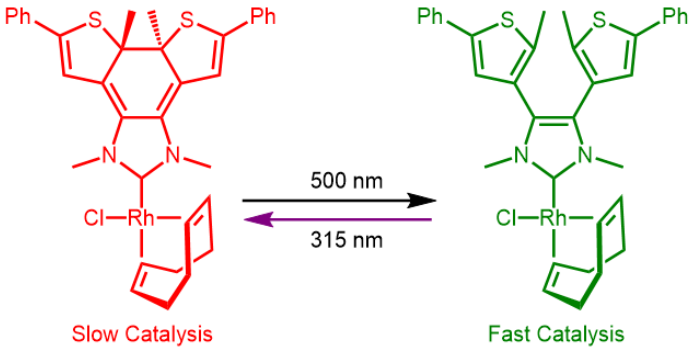

It is important to note that in the examples shown for Lewis acid responsive ligands, redox-active ligands, and photo switchable ligands, the reactivity changes after application of the stimuli. In these cases, electronic arguments can be used to rationalize how and why reactivity changed. Nonetheless, they represent clever ways to alter reactivity by designing ligands that would respond to external stimuli.

1.3 Supramolecular Systems

Methods to exquisitely control substrate access to metal centers have been developed that mimic allosteric regulation of enzymes. [54,55] By combing the concepts of reversible ligand binding and stimuli responsive switching, metal centers can be concealed within a framework that physically blocks substrate access in a closed form. Addition of stimuli causes a conformational change that opens up substrate access to a metal center and starts reactivity.

Switchable polymerization of ε-caprolactone was achieved by utilizing the triple layer construct in a Rh_2/Al system.[56] The center layer consisted of an active aluminum complex that could be obscured by large blocking groups connected to hemilabile rhodium nodes (Scheme 1.10). The hemilabile construct on rhodium contains a phosphine donor that anchors the ligand via strong Rh–P boind, and a substituted amine containing large blocking groups. From the

closed form, addition of Cl^- displaces the Rh–N bond clearing the path for ε-caprolactone binding at Al and polymerization. Addition of Na^+ halts catalysis via Cl^- abstraction, and NaCl precipitation. This process of Cl^- addition/Cl^- abstraction is fully reversible and can be used multiple times to start/stop catalysis. This example represents a clever, albeit elaborate, method to utilize static hemilability in one metal to control substrate access to a separate metal. As such, this impressive method of physically blocking substrate access[57] to control catalysis requires careful ligand design and considerable synthesis.

Scheme 1.10

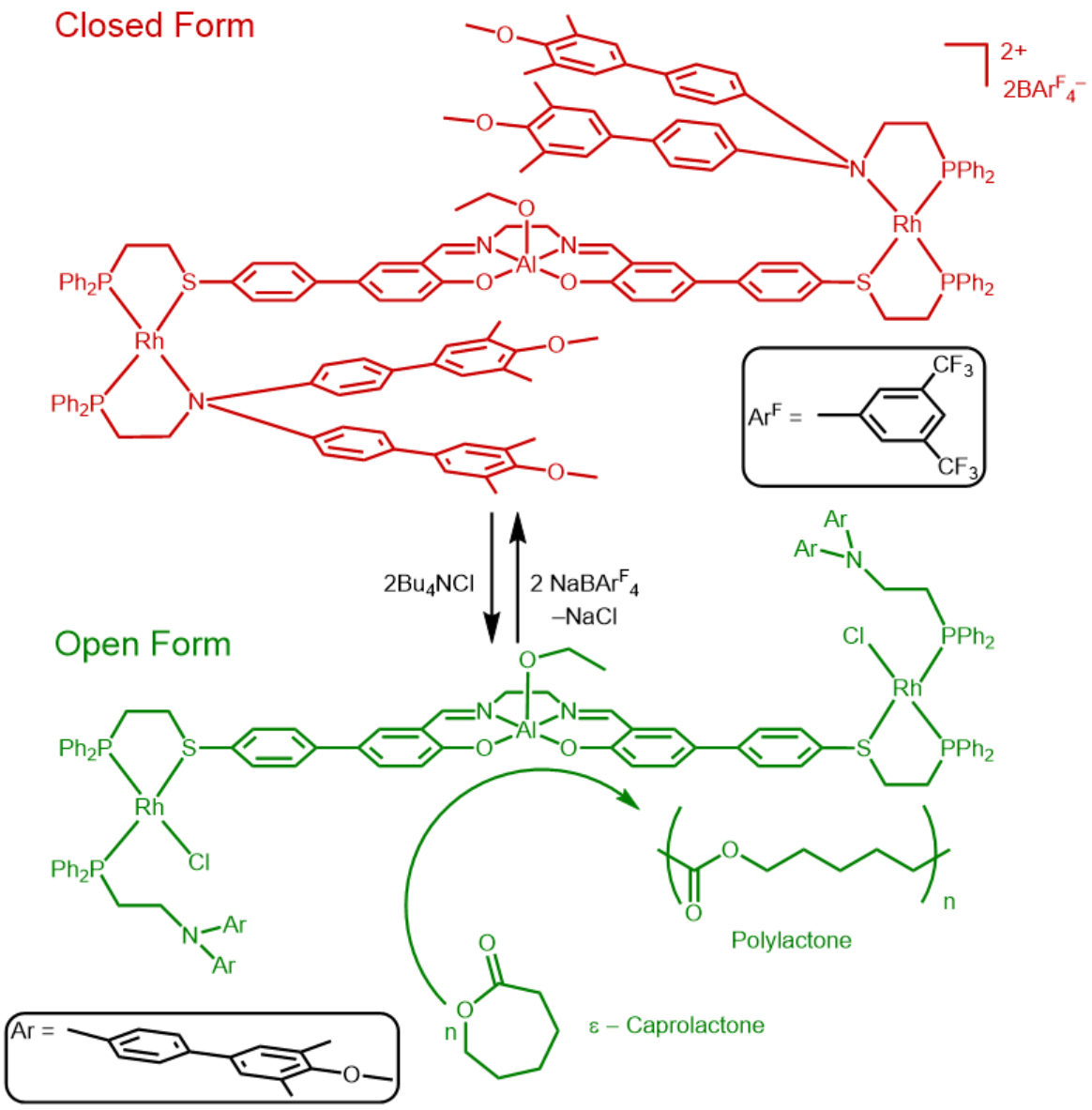

1.3 Towards Tunable Hemilabile Systems

In the examples mentioned for supramolecular constructs, photo-switchable systems, and redox-active ligands, external additives add tunable functionality to the systems for greater control over reactivity. In examples containing dynamic hemilabile ligands however, few examples exist where external stimuli function to tune the reactivity. We were interested in developing an approach where external stimuli could interact with the open form of a dynamic

hemilabile system to tune the approach of substrates to the primary metal coordination sphere. We thus set out to create a new method to tune dynamic hemilabilty. To achieve this goal, systems were imagined that could tune chelate opening with chemical additives *that would bind to the dissociated form of the ligand but not bind to the metal center*. As shown in scheme 1.11, an external chemical additive would bind the dissociated ligand in the secondary coordination sphere, providing a new method for tuning substrate access. Each unique chemical additive could have a different equilibrium interaction with the hemilabile ligand, thus providing a range of reactivity based on choice of additives.

Scheme 1.11

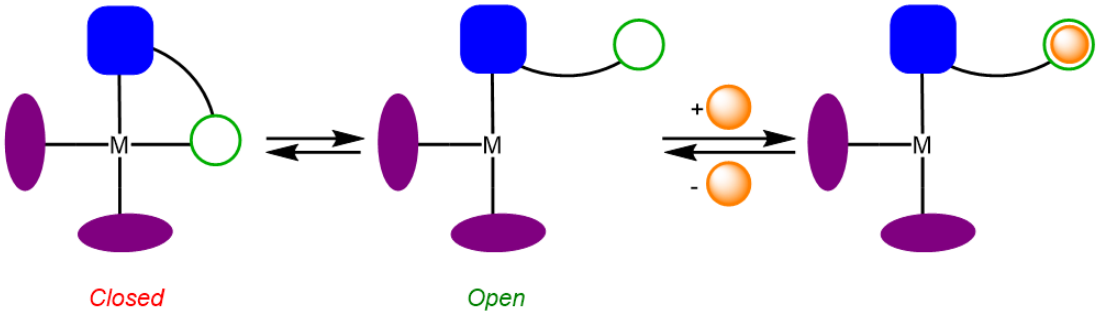

Most ligands are Lewis basic, so strong interactions would most likely be possible with Lewis acidic additives. To best apply this proposed method, we sought families of Lewis acids that contain large variation and are readily available. From this perspective, metal cations were the obvious choice. Alkali metal cations (Li^+, Na^+, K^+, Rb^+) are all monocationic but can be used to tune the secondary coordination equilibrium based on size. Alternatively, the equilibrium can be tuned by changing the charge on the cation (K^+, Ca^{2+}, Sc^{3+}) while maintaining similar size. The many metal cations available means the reactivity of one transition metal complex can be tuned based on cation choice, and does not necessitate the synthesis of a new complex.

Organic chemists have documented the interactions of crown ethers with Lewis acidic cations in great detail, providing a solid foundation for predicting and understanding reactivity.[58–60] The incorporation of crown-ether groups in transition metal complexes was first reported in 1978 in a crown-ether substituted phosphine-ligated to platinum.[61] Since that initial report, many other transition metal complexes with crown-ether functionality have been reported.[62–64] None of the metallo-crown ether complexes have featured hemilabile crown ether groups, however.

We thus hypothesized that it would be possible to tune dynamic hemilabilty utilizing a transition metal complex containing a hemilabile crown-ether functionality. A transition metal complex containing a crown ether functional group could bind a metal center forming multiple M–O bonds reversibly. When the M–O bonds dissociate to the open form, the Lewis basic sites on the crown ether macrocycle can interact with Lewis acidic cations. This binding event can make the open form more favorable, thus altering the concentration of unbound ligand, effectively creating a way to tune substrate access to the metal center.

To realize a transition metal complex with Lewis acid tunable dynamic hemilability we sought a new pincer-crown ether ligand that could bind a transition metal securely, but also feature multiple hemilabile M–O bonds. Next, simple ligand displacement reactions would be performed to understand the mechanism of substrate binding, and how cations affect this process. This fundamental understanding of the system could then be translated into reactivity studies and catalysis. Ultimately these studies will provide a framework for understanding the features needed to achieve stimuli-tunable dynamic hemilability.

Chapter 2 : SYNTHESIS OF IRIDIUM PINCER-CROWN ETHER COMPLEXES

Reproduced in part with permission from:

Kita, M. R.; Miller, A. J. M. *J. Am. Chem. Soc.* **2014**, *136*, 14519–14529.

Grajeda, J.; Kita, M. R.; Gregor, L. C.; White, P. S.; Miller, A. J. M. *Organometallics,* **2016**, *35*, 306-316.

Camp, A. M.; Kita, M. R.; Grajeda, J.; White, P. S.; Miller, A. J. M. *Inorganic Chemistry*, submitted.

2.1 Introduction

To target cation tunable hemilabile ligands, a robust framework was envisioned that would contain:

1) Strong chelating donors to prevent full ligand dissociation
2) A phosphine with tunable steric and electronic properties
3) One or more weak hemilabile ether and amine donors
4) A cation binding pocket via crown-ether functionality

Aminophosphine pincer ligands offered all of the needed features. The weak macrocyclic aza-crown ether donor would be balanced by strong phosphinite and phenyl anion donors (Scheme 2.1 A). Such "pincer-crown ether" ligands can be altered to tune the steric and electronic properties of the phosphine moiety, and the cation accepting preference via crown-ether size. For example, we hypothesized ^{15c5}NCOP^{iPr} would prefer smaller cations than ^{18c6}NCOP^{iPr}, whereas

^{15c5}NCOP^{tBu} would provide more steric congestion around the metal center than ^{15c5}NCOP^{iPr} (Scheme 2.1 B).

Scheme 2.1: Pincer-crown ether ligands

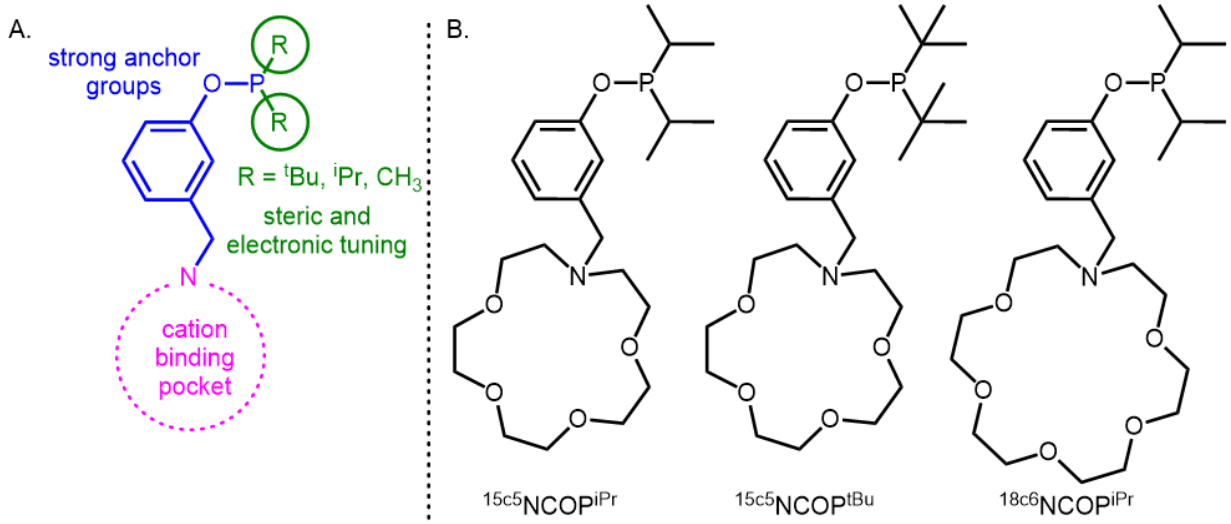

Pincer-crown ether ligands could conceivably bind a transition metal fragment L_nM in a number of binding modes. In scheme 2.2, pincer-crown ether ligand ^{15c5}NCOP^{R} binds a transition metal fragment L_nM to form numerous coordination modes ranging from κ^3 to κ^5. Cation binding is readily accessible from κ^3-(^{15c5}NCOP^{R})ML_n and could provide further electronic tuning, or guide anionic substrates towards the metal center. From κ^4-(^{15c5}NCOP^{R})ML_n and κ^5-(^{15c5}NCOP^{R})ML_n, M–O bond dissociation would likely be implicated prior to ligand substitution. Cations in solution could bind the dissociated form, stabilizing the species and aid ligand dissociation. Cation tunable hemilability was expected to be readily accessible from κ^4 and κ^5 modes, as M–O bonds can be weak (~5–18 kcal•mol^{-1}). Scission of the tertiary amine bond from the κ^3 mode was expected to be more difficult (18-28 kcal•mol^{-}).[57]

Scheme 2.2: Various binding modes of $^{15c5}NCOP^{R}$

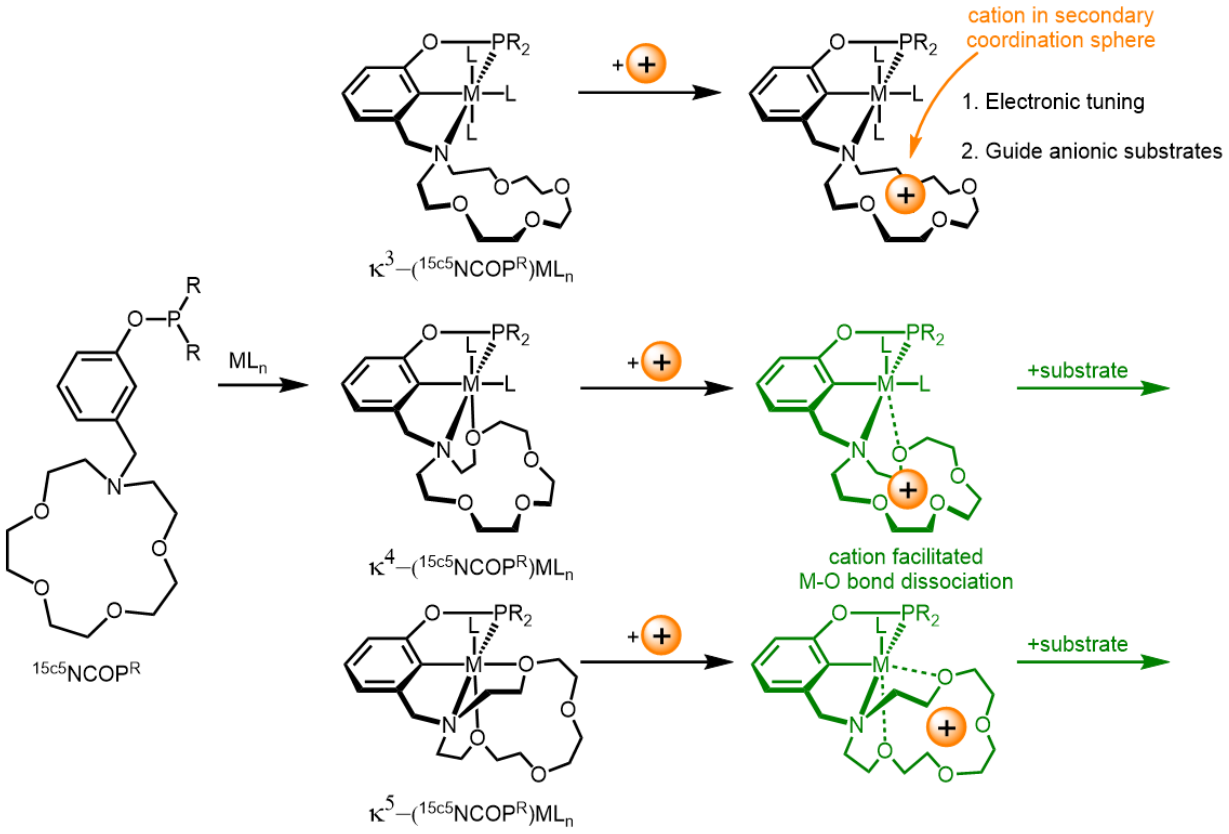

2.2 Results and Discussion

Ligand Synthesis

The aminophosphine ligand ($^{15c5}NCOP^{iPr}$)H, containing an aza-15-crown-5 macrocycle, was synthesized according to Scheme 2.3. Amination of 3-bromomethylphenol[65] with aza-15-crown-5 in refluxing acetonitrile afforded the aminophenol intermediate in 53% yield.[66] Subsequent phosphination using triethylamine and di-isopropyl-chlorophosphine gave ($^{15c5}NCOP^{iPr}$)H in 91% yield as a viscous, colorless oil. Phosphination of the aminophenol intermediate with di-tert-butylchlorophosphine produced ($^{15c5}NCOP^{tBu}$)H in 45% yield. Despite the structural similarity to diethylamino and morpholino containing NCOP ligands recently reported by Zargarian and coworkers,[67–69] their reductive amination procedure of 3-

hydroxybenzaldehyde with $NaBH_4$ was unable to install the poorly nucleophilic aza-crown amine arm. However, our group recently developed alternative reductive amination conditions using sodium triacetoxyborohydride $NaBH(OAc)_3$ to synthetize the aminophenol intermediates.[70]

Scheme 2.3: Synthesis of (^{15c5}NCOP^{iPr})H and (^{15c5}NCOP^{tBu})H

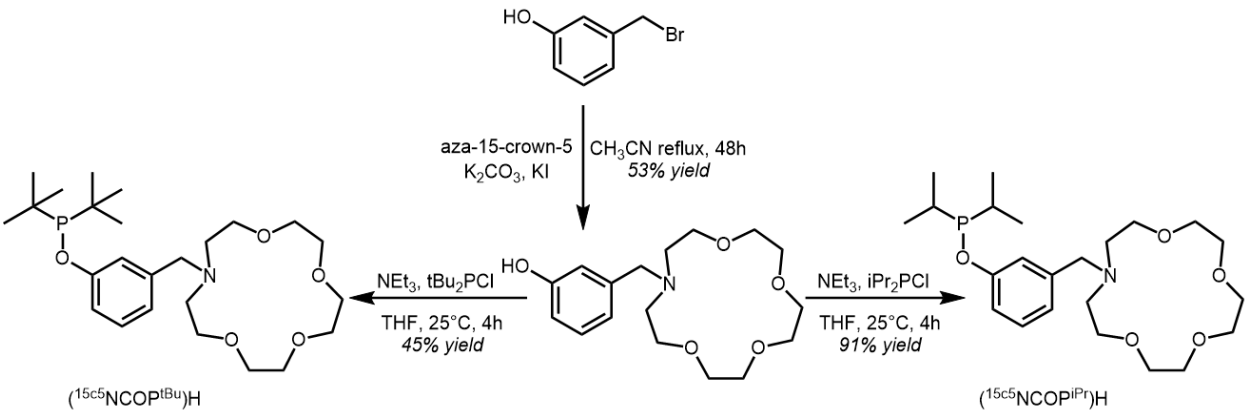

Metalation Attempt with (^{15c5}NCOP^{tBu})H

Allowing the more bulky ligand (^{15c5}NCOP^{tBu})H to react with $[Ir(Cl)(COD)]_2$ in benzene at 333 K did not yield the expected κ^3-(^{15c5}NCOP^{iPr})Ir geometry, but gave three different products according to the ^{31}P NMR spectrum, with one product accounting for ~80% of the iridium in solution. In the aromatic region of the ^{1}H NMR spectra, a 1H singlet and two 1H doublets were observed suggesting backwards metalation of (^{15c5}NCOP^{tBu})H according to scheme 2.4. After multiple attempts, we were never able to get this reaction to run cleanly. We hypothesized that the bulky *tert*-butyl groups produced too much steric clash about the Ir center to allow a κ^3-NCP coordination geometry.

Scheme 2.4: Proposed metalation product of (^{15c5}NCOP^{tBu})H

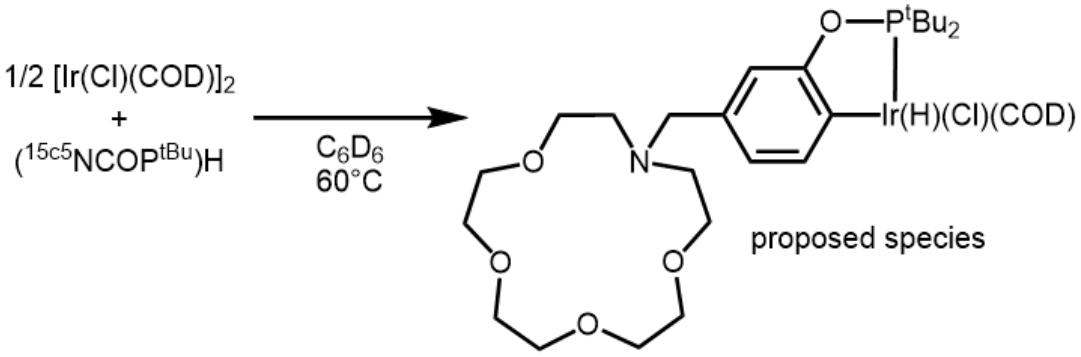

Synthesis of κ^4-(^{15c5}NCOP^{iPr})Ir(H)(Cl) (1)

We hypothesized that the smaller diisopropylphosphine containing ligand would be easier to metalate on Ir. Metalation proceeded smoothly when (^{15c5}NCOP^{iPr})H was allowed to react with [Ir(Cl)(COD)]$_2$ in benzene at 333 K for 12 hours forming κ^4-(^{15c5}NCOP^{iPr})Ir(H)(Cl) **(1)** (Scheme 2.5). A single resonance was observed in the ^{31}P{^{1}H} NMR spectrum (δ 143). From the ^{1}H NMR spectrum of **1**, it is immediately apparent that the plane of symmetry containing the phenyl ring is broken, with four independent isopropyl methyl doublet of doublet resonances. The expected tridentate NCP coordination was suggested by the presence of three 1H resonances in the aromatic region appearing as two doublets and a triplet. However, the tetradentate coordination mode shown in Scheme 2.5 was initially suggested by the hydride resonance of **1** (δ –31.2), which was found in an unusual region for iridium hydrochloride complexes. Five-coordinate iridium hydrochloride complexes such as (POCOP)Ir(H)(Cl) (POCOP is 2,6-bis[di-(tert-butyl)phosphinyloxy)]phenyl) are typically found far upfield (δ –40 to –42), whereas 6-

coordinate iridium hydrochloride complexes are typically found at lower field (δ –15 to –25).[71] The intermediate hydride chemical shift is consistent with a weak donor trans to the hydride.[72] The aza-crown ether resonances are also found in unusual spectral regions, with downfield multiplets (δ 5.04, 4.94) reminiscent of Ir(III) complexes of tetradentate bis-NHC ligands with chelating alkyl ether arms.[73] Utilizing different multinuclear NMR techniques, the unusual down field shifts were attributed to two protons with close proximity to the Cl^- ligand.[74] These protons are subjected to anisotropic effects from the Cl^- and thus shift downfield.

Scheme 2.5: Synthesis of κ^4-(^{15c5}NCOP^{iPr})Ir(H)(Cl)

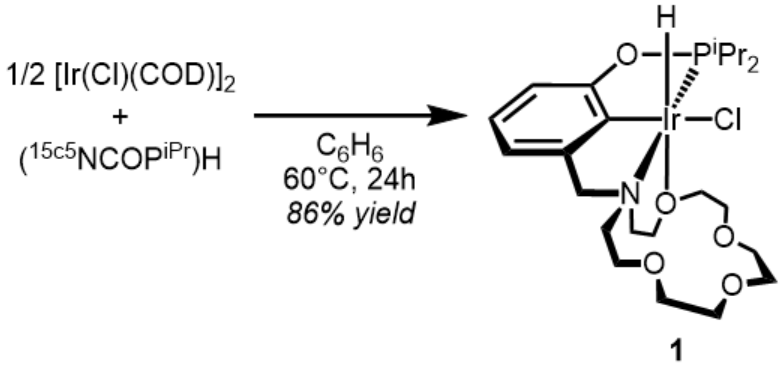

Lemon yellow single crystals of **1** suitable for an X-ray diffraction (XRD) study were obtained from a toluene solution layered with pentane at 243 K. XRD of **1** confirmed the tetradentate coordination mode, with one of the crown ether oxygen atoms bound *trans* to the hydride (Figure 2.1). The *κ⁴-mer,fac* coordination features a long Ir–O distance (2.355(4) Å) and an acute 78.5º N–Ir–O bond angle. Chelating dialkyl ether donors typically exhibit Ir–O distances in the range 2.10–2.25 Å,[75–78] although examples with longer distances have been reported.[79]

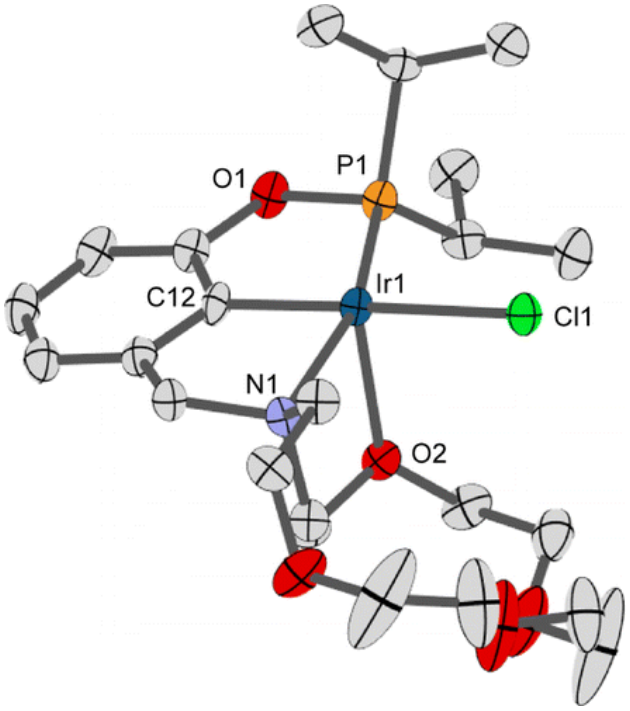

Figure 2.1: Structural representation of **1** with ellipsoids drawn at the 50% probability level. Hydrogen atoms are omitted for clarity. Selected distances (Å) and angles (deg): Ir1–P1 2.1825(14), Ir1–O2 2.355(4), Ir1–C12 1.979(5), Ir1–N1 2.222(5), Ir1–Cl1 2.4672(13); P1–Ir1–O2 99.63(10), O2–Ir1–Cl1 93.28(10), C12–Ir1–O2 88.23(19), C12–Ir1–Cl1 174.73(17), N1–Ir1–O2 78.46(15).

Synthesis of [κ^5-(^{15c5}NCOP^{iPr})Ir(H)][BAr$^F{}_4$]

Addition of NaBAr$^F{}_4$ (Ar^F is 3,5-bis(trifluoromethyl)phenyl) to a lemon yellow dichloromethane solution of **1** resulted in rapid color change to a dark orange solution, that slowly changes to a pale orange as precipitation of NaCl and formation of [κ^5-(^{15c5}NCOP^{iPr})Ir(H)][BAr$^F{}_4$] (**2**) occurred (Scheme 2.6). Solutions of **2** in $CDCl_3$ reveal two new BAr$^F{}_4$ singlets by ^{1}H NMR spectroscopy in the aromatic region, integrating to the expected 4H and 8H. In the crown ether region of the ^{1}H NMR spectra, 0.5 ppm upfield shifts relative to complex **1** were observed with loss of Cl^- anisotropy,[74] while the hydride region showed only a subtle shift (Ir–H δ –30.2) indicating that the trans Ir–O bond was maintained. Clean conversion to a new species was supported by the formation of a new singlet by ^{31}P{^{1}H} NMR at δ 141.

Scheme 2.6: Synthesis of [κ^5-(^{15c5}NCOP^{iPr})Ir(H)][BAr$^F_4$]

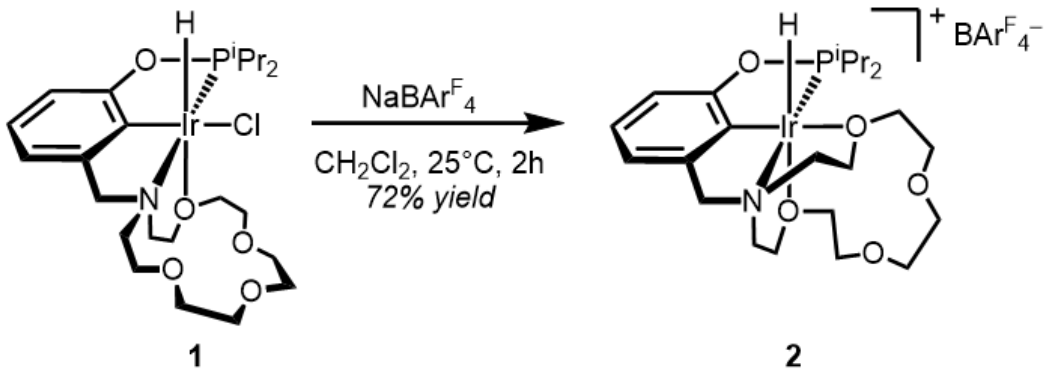

1 **2**

Vapor diffusion of pentane into toluene solutions of complex **2** produced single crystals at 243 K. An XRD study confirmed chloride abstraction and revealed coordination of a second crown ether oxygen. The Ir1–O2 distance (*trans* to hydride) of 2.229(2) Å and the Ir1–O5 distance (*trans* to phenyl) of 2.277(2) Å are different in length, but still contracted relative to the Ir–O distance in **1**, as expected in moving to a cationic complex. The pentadentate coordination mode appears even more strained than the binding in **1**, however, with an acute N1-Ir-O5 bond angle of 76.5° (Figure 2.2). Complex **2** also exhibits an 11º torsion angle between the plane of the phenyl ring and the plane containing the N–Ir–P bonds (c.f. 5º in **1**).

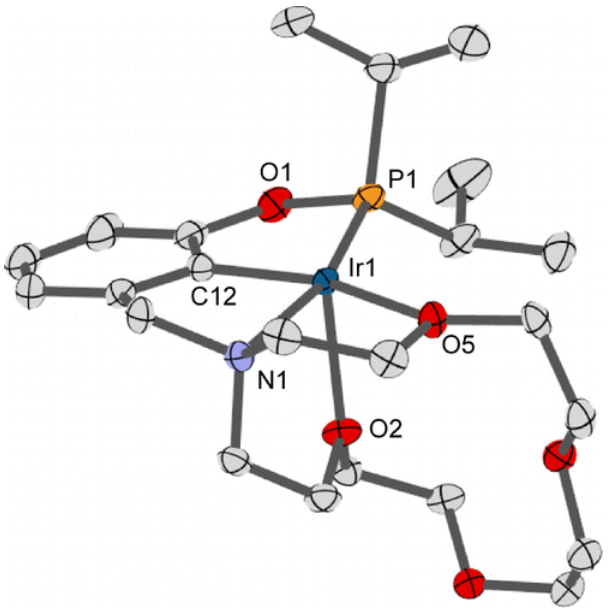

Figure 2.2: Structural representation of 2 with ellipsoids drawn at the 50% probability level. Hydrogen atoms and BArF4 anion omitted for clarity. Selected distances (Å) and angles (deg): Ir1–O2 2.228(2), Ir1–O5 2.276(2), Ir1–P1 2.2115(7), Ir1–N1 2.154(3), Ir1–C12 1.958(3); O2–Ir1–O5 85.90(8), N1–Ir1–O2 78.74(9), N1–Ir1–O5 76.55(9), C12–Ir1–O5 158.00(11).

The structural features of complexes **1** and **2** highlight the flexible coordination chemistry available to pincer-crown ether complexes. While a variety of crown ether-containing ligands,[63,80] including a few pincer ligands,[62,81] have been investigated, the Lewis basic sites on the macrocycle are rarely involved in the primary coordination sphere.[64] The ability of ^{15c5}NCOP^{iPr} to provide additional donors contrasts with the reactivity of (POCOP)Ir(H)(Cl), which undergoes halide abstraction to form weakly bound solvento complexes such as $[(POCOP)Ir(H)(CH_2Cl_2)]^+$.[82]

Addition of Ethers, Halides, and Nitriles to Displace the Ir–O Bond in Complex 1

The relative metal–ligand bond strengths in complexes **1** and **2** can be assessed experimentally through reactivity studies with nucleophiles: weak Ir–O bonds will be displaced by weakly Lewis basic donors; strong Ir–O bonds will only be displaced by strongly Lewis basic donors. The resulting products would possess the typical tridentate pincer geometry.

Weakly basic THF was investigated first. Addition of up to 300 equivalents of THF to a $CDCl_3$ solution of **2** did not result in any new species visible by ^1H or $^{31}P\{^1H\}$ NMR spectroscopy. THF is apparently too poor a ligand to displace the chelating ether donors in **2**.

Scheme 2.7: Formation of $[(\kappa^3\text{-}^{15c5}NCOP^{iPr})Ir(H)(Cl)_2]^-$

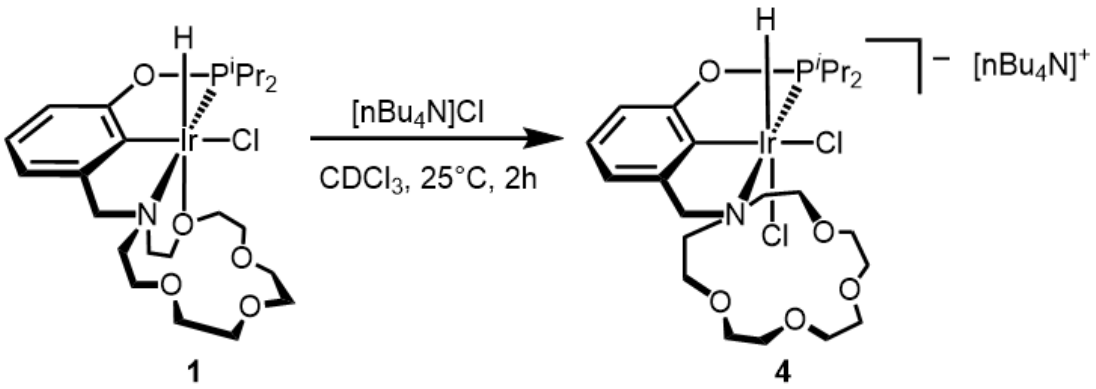

Unlike THF, a weak neutral donor, addition of $[Bu_4N][Cl]$ to **1** led to a mixture containing unreacted **1** along with a new species assigned as $[(\kappa^3\text{-}^{15c5}NCOP^{iPr})Ir(H)(Cl)_2]^-$ (**4**) (Scheme 2.7).[83] The hydride resonance of **4** (δ –24.17) indicates replacement of the ether ligand *trans* to the hydride site with a stronger donor.[71] When the analogous reaction with $[Bu_4N][Br]$ was carried out, we were surprised to observe *six* species by NMR spectroscopy. The hydride signals of these six species were observed as closely spaced pairs in three different regions (Figure 2.3) prompting the following assignments: **1**; the bromo analogue of **1**, $(\kappa^4\text{-}^{15c5}NCOP^{iPr})Ir(H)(Br)$; dichloride **4**; the dibromide analogue of **4**, $[(\kappa^3\text{-}^{15c5}NCOP^{iPr})Ir(H)(Br)_2]^-$; and the two possible bromochloride anion isomers. The presence of all possible halide species indicates that halide substitution is facile in chlorinated solvents.

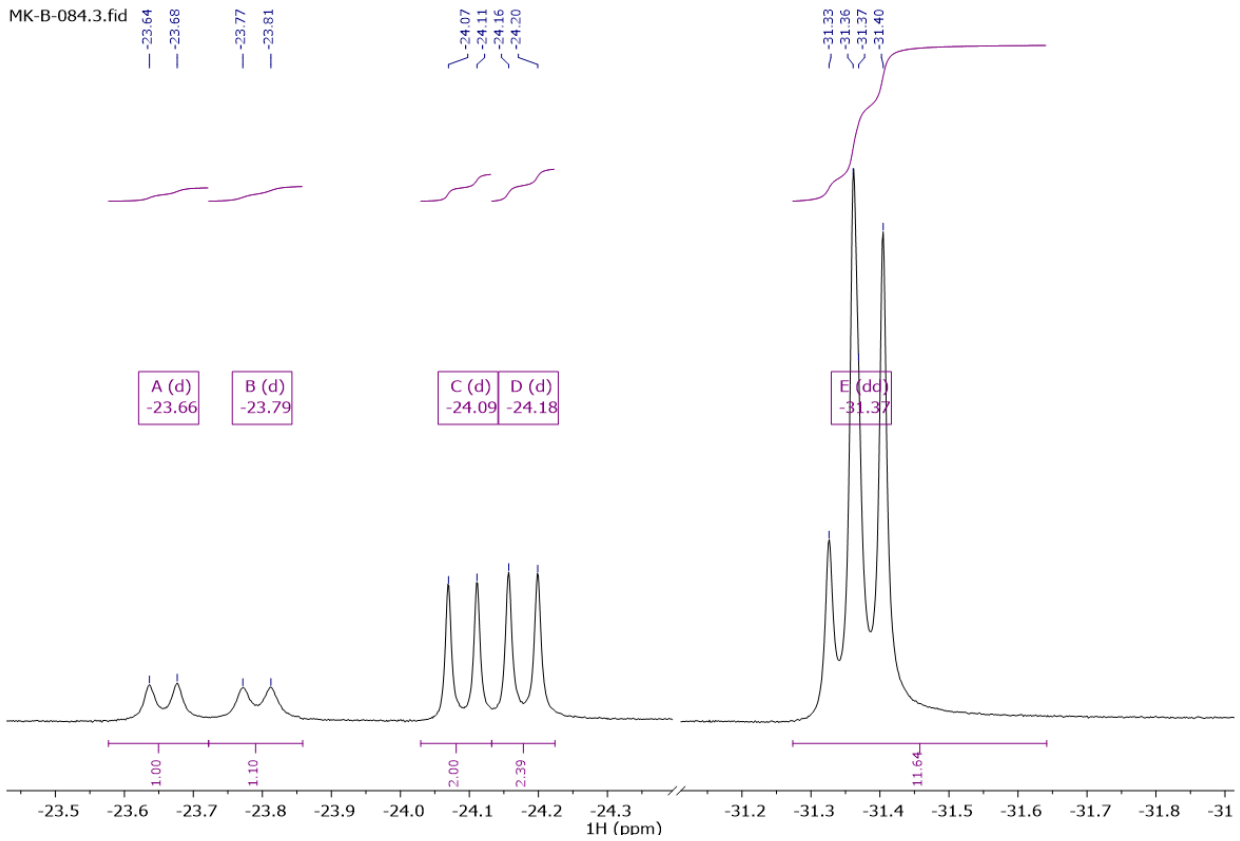

Figure 2.3: Hydride region for halide speciation from the addition of **1** and NBu_4Br in CD_2Cl_2. The peak at –31.39 is complex **1**; the overlapping peak at –31.34 is assigned to (^{15c5}NCOP^{iPr})Ir(H)(Br); the peak at –24.18 is [(^{15c5}NCOP^{iPr})Ir(H)(Cl)$_2$]$^-$; the peak at –24.09 is therefore assigned as the *cis*-hydrobromide [(^{15c5}NCOP^{iPr})Ir(H)(Br)(Cl)]$^-$; the peaks at –23.66 and –23.79 are assigned to the *cis*-hydrochloride [(^{15c5}NCOP^{iPr})Ir(H)(Cl)(Br)]$^-$ and the dibromide [(^{15c5}NCOP^{iPr})Ir(H)(Br)$_2$]$^-$.

The macrocyclic ether ligand of hydrochloride **1** is also readily displaced by CH_3CN, but the crown ether signals of **1** broadened substantially during addition, suggesting an additional fluxional process. Upon cooling to 273 K, the resonances sharpened and an additional species appeared. The two new species were hypothesized to be the stereoisomers of (κ^3-^{15c5}NCOP^{iPr})Ir(H)(Cl)($NCCH_3$) with *cis*-hydrochloride (**3**) and *trans*-hydrochloride (**3'**) arrangements.[84,85] The species were distinguished using an isotopic labeling experiment wherein$^{15}NCCH_3$ was added to **1**. The nucleus of ^{15}N is spin ½ which can couple to the Ir–H depending on geometry according to the Karplus equation. We expect small $^2J_{NH}$ coupling at 90˚,

and larger $^{2}J_{NH}$ coupling at 180˚. As shown in Figure 2.4, the broad hydride resonance at δ –21.9, previously observed as a doublet ($^{2}J_{PH}$ = 25.8 Hz), sharpened into a triplet ($^{2}J_{PH}$ = $^{2}J_{NH}$ = 26.3 Hz) upon cooling. The observed coupling constant assigns this minor product as **3**, with the hydride *trans* to $^{15}NCCH_3$. The major product observed at room temperature thus is *not* **3**, as expected, but rather the *trans*-hydrochloride isomer **3'**. Consistent with this assignment, the hydride resonance of **3'** (δ –23.05) exhibited weaker N-H coupling and remained a doublet in the labeling experiment ($^{2}J_{PH}$ = 23.5 Hz, $^{2}J_{NH}$ < 2 Hz).

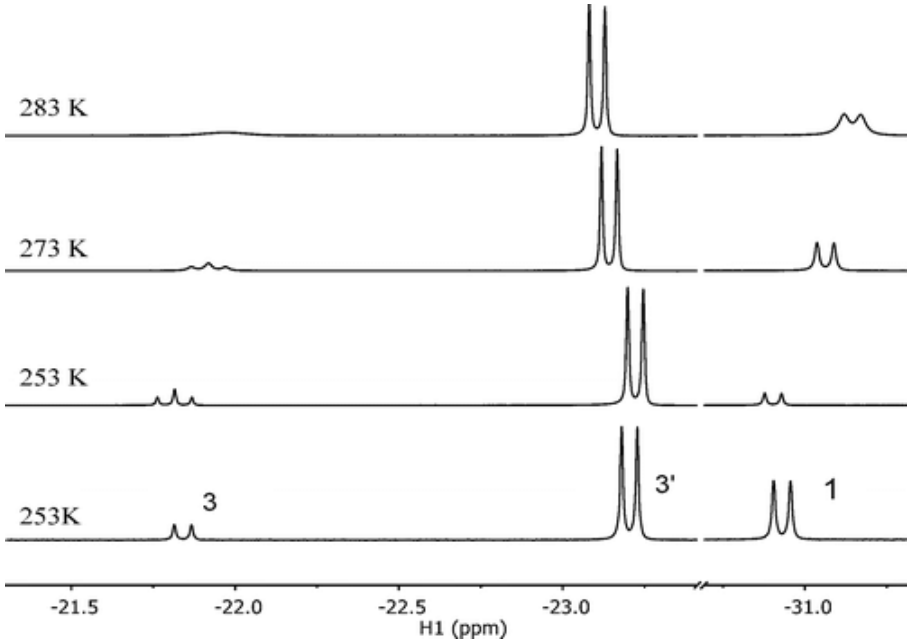

Figure 2.4: ^{1}H NMR spectra (hydride region) after addition of $^{15}NCCH_3$ to 1, at 283, 273, and 253 K. The bottom spectrum shows the mixture after addition of unlabeled CH_3CN to 1 at 253 K.

A plausible mechanism for the formation of **3** and **3′** from **1** that is consistent with the experimental observations is shown in Scheme 2.8. The roughly simultaneous broadening of signals for **1**, **3**, and free CH_3CN indicates that **1** and **3** are in dynamic equilibrium on the time scale of NMR spectral acquisition. Isomer **3′** could be formed by one of two slower processes, as shown in Scheme 2.8 via an unfavorable (and unobserved) cationic intermediate (path a) or

via **3** followed by isomerization (path b). The rapid scrambling observed upon addition of [Bu_4N][Br] to **1** suggest that path a is possible.

Scheme 2.8: $NCCH_3$ Binding pathways to 1

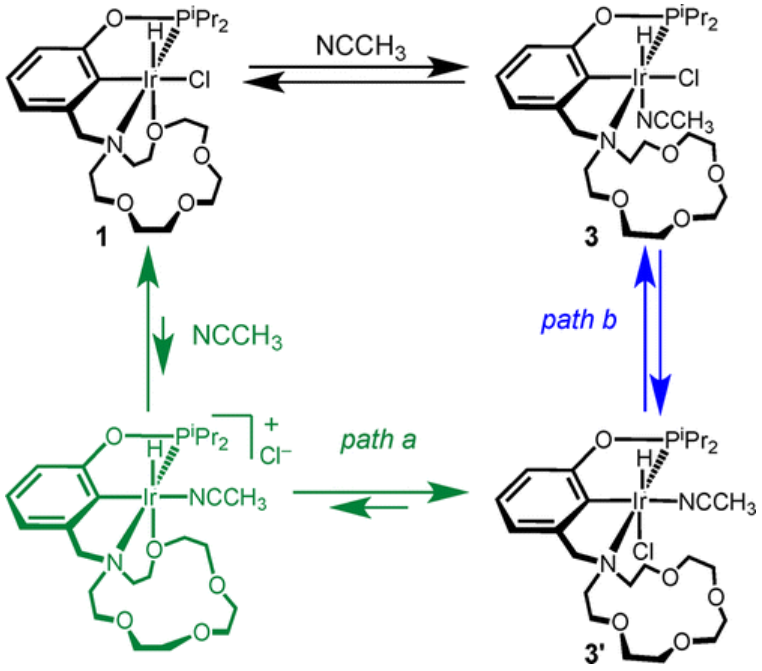

Thermodynamics of Nitrile Addition to Complex 1

Thermodynamic parameters for acetonitrile binding to **1** to form **3** and **3'** were extracted based on variable temperature (VT) NMR experiments using a Van 't Hoff analysis (Figure 2.5). Thermodynamic parameters for the conversion of **1** to **3** were as follows: ΔH^o = –8.67 kcal·mol^{-1}, ΔS^o = –26.6 cal·mol^{-1}·K^{-1}. The thermodynamic parameters for the conversion of **1** to **3'** were similar: ΔH^o = –8.50 kcal·mol^{-1}, ΔS^o = –22.4 cal·mol^{-1}·K^{-1}. The large negative entropy of reaction values are consistent with adduct formation being involved in each equilibrium.

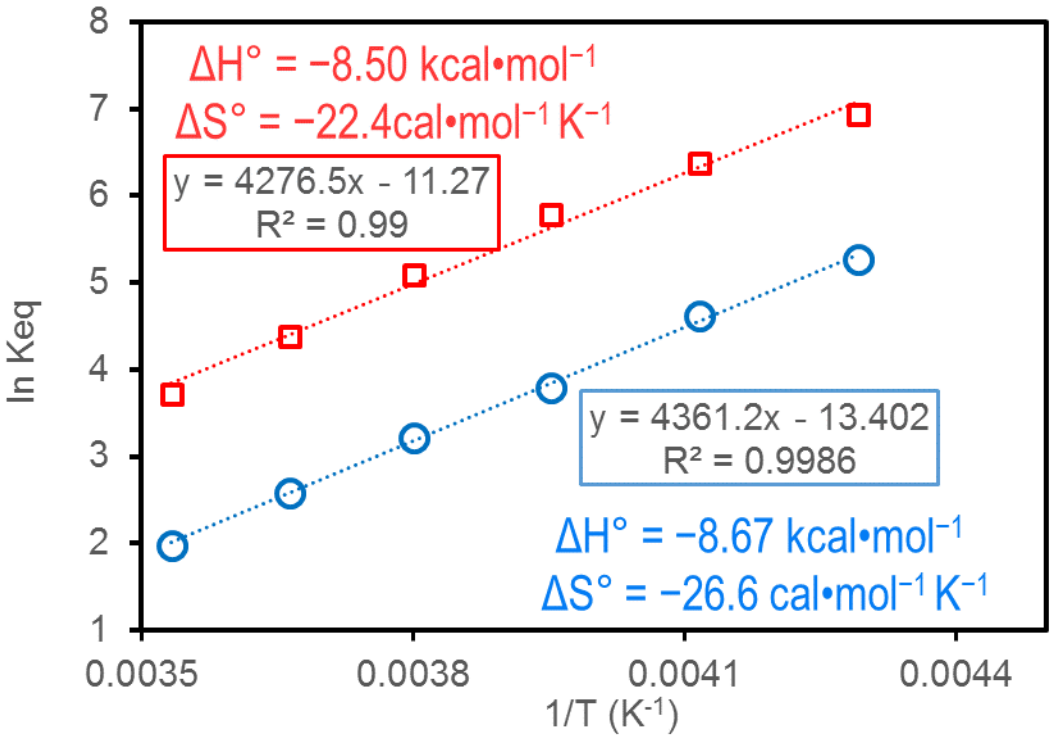

Figure 2.5: Van 't Hoff analysis of adduct formation between **1** and CH_3CN to produce **3** (empty blue circles with blue linear fit) and **3′** (empty red squares with red linear fit)

Thermodynamics of Nitrile Addition to Complex 2

Pentadentate-coordinated complex **2** reacts with acetonitrile as shown in Scheme 2.9. Addition of up to one equivalent of CH_3CN gave smooth, complete conversion to [(κ^4-^{15c5}NCOP)Ir(H)($NCCH_3$)]$^+$ (**5**) Binding was too strong for an equilibrium constant to be measured. Complex **5** has a *cis*-hydridonitrile geometry, as evidenced by the small (0.35 ppm) upfield shift of the hydride resonance consistent with an ether ligand remaining *trans* to hydride. Accordingly, when the $^{15}NCCH_3$ analogue of **5** was formed, no N–H coupling was observed.

The addition of more CH_3CN to **5** engaged an equilibrium between **5**, [(κ^3-^{15c5}NCOP^{iPr})Ir(H)($NCCH_3$)$_2$]$^+$ (**6**), and free CH_3CN (Scheme 2.9), K_{eq} = 34.0 M^{-1} at 298 K. The equilibrium between **5** and **6** with $NCCH_3$ was examined using VT NMR experiments. Thermodynamic parameters for the second step of Scheme 2.9 were obtained by Van 't Hoff

analysis (Figure 2.6): $\Delta H^o = -7.8$ kcal·mol^{-1} and $\Delta S^o = -19.6$ cal·mol^{-1}·K^{-1} The preference for substitution *trans* to phenyl is consistent with the longer, more strained Ir–O bond being more weakly bound. Both equilibria in scheme 2.9 are fully reversible, exposing mixtures of **5** and **6** to high vacuum lead to the reformation of complex **2.**

Scheme 2.9: $NCCH_3$ adduct formation with **2**

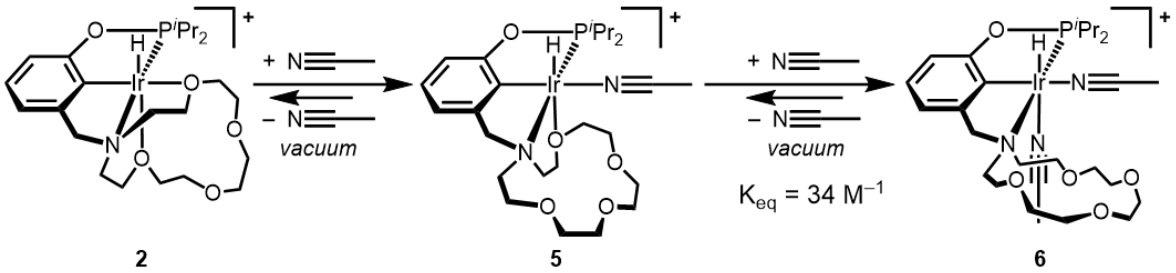

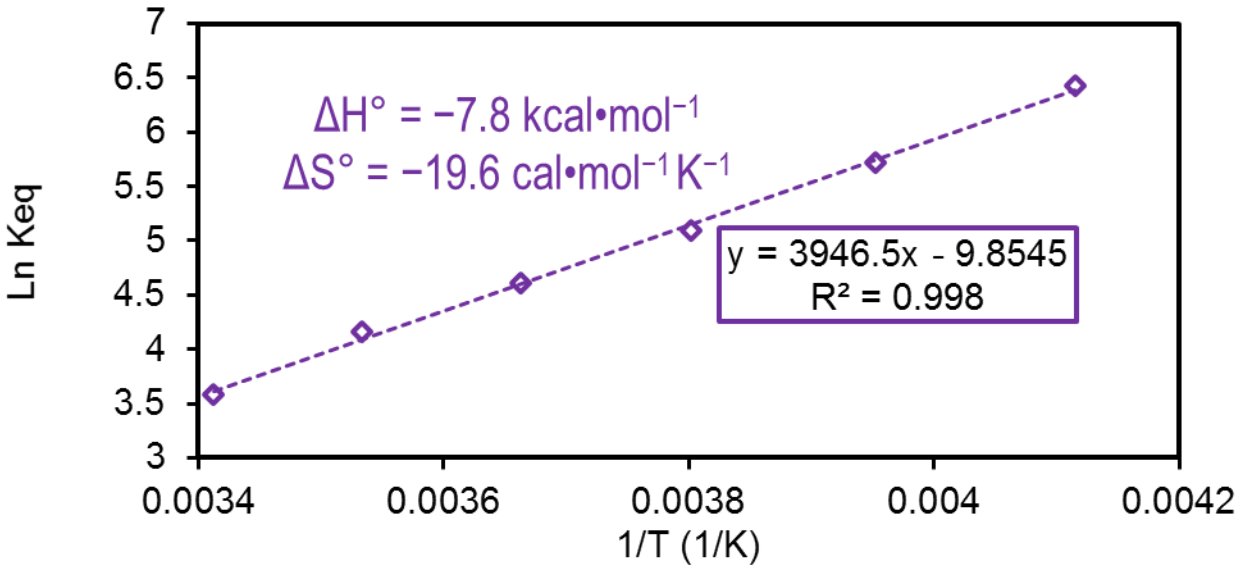

Figure 2.6: Van 't Hoff analysis for adduct formation between **5** and CH_3CN to produce **6** (purple diamonds with dashed linear fit)

Addition of H_2O to Complex 2

Trace amounts of H_2O in dichloromethane solutions of **2** were found to bind the Ir center and shift the hydride resonance upfield to δ –32.5. This small upfield shift is consistent with breaking the Ir–O bond *cis* to the Ir–O, maintaining the *trans* Ir–O. Exposing an authentic CD_2Cl_2 solution of **2** to excess H_2O and D_2O according to scheme 2.10 produced the expected hydride shift, and a singlet at δ 6.15. In the H_2O case, the singlet at δ 6.15 integrated to 2H and was assigned to the Ir–OH_2 species [κ^4-(^{15c5}NCOP^{iPr})Ir(H)(OH_2)][$BAr^F{}_4$] **(11)**.

Scheme 2.10:

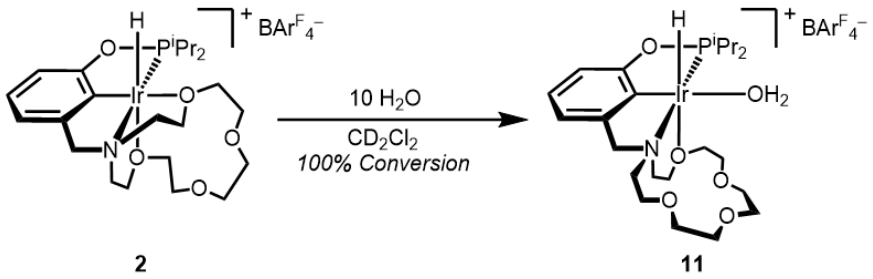

2 **11**

Addition of CO to complex 1

Continuing with our Lewis base screening, we decided to investigate the binding of CO to complexes **1** and **2**. As a ligand, CO has weak σ donor character, but strong π acidic character, therefore we expected the binding to be different than what was observed with $NCCH_3$.

Scheme 2.11

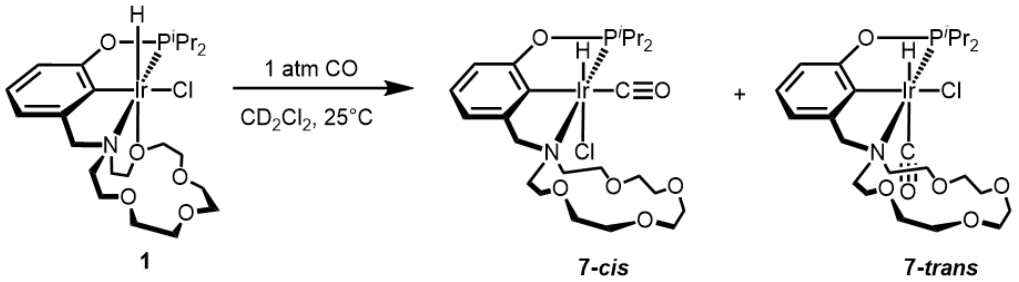

1 ***7-cis*** ***7-trans***

Exposing a pale-yellow solution of **1** in CD_2Cl_2 to 1 atm CO at 298 K produces a clear colorless solution. By ^1H NMR spectroscopy, two distinct hydride signals were observed at a ratio of 15:1 indicating CO adduct formation to generate cis/trans isomers of κ^3-(^{15c5}NCOP^{iPr})Ir(H)(Cl)(CO) **(7-*trans/cis*)** (Scheme 2.11). The major species in solution **(7-*trans*)** features a hydride resonance at δ –7.02 in the ^1H NMR spectrum, and a carbonyl carbon appearing as a doublet of doublets (δ 178.88, $^2J_{HC}$ = 56.6, $^2J_{PC}$ = 3.41) in the ^{13}C NMR spectum. Such a pattern is expected for a CO ligand binding *trans* to the hydride forming *trans*- κ^3-(^{15c5}NCOP^{iPr})Ir(H)(Cl)(CO) giving rise to hydride and phosphorus coupling. The minor species **(7-*cis*)** features a hydride resonance at δ –19.22 and no hydride coupling in the ^{13}C NMR spectra (δ 180.76, $^2J_{PC}$ = 4.59).

Upon heating the 15:1 solution of **(7-*trans/cis*)** to 50˚C for 60 h, thermal redistribution produced a 1:3 mixture of **(7-*trans/cis*)**, suggesting that **7-*cis*** is the thermodynamic product. This indicates that exposure of **1** to CO produces the kinetically favoured **7-*trans*** product via ether substitution. To confirm this result, an alternate synthesis of **7-*cis*** was targeted.

Allowing (^{15c5}NCOP^{iPr})H to react with Ir(*p*-toluidine)$(CO)_2$(Cl) in refluxing toluene produced *trans*-κ^3-(^{15c5}NCOP^{iPr})Ir(H)(Cl)(CO) **(7-*cis*)** in 95% yield as a brown-yellow solid (scheme 2.12). IR spectroscopy confirmed CO coordination with a diagnostic stretch at (ν_{CO} = 2010 cm^{-1}). Full characterization of **7-*cis*** via single crystal X-ray diffraction was reported by Grajeda et al and confirms the *cis*-hydriocarbonyl geometry.[86]

Scheme 2.12

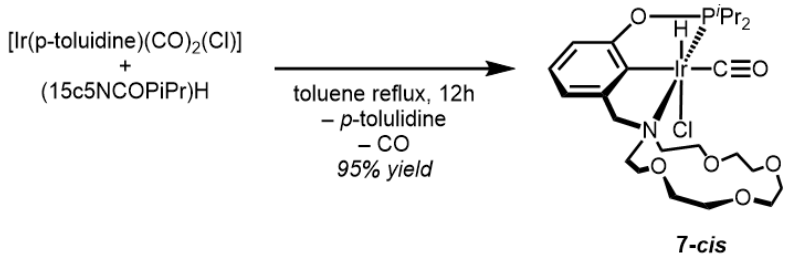

Halide abstraction from **7-*cis*** produced the cationic [κ^4-(^{15c5}NCOP^{iPr})Ir(H)(CO)][BAr$^F_4$] **(8)** in 92% yield upon mixing **7-*cis*** with NaBAr$^F_4$ in room temperature CH_2Cl_2 (Scheme 2.13). The diagnostic hydride shift (δ –25.8) in **8** suggests weak ether donor coordination *trans* to the hydride in tetradentate PCNO-*mer-fac* binding for the pincer-crown ether ligand. This geometry was confirmed via single crystal X-ray diffraction.[83] Surprisingly, **7-*cis*** and **7-*trans*** have different reactivity patterns with Na^+: halide abstraction from **7-*trans*** yields only trace amounts of **8** at room temperature. Even heating the mixture of **7-*trans*** and NaBAr$^F_4$ at 50˚C did not yield full conversion. We hypothesize that **7-*trans*** must isomerize to **7-*cis*** prior to Cl^- loss and ether oxygen coordination to yield **8.**

Scheme 2.13

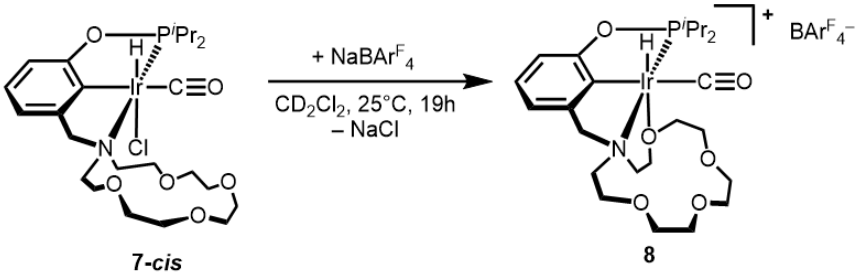

Alternative access to **8** can be achieved by exposing $CDCl_3$ solutions of cationic **2** to 1 atm CO at room temperature (Scheme 2.14). Upon CO exposure, an equilibrium mixture of

tetradentate **8** and tridentate [κ^3-(^{15c5}NCOP^{iPr})Ir(H)(CO)$_2$][BAr$^F{}_4$] **(9)** is observed. The identity of **9** features a hydride shift at δ –9.43, indicating a strong CO donor trans to the hydride and two CO resonances in the ^{13}C spectra (δ 168.51 (d, J = 2.85 Hz, trans-*C*O) 169.81 (s, cis-*C*O)). The *trans* CO in **9** is removed upon subjecting the solution to dynamic vacuum to produce **8**.

Scheme 2.14

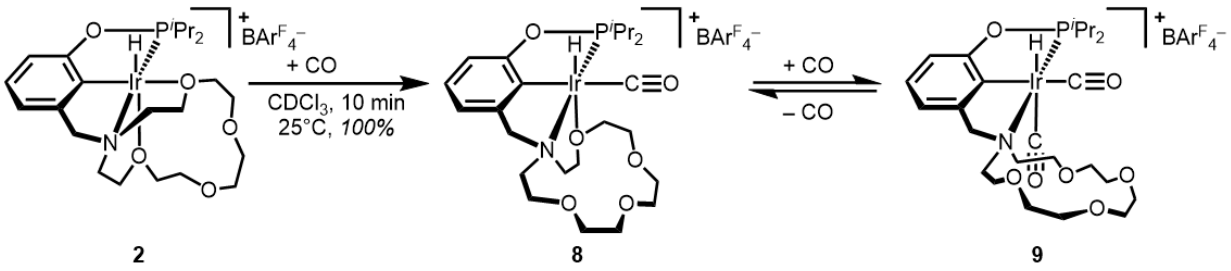

Group 9 carbonyl complexes are of particular interest for their potential application in methanol carbonylation.[87–89] Iridium carbonyl complexes used in methanol carbonylation must be able to successfully complete multiple 2e$^-$ redox events between Ir(III) and Ir(I). In this context, we were eager to reduce the above Ir(III) carbonyl complexes to form a Ir(I) carbonyl species. Reduction to Ir(I) was achieved according to scheme 2.15 via hydrodehalogenation. Reaction of **7-*cis*** with 1.5 equivalents KO^{t}Bu in benzene afforded the bright yellow κ^3-(^{15c5}NCOP^{iPr})Ir(CO) **(10)** in 78% yield.

Scheme 2.15

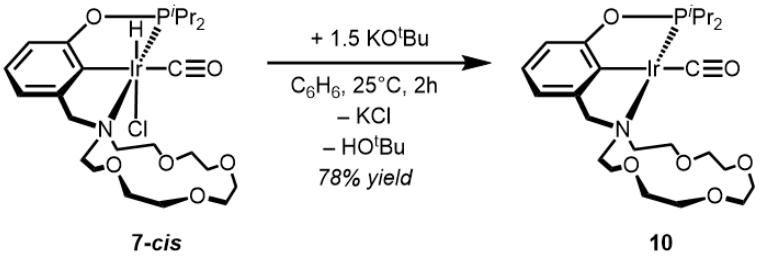

Aza-18-crown-6 Complexes on Iridium

Knowing that different crown ether sizes have varying affinities for lewis acidic cations,[58,60,90] we decided to target variants of complexes **1** and **2** with a larger aza-18-crown-6 macrocycle. The synthesis of (^{18c6}NCOP^{iPr})H was accomplished via the method reported by Gregor et al.[70] Allowing (^{18c6}NCOP^{iPr})H to react with 0.44 equivalents $[Ir(Cl)(COD)]_2$ in benzene at 343 K produced κ^4-(^{18c6}NCOP^{iPr})Ir(H)(Cl) **(12)** as a yellow solution (Scheme 2.16). A single resonance was observed in the $^{31}P\{^1H\}$ NMR spectrum (δ 142.9), along with a single hydride resonance at δ –31.26 in the ^{1}H NMR spectrum. These spectral features are similar to **1** suggesting similar coordination. The product was crystallized in 88% yield by layering pentane on a toluene solution of **12** at 25°C. Lemon yellow crystals of **12** suitable for XRD were obtained from the mixture to obtain a crystal structure shown in Figure 2.7.

Scheme 2.16:

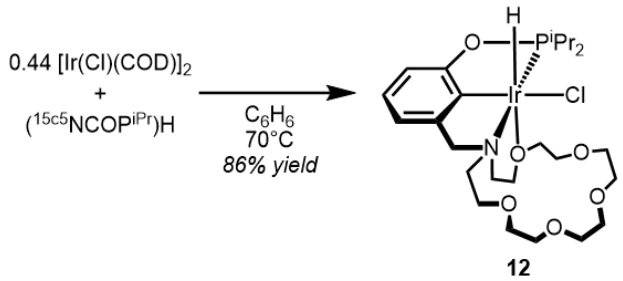

The crystal structure for **12** confirmed the same tetradentate *κ^4-mer,fac* coordination observed in **1** featuring a 0.028 Å shorter Ir–O distance (2.4545(9) Å), and an acute 79.6° N–Ir1–O bond angle. The Ir–Cl bond in **12** contracts 0.0127 Å relative to **1**, while the other bond distances in the primary coordination sphere are comparable within 0.0073 Å.

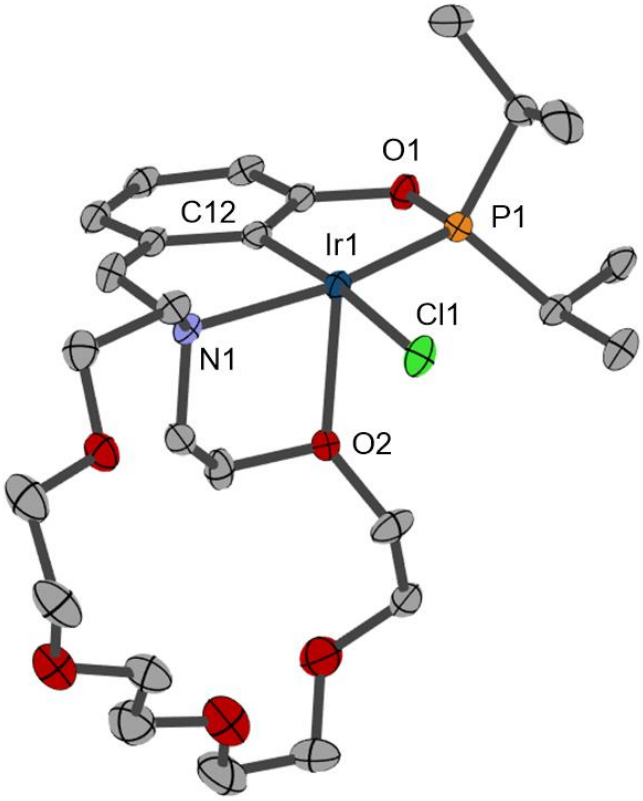

Figure 2.7: Structural representation of **12** with ellipsoids drawn at the 50% probability level. Hydrogen atoms are omitted for clarity. Selected distances (Å) and angles (deg): Ir1–P1 2.1897(9), Ir1–O2 2.327(2), Ir1–C12 1.973(4), Ir1–N1 2.219(3), Ir1–Cl1 2.4545(9); P1–Ir1–O2 99.00(7), O2–Ir1–Cl1 89.15(7), C12–Ir1–O2 88.71(12), C12–Ir1–Cl1 173.26(11), N1–Ir1–O2 79.63(10).

Dehalogenation of κ^4-(^{18c6}NCOP^{iPr})Ir(H)(Cl) with NaBAr$^F{}_4$ was attempted by mixing **12** with 1.1 equivalents NaBAr$^F{}_4$ in CH_2Cl_2. Upon mixing the yellow-orange solution of **12** with NaBAr$^F{}_4$, brick red [Na$^+$@κ^4(^{18c6}NCOP^{iPr})Ir(H)(Cl)][BAr$^F{}_4$] **(13)** formed within minutes (Na$^+$@ implies Na$^+$ coordination in the crown) (Scheme 2.17). A single hydride resonance 1.7 ppm *upfield* of **12** was observed at δ –32.96. In the dehalogenation of **1** to form **2**, the hydride resonance shifts *downfield* by ~1 ppm, with little change in the ^{31}P{^{1}H} NMR spectrum. In the ^{31}P{^{1}H} NMR spectrum of **13**, a single resonance at δ 132.1 was observed, 10.7 ppm upfield compared to **12**.

Scheme 2.17:

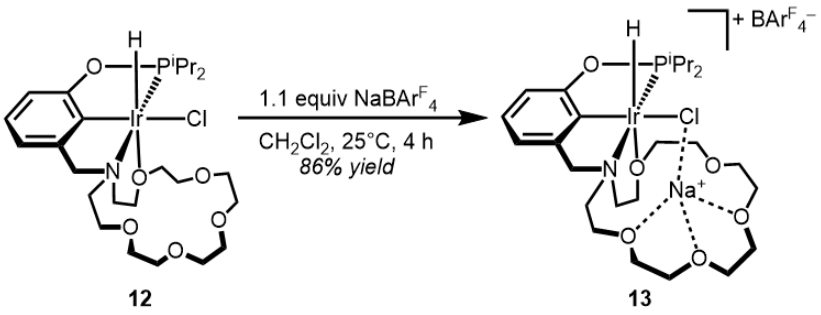

Single crystals suitable for XRD were grown from pentane layering on a toluene solution of **12** (Figure 2.8). The structure confirms the reaction product to be $[Na^{+}@\kappa^{4}(^{18c6}NCOP^{iPr})Ir(H)(Cl)][BAr^{F}{}_{4}]$ **(13)** featuring Na^{+} coordinated to the five crown ether oxygens (O–Na range 2.353-2.883 Å), and Cl^{-} (Na–Cl = 2.6415(17) Å). The Ir–Cl bond (2.4644(8) Å) only lengthens by 0.01 Å compared to **12**. Heating solutions of **13** to 83°C in 1,2-dichloro ethane failed to remove the NaCl unit by precipitation indicating that **13** is quite stable to Cl^{-} removal which is accounted for by the relatively unchanged Ir–Cl distance, long Na–Cl contact, and five O–Na contacts. We attribute the strong affinity of Na^{+} for 18-crown-6 for the lack of dehalogenation, which helps keep Na^{+} in solution.

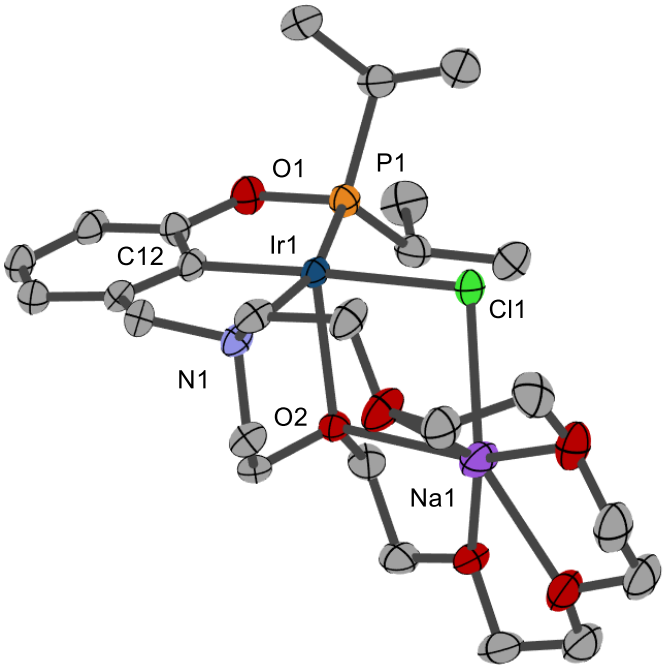

Figure 2.8: Structural representation of **13** with ellipsoids drawn at the 50% probability level. Hydrogen atoms are omitted for clarity. Selected distances (Å) and angles (deg): Ir1–P1 2.2052(9), Ir1–O2 2.349(2), Ir1–C12 1.991(3), Ir1–N1 2.289(3), Ir1–Cl1 2.4644(8); P1–Ir1–O2 108.07(6), O2–Ir1–Cl1 81.25(6), C12–Ir1–O2 96.11(11), C12–Ir1–Cl1 176.98(10), N1–Ir1–O2 75.69(9).

In an effort to remove Cl^-, a CH_2Cl_2 solution of **12** was treated with 1 equivalent $AgPF_6$ for one hour. The initial yellow-orange solution darkened overtime to an orange brown. The reaction mixture was filtered to remove AgCl, and solvent was removed in vacuo. The crude mixture was then dissolved in fresh CH_2Cl_2 and treated with 1.1 equivalents $NaBAr^F{}_4$ to drive $NaPF_6$ precipitation (Scheme 2.18). The reaction mixture was worked up by filtering off precipitates, and removing the solvent in vacuo. Toluene extraction on the solids yielded [κ^4-(^{18c6}NCOP^{iPr})Ir(H)(OH_2)][$BAr^F{}_4$] **(13)**. A single hydride resonance was observed at δ –32.5, nearly identical to that of **11**. Consistent with bound OH_2, a 2H singlet was observed at δ 5.56 that scrambled upon D_2O addition, and contained no cross peak in a ^{1}H-^{13}C HSQC.

Scheme 2.18

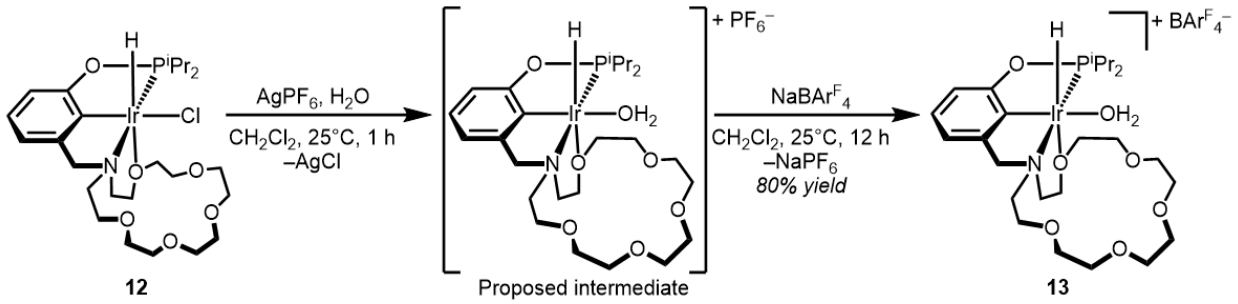

The OH_2 ligand on **13** was successfully removed according to scheme 2.19 by slowly heating solids of **13** under high vacuum to 105°C to yield [κ^5-(^{18c6}NCOP^{iPr})Ir(H)][BAr^F_4] **(14)**. A single hydride resonance was observed at δ –29.5, which matches closes with the aza-15-crown-5 analogue **2**. Additional development is needed to optimize this synthesis.

Scheme 2.19

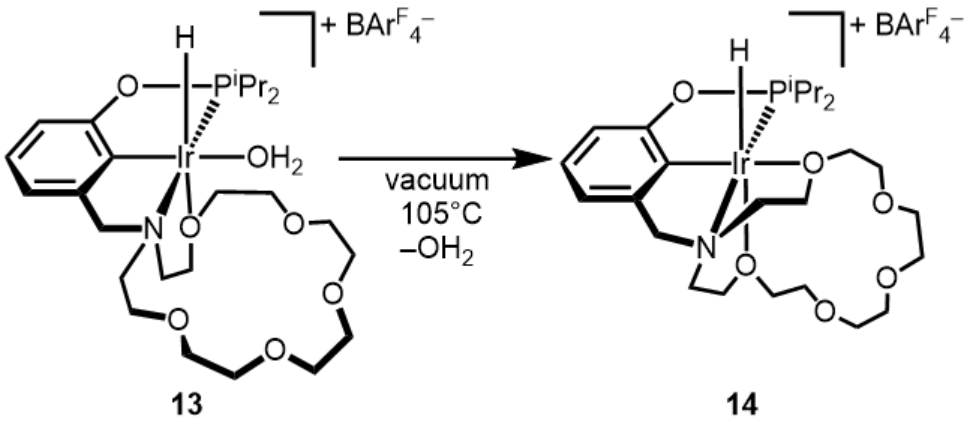

Conclusions

Towards the goal of controlling hemilability using chemical additives, we have successfully synthesized new iridium pincer-crown ether complexes with cation responsive aza-crown-ether macrocycles. The pincer-crown ether ligands bind iridium with reversible hemilabile behavior in a number of coordination modes ranging from κ^3 to κ^5. Weakly coordinating solvents like C_6D_6, CD_2Cl_2, and $CDCl_3$ do not displace Ir–O bonds, whereas

stronger donors like $NCCH_3$ bind the iridium center. In the context of future studies involving cation modulated hemilability, these weakly coordinating solvents should be used to maintain the Ir–O bonds.

2.3 Experimental Details

General Considerations

All compounds were manipulated using standard vacuum line or Schlenk techniques or in a glovebox under a nitrogen atmosphere. NMR scale reaction mixtures were prepared under nitrogen in a glovebox and kept in Teflon-sealed tubes. Under standard glovebox operating conditions, pentane, diethyl ether, benzene, toluene, and tetrahydrofuran were used without purging, such that traces of those solvents were present in the atmosphere and in the solvent bottles. ^{1}H, ^{31}P, ^{19}F, and ^{13}C NMR spectra were recorded on 400, 500, and 600 MHz spectrometers. NMR characterization data are reported at 298 K, unless specified otherwise. All NMR solvents and isotopically labeled reagents were purchased from Cambridge Isotope Laboratories, Inc. Benzene-d_6 (C_6D_6), chloroform-*d* ($CDCl_3$), and methylene chloride-d_2 (CD_2Cl_2) were freeze–pump–thaw degassed three times before drying by passage through a small column of activated alumina. Tetrahydrofuran-d_8 (THF-d_8) was purchased in a sealed ampule, which was broken under an N_2 atmosphere before filtration through activated alumina. Chemical shifts for ^{1}H and ^{13}C NMR spectra are reported in ppm relative to residual proteo solvent impurity.[91] ^{31}P resonances are reported relative to 85% H_3PO_4 external standard (0 ppm). ^{19}F resonances are reported relative to 0.05% trifluorotoluene ($C_6H_5CF_3$) in $CDCl_3$ as an external standard (−63.72 ppm). $NaBAr^F{}_4$,[92] $[H\cdot(OEt_2)_2][BAr^F{}_4]$,[93] and *m*-(bromomethyl)phenol[65] were synthesized according to literature procedures. All other reagents were commercially available and were used without further purification. Elemental analyses

were performed by Atlantic Microlabs (Norcross, GA) and Robertson Microlit Laboratories (Ledgewood, NJ).

Single-crystal X-ray diffraction (XRD) data for all complexes were collected on a Bruker Smart Apex-II diffractometer at 100 ± 2 K with Cu Kα radiation (λ = 1.54175 Å). Integration of diffraction profiles was done using the program SAINT. Absorption corrections were applied using TWINABS or SADABS. Structures for complex **1** and **2** were solved using direct methods and refined using the XL refinement package via least squares.[94] Hydrogen atoms were generated theoretically and refined isotropically with fixed thermal factors.

High-resolution mass spectrometry (HRMS) (resolution 100000, mass error ≤1 ppm) measurements were performed in positive ion mode on a Thermo Scientific LTQ-FT (Waltham, MA).

Synthesis of *m*-(Aza-15-crown-5)methylphenol

A 250 mL Schlenk flask was charged with 0.7943 g (4.077 mmol) of aza-15-crown-5, 0.567 g (4.103 mmol) of K_2CO_3, 0.690 g (4.096 mmol) of KI, 0.762 g (4.103 mmol) of *m*-(bromomethyl)phenol, and 100 mL of acetonitrile. The solution was degassed by sparging with nitrogen for 20 min. A reflux condenser was attached under N_2 counter flow, and the reaction mixture was refluxed for 48 h. The reaction mixture was cooled to room temperature and filtered in air, and the remaining solids were washed with acetonitrile. Solvent was removed from the filtrate by rotary evaporation to yield a white powder. This powder was dissolved in water and extracted with chloroform to remove any salts trapped in the macrocycle. The organic fractions were combined and concentrated by rotary evaporation to afford 0.604 g (53% yield) of *m*-(aza-15-crown-5)methylphenol as a brown oil. ^{1}H NMR (400 MHz, acetone-d_6): δ 7.10 (t, J = 7.8, 1H), 6.93 (s, 1H), 6.71 (dd, J = 8.0, 2.6, 2H), 3.67 (d, J = 3.0, 8H), 3.66–3.58 (m, 10H), 2.70

(t, J = 5.1, 4H). ^{1}H NMR (600 MHz, benzene-d_6): δ 7.86 (dd, J = 2.7, 1.4 Hz, 1H), 7.16 (t, J = 7.6 Hz, 1H), 7.02 (dd, J = 8.0, 2.6 Hz, 1H), 6.72 (dt, J = 7.5, 1.1 Hz, 1H), 3.53 (s, 2H), 3.43–3.39 (m, 8H), 3.36–3.33 (m, 4H), 3.32–3.28 (m, 4H), 2.57–2.53 (m, 4H). ^{13}C{^{1}H} NMR (151 MHz, benzene-d_6): δ 158.40, 143.13, 118.32, 116.48, 113.96, 71.28, 70.81, 70.17, 69.95, 59.86, 56.75. HRMS: m/z calcd for $C_{17}H_{28}O_5N$ ($M + H^+$) 326.19620, found m/z 326.19616.

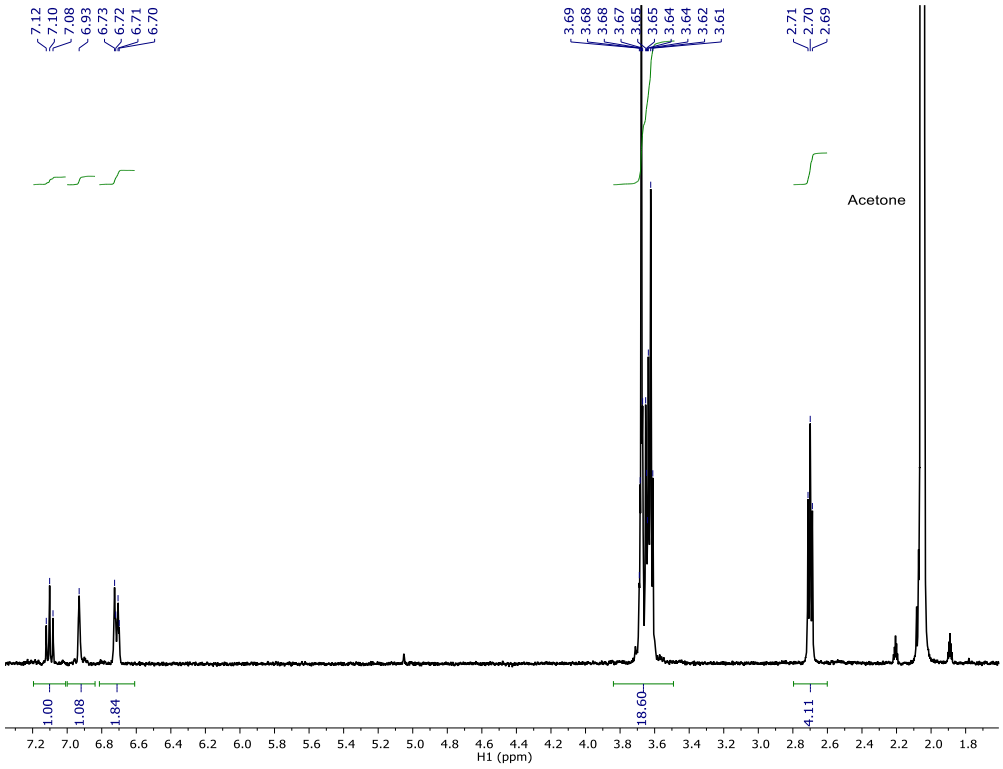

Figure 2.9: ^{1}H-NMR of 3-(aza-15-crown-5 ether)-methyl-phenol in Acetone-d_6

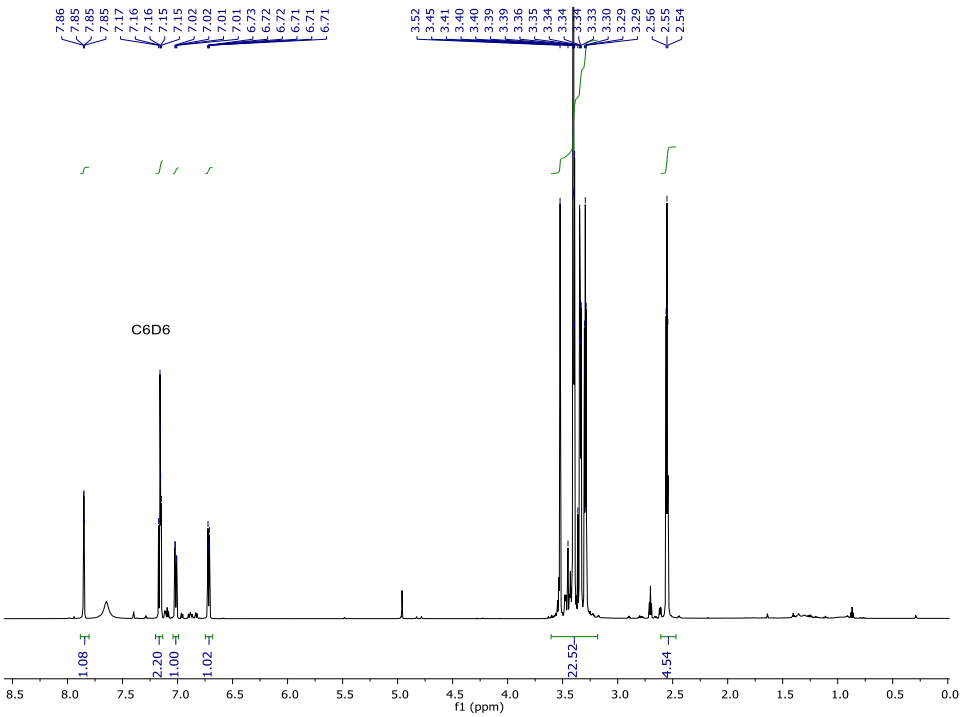

Figure 2.10: ^{1}H-NMR of 3-(aza-15-crown-5 ether)-methyl-phenol in C_6D_6

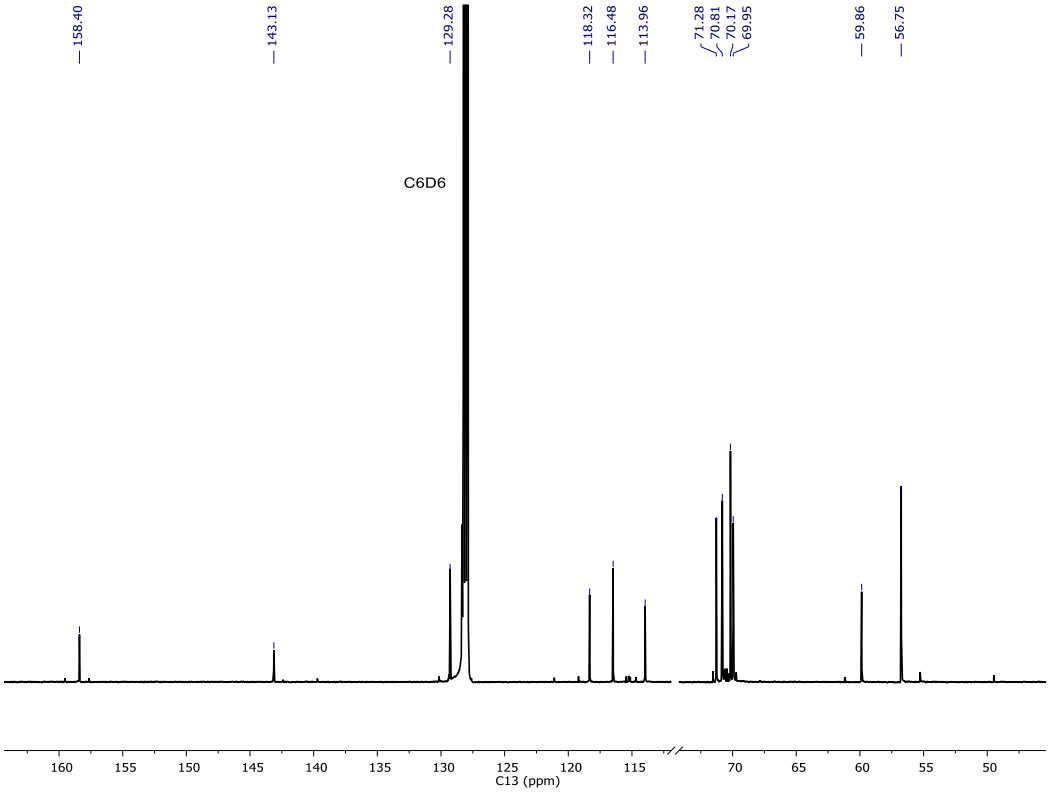

Figure 2.11: ^{13}C{^{1}H} NMR of 3-(aza-15-crown-5 ether)-methyl-phenol in C_6D_6

Synthesis of (^{15c5}NCOP^{iPr})H

In a glovebox, a 20 mL scintillation vial was charged with 0.134 g (0.412 mmol) of *m*-(aza-15-crown-5)methylphenol and 10 mL of THF. To the clear, colorless solution was added 64 μL (0.454 mmol) of triethylamine dropwise by syringe with stirring. After the mixture was stirred for 15 min, 65 μL (0.412 mmol) of diisopropylchlorophosphine was added dropwise by syringe with continued stirring. After chlorophosphine addition, the solution developed a light yellow-brown color. The solution was stirred for 4 h, during which time a white precipitate formed. Removal of solvents in vacuo yielded a mixture of an oil and a white powder. The oil was extracted with ether (5 × 2 mL) and filtered. The ether was removed in vacuo to yield 0.166 g (91% yield) of (^{15c5}NCOP^{iPr})H as a colorless oil. ^{1}H NMR (400 MHz, chloroform-*d*): δ 7.16 (t, *J* = 7.8 Hz, 1H), 7.05 (d, *J* = 2.0 Hz, 1H), 6.94 (dd, *J* = 11.0, 7.9 Hz, 2H), 3.72–3.58 (m, 16H), 2.79 (t, *J* = 6.1 Hz, 4H), 1.91 (sept d, *J* = 7.1, 2.4 Hz, 2H), 1.27–0.99 (m, 12H). ^{13}C NMR (151 MHz, chloroform-*d*): δ 159.45 (d, $^{2}J_{P–C}$ = 8.4 Hz), 141.51, 129.10, 122.17, 119.04 (d, $^{3}J_{P–C}$ = 9.6 Hz), 117.09 (d, $^{3}J_{P–C}$ = 10.9 Hz), 71.16, 70.72, 70.36, 70.27, 60.79, 54.43, 28.45 (d, $^{1}J_{P–C}$ = 17.4 Hz), 17.93 (d, $^{2}J_{P–C}$ = 20.1 Hz), 17.20 (d, $^{2}J_{P–C}$= 8.4 Hz). ^{31}P{^{1}H} NMR (162 MHz, chloroform-*d*): δ 149.86. HRMS: *m*/*z* calcd for $C_{23}H_{41}NO_5P$ ($M + H^+$) 442.27169, found *m*/*z* 442.27188.

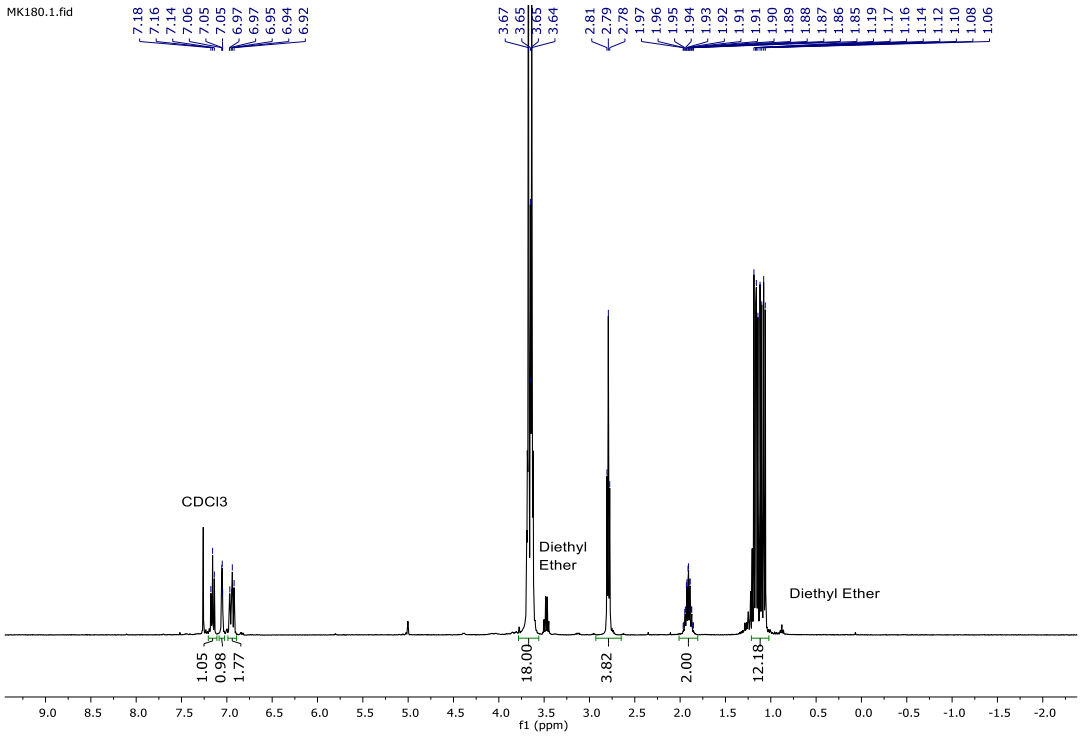

Figure 2.12: ^{1}H NMR of $^{15c5}NCOP^{iPr}$ in $CDCl_3$

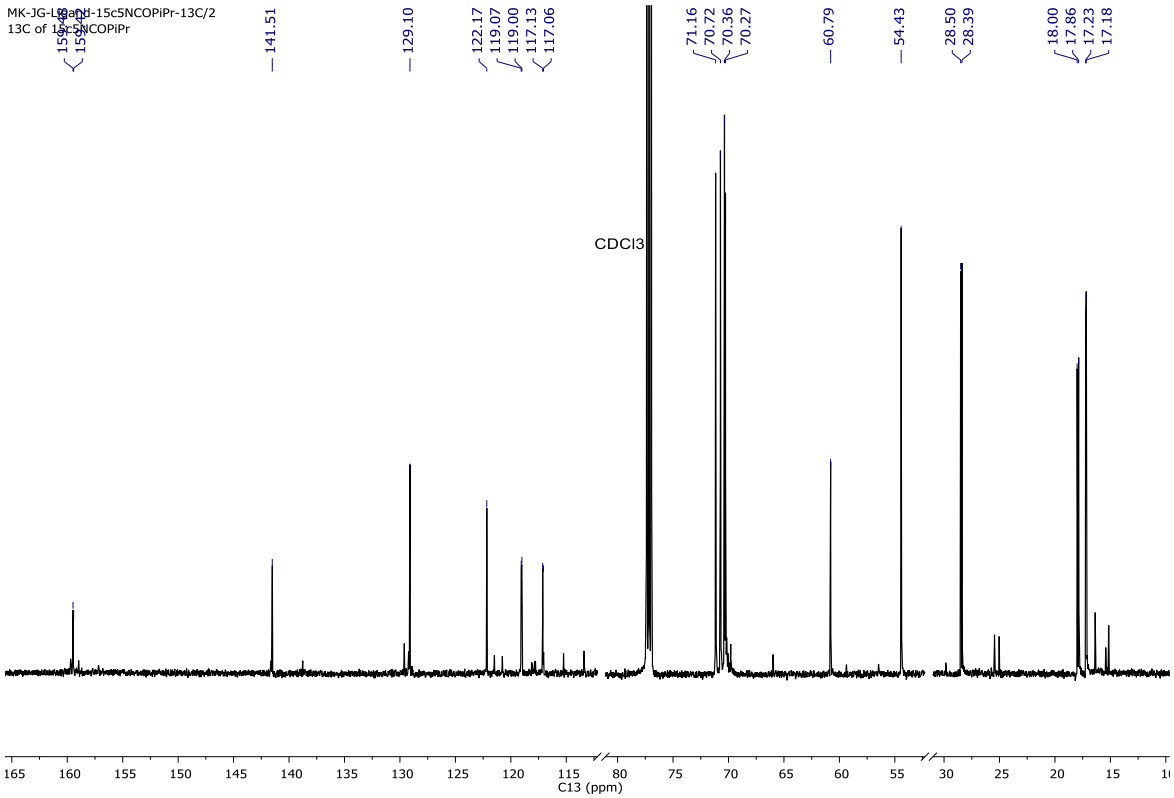

Figure 2.13: $^{13}C\{^{1}H\}$ NMR of ($^{15c5}NCOP^{iPr}$)H

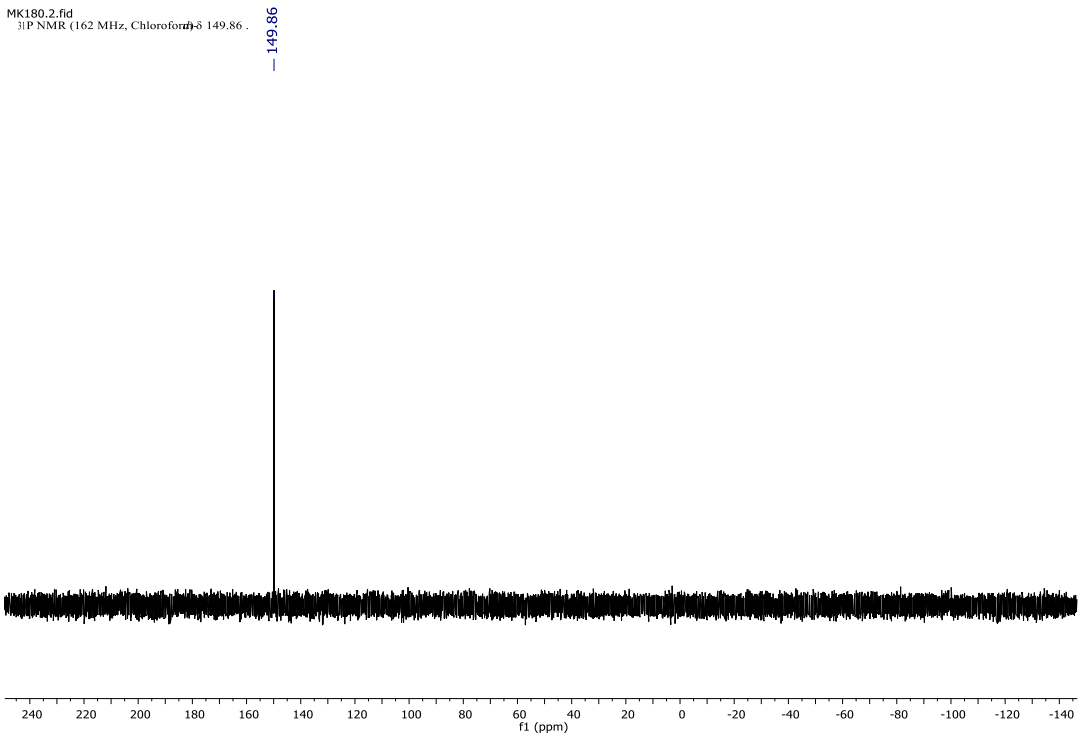

Figure 2.14: $^{31}P\{^{1}H\}$ NMR of ($^{15c5}NCOP^{iPr}$)H in $CDCl_3$

Synthesis of ($^{15c5}NCOP^{tBu}$)H

In a glovebox, a 20 mL scintillation vial was charged with 0.0375 g (0.115 mmol) of *m*-(aza-15-crown-5)methylphenol and 3 mL of THF. To the clear, colorless solution was added 18 μL (0.127 mmol) of triethylamine dropwise by syringe with stirring. After the mixture was stirred for 15 min, 22 μL (0.116 mmol) of ditertbutylchlorophosphine was added dropwise by syringe with continued stirring. After chlorophosphine addition, the solution developed a light yellow-brown color. The solution was stirred for 4 h, during which time a white precipitate formed. Removal of solvents in vacuo yielded a mixture of an oil and a white powder. The oil was extracted with ether (5 × 2 mL) and filtered. The ether was removed in vacuo to yield 0.0244 g (45% yield) of ($^{15c5}NCOP^{tBu}$)H as a colorless oil. ^{1}H NMR (400 MHz, Benzene-d_6) δ 7.51 (d, J = 2.1 Hz, 1H), 7.24 (d, J = 8.1 Hz, 1H), 7.13 (d, J = 8.0 Hz, 1H), 7.01 (d, J = 7.5 Hz, 1H), 3.61

(t, J = 6.0 Hz, 4H), 3.57 – 3.35 (m, 14H), 2.83 (t, J = 6.0 Hz, 4H), 1.15 (d, $^{3}J_{PH}$ = 11.6 Hz, 18H)

^{31}P NMR (162 MHz, Benzene-d_6) δ 147.60.

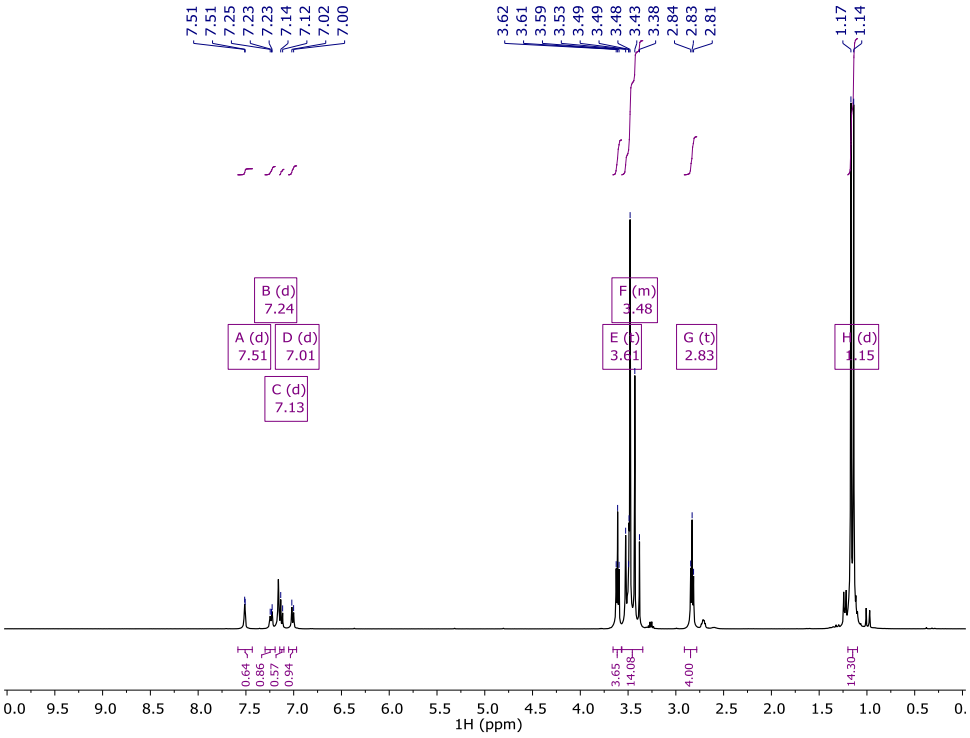

Figure 2.15: ^{1}H NMR of (^{15c5}NCOP^{tBu})H in C_6D_6

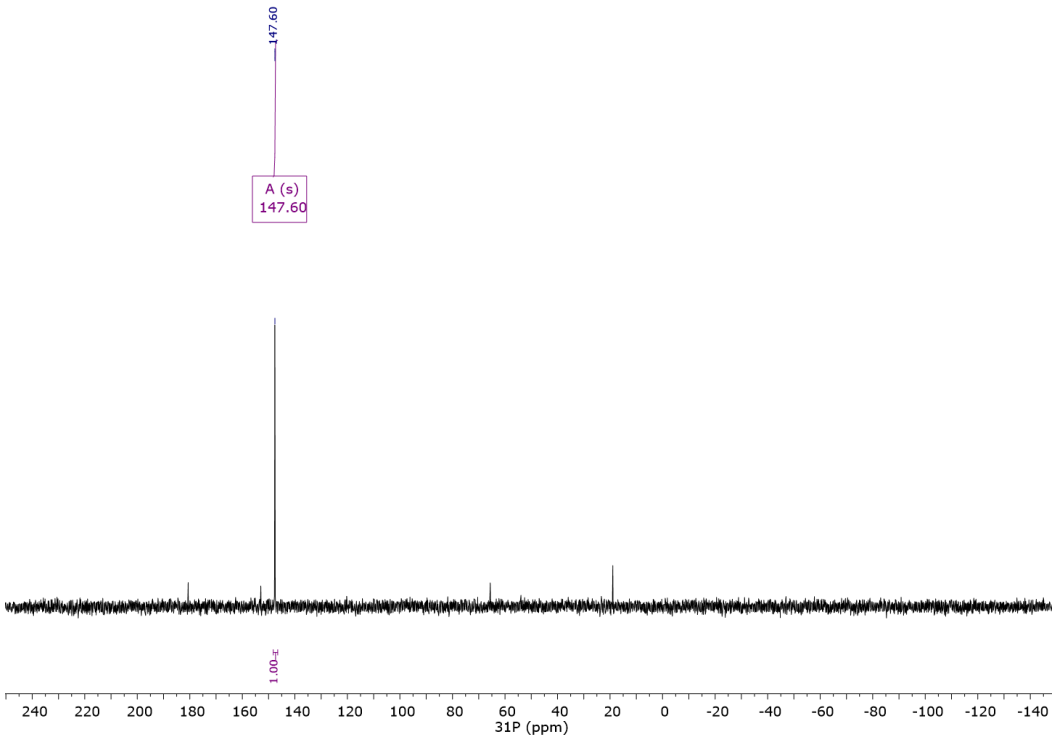

Figure 2.16: $^{31}P\{^{1}H\}$ NMR of (^{15c5}NCOP^{tBu})H in C_6D_6

Synthesis of (^{15c5}NCOP^{iPr})Ir(H)(Cl) (1)

In a glovebox, 198.5 mg (0.4496 mmol) of (^{15c5}NCOP^{iPr})H, 133.3 mg (0.1980 mmol) of $[Ir(Cl)(COD)]_2$, and 15 mL of toluene were added to a 100 mL Teflon-sealed pressure vessel. The reaction flask was removed from the glovebox and heated to 333 K for 12 h. After the mixture was cooled to room temperature, the volatiles were removed in vacuo to afford green-yellow solids. The crude mixture was solubilized in a minimal amount of toluene and layered with pentane to crash out yellow crystals of (^{15c5}NCOP^{iPr})Ir(H)(Cl) (**1**). The solvent was decanted away, and the crystals were rinsed with pentane (3 × 4 mL). The crystals were dried in vacuo to afford 228.2 mg (86% yield) of yellow crystalline **1**. Crystals suitable for X-ray diffraction were grown by vapor diffusion of pentane into a concentrated solution of the product in toluene at 243 K. ^{1}H NMR (600 MHz, chloroform-*d*): δ 6.69 (t, *J* = 7.7 Hz, 1H), 6.56 (d, *J* = 7.9 Hz, 1H), 6.53 (d, *J* = 7.5 Hz, 1H), 5.04 (t, *J* = 10.6 Hz, 1H), 4.94 (dd, *J* = 15.2, 11.3 Hz, 1H), 4.50–4.37 (m,

2H), 4.28 (dd, *J* = 13.9, 11.1 Hz, 1H), 4.15–4.02 (m, 2H), 3.94 (dd, *J* = 13.4, 10.0 Hz, 1H), 3.91–3.59 (m, 10H), 3.52 (dd, *J* = 11.9, 6.4 Hz, 1H), 3.45 (dd, *J* = 10.5, 6.4 Hz, 1H), 3.36 (d, *J* = 11.2 Hz, 1H), 3.29 (dd, *J* = 15.6, 3.1 Hz, 1H), 2.99 (dd, *J* = 14.6, 3.6 Hz, 1H), 2.60–2.47 (m, 1H), 1.39 (ddd, *J* = 33.7, 15.2, 7.1 Hz, 6H), 1.18 (dd, *J* = 18.9, 7.0 Hz, 3H), 0.88 (dd, *J* = 15.4, 7.0 Hz, 4H), −31.25 (d, *J* = 26 Hz). ^{1}H NMR (600 MHz, benzene-d_6): δ 6.90 (d, *J* = 7.9 Hz, 1H), 6.84 (t, *J* = 7.7 Hz, 1H), 6.47 (d, *J* = 7.3 Hz, 1H), 5.28 (t, *J* = 10.4 Hz, 1H), 5.07 (dd, *J* = 15.4, 11.1 Hz, 1H), 4.10 (t, *J* = 12.6 Hz, 1H), 3.95 (d, *J* = 14.7 Hz, 2H), 3.82 (dd, *J* = 15.3, 3.0 Hz, 1H), 3.75 (dd, *J* = 13.7, 11.1 Hz, 1H), 3.64 (t, *J* = 12.1 Hz, 1H), 3.62–3.43 (m, 5H), 3.39 (dd, *J* = 10.8, 7.4 Hz, 1H), 3.28–3.13 (m, 3H), 3.09–2.93 (m, 3H), 2.73 (dd, *J* = 14.4, 3.9 Hz, 1H), 2.48 (ddd, *J* = 14.5, 11.7, 7.1 Hz, 1H), 2.23 (dp, *J* = 13.6, 6.9 Hz, 1H), 1.43 (dd, *J* = 16.6, 7.6 Hz, 3H), 1.38–1.24 (m, 6H), 1.01 (dd, *J* = 15.4, 6.8 Hz, 3H), −30.93 (d, *J* = 26.3 Hz, 1H). ^{13}C{^{1}H} NMR (126 MHz, benzene-d_6): δ 163.97 (d, *J* = 3.7 Hz), 148.84 (d, *J* = 3.2 Hz), 135.94 (d, *J* = 4.6 Hz), 122.96, 113.60, 107.71 (d, *J* = 11.3 Hz), 76.29, 73.44, 73.11, 72.93, 70.70, 70.54, 69.33, 68.87, 67.26 (d, *J* = 2.4 Hz), 65.01 (d, *J* = 2.2 Hz), 63.43 (d, *J* = 2.8 Hz), 31.82 (d, *J* = 32.6 Hz), 29.82 (d, *J* = 38.3 Hz), 18.00 (d, *J* = 7.6 Hz), 17.80, 17.08 (d, *J* = 4.6 Hz), 16.54 (d, *J* = 3.5 Hz). ^{31}P{^{1}H} NMR (162 MHz, benzene-d_6): δ 142.95. Anal. Calcd for $C_{23}H_{40}ClIrNO_5P$: C, 41.57; H, 6.02; N, 2.15. Found: C, 41.28; H, 5.93; N, 2.09.

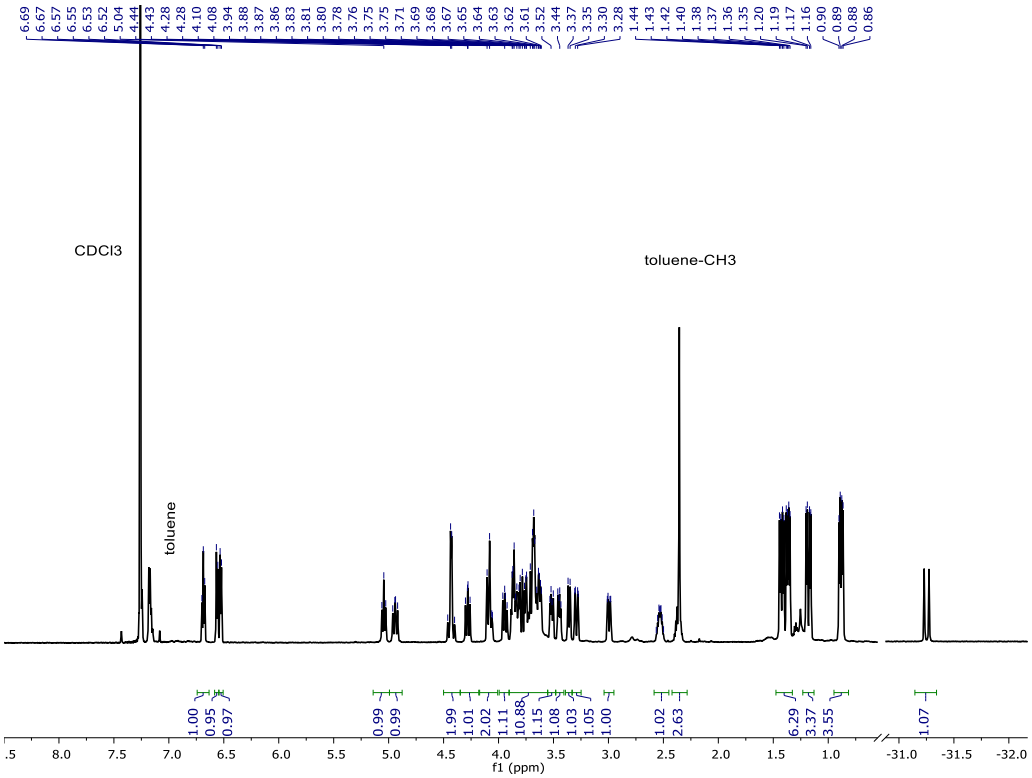

Figure 2.17: ^{1}H NMR of (^{15c5}NCOP^{iPr})IrHCl **(1)** in $CDCl_3$

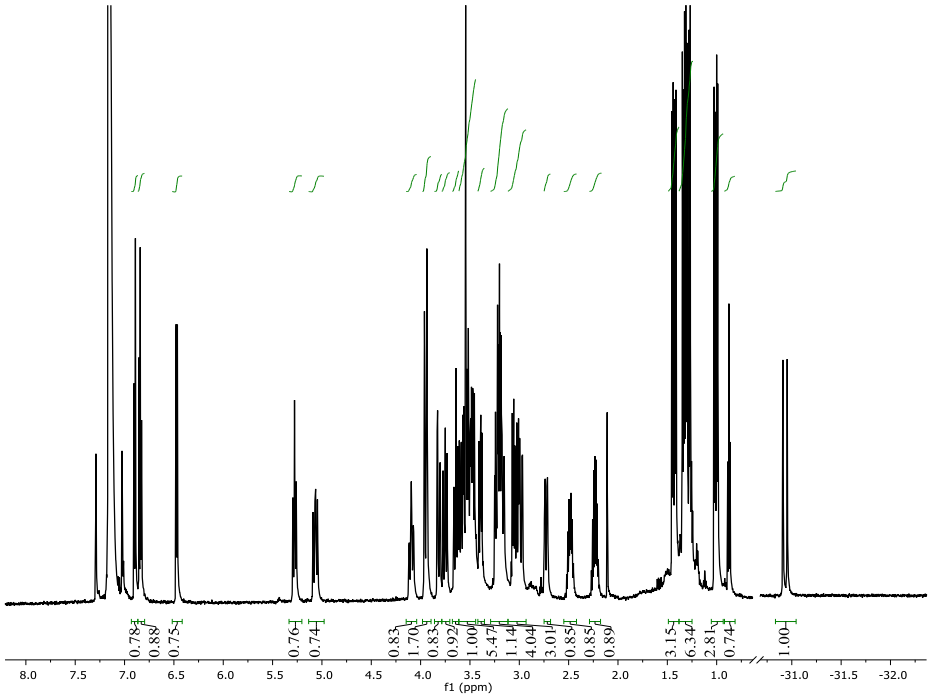

Figure 2.18: ^{1}H NMR of (^{15c5}NCOP^{iPr})IrHCl **(1)** in C_6D_6

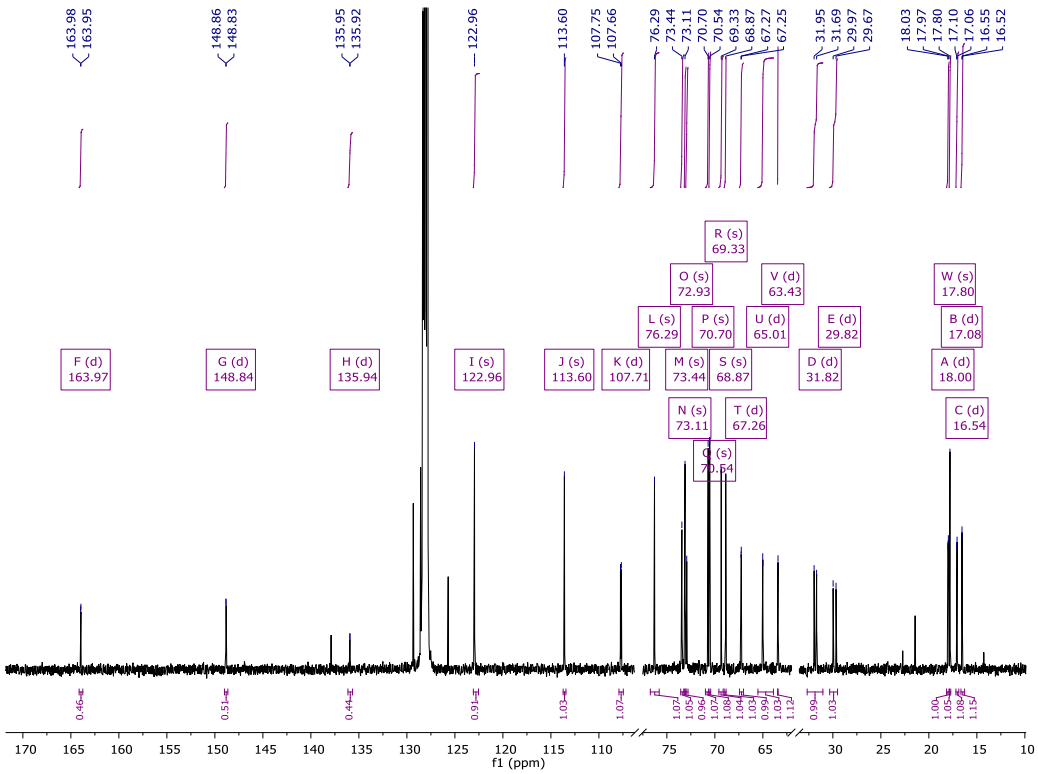

Figure 2.19: $^{13}C\{^{1}H\}$ NMR of ($^{15c5}NCOP^{iPr}$)IrHCl **(1)** in C_6D_6

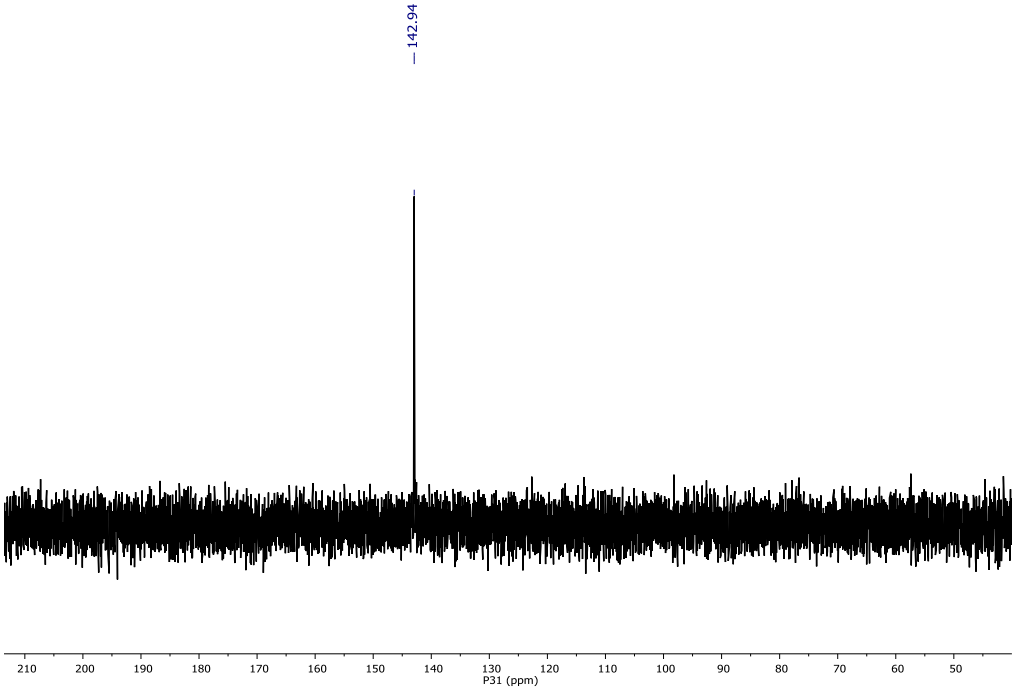

Figure 2.20: $^{31}P\{^{1}H\}$ NMR of ($^{15c5}NCOP^{iPr}$)IrHCl **(1)** in C_6D_6

Synthesis of [(^{15c5}NCOP^{iPr})Ir(H)][BAr$^{F}_{4}$] (2)

A 20 mL scintillation vial was charged with 23.2 mg (0.0347 mmol) of **1**, 35.0 mg (0.0404 mmol) of NaBAr$^{F}_{4}$, and 6 mL of methylene chloride. The mixture was stirred for 2 h as the color changed from yellow to dark orange. Volatiles were removed in vacuo, and the mixture was dissolved in toluene and filtered through sintered glass. The filtrate was evaporated in vacuo to yield **2** as a dark orange powder (72% yield). Light yellow single crystals suitable for an XRD study were grown by slow vapor diffusion of pentane into a concentrated solution of **2** in toluene at 243 K. ^{1}H NMR (600 MHz, chloroform-*d*): δ 6.78 (t, *J* = 7.8 Hz, 1H), 6.56 (d, *J* = 8.0 Hz, 1H), 6.50 (d, *J* = 7.6 Hz, 1H), 4.48 (d, *J* = 15.7 Hz, 1H), 4.31–4.07 (m, 5H), 4.01 (t, *J* = 12.4 Hz, 1H), 3.94 (d, *J* = 11.0 Hz, 1H), 3.87 (d, *J* = 12.5 Hz, 1H), 3.80 (d, *J* = 12.9 Hz, 1H), 3.78–3.71 (m, 2H), 3.62 (td, *J* = 19.5, 17.0, 10.0 Hz, 3H), 3.56–3.38 (m, 4H), 3.35 (d, *J* = 13.7 Hz, 1H), 3.05 (d, *J* = 13.8 Hz, 1H), 2.38 (dt, *J* = 13.7, 6.8 Hz, 1H), 2.31 (p, *J* = 7.1 Hz, 1H), 1.29 (dt, *J* = 13.8, 6.9 Hz, 4H), 1.20 (dd, *J* = 15.4, 7.2 Hz, 3H), 1.03 (dd, *J* = 19.8, 7.1 Hz, 3H), 0.94 (dd, *J* = 16.1, 6.9 Hz, 3H), −30.03 (d, *J* = 27.2 Hz, 1H). ^{13}C{^{1}H} NMR (151 MHz, chloroform-*d*): δ 163.07, 161.81 (q, $^{1}J_{BC}$ = 49.9 Hz), 144.64 (d, *J* = 3.9 Hz), 134.93, 129.07 (q $^{2}J_{FC}$ = 31.7), 125.25, 124.69 (q, $^{1}J_{FC}$ = 272.6 Hz), 117.76, 115.46, 108.91, 108.84, 78.44, 74.76, 73.93, 73.38, 70.72, 70.62, 68.65, 68.13, 67.27, 63.05, 60.66, 30.78 (d, $^{1}J_{PC}$ = 34.2 Hz), 28.90 (d, $^{1}J_{PC}$ = 41.4 Hz), 17.80, 16.55 (d, $^{2}J_{PC}$ = 7.6 Hz), 16.47, 16.31 (d, $^{2}J_{PC}$ = 1.8 Hz). ^{31}P{^{1}H} NMR (162 MHz, chloroform-*d*): δ 141.03. Anal. Calcd for $C_{55}H_{52}BF_{24}IrNO_5P$: C, 44.13; H, 3.50; N, 0.94. Found: C, 44.55; H, 3.60; N, 0.97.

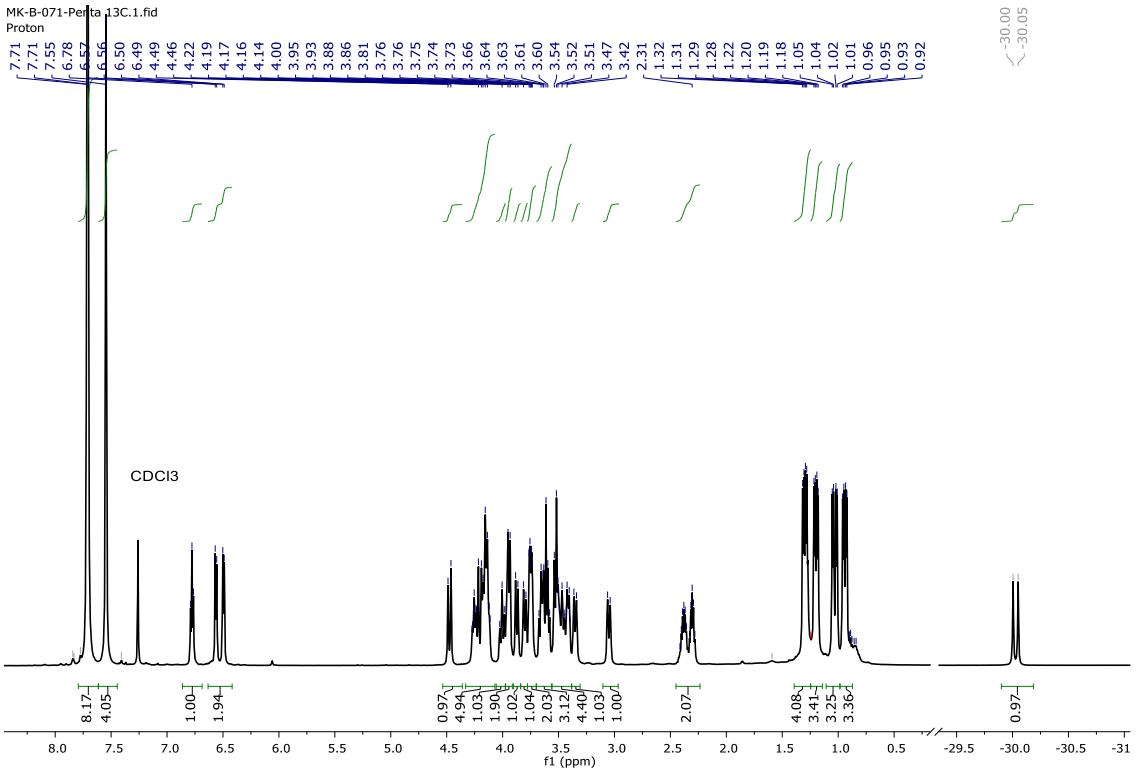

Figure 2.21: ^{1}H NMR of Complex **2** in $CDCl_3$

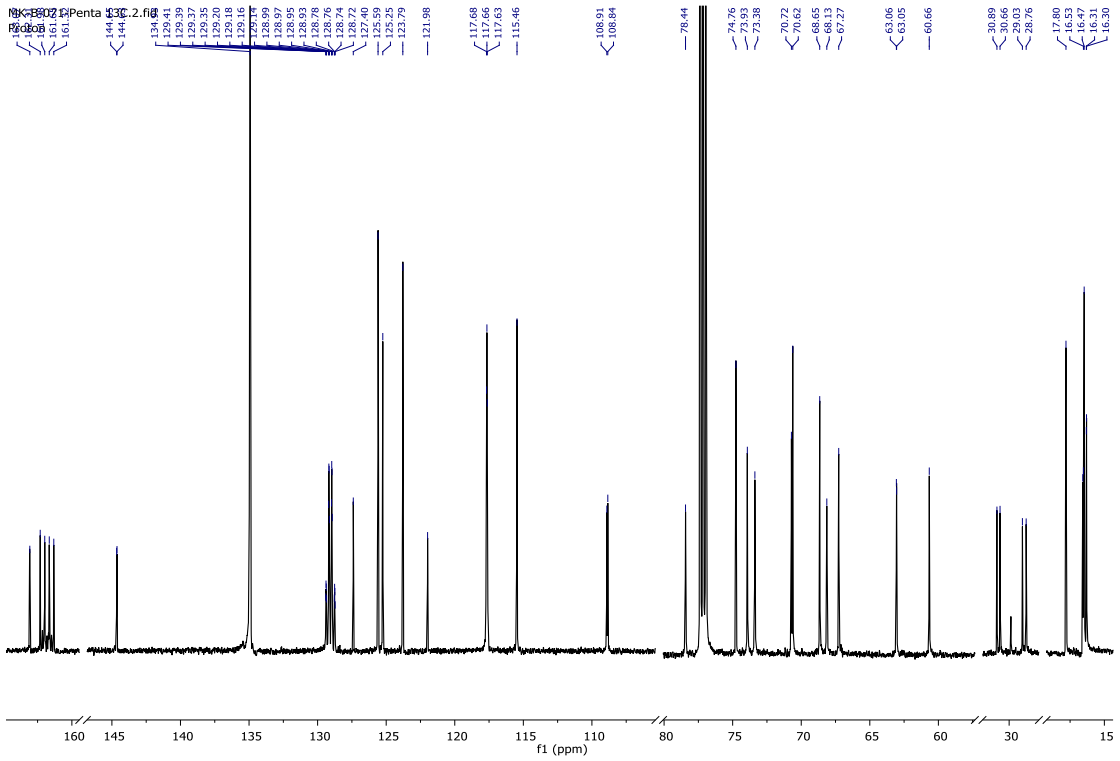

Figure 2.22: $^{13}C\{^{1}H\}$ NMR of complex **2** in $CDCl_3$

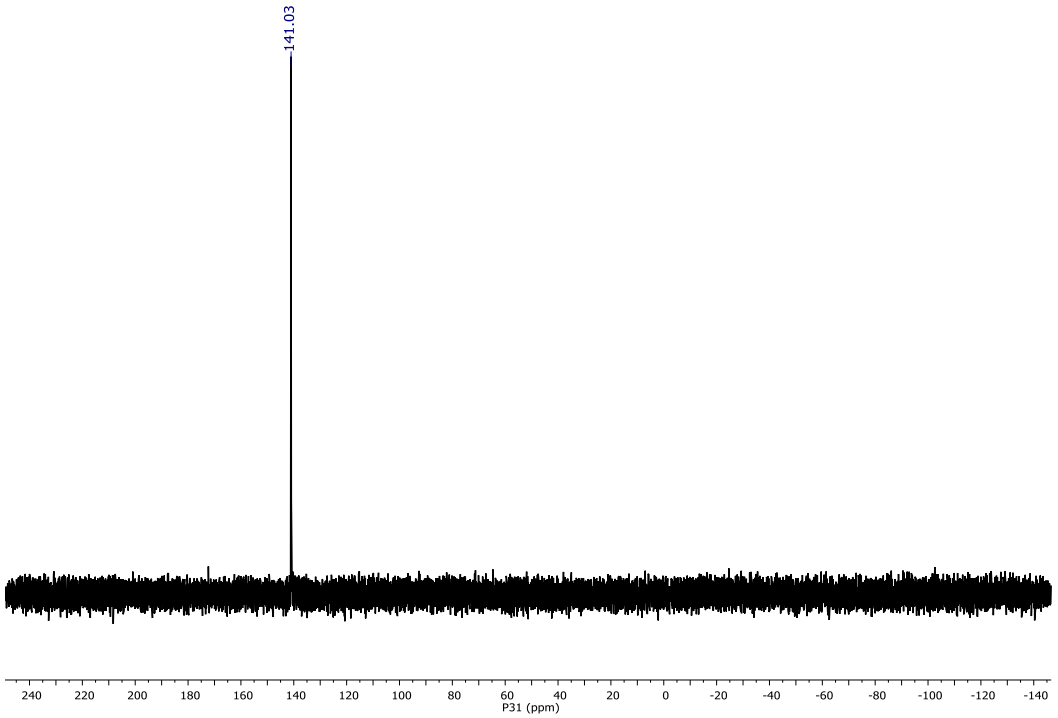

Figure 2.23: $^{31}P\{^{1}H\}$ NMR of complex **2** in $CDCl_3$

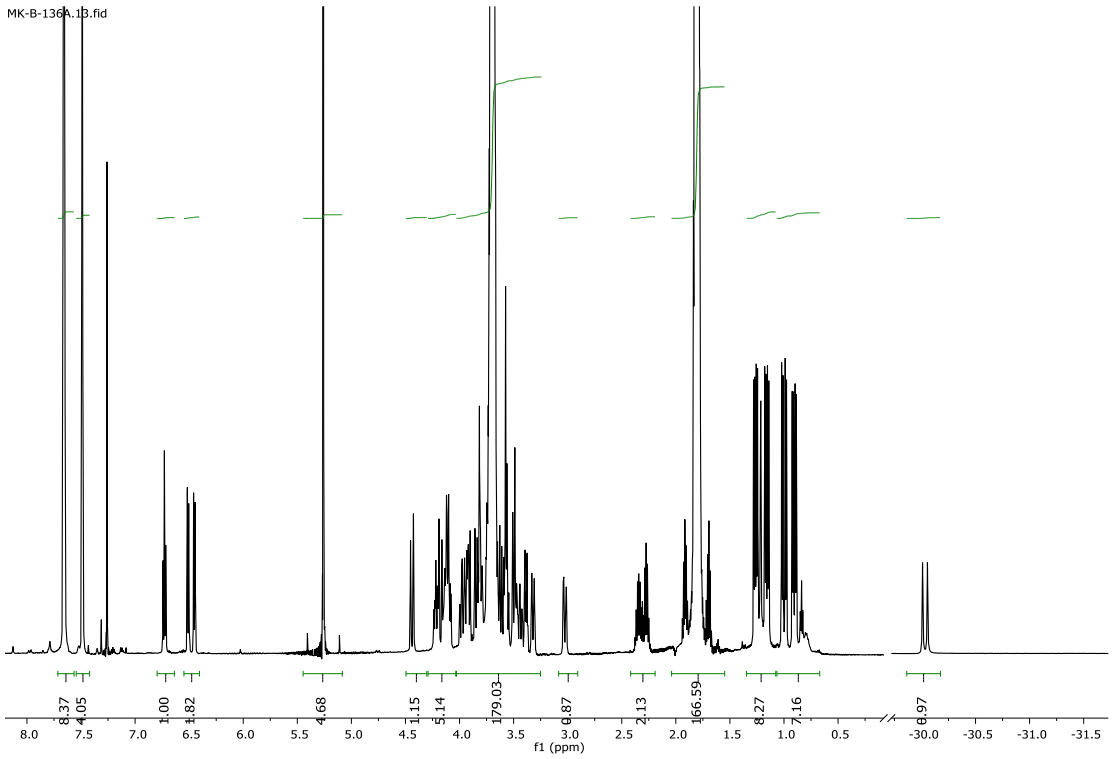

Figure 2.24: ^{1}H NMR spectrum showing no adduct formation between complex 2 and tetrahydrofuran (40 equivalents) in $CDCl_3$.

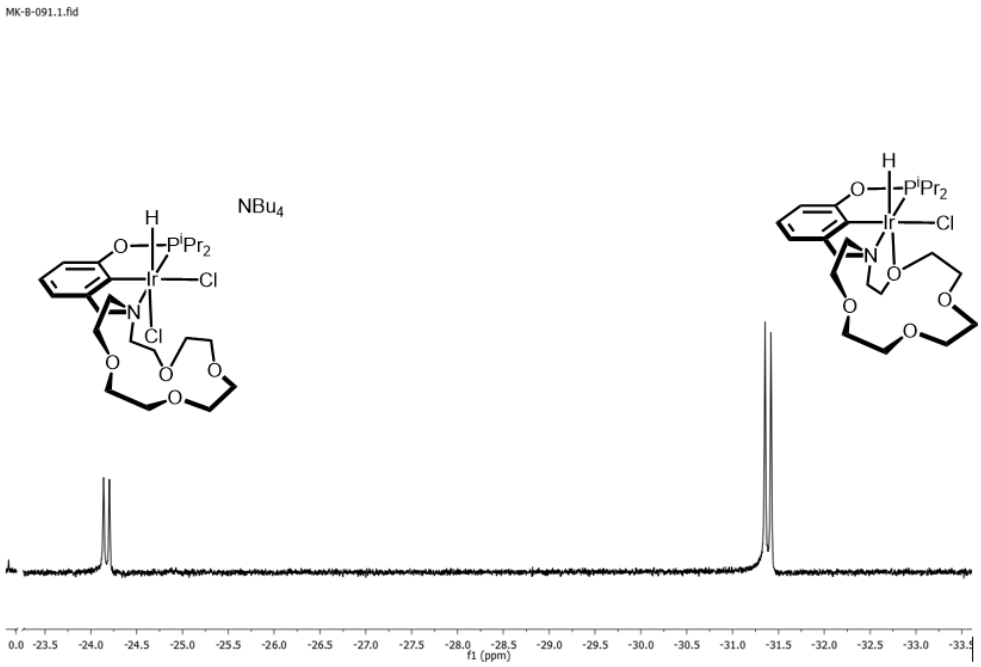

Figure 2.25: Hydride region for the formation of **4** from the combination 0.0041 g (0.00613 mmol) 1, 0.0015 g (0.00540 mmol) NBu_4Cl, and 600 μL CD_2Cl_2.

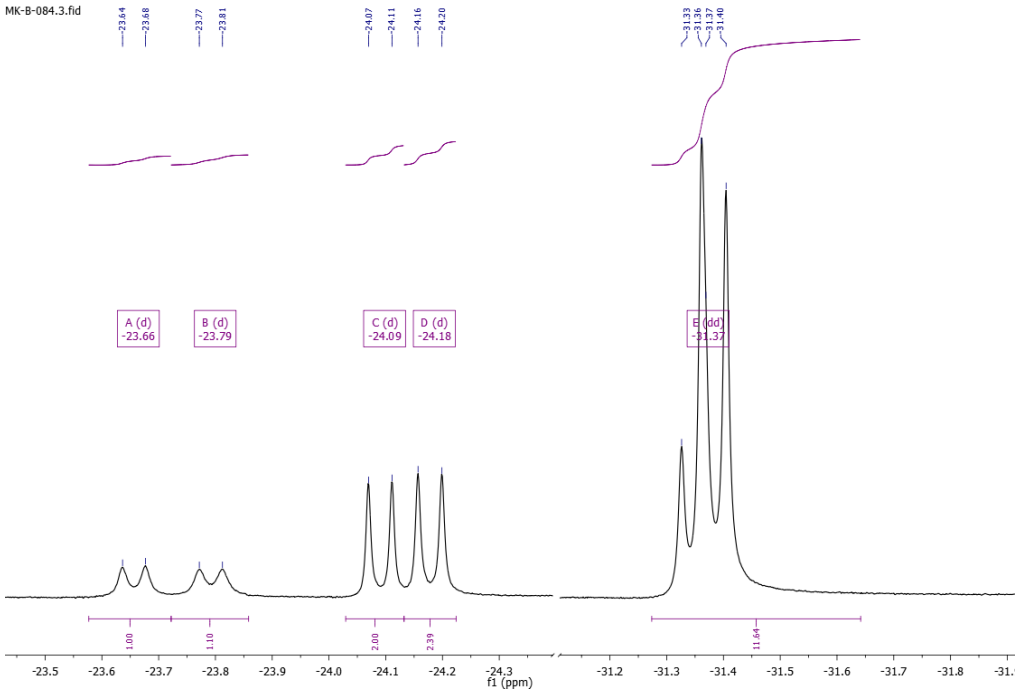

Figure 2.26: ^{1}H NMR spectrum (hydride region) after addition of 0.003 g (0.00931 mmol) NBu_4Br to 0.0092 g (0.0137 mmol) **1** in CD_2Cl_2. The peak at –31.39 is complex **1**; the overlapping peak at –31.34 is assigned to ($^{15c5}NCOP^{iPr}$)Ir(H)(Br); the peak at –24.18 is [($^{15c5}NCOP^{iPr}$)Ir(H)$(Cl)_2$]$^{-}$; the peak at –24.09 is therefore assigned as the *cis*-hydrobromide

[(^{15c5}NCOP^{iPr})Ir(H)(Br)(Cl)]$^{-}$; the peaks at –23.66 and –23.79 are assigned to the *cis*-hydrochloride [(^{15c5}NCOP^{iPr})Ir(H)(Cl)(Br)]$^{-}$ and the dibromide [(^{15c5}NCOP^{iPr})Ir(H)(Br)$_2$]$^{-}$.

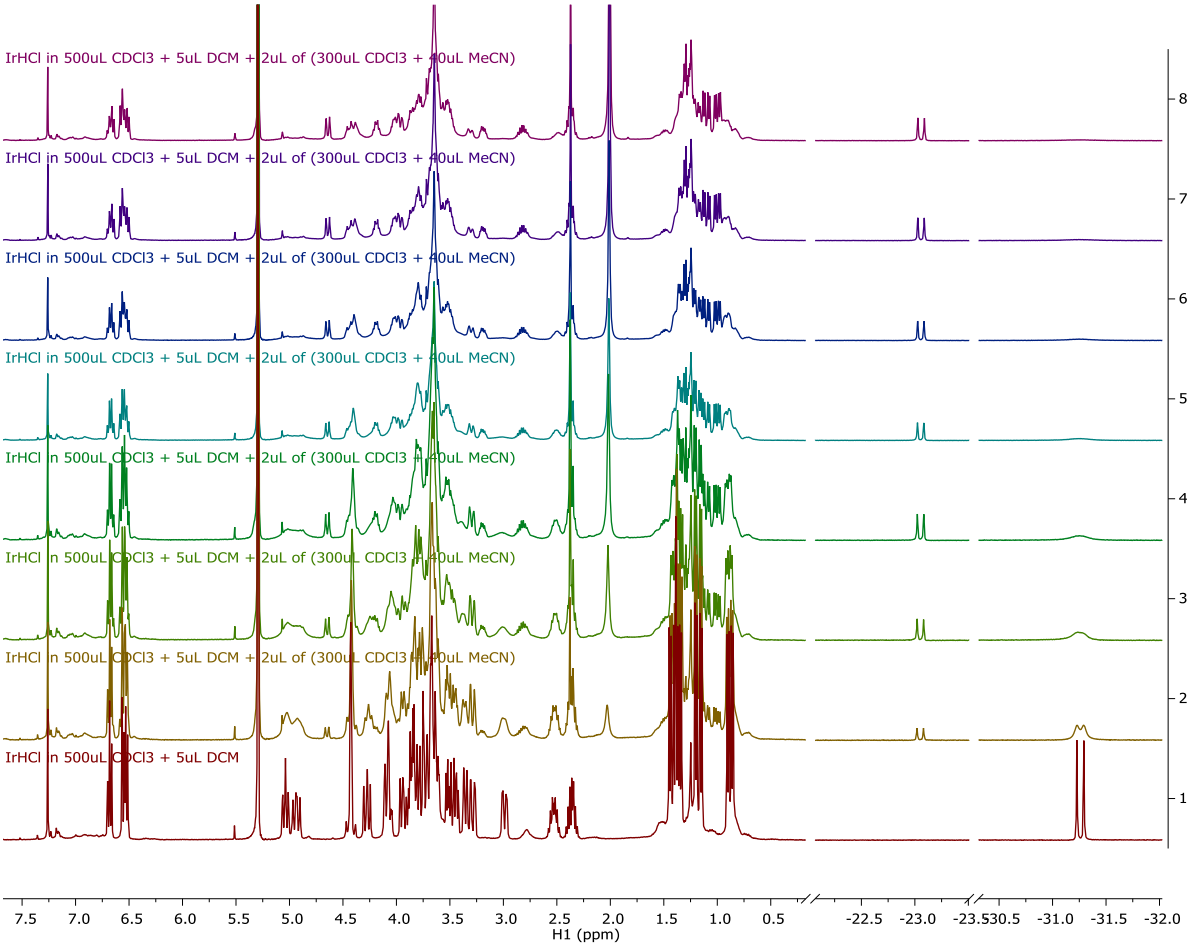

Figure 2.27: ^{1}H NMR spectra showing addition of CH_3CN to complex **1** (298 K).

Table 2.1: Equilibrium constant determination for reaction of **1** with CH_3CN to form **3'** (298 K).

CH_3CN (M)	3' (M)	1 (M)	K_{eq}
0.011	0.006	0.036	14.029
0.026	0.011	0.029	15.208
0.038	0.016	0.025	16.522
0.050	0.018	0.023	15.566
0.065	0.022	0.019	17.694
		Mean	15.804
		Std Dev	1.383

Equilibrium Studies With 1 and $NCCH_3$

A Teflon-sealed NMR tube containing 18.0 mg (0.0269 mmol) of (κ^4-^{15c5}NCOP^{iPr})Ir(H)(Cl) (**1**), $CDCl_3$ (0.5 mL), and acetonitrile-^{15}N (0.008 mL, 0.153 mmol) was placed in the NMR probe at 293 K. The probe was cooled at 10 K increments from 293 to 233 K, and the relative concentrations of **1**, *cis*-(^{15c5}NCOP^{iPr})Ir(H)(Cl)($NCCH_3$) (**3**), and *trans*-(^{15c5}NCOP^{iPr})Ir(H)(Cl)($NCCH_3$) (***3′***) were obtained by ^{1}H NMR spectral analysis. Thermodynamic parameters for the conversion of **1** to **3** ($\Delta H° = -8.67$ kcal mol^{-1}, $\Delta S° = -26.63$ cal mol^{-1} K^{-1}) were obtained from a van 't Hoff analysis (Figure 3.1). Thermodynamic parameters for the conversion of **1** to ***3′*** ($\Delta H° = -8.50$ kcal mol^{-1}, $\Delta S° = -22.4$ cal mol^{-1} K^{-1}) were obtained from a van 't Hoff analysis (Figure 2.5).

Table 2.2: Equilibrium data used for Van 't Hoff analysis of adduct formation between **1** and CH_3CN to form **3** (K_{eq}) and **3'** (K_{eq}').

T (K)	1/T (K^{-1})	CH_3CN (M)	**1** (M)	**3** (M)	**3'** (M)	$ln(K_{eq})$	$ln(K_{eq}')$
283.0	0.003534	0.03764	0.01844	0.005004	0.02847	1.975	3.714
272.9	0.003664	0.03088	0.01344	0.005513	0.03311	2.587	4.379
263.1	0.003801	0.02590	0.008981	0.005801	0.03781	3.217	5.091
253.0	0.003953	0.02231	0.005765	0.005738	0.04160	3.798	5.779
242.9	0.004117	0.02039	0.003547	0.007327	0.04275	4.618	6.382
233.0	0.004292	0.01932	0.002175	0.008159	0.04315	5.269	6.934

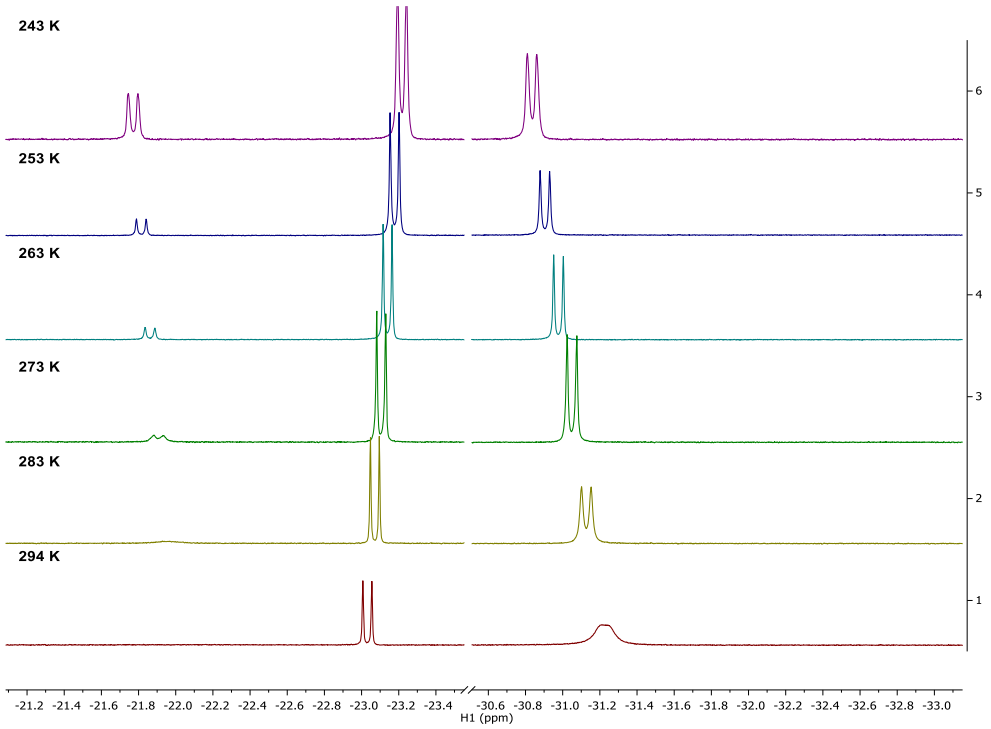

Figure 2.28: ^1H NMR spectrum (hydride region) of 0.0418 M **1** with 0.0105 mmol CH_3CN added at various temperatures in $CDCl_3$.

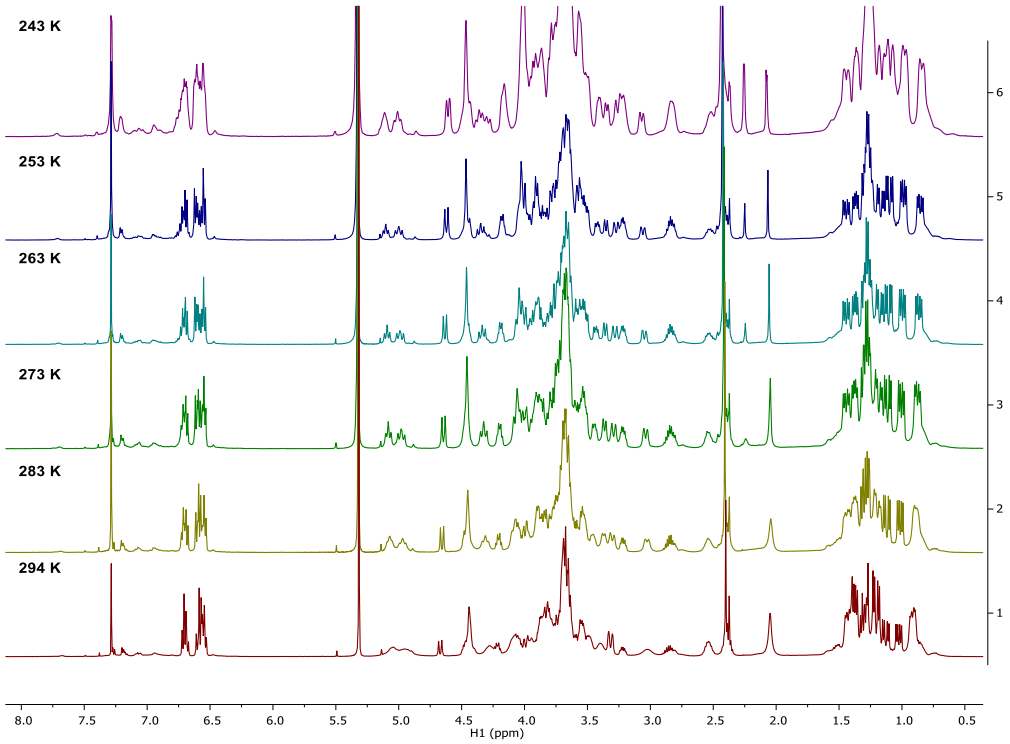

Figure 2.29: ^{1}H NMR spectrum (aliphatic and aromatic regions) of 0.0418 M **1** with 0.0105 mmol CH_3CN added at various temperatures in $CDCl_3$.

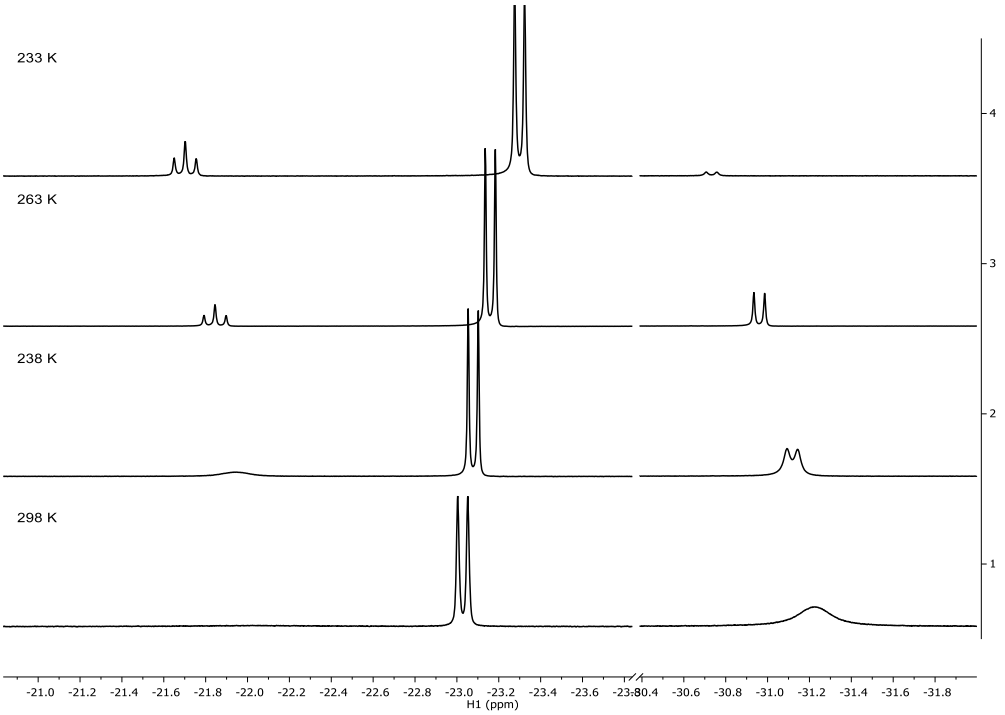

Figure 2.30: ^{1}H NMR spectrum (hydride region) of **1** and $^{15}NCCH_3$ at various temperatures in $CDCl_3$.

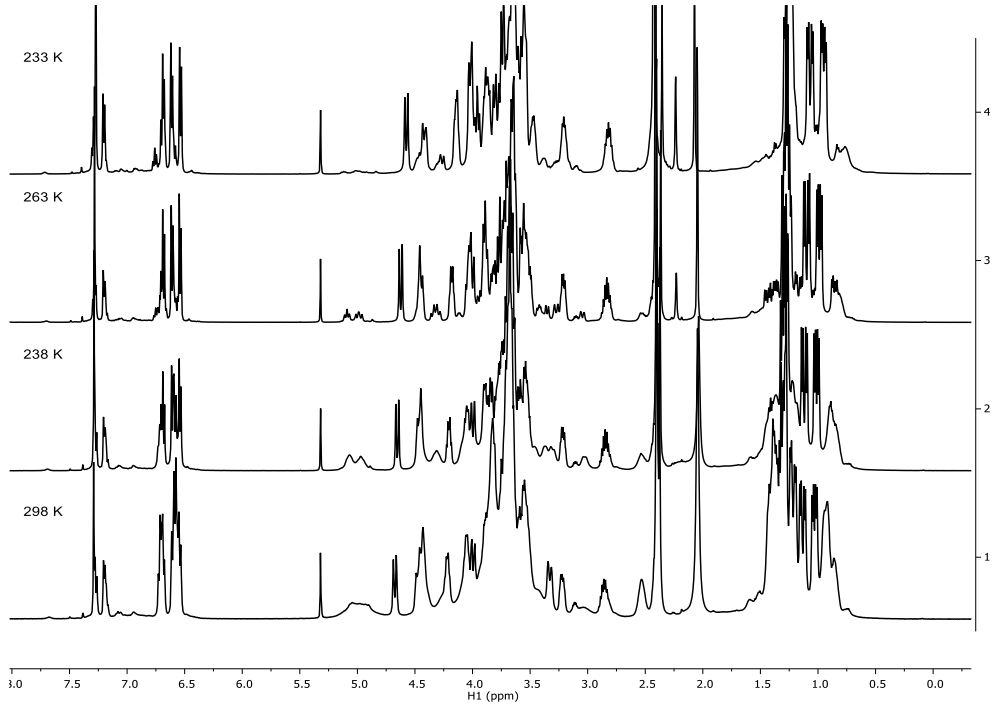

Figure 2.31: ^{1}H NMR spectrum (aliphatic and aromatic region) of **1** and $^{15}NCCH_3$ at various temperatures in $CDCl_3$.

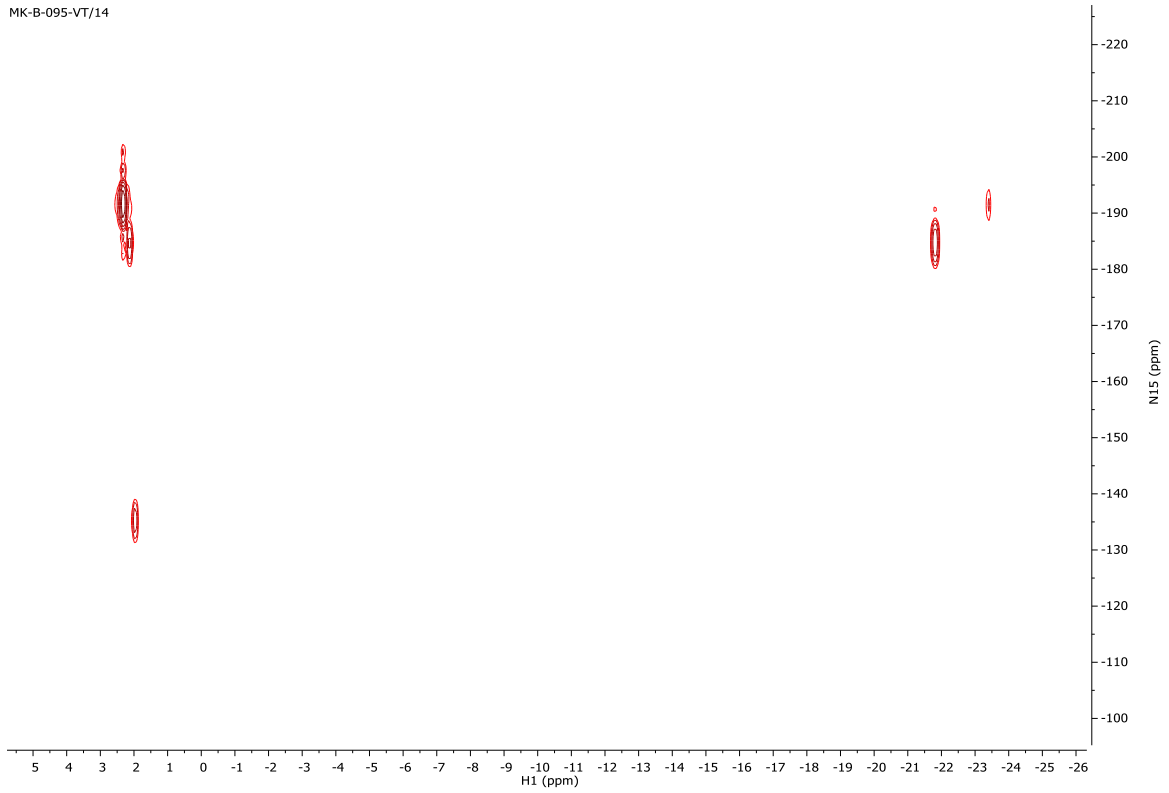

Figure 2.32: ^{1}H-^{15}N HMBC spectrum for the adduct formation of **1** and $^{15}NCCH_3$.

Equilibrium Studies with 2 and $NCCH_3$ to form 5 and 6

In a Teflon-sealed NMR tube containing 0.430 mL of a stock solution of [(κ^5-^{15c5}NCOP^{iPr})Ir(H)][BAr$^F_4$] (**2**; 0.0322 M in $CDCl_3$) was added 0.0013 mL (0.0419 mmol) of acetonitrile. The tube was sealed and placed in the NMR probe at 293 K. The probe was cooled in 10 K increments from 293 to 243 K, and the relative concentrations of CH_3CN, [(κ^4-^{15c5}NCOP^{iPr})Ir(H)($NCCH_3$)]$^+$ (**5**), and [(κ^3-^{15c5}NCOP^{iPr})Ir(H)($NCCH_3$)$_2$]$^+$ (**6**) were obtained by ^{1}H NMR analysis. Thermodynamic parameters for the conversion of **5** to **6** ($\Delta H° = -7.84$ kcal mol^{-1}, $\Delta S° = -19.6$ cal mol^{-1} K^{-1}) were obtained from a van 't Hoff analysis (Figure 2.6).

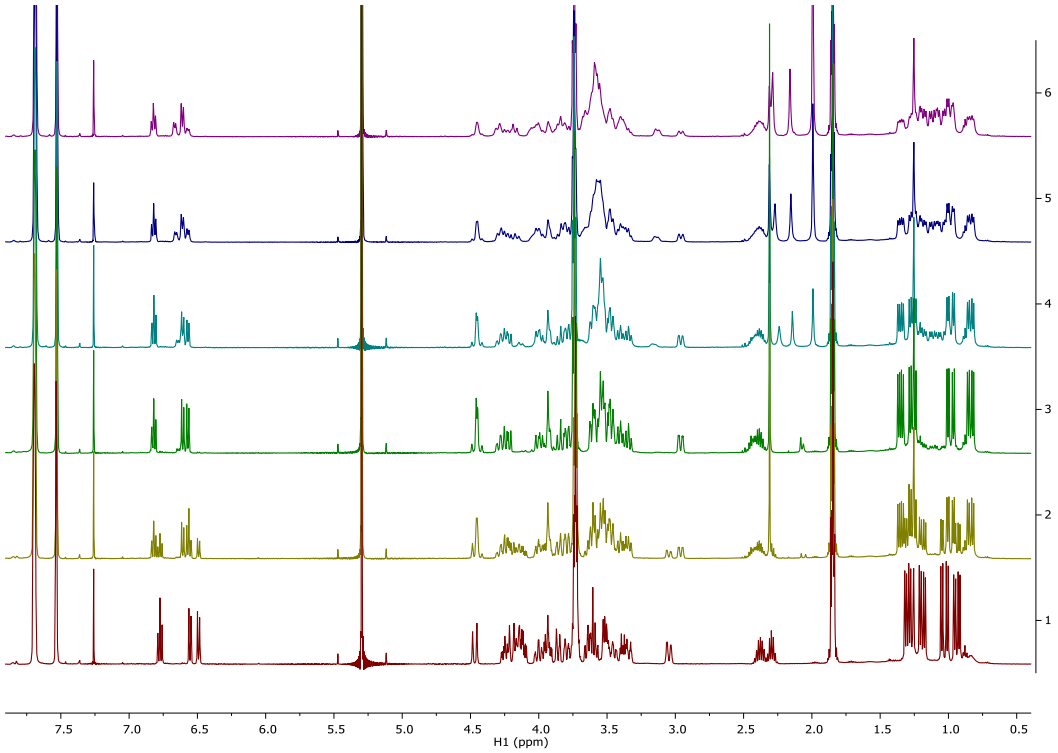

Figure 2.33: ^{1}H NMR spectra (aliphatic and aromatic regions) showing 0.0248 M **2** with increasing amounts of CH_3CN (298 K).

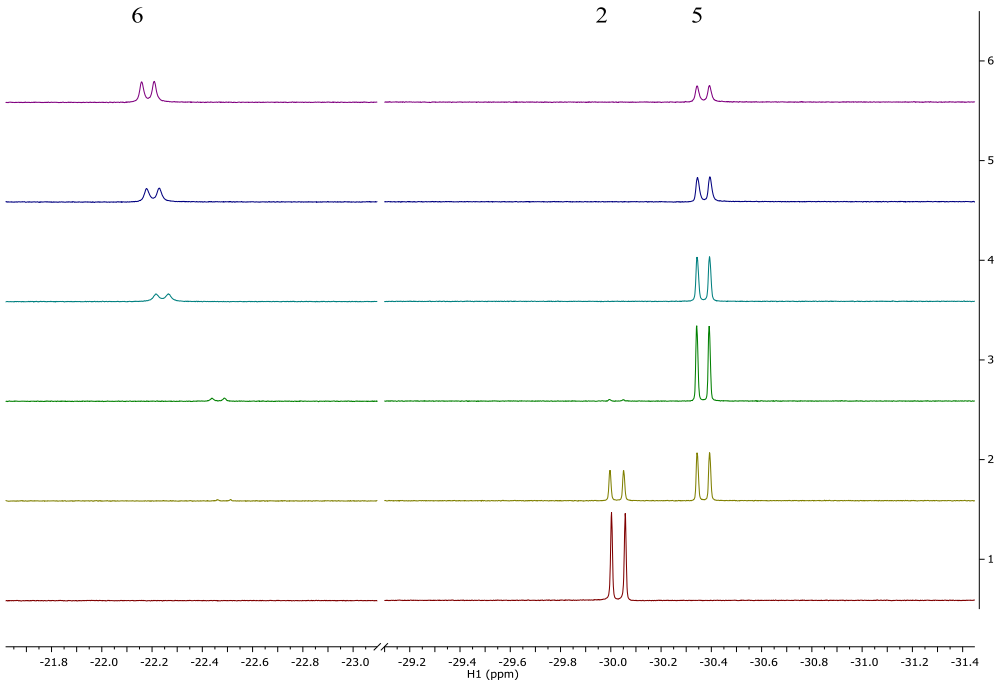

Figure 2.34: ^{1}H NMR spectra (hydride region) showing 0.0248 M **2** with increasing amounts of CH_3CN (298 K).

Table 2.3: Equilibrium determination of 23.58mM **2** + CH_3CN at 293 K

$Ir(NCCH_3)$ (**5**) (M)	CH_3CN (M)	$Ir(NCCH_3)_2$ (**6**) (M)	K_{eq} (M^{-1})
0.0175	0.01033	0.0065	35.96
0.014028	0.02272	0.010337	32.43
0.010072	0.038612	0.013094	33.67
		Average	34.02
		Std Deviation	1.79

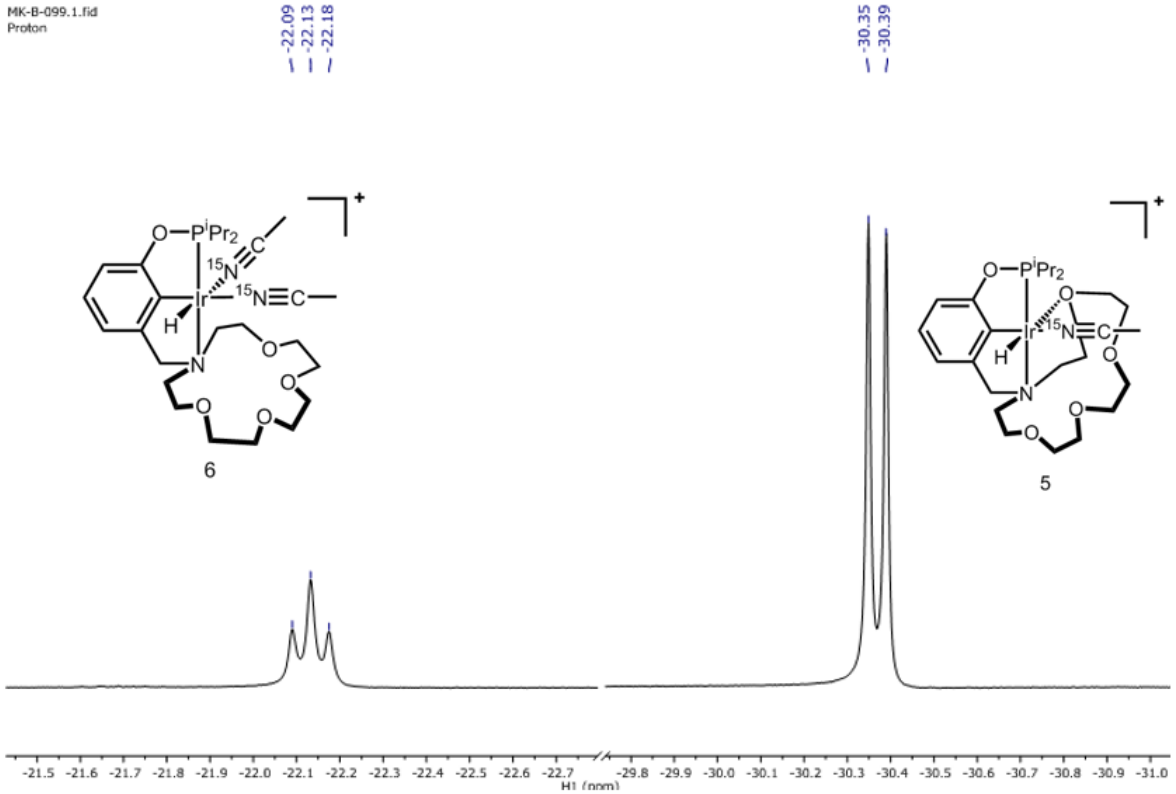

Figure 2.35: ^1H NMR spectrum (hydride region) of 0.0523 M 2 in $CDCl_3$ + $^{15}NCCH_3$ to determine geometry of **5** and **6**.

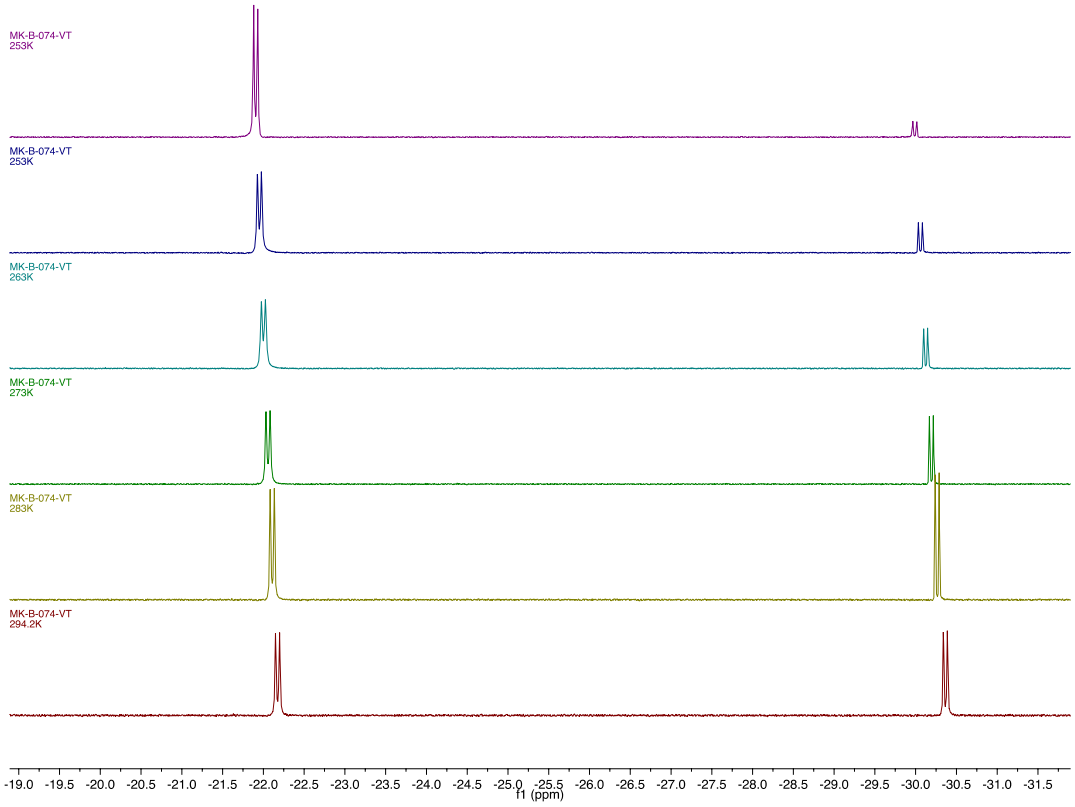

Figure 2.36: ^{1}H NMR spectra (hydride region) of 32.20 mM 2 + 1.3 µL CH_3CN at various temperatures.

Table 2.4: Equilibrium data used for Van ' Hoff analysis for adduct formation of **5** with CH_3CN to form **6.**

T (K)	1/T (K^{-1})	[CH_3CN] (M)	[**5**] (M)	[**6**] (M)	K_{eq} (M^{-1})	ln(K_{eq})
293	0.003413	0.0318	0.0190	0.0219	36.2	3.589
283	0.003534	0.0278	0.0149	0.0265	63.9	4.157
273	0.003663	0.0254	0.0116	0.0293	100	4.605
263	0.003802	0.0230	0.00868	0.0327	163	5.097
253	0.003953	0.0203	0.00579	0.0355	303	5.715
243	0.004115	0.0186	0.00331	0.0380	618	6.427

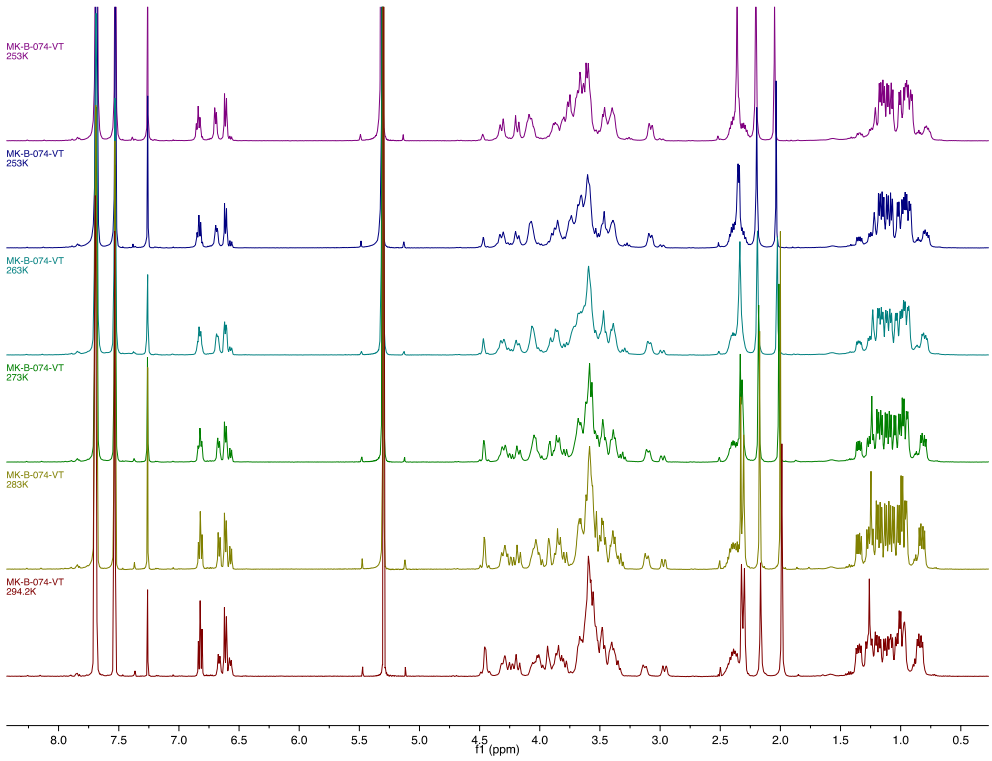

Figure 2.37: ^{1}H NMR spectra (aliphatic and aromatic regions) of 32.20 mM 2 + 1.3 μL CH_3CN at various temperatures.

Synthesis of [(^{15c5}NCOP^{iPr})Ir(H)(OH_2)][BAr$^{F}_4$] (11)

A scintillation vial was charged with 0.0125 g (0.00835 mmol) complex **2** and 1.00 mL CD_2Cl_2. A 500 μL aliquot was transferred to an NMR tube where 2 μL (0.111 mmol) water was added. The product was then characterized using ^{1}H, ^{13}C, and ^{31}P NMR spectroscopy. A similar experiment was performed using D_2O producing identical ^{1}H, ^{31}P, and ^{13}C spectra with the exception of the δ 6.15 shift in the ^{1}H spectra which under integrated, allowing assignment of the bound water peak. ^{1}H NMR (600 MHz, CD_2Cl_2) δ 7.82 – 7.65 (m, 8H), 7.56 (s, 4H), 6.74 (t, *J* = 7.7 Hz, 1H), 6.63 (d, *J* = 7.4 Hz, 1H), 6.58 (d, *J* = 8.0 Hz, 1H), 6.15 (s, 2H, OH_2 bound), 4.37 – 4.23 (m, 2H), 4.16 (td, *J* = 12.7, 3.2 Hz, 1H), 4.08 – 3.89 (m, 3H), 3.89 – 3.75 (m, 4H), 3.73 – 3.58 (m, 4H), 3.58 – 3.46 (m, 4H), 3.42 (dd, *J* = 14.4, 5.9 Hz, 1H), 3.24 (tt, *J* = 12.9, 4.4 Hz, 2H), 2.73 (dp, *J* = 13.9, 2.6 Hz, 1H), 2.56 (h, *J* = 7.3 Hz, 1H), 2.41 (tq, *J* = 14.0, 6.9 Hz, 1H), 1.56 (s, residual

water), 1.38 (dd, *J* = 13.8, 6.9 Hz, 3H), 1.32 (dd, *J* = 16.8, 7.4 Hz, 3H), 1.05 (dd, *J* = 20.1, 7.0 Hz, 3H), 0.80 (dd, *J* = 15.8, 7.0 Hz, 3H), -32.52 (d, *J* = 25.8 Hz, 1H).^{31}P NMR (202 MHz, CD_2Cl_2) δ 139.01. ^{13}C NMR (151 MHz, CD_2Cl_2) δ 164.26, 162.08 (q, $^{1}J_{BC}$ = 49.37 Hz), 144.03, 135.13, 129.17 (q, $^{2}J_{FC}$ = 30.50 Hz), 124.94 (q, $^{1}J_{FC}$ = 272.4 Hz), 124.54, 117.94 – 117.70 (m), 116.11, 108.65, 108.57, 74.70, 72.64, 71.57, 71.01, 70.29, 69.31, 68.93, 67.46, 65.62, 62.91, 61.19, 30.39 (d, *J* = 35.4 Hz), 29.12 (d, *J* = 39.5 Hz), 17.20, 17.14, 16.47, 16.43.

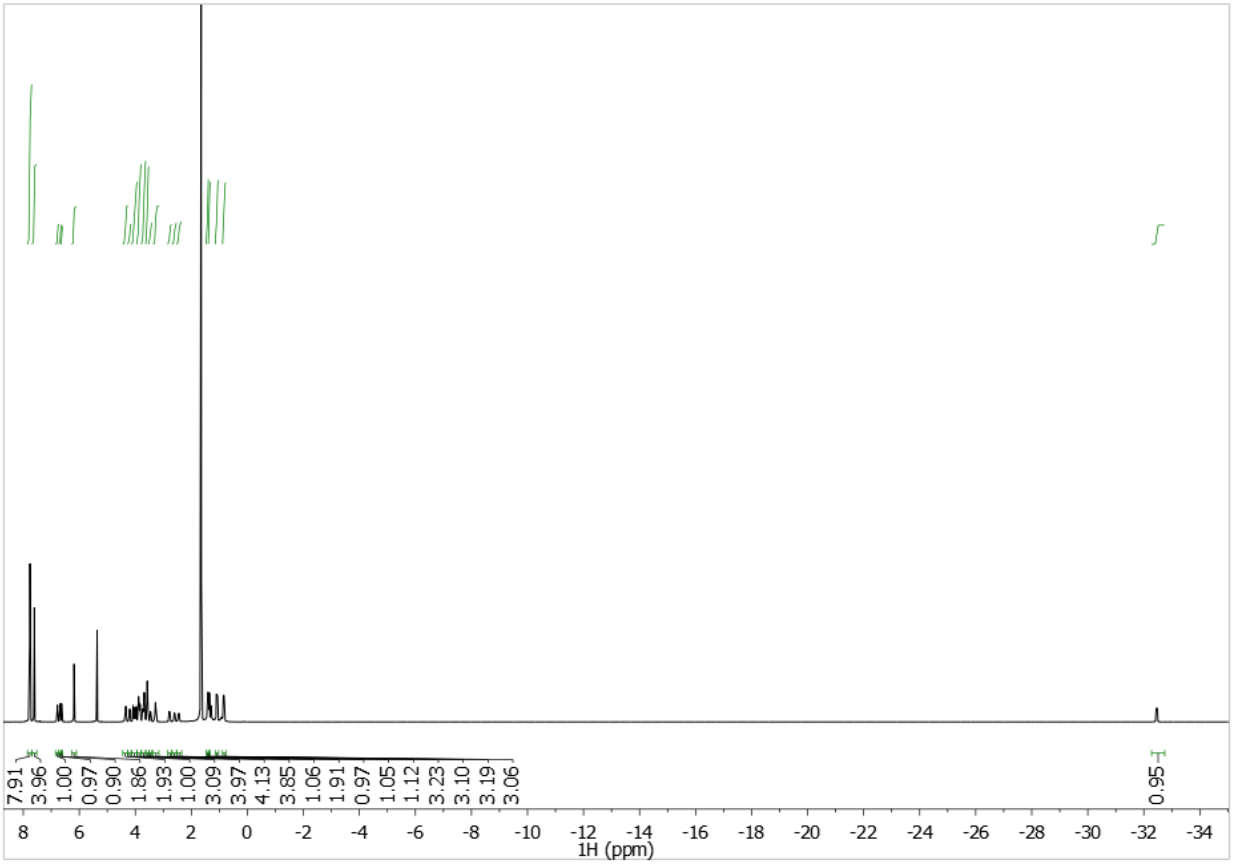

Figure 2.38: ^{1}H NMR spectrum of [(^{15c5}NCOP^{iPr})Ir(H)(OH_2)][BAr^F_4] **(11).**

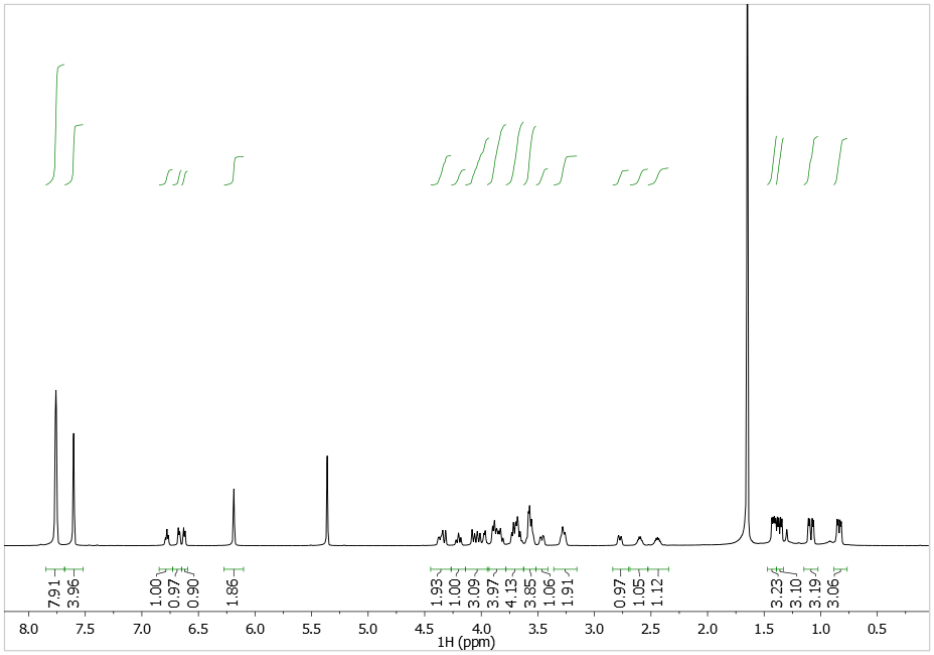

Figure 2.39: ^{1}H NMR spectrum of [($^{15c5}NCOP^{iPr}$)Ir(H)(OH_2)][BAr^{F}_4].

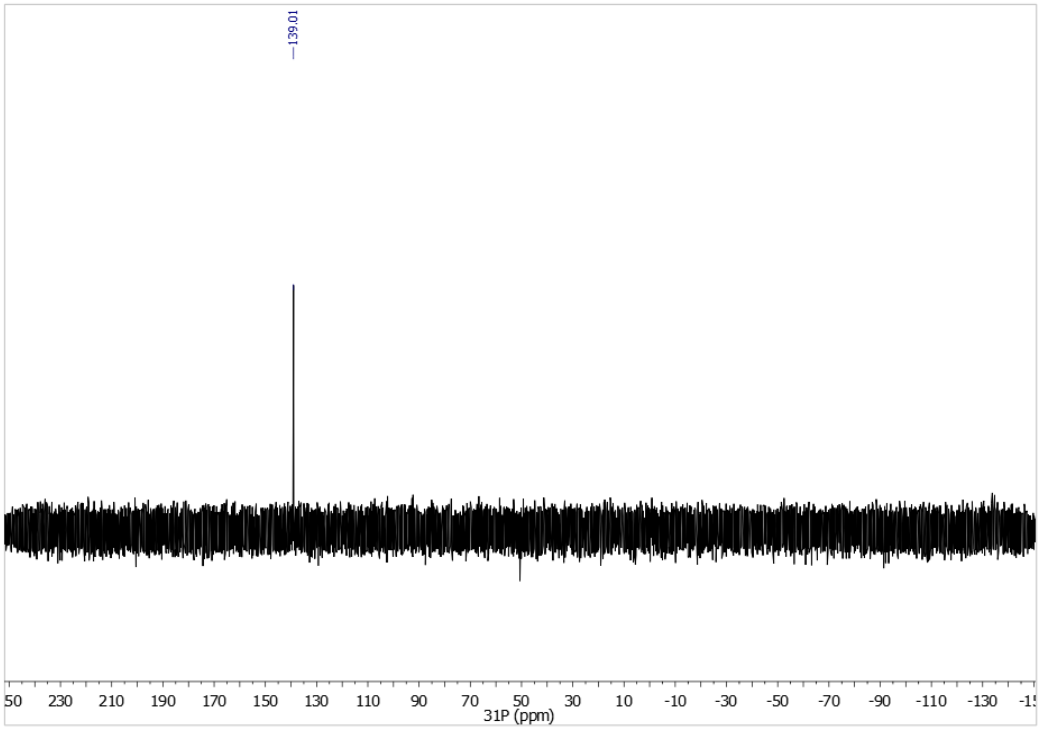

Figure 2.40: $^{31}P\{^{1}H\}$ spectrum of [($^{15c5}NCOP^{iPr}$)Ir(H)(OH_2)][BAr^{F}_4]

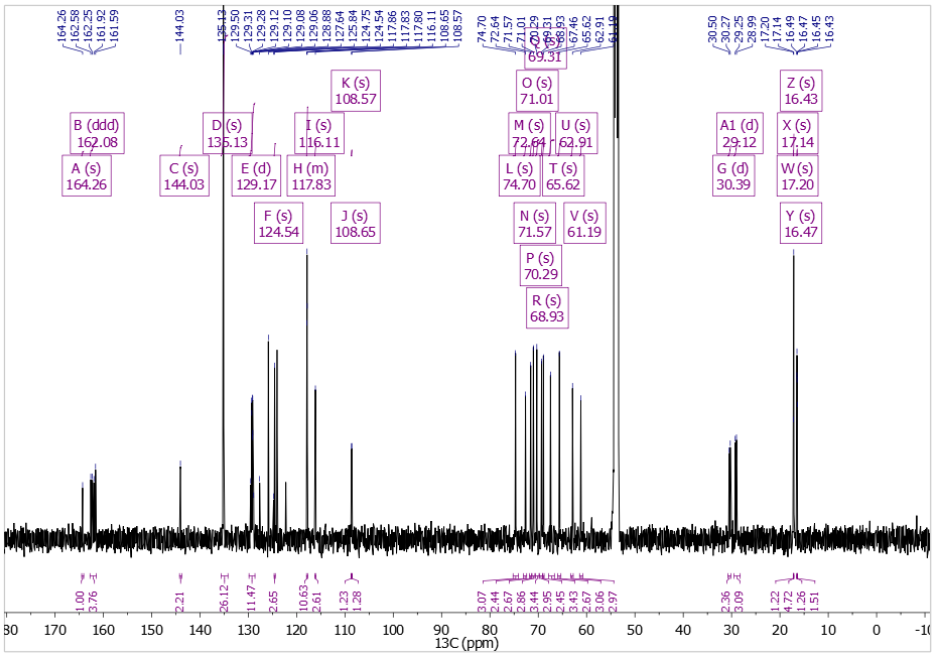

Figure 2.41: ^{13}C NMR spectrum of [($^{15c5}NCOP^{iPr}$)Ir(H)(OH_2)][BAr^F_4] **(11)**

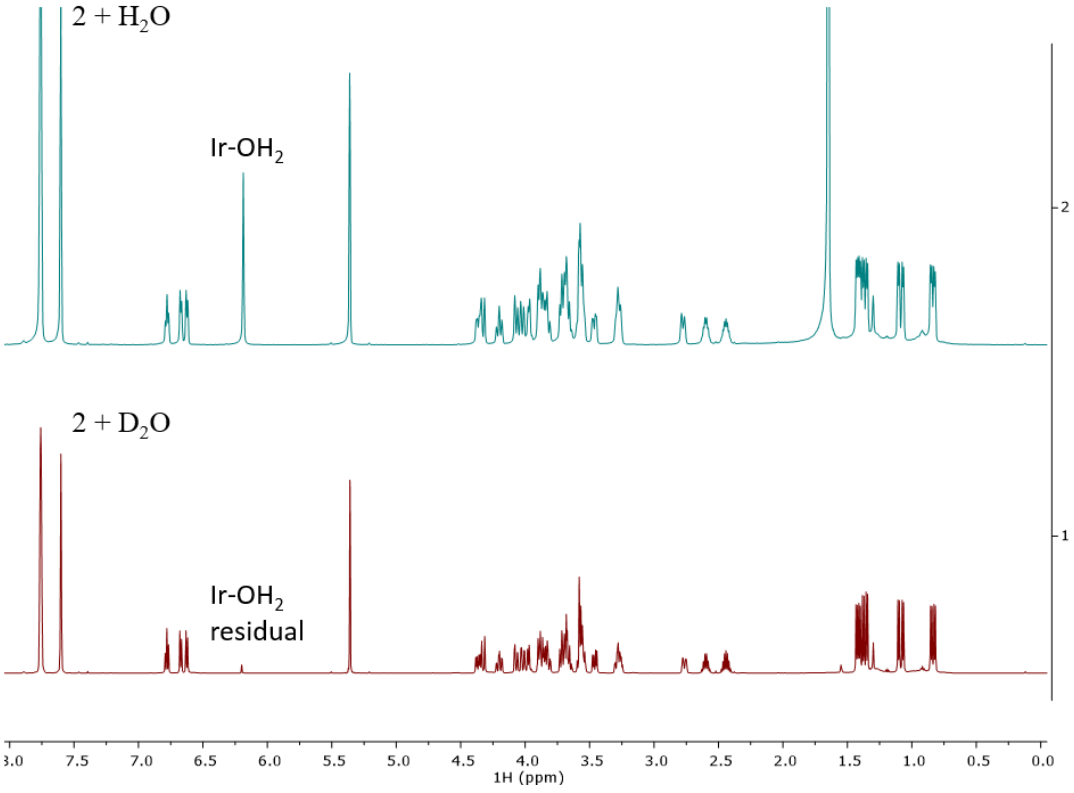

Figure 2.42: ^1H NMR spectra stack of **2** + H_2O (top spectra), and 2 + D_2O (bottom spectra), to assign the bound water peak.

Synthesis of κ^4-(^{18c6}NCOP^{iPr})Ir(H)(Cl) (12)

In a glovebox, 242.5 mg (0.4994 mmol) of (^{18c6}NCOP^{iPr})H, 141.2 mg (0.2102 mmol) of [Ir(Cl)(COD)]$_2$, and 20 mL of benzene were added to a 100 mL Teflon-sealed pressure vessel. The reaction flask was removed from the glovebox and heated to 343 K for 12 h. After the mixture was cooled to room temperature, the benzene was frozen in an ice bath, and removed in vacuo to afford green-yellow solids. The crude mixture was solubilized in a minimal amount of toluene and layered with pentane to crash out yellow crystals of (^{18c6}NCOP^{iPr})Ir(H)(Cl) (**12**). The solvent was decanted away, and the crystals were rinsed with pentane (3 × 4 mL). The crystals were dried in vacuo to afford 257.1 mg (86% yield) of yellow crystalline **1**. Crystals suitable for X-ray diffraction were picked from the initial crystallization prior to pentane rinse. ^{1}H NMR (600 MHz, Methylene Chloride-d_2) δ 6.66 (t, *J* = 7.6 Hz, 1H), 6.57 (d, *J* = 7.4 Hz, 1H), 6.51 (d, *J* = 7.8 Hz, 1H), 4.63 (dd, *J* = 15.4, 8.7 Hz, 1H), 4.49 (dd, *J* = 15.0, 3.3 Hz, 1H), 4.35 (d, *J* = 15.0 Hz, 1H), 4.24 (ddd, *J* = 12.4, 6.2, 2.4 Hz, 1H), 4.03 (dd, *J* = 13.8, 6.5 Hz, 1H), 3.97 (ddd, *J* = 11.1, 9.0, 1.5 Hz, 1H), 3.91 – 3.78 (m, 3H), 3.76 – 3.65 (m, 2H), 3.61 – 3.45 (m, 12H), 3.44 – 3.38 (m, 1H), 3.29 (dd, *J* = 15.1, 5.2 Hz, 1H), 3.02 – 2.91 (m, 1H), 2.46 (dp, *J* = 10.5, 7.2 Hz, 1H), 2.32 (dh, *J* = 13.7, 6.9 Hz, 1H), 1.39 (dd, *J* = 16.8, 7.4 Hz, 3H), 1.33 (dd, *J* = 13.6, 7.0 Hz, 3H), 1.09 (dd, *J* = 18.9, 6.9 Hz, 3H), 0.79 (dd, *J* = 15.4, 6.9 Hz, 3H), -31.26 (d, *J* = 26.1 Hz, 1H). ^{13}C NMR (151 MHz, Methylene Chloride-d_2) δ 163.33 (d, *J* = 3.6 Hz), 147.96 (d, *J* = 3.2 Hz), 135.51 , 122.77 , 114.54 , 107.39 (d, *J* = 11.2 Hz), 72.59 , 72.23 , 72.15 , 71.80 , 71.07 , 71.03 , 70.92 , 70.71 , 70.16 , 69.79 , 68.12 (d, *J* = 2.4 Hz), 61.04 , 59.32 , 31.61 (d, *J* = 32.5 Hz), 29.88 (d, *J* = 38.1 Hz), 17.46 (t, *J* = 3.8 Hz), 17.15 (d, *J* = 4.2 Hz), 16.56 (d, *J* = 3.2 Hz). ^{31}P NMR (243 MHz, Methylene Chloride-d_2) δ 142.87. Anal. Calcd for $C_{25}H_{44}ClIrNO_6P$: C, 42.10; H, 6.22; N, 1.96. Found: C, 41.86; H, 6.01; N, 1.85.

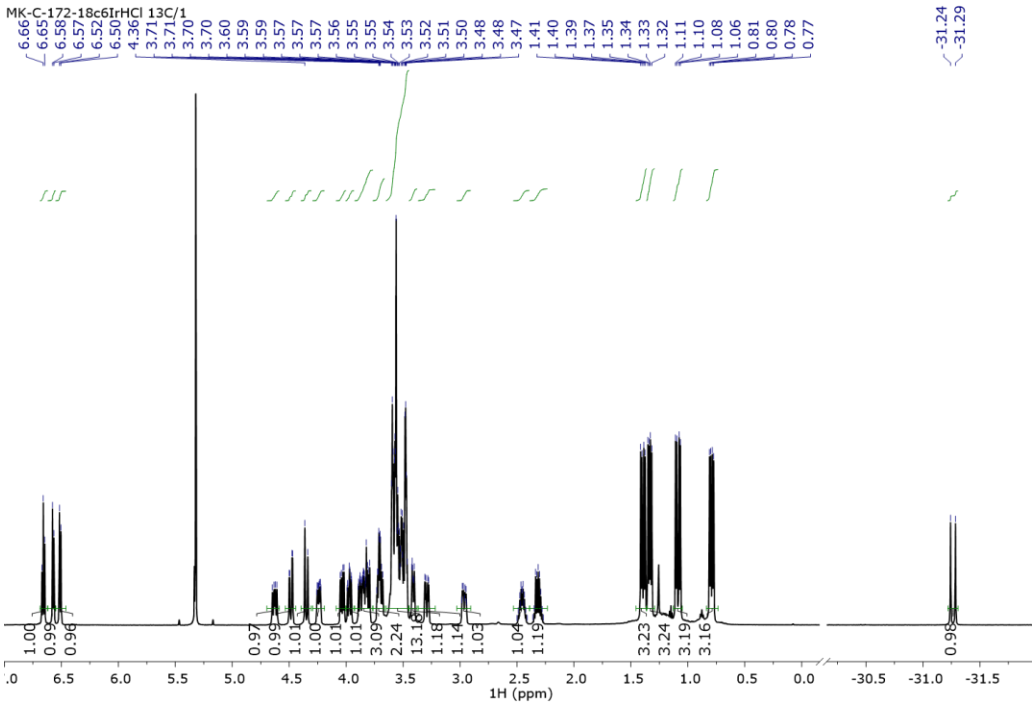

Figure 2.43: ^{1}H NMR spectra for κ^4-($^{18c6}NCOP^{iPr}$)Ir(H)(Cl) **(12)**

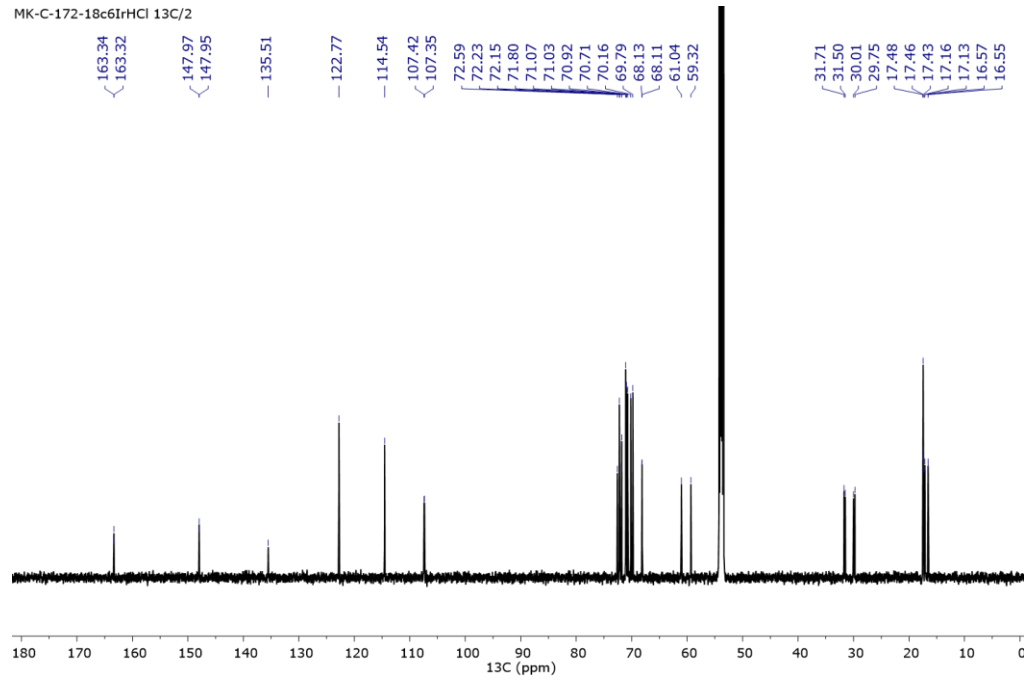

Figure 2.44: $^{13}C\{^{1}H\}$ NMR spectra for κ^4-($^{18c6}NCOP^{iPr}$)Ir(H)(Cl) **(12)**

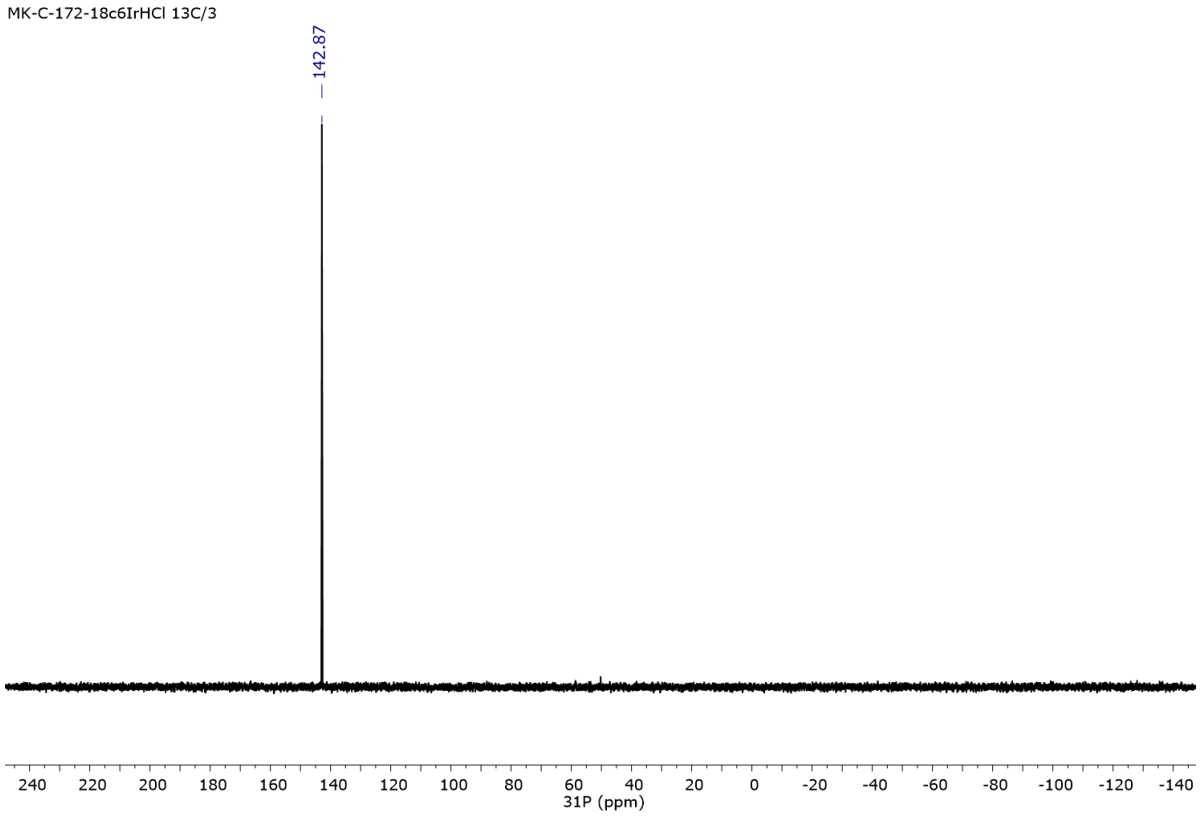

Figure 2.45: $^{31}P\{^{1}H\}$ NMR spectra for κ^4-(^{18c6}NCOP^{iPr})Ir(H)(Cl) **(12)**

Synthesis of [κ^4-(^{18c6}NCOP^{iPr})Ir(H)(OH$_2$)][BAr$^F{}_4$] (13)

A 20 mL scintillation vial was charged with 10.3 mg (0.0145 mmol) **12**, 4.4 mg (0.0174 mmol) $AgPF_6$, and 4 mL CH_2Cl_2. The materials used were not vigorously dried and contained trace amounts of adventitious water. The initially orange reaction mixture was allowed to stir for one hour as the color darkened to a deeper orange. The reaction mixture was filtered to remove AgCl, and the solvent was removed in vacuo. To the solids, 15.0 mg (0.0169 mmol) $NaBAr^F{}_4$, and 4 mL CH_2Cl_2 were added. The reaction was stirred for 12 hours, and then the solvent was removed in vacuo. The solids were extracted with toluene to remove $NaBAr^F{}_4$ and $NaPF_6$. The toluene solution was pumped to a solid to yield 18 mg (0.0115 mmol) **13** in 80% yield. ^{1}H NMR (600 MHz, Methylene Chloride-d_2) δ 7.76 – 7.65 (m, 8H), 7.56 (s, 4H), 6.74 (t, J = 7.7 Hz, 1H), 6.62 (d, J = 7.4 Hz, 1H), 6.57 (d, J = 7.8 Hz, 1H), 5.56 (s, 2H), 4.35 – 4.17 (m, 3H), 3.99 – 3.79 (m, 5H), 3.74 (td, J

= 10.1, 2.4 Hz, 1H), 3.61 (dtdd, *J* = 32.9, 16.1, 9.2, 2.6 Hz, 9H), 3.52 – 3.41 (m, 3H), 3.33 (dd, *J* = 12.1, 2.2 Hz, 1H), 3.30 – 3.17 (m, 2H), 3.04 (dt, *J* = 13.0, 5.8 Hz, 1H), 2.75 – 2.59 (m, 2H), 2.40 (dt, *J* = 13.9, 7.0 Hz, 1H), 1.42 – 1.31 (m, 6H), 1.07 (dd, *J* = 20.2, 6.9 Hz, 3H), 0.80 (dd, *J* = 15.5, 6.9 Hz, 3H), -32.53 (d, *J* = 26.0 Hz, 1H). ^{31}P NMR (202 MHz, Methylene Chloride-d_2) δ 139.15.

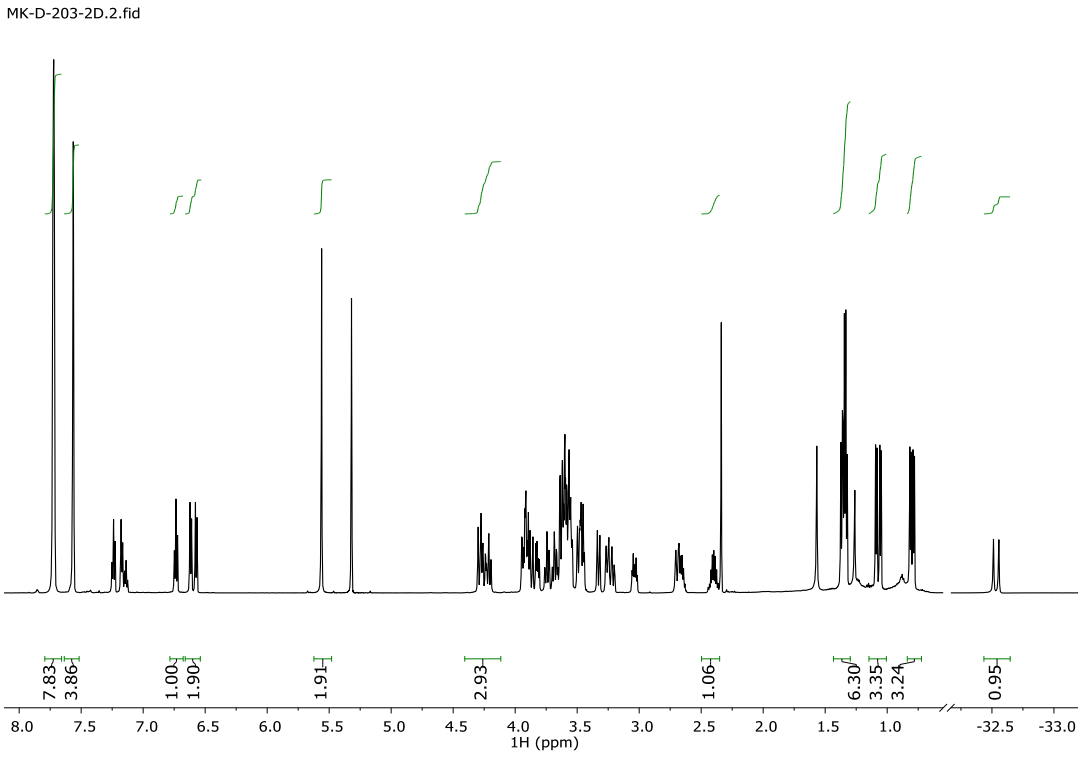

Figure 2.46: ^{1}H NMR spectra for [κ^4-(^{18c6}NCOP^{iPr})Ir(H)(OH$_2$)][BAr$^F{}_4$] **(13)**

Chapter 3 : MODULATING SUBSTRATE BINDING TO IRIDIUM HYDRIDE PINCER-CROWN ETHER COMPLEXES USING CATIONS

Reproduced in part with permission from Kita, M. R.; Miller, A. J. M. *J. Am. Chem. Soc.* **2014**, *136,* 14519–14529.

3.1 Introduction

Homogeneous catalysts featuring hemilabile ligands,[37] chelates in which one donor exhibits reversible coordination to the metal center, often display an uncommon combination of high activity and longevity.[38] The beneficial properties are ascribed to the ability of the ligand to move between a bound form that is stable toward decomposition and a dissociated form that is highly active. Unfortunately, tuning the reactivity of hemilabile catalysts is difficult: in order to change the hemilabile binding properties, a new ligand—for example, with a longer linker or different steric bulk—must be synthesized, often through arduous synthetic routes.[36,46,95]

The pincer-crown ether ligands introduced in Chapter 2 feature hemilabile Ir–O bonds that can bind reversibly in multiple coordination modes. These iridium pincer-crown ether complexes provide a strategy for controlling substrate access to the primary coordination sphere using non-covalent interactions to tune the Ir–O hemilability. Assuming a dissociative mechanism prior to substrate binding, understanding the Ir–O bond strengths can help determine how an open site on iridium is generated (Scheme 3.1). From this standpoint we can better understand how substrate access to the iridium primary coordination sphere is effected by cations.

Scheme 3.1

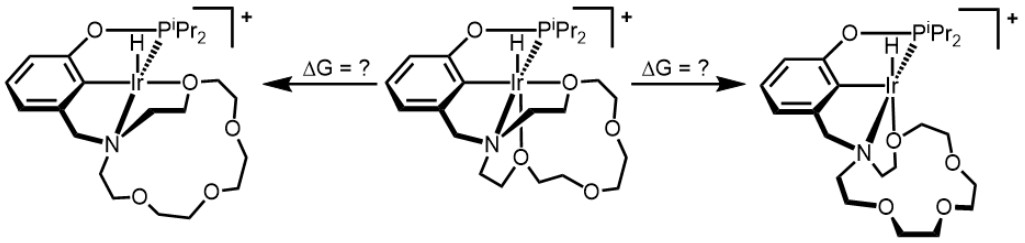

Here we report that iridium hydride pincer-crown ether complex **2** enables control of hemilability on the basis of alkali metal cation–macrocycle interactions. Density functional theory (DFT) was used to calculate bond strengths and better understand how an open site is generated. Substrate binding studies using $NCCH_3$ and H_2 are then examined using cations. The flexible, cation-modulated coordination chemistry and hydrogen activation reactivity of iridium pincer-crown ether complexes is demonstrated using these studies. Interconversion between tridentate, tetradentate, and pentadentate binding modes is modulated by alkali metal cations that can interact with the macrocyclic ligand arm, enabling dramatic and cation-tunable acceleration of dihydrogen activation.

3.2 Results and Discussion

Before Substrate Binding - Estimating Bond Strengths

Catalysis and reactivity involving pincer-crown ether complexes **1** or **2** would likely require initiation by displacement of one or more ether donors by a substrate. The metal–ligand bond strength of the crown ether complexes is therefore likely to be a critical factor in catalysis. Density functional theory (DFT) was used to estimate the Ir–O bond strengths of **1** and **2**. Calculations were performed using a slightly truncated form of the ligand (isopropyl groups replaced by methyl groups) and a polarized continuum model was applied to simulate the CH_2Cl_2 solution unless otherwise noted (for full computational details see the experimental

section). Starting from the crystallographic coordinates, the optimized structures of **1-Me** (in the gas phase) and **2-Me** were similar to the crystallographically determined structures (all bond lengths within 0.025 Å).

Scheme 3.2

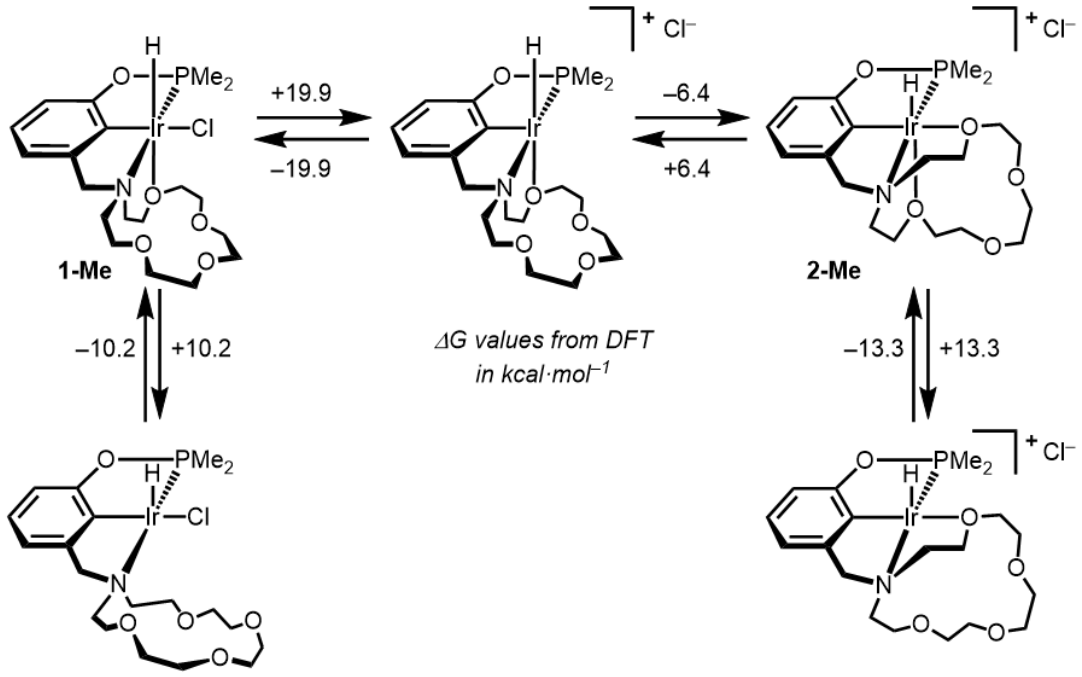

To probe the dative Ir–O bond strength, the free energies of **1** and **2** were compared to those of conformations without Ir–O bonds. In all cases, the Ir–O bonds did not re-form upon minimization. Due to the flexibility of the macrocycle after decoordination, multiple conformations were calculated, with free energy variations of ∼2 kcal mol^{-1} observed. Scheme 3.2 summarizes the calculated energy differences between bound and unbound forms of the ligand (lowest energy conformers given). As expected on the basis of the long bonds, dative Ir–O bonds in **1** and **2** are quite weak, with Δ*G* values between +6.4 and +13.3 kcal mol^{-1}. The ether ligand *trans* to the phenyl ring is thermodynamically the easiest Ir–O bond to break, consistent with crystallographically apparent strain (Chapter 2). The Ir–O bonds

in **1** and **2** appear to be substantially weaker than those of related hemilabile systems involving Ir–N bonds (21–28 kcal•mol^{-1} dissociation energy).[47] The activation energies of hemilabile binding of phosphinoethers to late transition metals are typically 11–16 kcal•mol^{-1}.[36] Complexes **1** and **2** are related by chloride dissociation. While removing chloride from **1** without any macrocycle rearrangement is quite unfavorable, subsequent chelation to pentadentate binding provides an overall ΔG = 13.5 kcal•mol^{-1}—only slightly more unfavorable than ether dissociation in some cases.

The CH_3CN binding process studied by VT NMR spectroscopy in chapter 2 was also examined computationally. The conversion of **1-Me** to the *cis*-hydrochloride isomer **3-Me** was calculated to be uphill by ΔG = 9.0 kcal•mol^{-1}, with **3′-Me** being more stable than **3-Me** ($\Delta\Delta G$ = −0.5 kcal•mol^{-1}at 298 K). While the calculations reproduce the relative energies of **3′** and **3** ($\Delta\Delta G°$ = −1.0 kcal•mol^{-1} on the basis of NMR data), the overall free energy values do not agree very well. Noncovalent interactions with CH_2Cl_2 or CH_3CN may be involved, as weak H-bonding interactions have been shown (in experiment and theory) to be enthalpically favorable by 5–20 kcal•mol^{-1}.[90,96,97] More detailed computational models accounting for all noncovalent interactions are needed in the future.

DFT calculations are qualitatively consistent with the observed adduct formation in **2**. Reaction of **2-Me** with one equiv of CH_3CN to form **5-Me** was calculated to be favorable (ΔG = –6.6 kcal•mol^{-1}). Formation of the other (unobserved) isomer of **5-Me** was calculated to be unfavorable with respect to **2-Me** and free CH_3CN (ΔG = + 4.7 kcal·mol^{-1}). Reaction of **5-Me** with a second equiv of CH_3CN to generate **6-Me** is calculated to be close to thermoneutral (ΔG = +1.9 kcal·mol^{-1}), consistent with the observed equilibrium.

Combing the DFT studies with the binding studies in chapter 2 provide us with a good basis for understanding how substrates bind to complex **2**. First we expect that the Ir–O bond *cis* to the Ir–H will dissociate, providing an open site for substrate binding. Dissociation of the Ir–O bond *trans* to the Ir–H to generate a five coordinate substrate bound complex is expected to be more difficult, which is reflected by the calculations, and the equilibria engaged between **5** and **6**. These processes can be rapid, with fluxional NMR processes observed in some cases. From this understanding, we wanted to observe how cations affect substrate binding to **2**.

Cation-Modulated Binding Equilibria

The pincer-crown ether ligand was designed to promote cation–macrocycle interactions. Cation intercalation seemed likely to perturb the ligand substitutions discussed above, since the resulting dissociated macrocycle would be free to interact with s-block cations. Cation–macrocycle interactions were therefore targeted in subsequent studies. Lithium and sodium salts of the weakly coordinating, lipophilic BAr^F_4 anion were used, on the basis of early indications that triflato ions bind Ir (Figure 3.9-3.10 in the experimental section).[92]

Addition of $LiBAr^F_4$ or $NaBAr^F_4$ to CD_2Cl_2 solutions of **2** (containing 125 mM Et_2O for improved solubility) resulted in no observable shifts in the resonances of **2**. Whether or not the macrocyclic oxygen ligands are dissociating, this indicates that any equilibrium formation of low-coordinate or solvento species is strongly disfavored under these conditions.

Alkali metal cations present in solution dramatically perturb adduct-forming equilibria involving **2** (Scheme 3.3). Whereas adduct formation between CH_3CN and **2** establishes equilibrium in the absence of salts (Scheme 3.3), the reaction is irreversible in the presence of $NaBAr^F_4$ (no free CH_3CN was observed, precluding equilibrium measurements). Even with less than 2 equiv of CH_3CN, the bis-nitrile complex is the major product under these conditions.

Attempts to reverse the reaction under reduced pressure (solids exposed to vacuum for 11 h) were unsuccessful, in sharply contrast with the facile removal of CH_3CN ligands from **6** in the absence of salts. Analogous behavior was observed upon addition of CH_3CN to solutions of **2** containing $LiBAr^F{}_4$.

Scheme 3.3

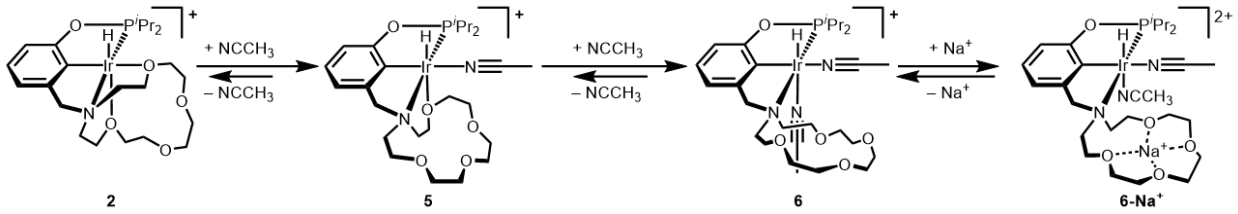

Perturbation of equilibria is attributed to cation–crown interactions. Figure 3.3 shows the effect of adding increasing amounts of Na^+ to an equilibrium mixture of CH_3CN, **5**, and **6**. The hydride resonance of **5** shows no change in chemical shift with increasing amounts of Na^+. The hydride resonance of **6**, however, broadens and shifts upfield, and another hydride resonance of similar chemical shift appears as more Na^+ is added. The cation-dependent chemical shift indicates rapid reversible adduct formation between Na^+ and **6**, made possible when the tridentate binding mode of the pincer-crown ligand is accessed (Scheme 3.3). The products must be closely related, as they feature overlapping hydride resonances and two sets of CH_3CN methyl resonances. The appearance of an extra set of peaks for the $BAr^F{}_4$ anion is consistent with different ion-pairing or aggregation states mediated by Na^+.[98–100] The data indicate that stronger cation–crown interactions are present in the tridentate coordination mode of **6** than in the tetradentate coordination mode of **5** (wherein no interaction with Na^+ is apparent by NMR spectroscopy). In CD_3CN, only one hydride resonance is observed, and similar sodium-dependent changes in chemical shift are observed by ^1H and $^{13}C\{^1H\}$ NMR spectroscopy (Figures 3.23-3.24 in the experimental section).

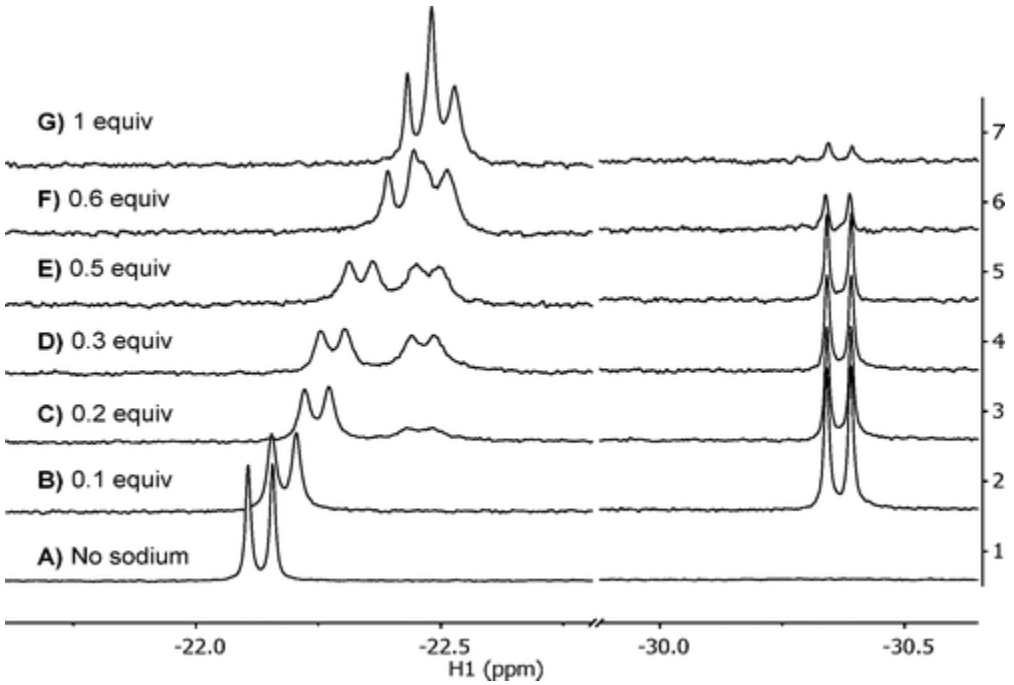

Figure 3.1: ^{1}H NMR spectra (hydride region) showing the reaction of 9.3 mM **2** in $CDCl_3$ (containing 185 mM Et_2O) with CH_3CN under various conditions: (A) addition of 192 equiv of CH_3CN to form complex 6 (δ −22.13); (B–G) addition of 3 equiv of CH_3CN to establish an equilibrium mixture of 5 (δ −30.37) and 6, followed by increasing amounts of Na^+ as indicated.

Cation-Accelerated Dihydrogen Splitting

The cation-modulated ligand substitution reactions above suggested that pincer-crown ether ligands could act as a "gate" for substrate binding in catalytic reactions. A weakly coordinating substrate would not readily undergo substitution reactions at the coordinatively saturated metal center. An appropriate cation could, however, alter the substrate binding constants, effectively opening the gate and initiating catalysis.

Scheme 3.4

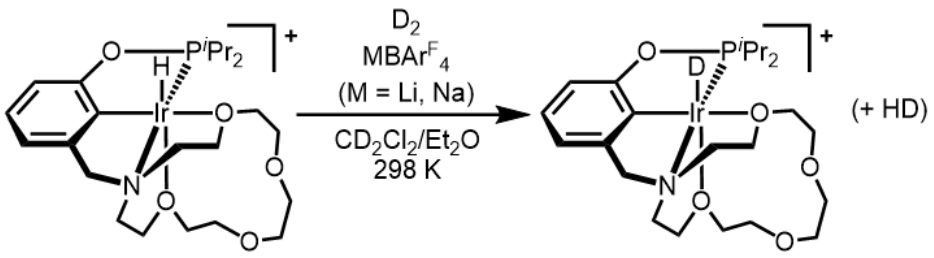

To test this hypothesis, we targeted the very weakly coordinating dihydrogen ligand,[101,102] the binding and activation of which is critical to numerous catalytic reactions. These reactions were carried out in chlorinated solvents with small amounts of diethyl ether to ensure full solubility of the alkali metal salts. Exposure of CD_2Cl_2 solutions containing 6.25 mM hydride **2** and 125 mM Et_2O to an atmosphere of D_2 gas resulted in slow H/D exchange (Scheme 3.4). The hydride signal of **2** exhibited exponential decay kinetics under 1 atm D_2 (k_{obs} = 7.23 x 10^{-5} min^{-1}, $t_{1/2}$ = 160 h), indicating a process that is first-order in **2**. During the reaction, only the ^1H NMR resonance for the Ir–H changed, gradually disappearing. By $^{31}P\{^1H\}$ NMR spectroscopy, however, two distinct resonances were observed, with the signal for **2** (δ 140.98) being consumed with simultaneous formation of a new resonance at nearly identical chemical shift (δ 141.26). The similarity in spectral signatures, along with the presence of a deuteride signal at δ –29.7 in the ^2H NMR spectrum, confirm that the product is [(κ^5-^{15c5}NCOP^{iPr})Ir(D)][BAr^F_4] (**2-D**). This rate of deuterium incorporation is much slower than [(POCOP)Ir(H)(D_2)]$^+$, which undergoes exchange within seconds.[103] The additional ether donors in **2** prohibit observation of a hydrido-dihydrogen complex and substantially hinder the reaction.

The reaction was repeated under identical conditions but in the presence of $LiBAr^F_4$ and $NaBAr^F_4$ additives. In the presence of just 0.3 equivalents of Na^+, the Ir–H was converted to Ir–D with a rate constant k_{obs} = 1.43 x 10^{-3} min^{-1} ($t_{1/2}$ = 8 h). It is noteworthy that this dramatic 20-fold rate enhancement occurs with a substoichiometric quantity of Na^+ in solution (Figure 3.2). Even faster rates of D_2 cleavage were observed when 0.4 equivalents of $LiBAr^F_4$ was added, with an observed rate constant of 1.82 x 10^{-2} min^{-1} ($t_{1/2}$ = 40 min) indicating a roughly 250-fold rate acceleration. The ability to modulate reaction rate based on the choice of alkali metal salt is particularly exciting: small differences in binding energies (< 1 kcal·mol^{-1} in many examples

involving Li^+/Na^+ adducts with 12-crown-4) result in rates that differ by an order of magnitude.[58,59] The catalyst is "selective" for lithium promotion over sodium promotion, presumably based on the macrocycle size. With only four donors (at most) available to interact with the *s*-block metal ion, interactions with smaller cations such as Li^+ may be favored.

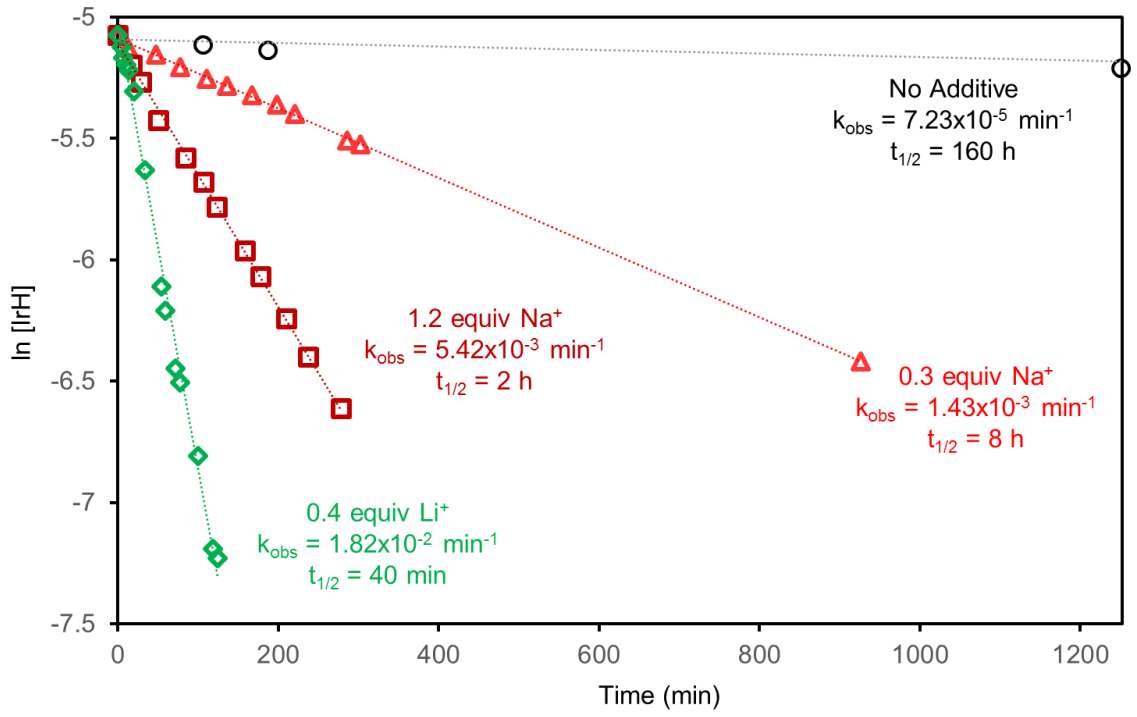

Figure 3.2: Plot of the natural log of concentration of hydride **2** versus time during the reaction with 1 atm of D_2. The reaction was run with no added salts (empty cirlces), 0.3 equiv of $NaBAr^F{}_4$ (red triangles), 1.2 equiv of $NaBAr^F{}_4$ (maroon squares), and 0.4 equiv of $LiBAr^F{}_4$ (green diamonds). Linear fits are given by dashed lines.

Additional $NaBAr^F{}_4$ leads to even faster conversion to Ir–D species **2-D**, as shown in Figure 3.2. Moving from 0.3 equiv Na^+ to 2.5 equiv Na^+, the reaction accelerates markedly (half life decreases from 483 minutes to 36 minutes). Thus, the reaction rate can be tuned over two orders of magnitude either by changing the identity of the cation (Li^+ vs. Na^+) or by adjusting the concentration of a particular cation (as shown in the experiments varying $[Na^+]$).

Interestingly, the plot of k_{obs} vs. concentration of Na^+ is non-linear (Figure 3.3A), with faster-than-expected rates at higher concentrations of Na^+. Assuming that reactivity is first order

in [Na^+], we would expect k_{obs} to increase linearly with [Na^+]. The non-linear behavior may reflect modest quenching of the Lewis acidity of Na^+ by Et_2O. At low [Na^+], more Et_2O relative to Na^+ will be present, which can donate to Na^+ and moderate the Lewis acidity. On the other hand, the [Et_2O] is constant while [Na^+] is increasing, so less Et_2O is present relative to Na^+, enhancing the ability of Na^+ to interact with the macrocyclic pincer ligand. This theory is buttressed by the observation that the ^{1}H NMR resonances of Et_2O shift as a function of [Na^+], indicating rapid adduct formation equilibrium (Figure 3.3B).

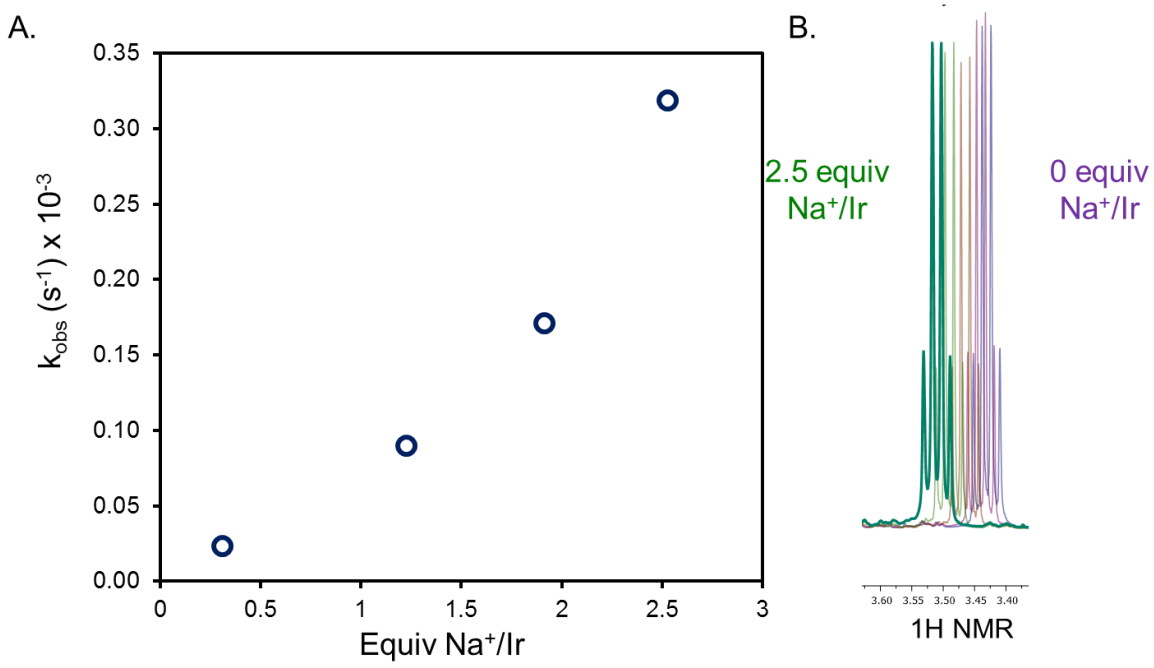

Figure 3.3: (A) Plot of observed first-order rate constant versus concentration of Na^+. Conditions: 6.25 mM **2**, 125 mM Et_2O, CD_2Cl_2, 298 K. For full details, see the experimental section. (B) ^{1}H NMR resonances for the Et_2O molecules in solution as a function of [Na^+].

A plausible mechanism involving tunable dynamic hemilability is proposed to account for the cation-dependent conversion of **2** to **2-D**, as shown in Scheme 3.5. We propose that hydrogen binds at the site cis to the hydride following Ir–O dissociation. Intercalation of lithium or sodium ion into the macrocycle stabilizes a reactive deuterium σ complex, which then

undergoes H/D exchange followed by release of the cation and HD gas. The observed influence of Li^+ and Na^+ on the equilibrium of acetonitrile substitution provides a basis for the proposed stabilization of the dihydrogen complex.

Scheme 3.5

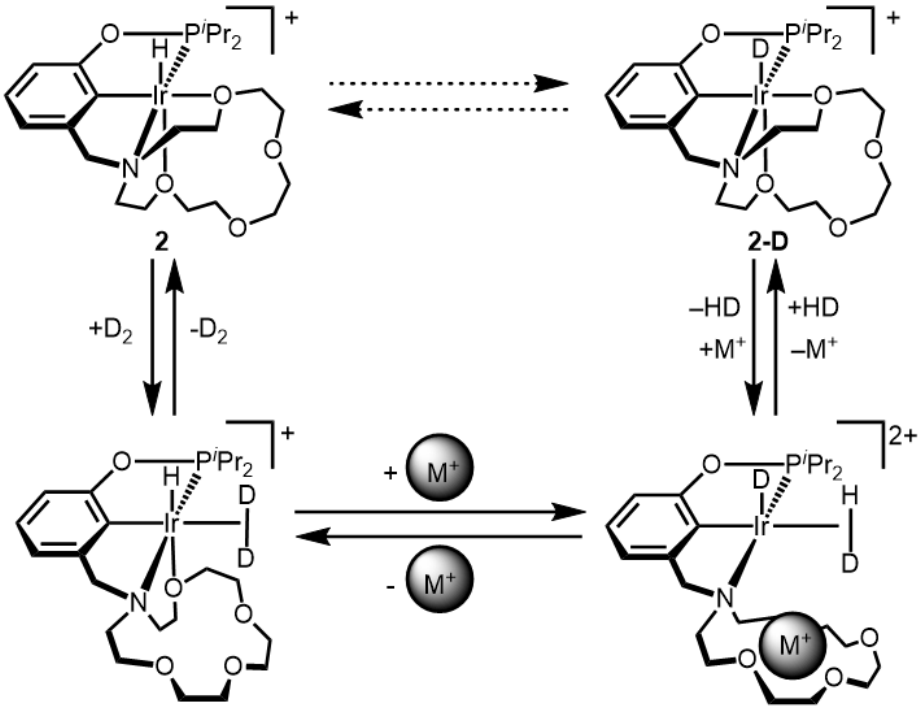

No intermediates were observed during *in situ* ^1H NMR spectroscopic monitoring, however, and no shifts in the resonances of **2** were observed with increasing amounts of Na^+ (although the resonances of Et_2O did shift, Fig 3.3B). These observations suggest that equilibrium dissociation of the macrocycle is kinetically accessible, but thermodynamically unfavorable — as is typical for hemilabile catalysts.[36,38] The more dramatic rate enhancement by Li^+ is attributed to larger shifts in the equilibrium constants due to stronger interactions with the four ether donors of the pendent macrocycle.

Following complete deuteration, the headspace was replaced with H_2 gas. The reactions proceeded to re-form hydride **2**, but at a slower rate than the forward reaction. In two

experiments with different salts, the forward reaction was faster by a factor of 2.65 (0.4 equiv Li^+, Figure 3.16 in the experimental section) and 2.29 (2.52 equiv Na^+, Figure 3.17 in the experimental section). These values reflect a primary isotope effect, suggesting that dihydrogen cleavage (and/or Ir–H/D cleavage) is involved in the rate-determining step.

The reaction can also be carried out in CD_2Cl_2 or $CDCl_3$ without added Et_2O. Similar rate enhancements were observed in the presence of $NaBAr^F_4$ ($t_{1/2}$ = 14 hours) and $LiBAr^F_4$ ($t_{1/2}$ = 11.9 minutes), which is remarkable given the almost complete insolubility of the BAr^F_4 salts under these conditions (based on relative integration of the Ar^F protons).

The reaction rate can be slowed by the removal of Na^+ from solution. Figure 3.4 shows the conversion of **2** as it reacts rapidly with D_2 in the presence of 1.9 equiv of $NaBAr^F_4$. The reaction was allowed to proceed to ~60% conversion, at which time the tube was degassed and 1.8 equiv of $[Bu_4N][Cl]$ was added. After the D_2 atmosphere was restored, the reaction proceeded—but at a rate 5 times slower than that before chloride addition. The reduction in rate and the observed white precipitate suggest that Na^+ was removed from solution as insoluble NaCl. The rate after chloride addition is consistent with the presence of only a small amount of residual Na^+.

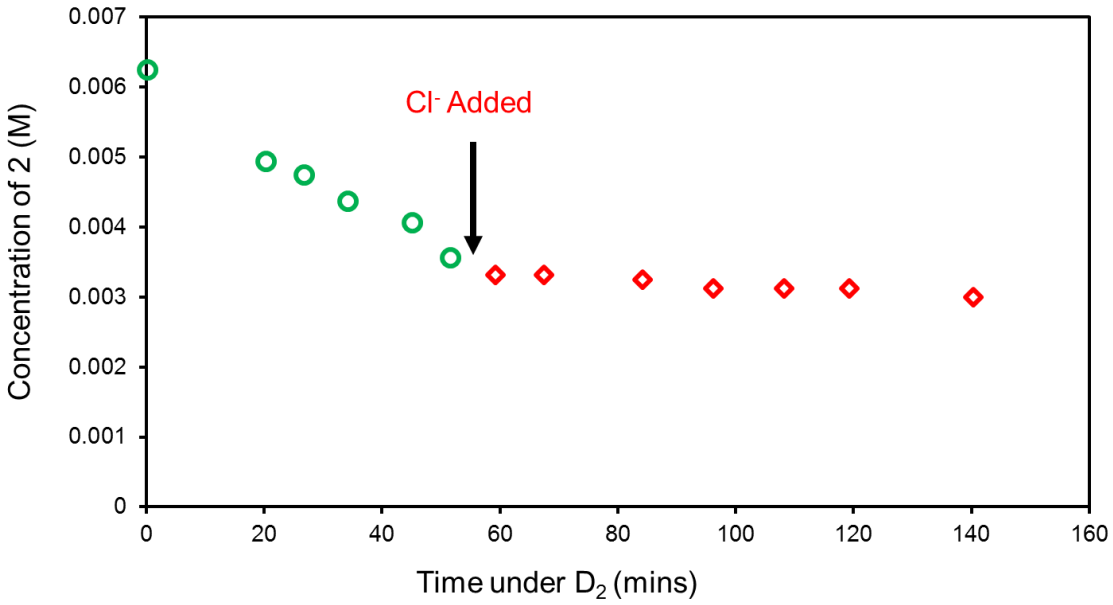

Figure 3.4: Progress of the reaction of **2** with 1 atm of D_2 in the presence of $NaBAr^F{}_4$(1.9 equiv) hindered by the addition of $[Bu_4N][Cl]$ (1.8 equiv) after 50 min. Conditions: 6.25 mM **2**, 125 mM Et_2O, CD_2Cl_2, 298 K.

Conclusions

The ability to speed up or slow down a reaction through sequential addition of Na^+ and Cl^- is reminiscent of Mirkin's catalysis involving static hemilability, but the roles of Na^+ and Cl^- are reversed: previous systems rely on Cl^- for activation and Na^+ for deactivation, whereas here Na^+ is the activating reagent and Cl^- deactivates the reaction.[56]

Most previous reports on controlling hemilability have focused on switchable catalysis using static hemilability.[57] These catalysts are either fully active or fully inactive. In contrast, the kinetics of hydrogen activation by **2** reveal the ability of cation–crown interactions to smoothly tune the reaction rate on the basis of the identity and concentration of the ion. Even with excess cation, the only observed species is a stabilized form of the complex, suggesting that the benefits of dynamic hemilability might be retained in catalysis (whereas a catalyst featuring static hemilability, with a fully dissociated ligand, might be prone to decomposition). The observation that Li^+ and Na^+exhibit different levels of activity is particularly intriguing, suggesting that

matching the cation to the macrocycle can tune catalyst activity in a highly controlled fashion. The weak cation–macrocycle interactions are well matched to the energy regimes found in catalysis, where small energy differences give large differences in activity or selectivity.

3.3 Experimental Section

General Considerations

All compounds were manipulated using standard vacuum line or Schlenk techniques or in a glovebox under a nitrogen atmosphere. NMR scale reaction mixtures were prepared under nitrogen in a glovebox and kept in Teflon-sealed tubes. Under standard glovebox operating conditions, pentane, diethyl ether, benzene, toluene, and tetrahydrofuran were used without purging, such that traces of those solvents were present in the atmosphere and in the solvent bottles. ^{1}H, ^{31}P, ^{19}F, and ^{13}C NMR spectra were recorded on 400, 500, and 600 MHz spectrometers. NMR characterization data are reported at 298 K, unless specified otherwise. All NMR solvents and isotopically labeled reagents were purchased from Cambridge Isotope Laboratories, Inc. Benzene-d_6 (C_6D_6), chloroform-*d* ($CDCl_3$), and methylene chloride-d_2 (CD_2Cl_2) were freeze–pump–thaw degassed three times before drying by passage through a small column of activated alumina. Tetrahydrofuran-d_8 (THF-d_8) was purchased in a sealed ampule, which was broken under an N_2 atmosphere before filtration through activated alumina. Chemical shifts for ^{1}H and ^{13}C NMR spectra are reported in ppm relative to residual proteo solvent impurity.[91] ^{31}P resonances are reported relative to 85% H_3PO_4 external standard (0 ppm). ^{19}F resonances are reported relative to 0.05% trifluorotoluene ($C_6H_5CF_3$) in $CDCl_3$ as an external standard (−63.72 ppm). $NaBAr^F{}_4$ was synthesized according to literature procedures.[92] All other reagents were commercially available and were used without further purification.

Elemental analyses were performed by Atlantic Microlabs (Norcross, GA) and Robertson Microlit Laboratories (Ledgewood, NJ).

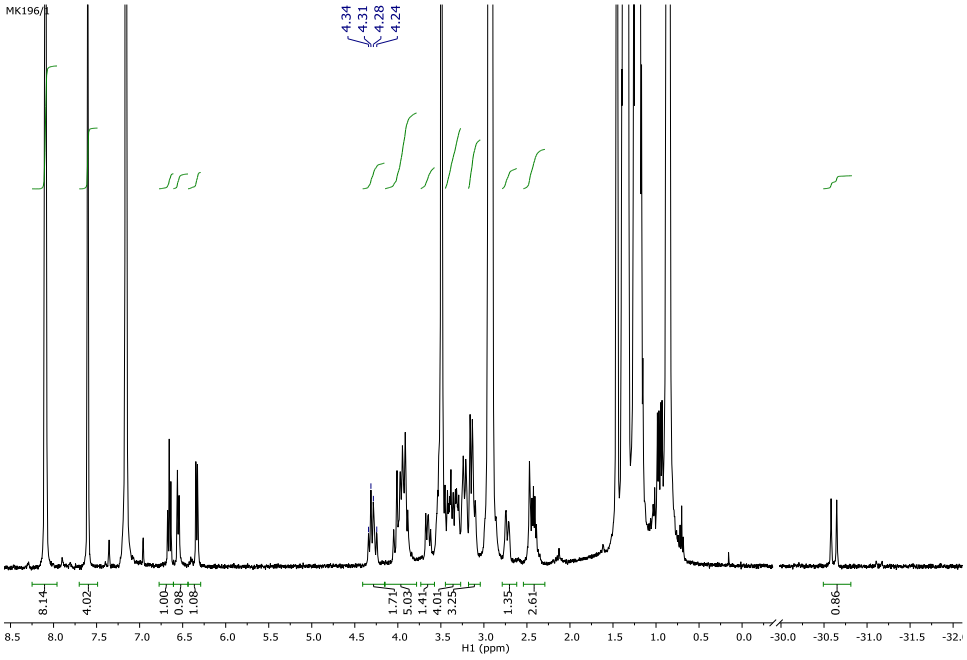

Figure 3.5: ^{1}H NMR for the addition of 5 equivalents NBu_4OTf to 2 in 2:1 C_6D_6:THF-d_8.

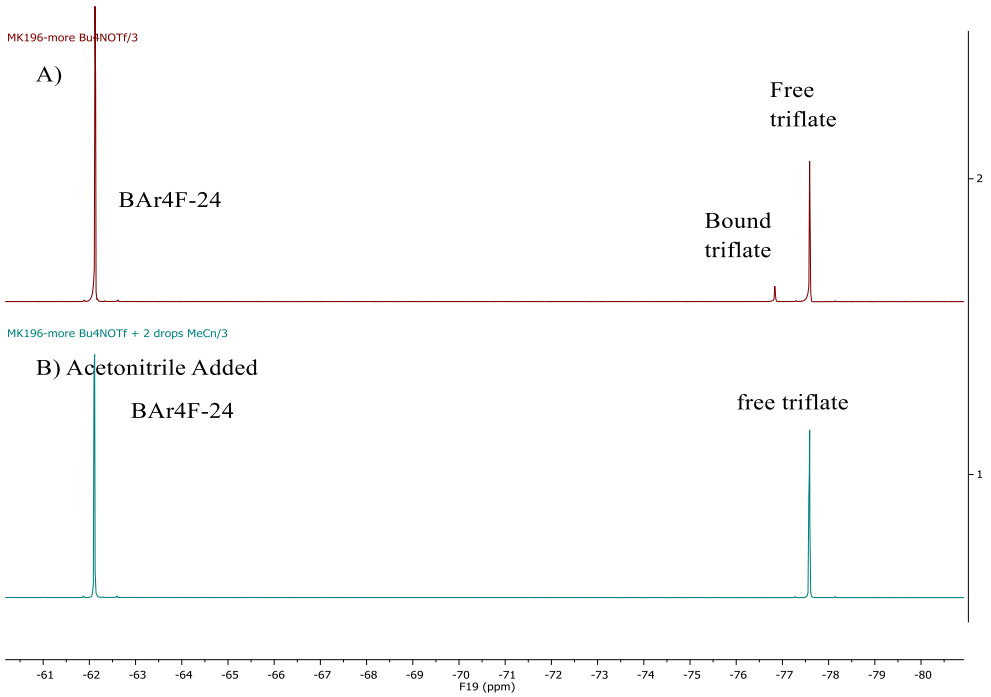

Figure 3.6: A) ^{19}F NMR for the reaction of 2 and NBu_4OTf in 2:1 C_6D_6:THF-d_8. B) ^{19}F NMR for the reaction of 2 and NBu_4OTf in 2:1 C_6D_6:THF-d_8 after addition of 20 equivalents CH_3CN.

Cation-modulated Binding Equilibrium

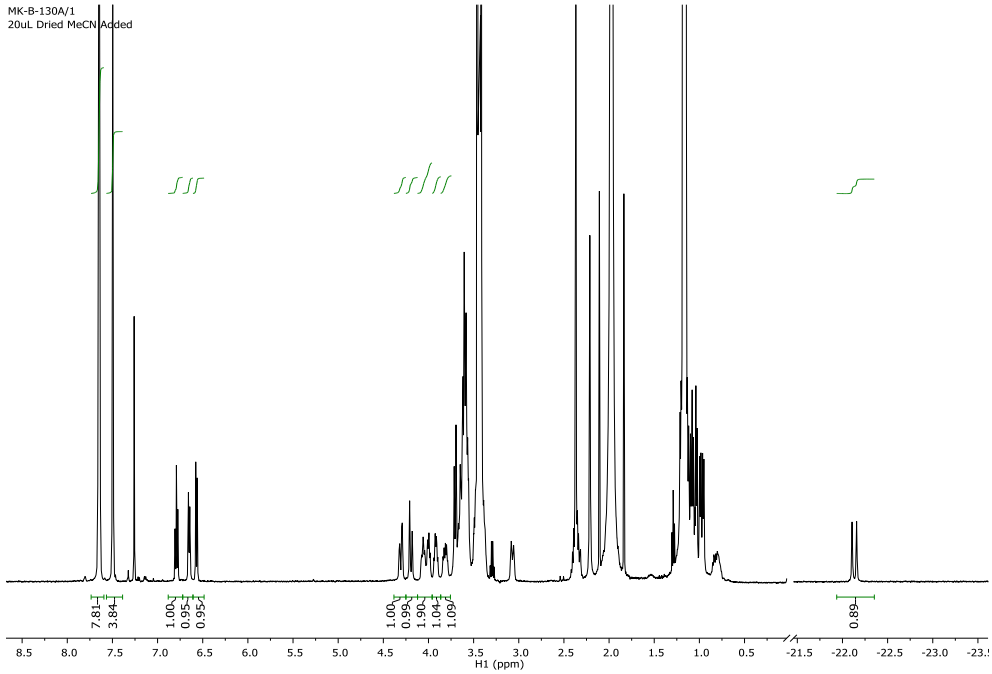

Figure 3.7: ^{1}H NMR of complex **6** formed from 9.3 mM 2 and 192 equiv CH_3CN in $CDCl_3$ with 185 mM Et_2O (no sodium added).

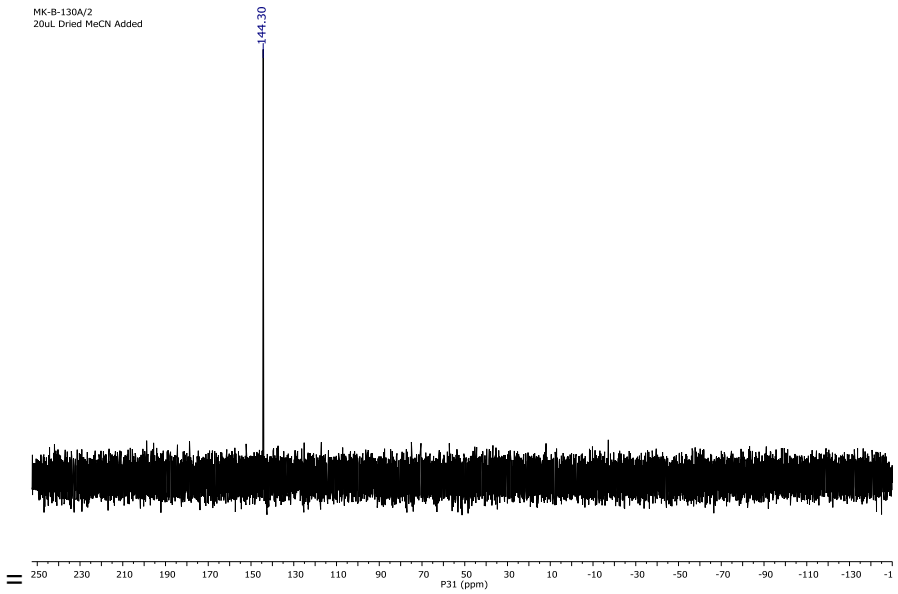

Figure 3.8: $^{31}P\{^{1}H\}$ NMR of complex 6 formed from 9.3 mM 2 and 192 equiv CH_3CN in $CDCl_3$ with 185 mM Et_2O (no sodium added).

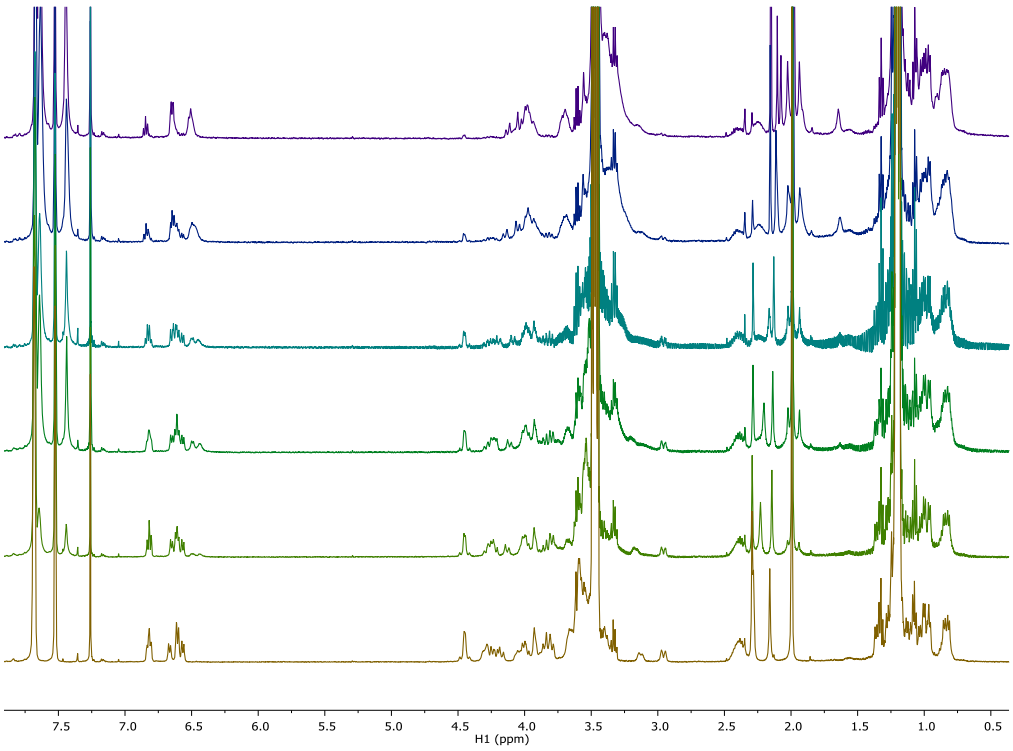

Figure 3.9: ^{1}H NMR spectra (aromatic and aliphatic regions) of 9.3 mM 2 and 3 equivalents CH_3CN with 1 eq $NaBAr^{F}_4$ (top), 0.6 equiv, 0.5 equiv, 0.3 equiv, 0.2 equiv, 0.1 equiv (bottom) in $CDCl_3$ with 185 mM Et_2O.

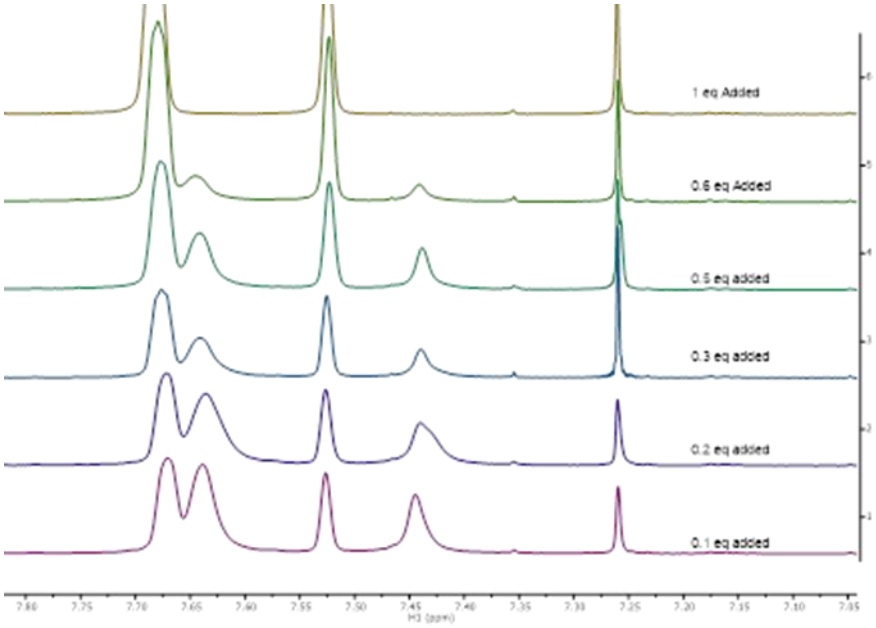

Figure 3.10: ^{1}H NMR spectra aromatic region of 9.3 mM 2 and 3 equivalents CH_3CN with different equiv $NaBAr^F_4$ in $CDCl_3$ with 185 mM Et_2O.

Dihydrogen Activation Reactions

A stock solution of 6.25 mM [(κ^5-^{15c5}NCOP^{iPr})Ir(H)][BAr^F_4] (**2**) in CD_2Cl_2 containing 125 mM Et_2O was prepared by dissolving 0.0531 g (0.0355 mmol) of **2** in 5.600 mL of CD_2Cl_2 and 0.0750 mL (0.7219 mmol) of Et_2O. Teflon-sealed NMR tubes were charged with 0.450 mL of the stock solution along with increasing amounts of $NaBAr^F_4$ or of $LiBAr^F_4$. Tubes containing no salts, 0.31 equiv of $NaBAr^F_4$, 1.23 equiv of $NaBAr^F_4$, 1.76 equiv of $NaBAr^F_4$, 2.52 equiv of $NaBAr^F_4$, and 0.40 equiv of $LiBAr^F_4$ were prepared. Initial NMR spectra were taken. The tubes were freeze–pump–thaw degassed twice to remove N_2 and back-filled with D_2 at 298 K. The reaction progress (**2** to **2-D**) was monitored over time and quantified by integration of the hydride peak relative to the phenyl backbone. To obtain kinetic isotope effect data, reactions were allowed to react for 3 days to ensure complete conversion to **2-D** before being

freeze–pump–thaw degassed twice and back-filled with H_2. The reaction progress (**2-D** to **2**) was monitored over time by NMR spectroscopy.

The reaction rate could be slowed by addition of chloride. The preceding procedure was followed, with 6.25 mM **2** and 1.94 equiv of $NaBAr^F{}_4$ under D_2 in CD_2Cl_2. When conversion of **2** to **2-D** had reached 57%, the tube was freeze–pump–thaw degassed. The tube was then charged with 1.76 equiv $[NBu_4][Cl]$ under N_2. The tube was freeze–pump–thaw degassed twice to remove N_2 and back-filled with D_2 at 298 K. The reaction was monitored over time by NMR spectroscopy.

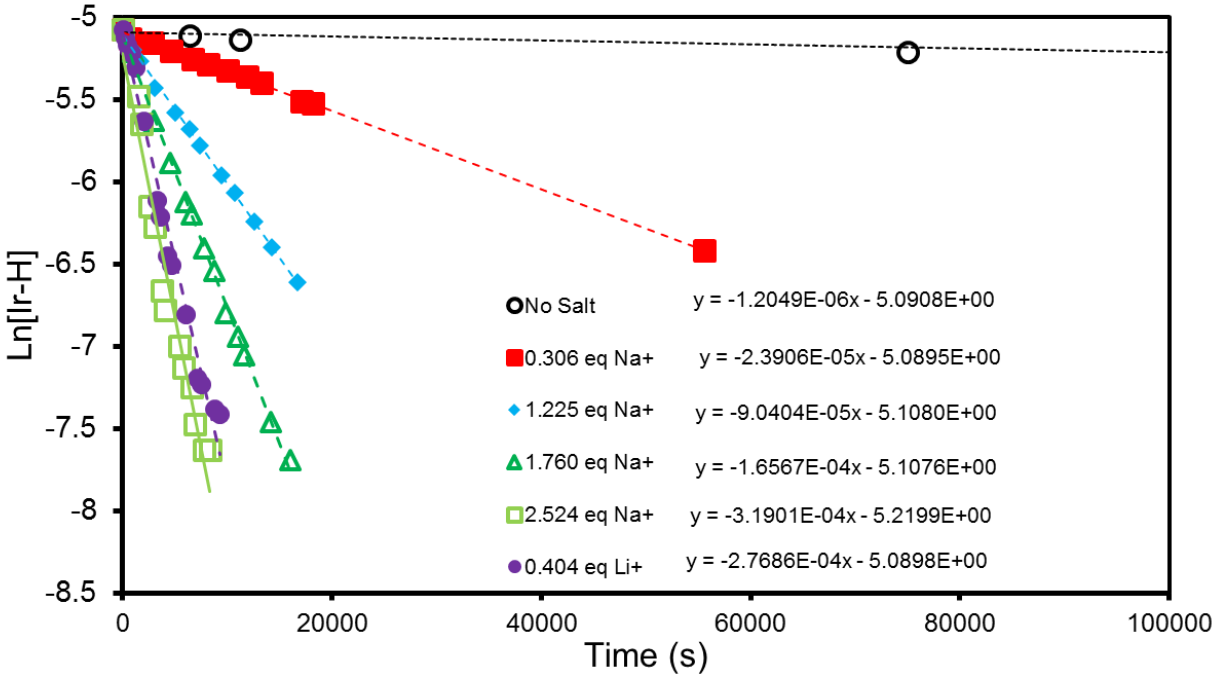

Figure 3.11: Consumption of hydride **2** at 0.0625 M to form **2-D** over time at varying cation concentrations.

Table 3.1: Rates for the consumption of hydride **2** at 0.0625 M to form **2-D** over time at varying cation concentrations.

Cation	Equivalents	k_{obs} (s^{-1})
none	0	1.20×10^{-6}
Sodium	0.306	2.39×10^{-5}
Sodium	1.225	9.04×10^{-5}
Sodium	1.706	1.66×10^{-4}
Sodium	2.524	3.19×10^{-4}
Lithium	0.404	2.77×10^{-4}

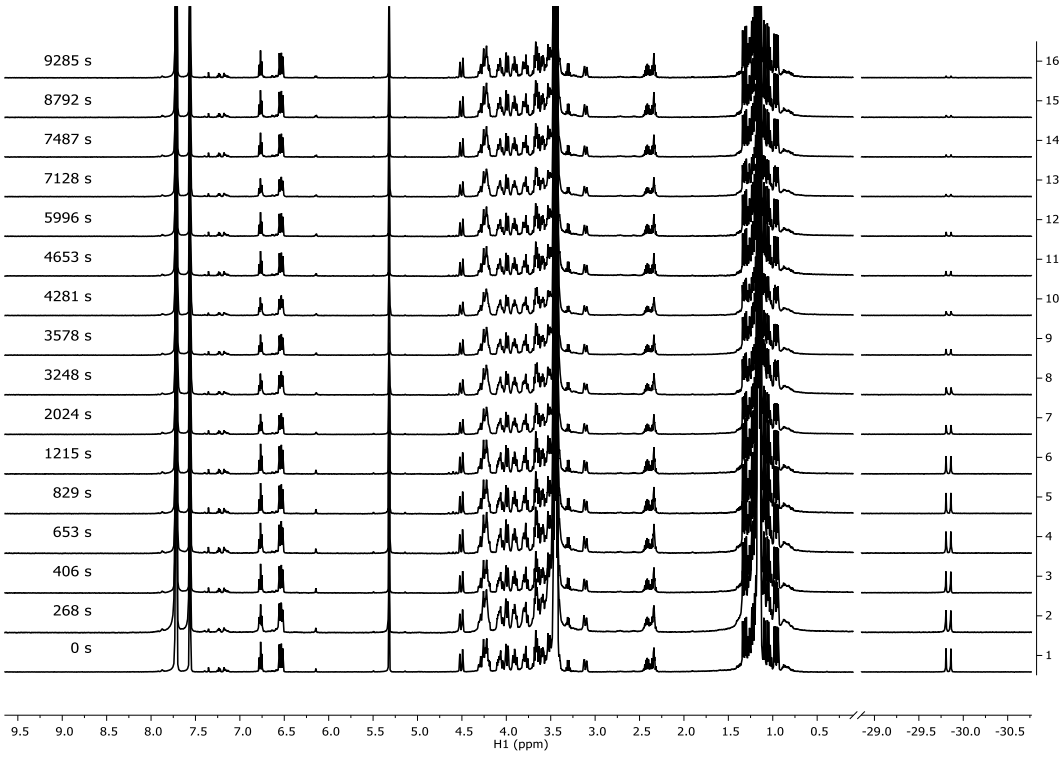

Figure 3.12: ^{1}H NMR time course for the conversion of 0.00625 M **2** to **2-D** with 0.404 equivalents $LiBAr^{F}_{4}$.

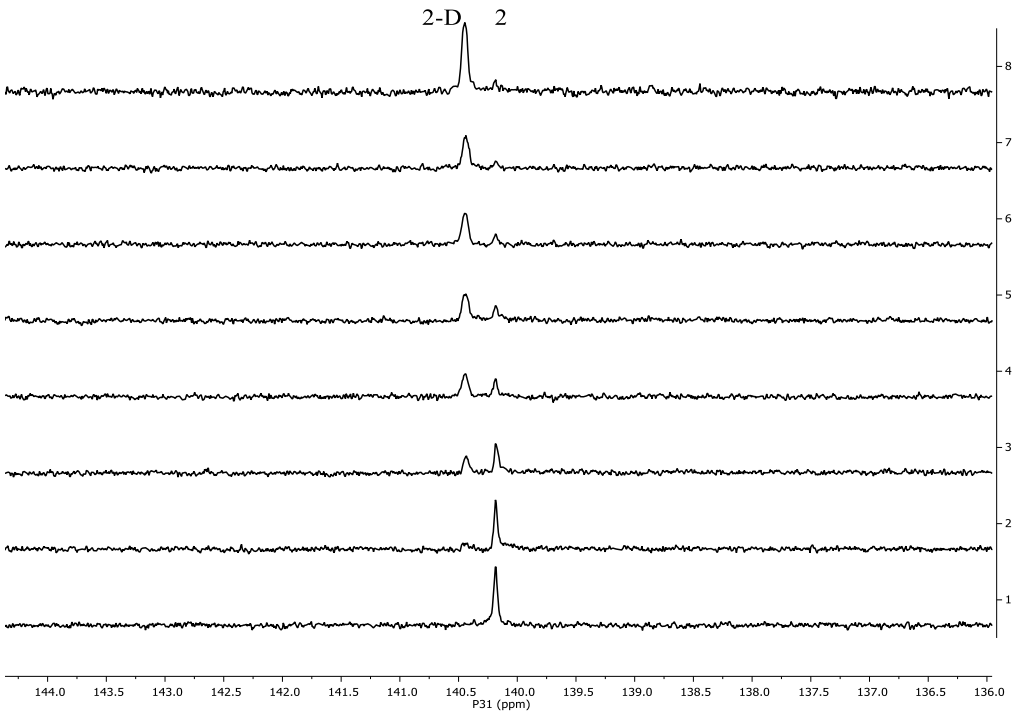

Figure 3.13: $^{31}P\{^{1}H\}$ NMR time course for the conversion of 0.00625 M **2** to **2-D** with 0.404 equivalents $LiBAr^{F}_{4}$.

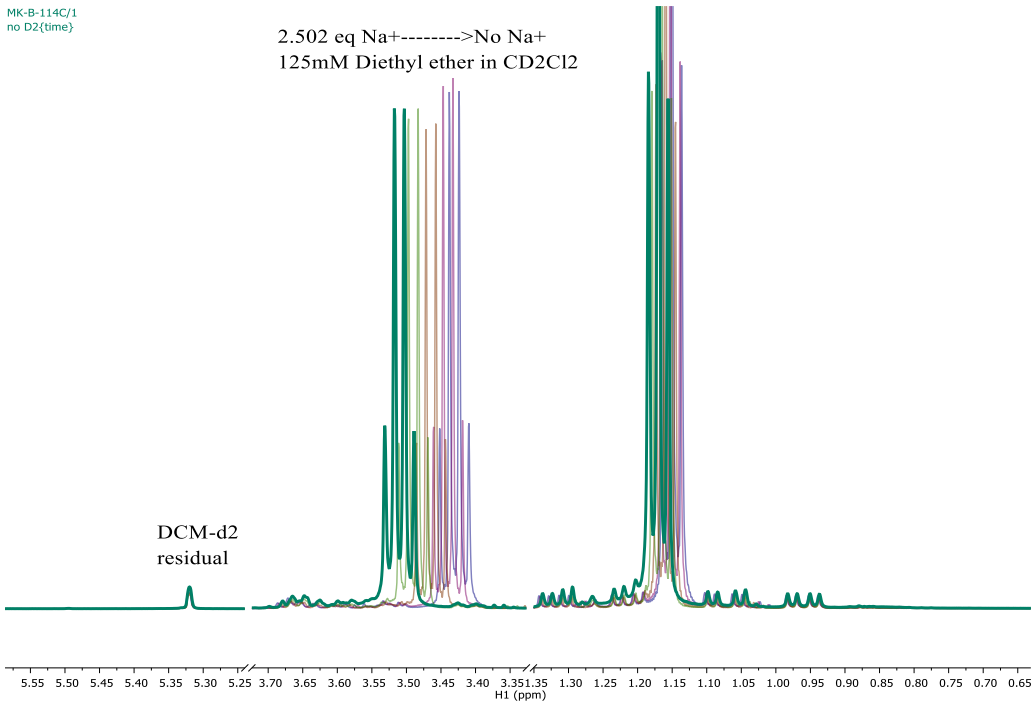

Figure 3.14: ^{1}H NMR overlay for the diethyl ether peaks in dihydrogen activation reactions. All tubes 6.25 mM **2** with 125 mM Et_2O with added amounts of $NaBAr^{F}_{4}$.

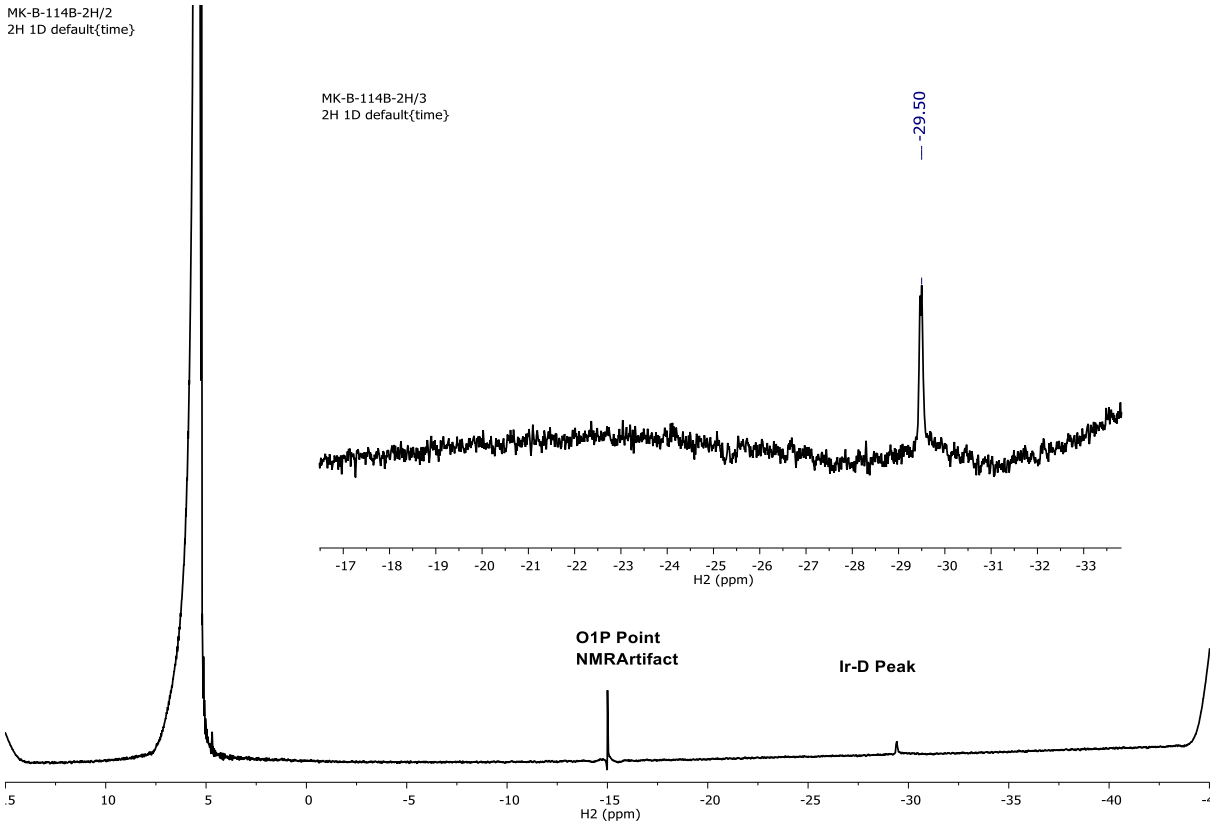

Figure 3.15: ^{2}H NMR spectrum of **2-D**, with inset showing hydride region.

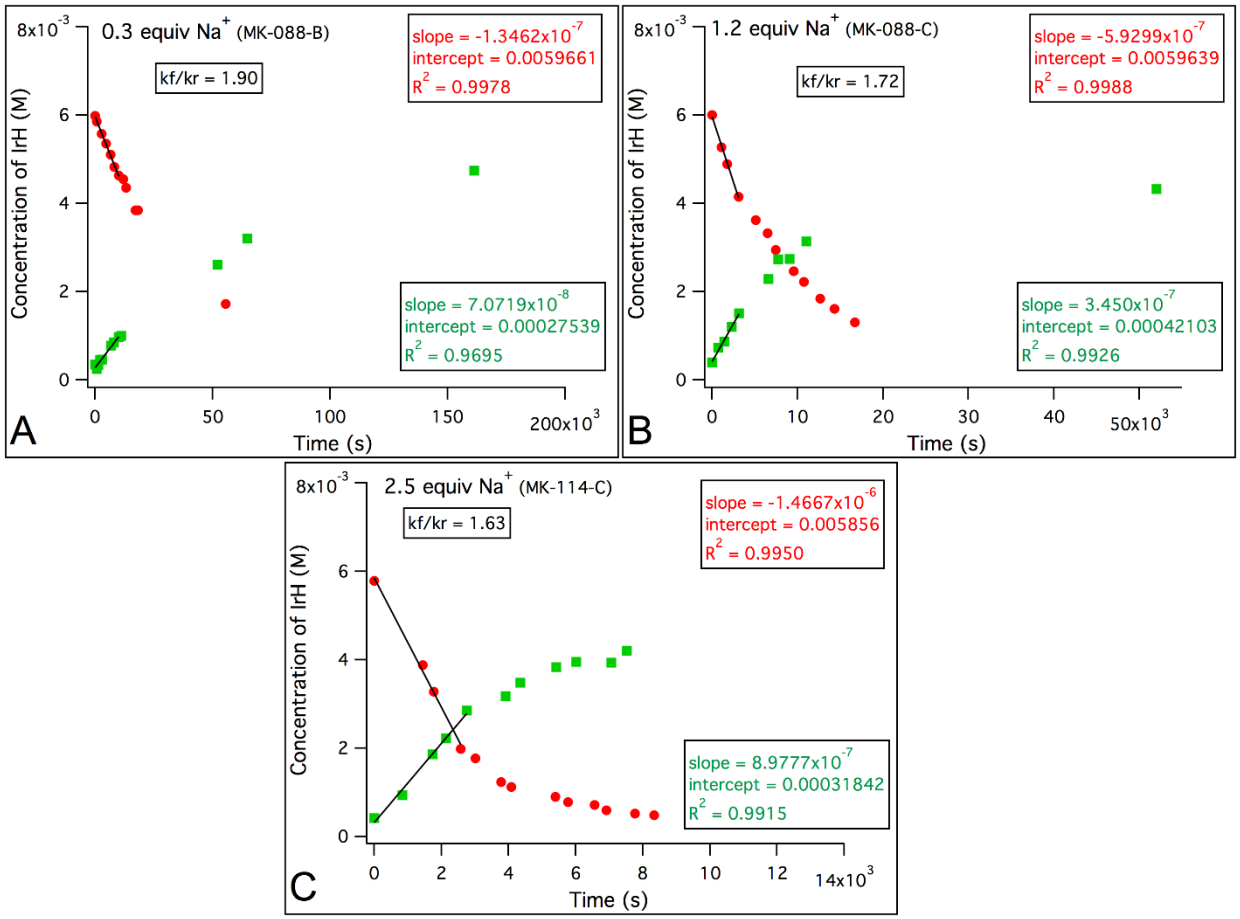

Figure 3.16: Time course of dihydrogen activation reactions used to determine kinetic isotope effect for $NaBAr^F_4$ reactions. The conversion of **2** under 1 atm D_2 (red circles) and the conversion of **2-D** to **2** under 1 atm H_2 (green squares) were monitored in the presence of 0.3 equiv $NaBAr^F_4$ (A), 1.2 equiv $NaBAr^F_4$ (B), and 2.5 equiv $NaBAr^F_4$ (C). A linear fit of the early portion of the data was used to determine an initial rate. The ratio of initial rates provided the kinetic isotope effect values as shown in each graph. Conditions: 6.25 mM Ir, 125 mM Et_2O, 298 K.

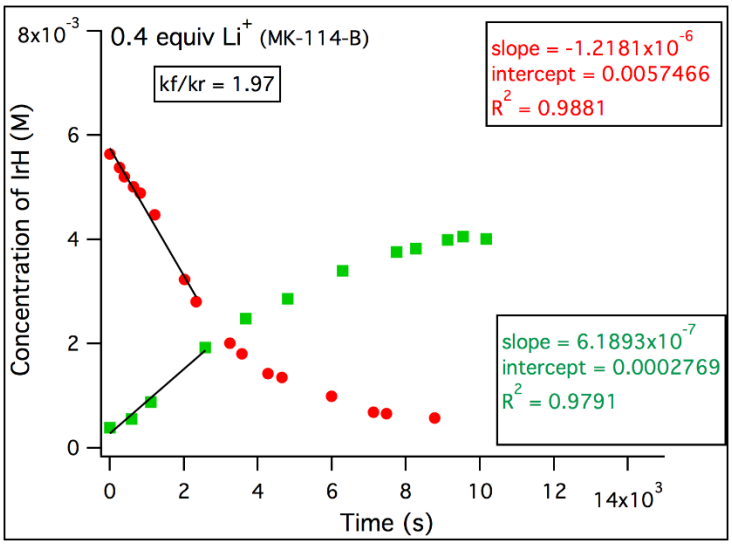

Figure 3.17: Time course of dihydrogen activation used to determine kinetic isotope effect for $LiBAr^F{}_4$ reaction. The conversion of **2** under 1 atm D_2 (red circles) and the conversion of **2-D** to **2** under 1 atm H_2 (green squares) were monitored in the presence of 0.4 equiv $LiBAr^F{}_4$. A linear fit of the early portion of the data was used to determine an initial rate. The ratio of initial rates provided the kinetic isotope effect value as shown in the graph. Conditions: 6.25 mM Ir, 125 mM Et_2O, 298 K.

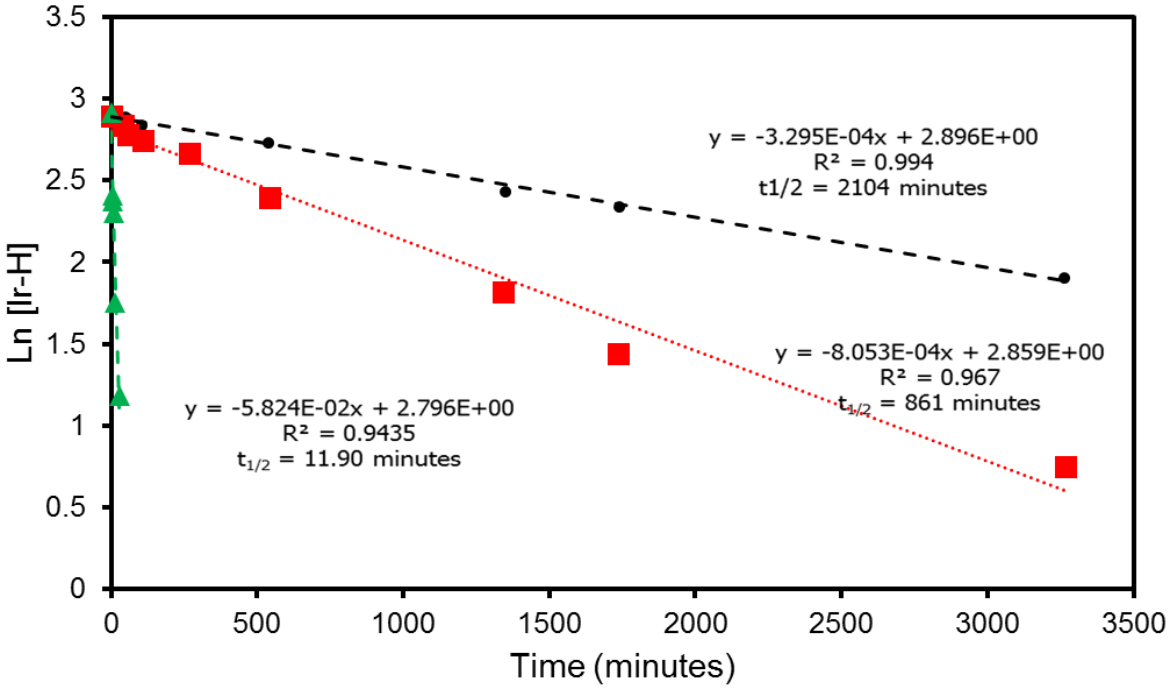

Figure 3.18: Dihydrogen activation reaction for 19.2 mM **2** in $CDCl_3$ with 1 atm D_2 and no cation added (black circles), $NaBAr^F{}_4$ added (red squares), and $LiBAr^F{}_4$ added (green triangles).

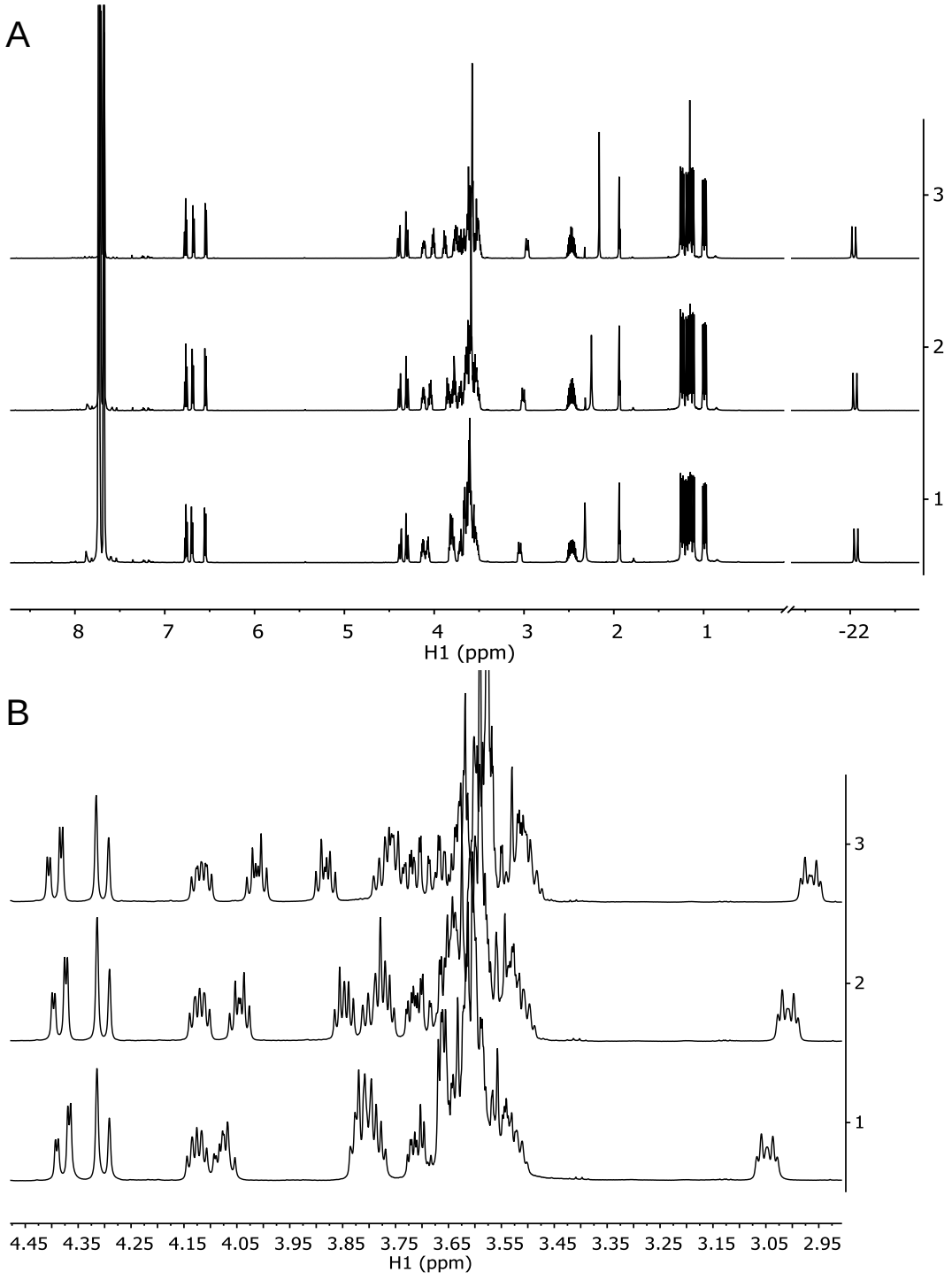

Figure 3.19: A) Full ^{1}H NMR spectra of **6** in CD_3CN (top); after addition of 1.1 equiv $NaBAr^F_4$ (middle), and after addition of 2.2 equiv $NaBAr^F_4$ (bottom). B) blow-up of crown ether region of the ^{1}H NMR spectra with no additive (top), after addition of 1.1 equiv $NaBAr^F_4$ (middle), and after addition of 2.2 equiv $NaBAr^F_4$ (bottom). The samples were initially prepared dissolving 2 in CD_3CN to form **6**.

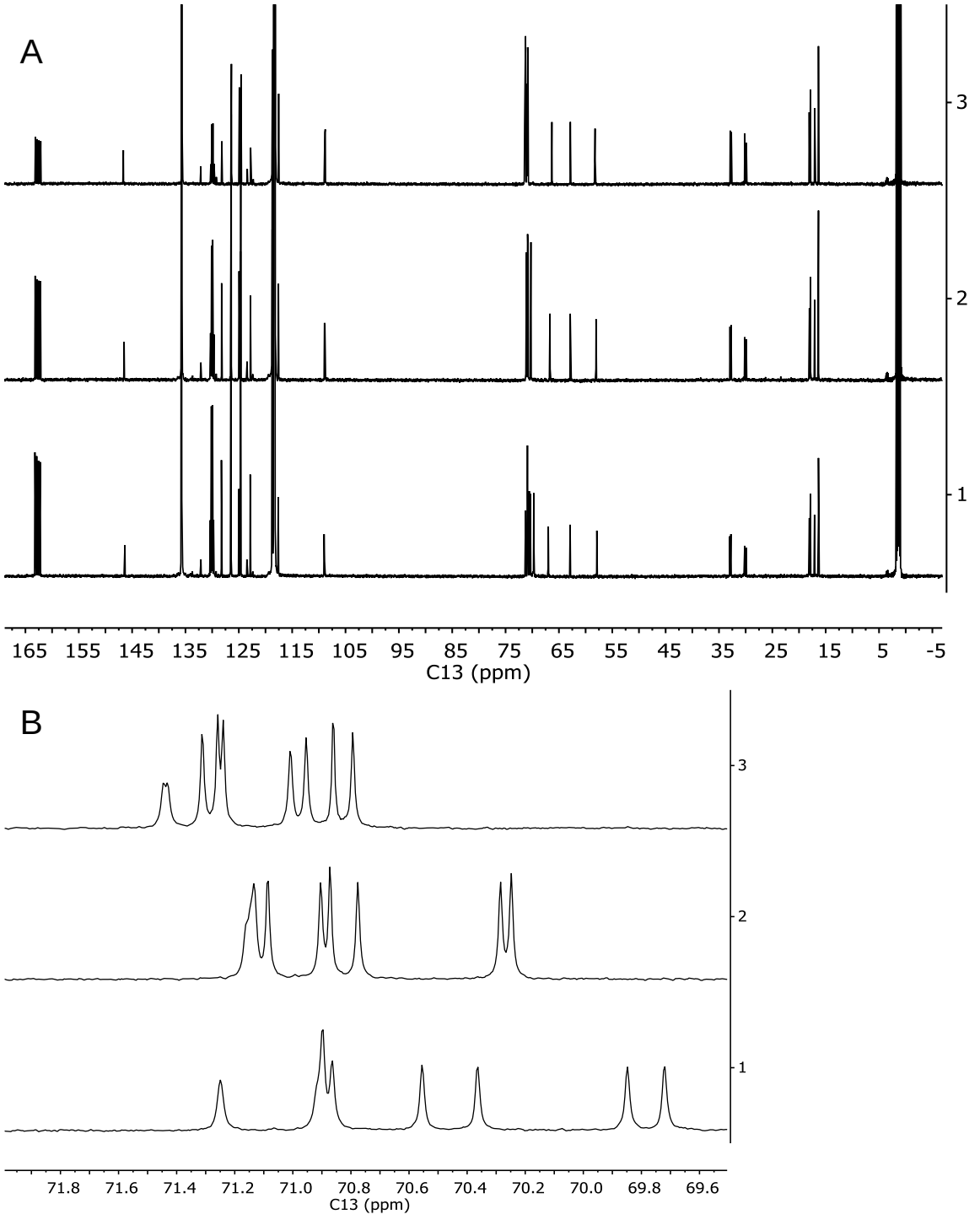

Figure 3.20: A) Full $^{13}C\{^{1}H\}$ NMR spectra of **6** in CD_3CN (top); after addition of 1.1 equiv $NaBAr^F_4$ (middle), and after addition of 2.2 equiv $NaBAr^F_4$ (bottom). B) blow-up of crown ether region of the $^{13}C\{^{1}H\}$ NMR spectra with no additive (top), after addition of 1.1 equiv $NaBAr^F_4$ (middle), and after addition of 2.2 equiv $NaBAr^F_4$ (bottom).

Computational Details

All calculations were performed using the Gaussian09 software package.[104] The PBE functional[105] was used for all calculations, with the LANL2DZ basis set[106] and pseudopotential used for Ir and the 6-311G(d,p) basis set[107,108] used for all other atoms. A slightly truncated ligand set was used, substituting methyl groups for isopropyl groups on the phosphine ligand. Initial geometries were based on the coordinates obtained from X-ray diffraction studies. After optimizing the structure, frequency optimizations were performed for each species to ensure that no imaginary frequencies were present and to compute Gibbs free energy values, which were used throughout. Except as noted, a polarizable continuum model (IEFPCM implemented by Gaussian09) approximated the effects of the CH_2Cl_2 solvent. The corresponding energy, enthalpy, and entropy values for each optimized structure are available below. Reaction thermodynamics are also available below in tabulated and graphical forms.

Structural Comparison

Table 3.2: Comparing Experimental and Computational Bond Lengths in (NCOP)Ir(H)(Cl) **(1)**. Gas phase.

Bond	XRD Length (Å)	DFT Length (Å)
Ir–P	2.183	2.189
Ir–C	1.979	1.972
Ir–N	2.222	2.221
Ir–Cl	2.467	2.491
Ir–H	[a]	1.546
Ir–O	2.355	2.341

[a]Hydride was not located in the difference map.

Table 3.3: Comparing Experimental and Computational Bond Lengths in $[(NCOP)Ir(H)]^+$ **(2)**. DCM PCM.

Bond Length / Angle	**XRD (Å or º)**	**DFT (Å or º)**
Ir–P	2.212	2.237
Ir–C	1.957	1.950
Ir–N	2.153	2.157
Ir–H	–	1.549
Ir–O2	2.229	2.305
Ir–O5	2.276	2.326
N–Ir–O5	76.5	75.8
N–Ir–O2	78.7	77.5
N–Ir–P	162.0	163.0

[a]Hydride was not located in the difference map.

*Thermodynamic Analysis of Ligand Dissociation from **1***

Table 3.4: Reactions of 1 with ΔE, ΔH, ΔS, ΔG (CH_2Cl_2 solvent model).

Reaction	ΔE (kcal·mol^{-1})	ΔH (kcal·mol^{-1})	ΔS (kcal·mol^{-1})	ΔG (kcal·mol^{-1})
(κ^4-NCOP)Ir(H)(Cl) → (κ^3-NCOP)Ir(H)(Cl)	11.84	11.46	4.31	10.17
(κ^4-NCOP)Ir(H)(Cl) → $[(\kappa^4$-NCOP)Ir(H)$]^+$ + Cl^-	27.56	27.57	25.59	19.94
(κ^4-NCOP)Ir(H)(Cl) → $[(\kappa^5$-NCOP)Ir(H)$]^+$ + Cl^-	20.17	20.38	23.04	13.51

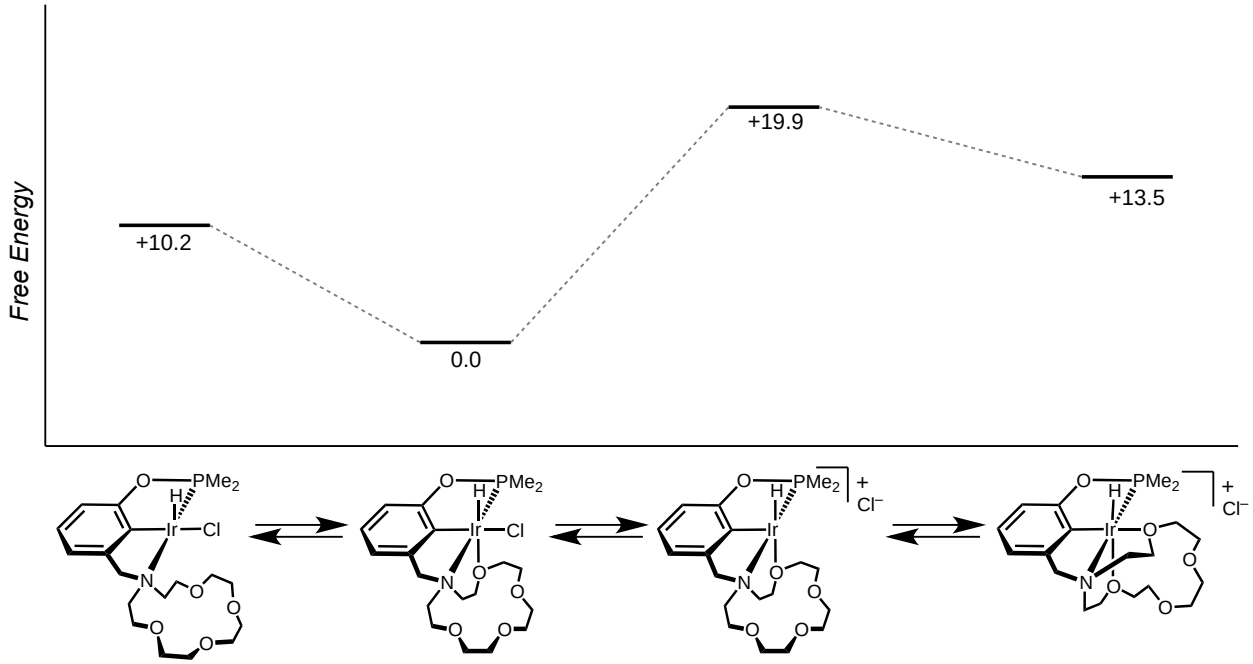

Figure 3.21: Ligand dissociation pathways of **1**, with CH_2Cl_2 solvent model.

*Thermodynamic Analysis of Ligand Dissociation from **2***

Table 3.5: Reactions of **2** with ΔE, ΔH, ΔS, ΔG (CH_2Cl_2 solvent model).

Reaction	ΔE (kcal·mol^{-1})	ΔH (kcal·mol^{-1})	ΔS (kcal·mol^{-1})	ΔG (kcal·mol^{-1})
[(κ^5-NCOP)Ir(H)]$^+$ → *trans*-[(κ^4-NCOP)Ir(H)]$^+$	7.39	7.19	2.54	6.43
[(κ^5-NCOP)Ir(H)]$^+$ → *cis*-[(κ^4-NCOP)Ir(H)]$^+$	14.85	14.23	3.05	14.23

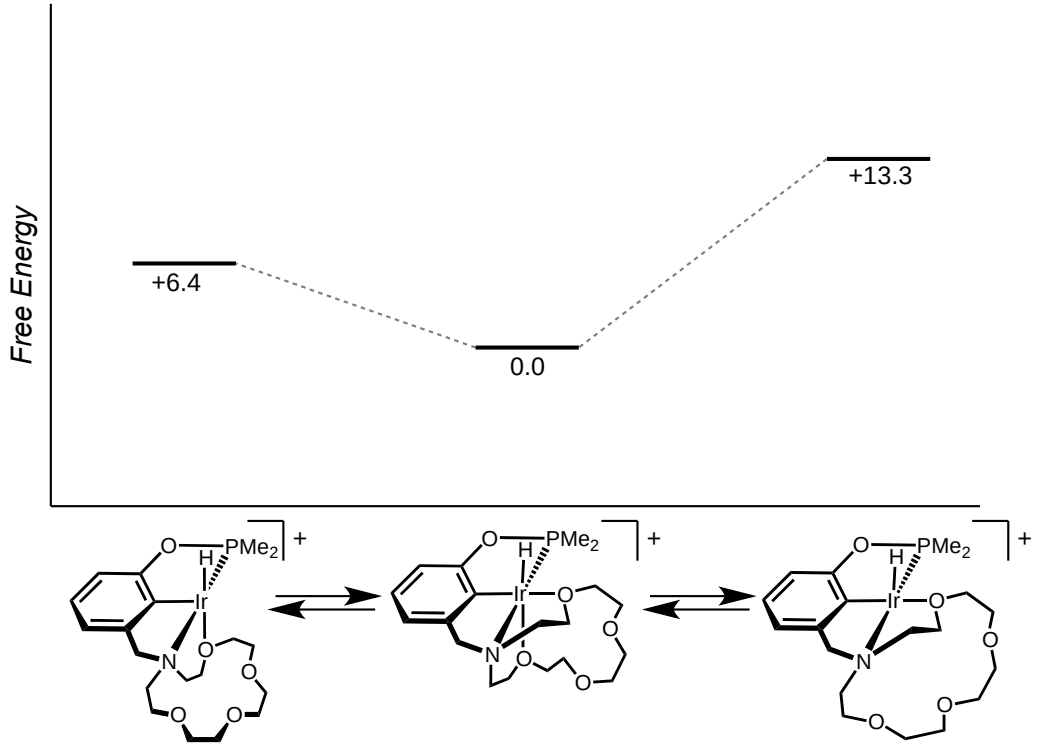

Figure 3.22: Ligand dissociation pathways of **2,** with CH_2Cl_2 solvent model.

*Thermodynamic Analysis of Acetonitrile Binding to **1***

Table 3.6: Reactions with ΔE, ΔH, ΔS, ΔG (CH_2Cl_2 solvent model).

Reaction	ΔE (kcal·mol^{-1})	ΔH (kcal·mol^{-1})	ΔS (kcal·mol^{-1})	ΔG (kcal·mol^{-1})
(κ^4-NCOP)Ir(H)(Cl) + CH_3CN → *cis*-(κ^3-NCOP)Ir(H)(Cl)($NCCH_3$) (Gas Phase)	3.08	4.15	-24.84	11.55
(κ^4-NCOP)Ir(H)(Cl) + CH_3CN → *trans*-(κ^3-NCOP)Ir(H)(Cl)($NCCH_3$) (Gas Phase)	-1.34	-0.34	-28.11	8.04
(κ^4-NCOP)Ir(H)(Cl) + CH_3CN → *cis*-(κ^3-NCOP)Ir(H)(Cl)($NCCH_3$)	0.04	1.40	-30.84	10.59
(κ^4-NCOP)Ir(H)(Cl) + CH_3CN → *trans*-(κ^3-NCOP)Ir(H)(Cl)($NCCH_3$)	-2.53	-1.37	-30.30	7.67
(κ^4-NCOP)Ir(H)(Cl)(CH_2Cl_2) + CH_3CN → *cis*-(κ^3-NCOP)Ir(H)(Cl)($NCCH_3$)(CH_2Cl_2)	-2.88	-1.70	-35.88	8.99
(κ^4-NCOP)Ir(H)(Cl)(CH_2Cl_2) + CH_3CN → *trans*-(κ^3-NCOP)Ir(H)(Cl)($NCCH_3$)(CH_2Cl_2)	-3.36	-2.35	-36.22	8.44

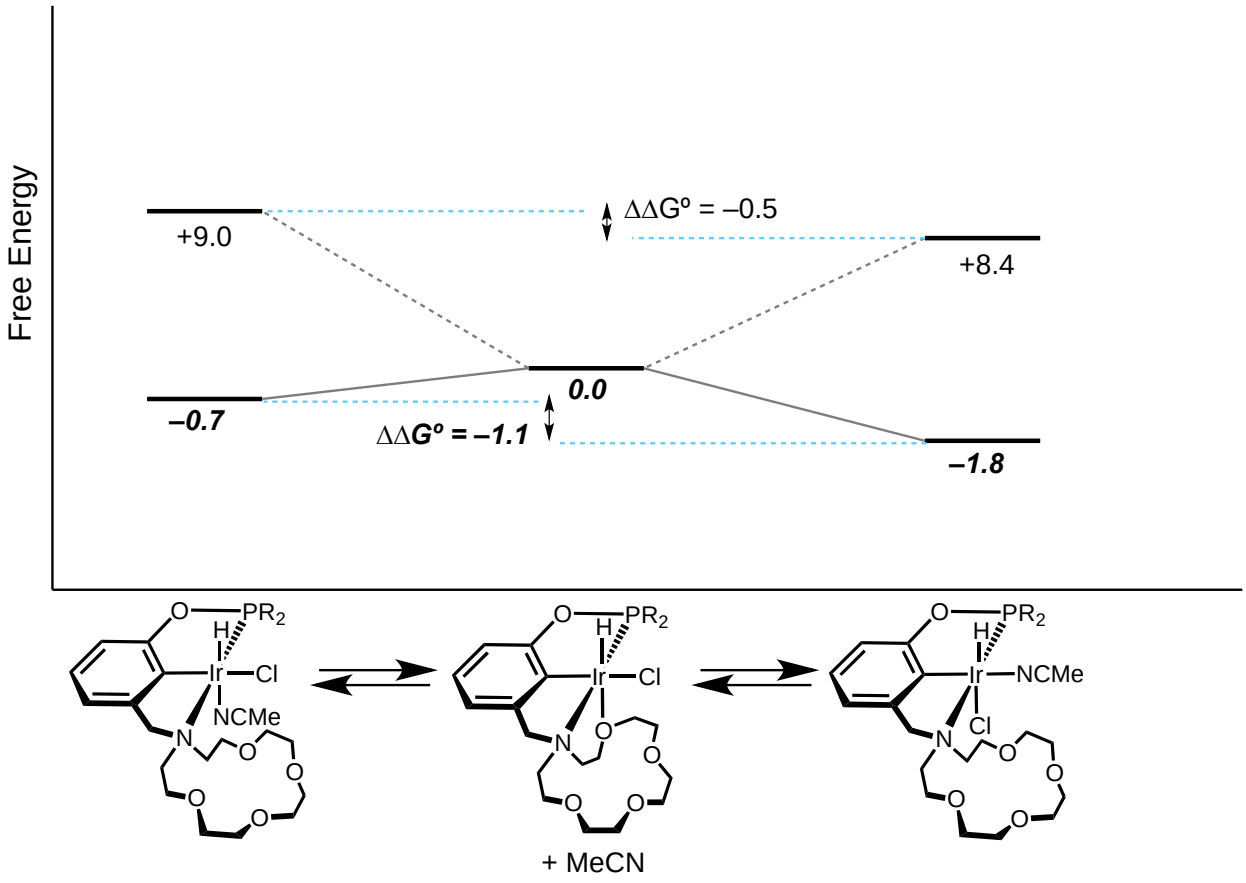

Figure 3.23: Comparing experimental and computational free energy of adduct formation in **1**. Experimental values are in plain font and DFT values are in *bold italics* (ΔG° at 298K). In addition to a PCM solvent continuum model, one explicit CH_2Cl_2 was modeled hydrogen bonding to one of the crown ether oxygen atoms. For experimental values, R = iPr; for computational values, R = Me.

*Thermodynamic Analysis of Acetonitrile Binding to **2***

Table 3.7: Reactions with ΔE, ΔH, ΔS, ΔG (CH_2Cl_2 solvent model).

Reaction	ΔE (kcal·mol^{-1})	ΔH (kcal·mol^{-1})	ΔS (kcal·mol^{-1})	ΔG (kcal·mol^{-1})
$[(\kappa^5\text{-NCOP})Ir(H)]^+ + 2CH_3CN \rightarrow$ *cis*-$[(\kappa^4\text{-NCOP})Ir(H)(NCCH_3)]^+ + CH_3CN$	-18.08	-16.66	-33.66	-6.63
$[(\kappa^5\text{-NCOP})Ir(H)]^+ + 2CH_3CN \rightarrow$ *trans*-$[(\kappa^4\text{-NCOP})Ir(H)(NCCH_3)]^+ + CH_3CN$	-5.94	-4.73	-31.53	4.67
$[(\kappa^4\text{-NCOP})Ir(H)(NCCH_3)]^+ + CH_3CN \rightarrow [(\kappa^3\text{-NCOP})Ir(H)(NCCH_3)_2]^+$	-6.76	-5.76	-25.75	1.92
$[(\kappa^5\text{-NCOP})Ir(H)]^+ + 2CH_3CN \rightarrow [(\kappa^3\text{-NCOP})Ir(H)(NCCH_3)_2]^+$	-24.84	-22.41	-59.41	-4.71

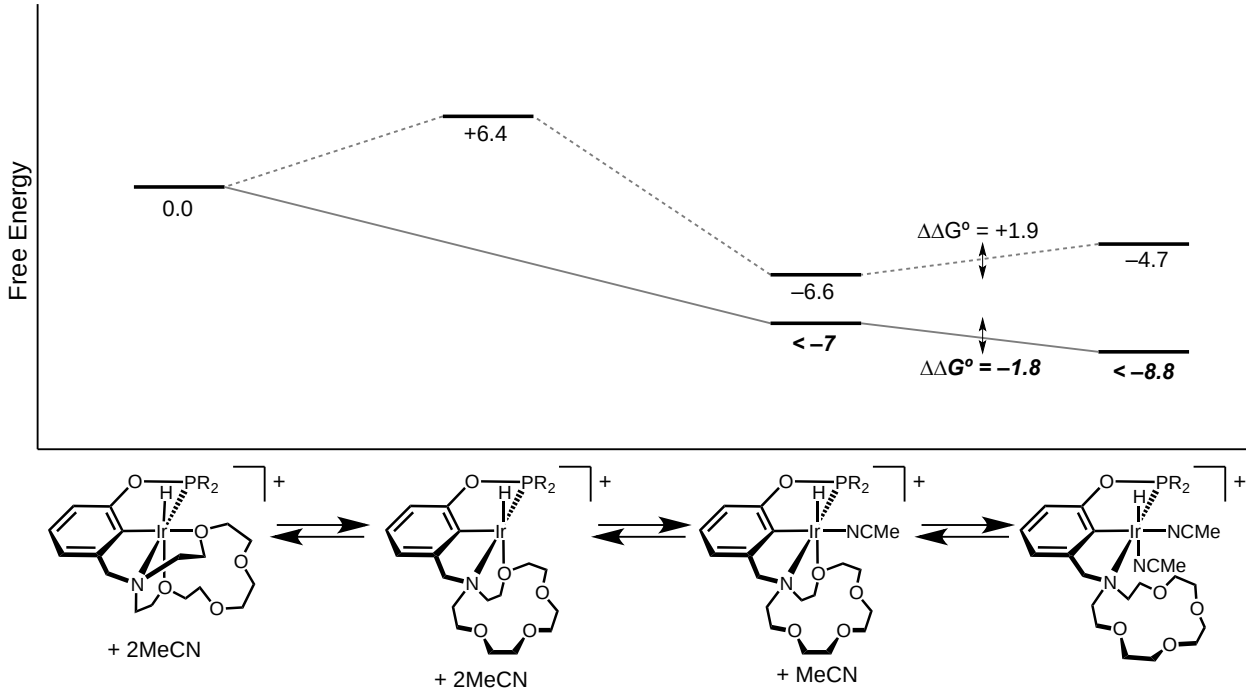

Figure 3.24: Comparing experimental and computational free energy for adduct formation in **2**. Experimental values are in plain font and DFT values are in *bold italics* (ΔG° at 298K). Note that according to Table 3.9, formation of the isomer of $[(\kappa^4\text{-NCOP})Ir(H)(NCCH_3)]^+$ (with CH_3CN *trans* to H) is 4.67 kcal·mol^{-1} uphill (~10 kcal·mol^{-1} less stable than the isomer shown above, with CH_3CN *cis* to H). For experimental values, R = iPr; for computational values, R = Me.

Chapter 4 : AN ION-RESPONSIVE PINCER-CROWN ETHER CATALYST SYSTEM FOR RAPID AND SWITCHABLE OLEFIN ISOMERIZATION

Reproduced in part with permission from Kita, M. R.; Miller, A. J. M. *Angew. Chem. Int. Ed.* **2017**, *20*, 5498-5502. Copyright Wiley-VCH Verlag GmbH & Co.

4.1 Introduction

Considering the lack of methods for controlling substrate binding in small organometallic catalysts, we have initiated a program to develop ligands with ion-tunable hemilability.[86,109–111] By using a macrocycle as a hemilabile ligand, dissociation of the chelate reveals a receptor for cation binding. With iridium hydride pincer-crown ether complexes, cations in solution can adjust the extent of acetonitrile binding and the rate of H_2 activation.[109] Only degenerate H/D exchange was observed, rather than productive catalysis, with mechanistic studies suggesting a tunable continuum between two different activity states. The complex investigated [(κ^5-^{15c5}NCOP^{iPr})Ir(H)][BAr$^F{}_4$] (**2**) contains two hemilabile Ir–O bonds. The weaker Ir–O bond cis to the Ir–H is the site substrate binding. We believe that in the hydrogen activation reactions, dissociation of the second Ir–O bond forms a reactive five coordinate intermediate with all crown ether oxygens are available for cation binding. Formation of this species likely results in dihydrogen activation, and is stabilized by cations, leading to large reactivity enhancements. These studies form the basis for ion tunable catalysis which will allow for careful control of catalytic rate depending on ion choice, and regioselectivity.

Ion-responsive olefin isomerization by a small organometallic catalyst is reported here. Starting from a completely inactive pincer-crown ether iridium chloride complex, sodium salts switch on activity by generating a cationic complex with hemilabile ether donors. Adding lithium salts to this form of the catalyst gives even more dramatic boosts in activity, with as much as 1000-fold rate enhancement and surprisingly high specificity for Li^+. Mechanistic studies suggest that ions are directly tuning metal–ligand bonding in the primary coordination sphere. This offers a complementary approach to encapsulating the active site within a large supramolecular construct. This is, to our knowledge, the first organometallic catalyst that can be readily switched *in situ* between three states of activity. Rate control is then applied to the isomerization of alkene substrates with multiple products to control regioselectivity.

4.2 Cation Effects in Olefin Isomerization

The catalytic isomerization of allylbenzene to β-methylstyrene was targeted as an ideal benchmark reaction applicable to a wide range of biomass- and petroleum-derived substrates.[112] The tetradentate hydrido chloride complex [κ^4-(^{15c5}NCOP^{iPr})Ir(H)(Cl)] (**1**)[109] was tested for isomerization activity under standard conditions, 5 mm **1** (1 mol %), and 0.5 M allylbenzene in CD_2Cl_2 (Scheme 4.1). After 140 h at 25 °C, β-methylstyrene was observed in <0.1 % yield. Hypothesizing that the chloride ligand was blocking olefin binding adjacent to the hydride ligand, we turned to the cationic hydride [κ^5-(^{15c5}NCOP^{iPr})Ir(H)]$^+$ (**2**) with $[BAr^F{}_4]^-$ as the anion, which features a pentadentate binding mode and a hemilabile ether donor (Scheme 4.1). Catalyst **2** converted allylbenzene to β-methylstyrene in >96% yield over 141 h, with an initial turnover frequency (TOF) of 1.82 h^{-1}. Greater than 99% selectivity for the *E* isomer, *trans*-β-methylstyrene, was observed. Other catalysts typically provide only up to 92% selectivity after isomerization at 60 °C or above for multiple hours.[112–115] The activity of

catalyst **2** is attributed to the hemilability of the ether ligand *cis* to the hydride ligand. The high selectivity is attributed to the mild reaction conditions, with the *E* isomer being thermodynamically favored at lower temperatures.[116]

Scheme 4.1

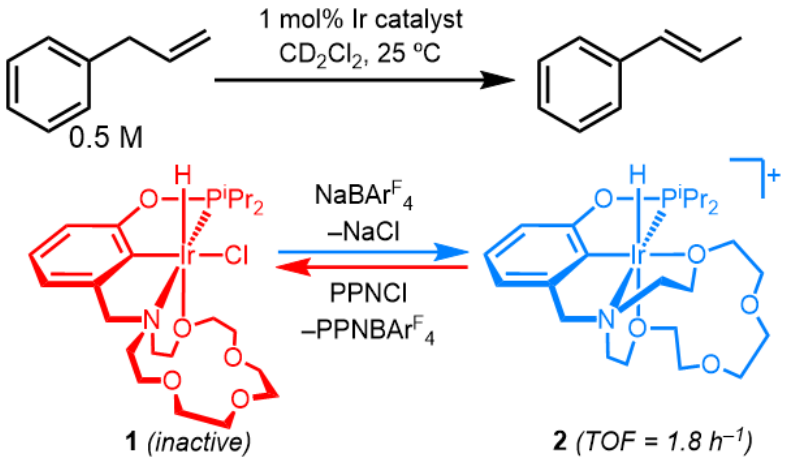

Isomerization Rate Tuning with Ions and Complex 2

We next sought to tune the activity of **2** using cation–crown interactions to adjust substrate-binding tendencies (Scheme 4.2). Carrying out allylbenzene isomerization in the presence of 1 mol % $KBAr^F_4$ and 350 mM Et_2O did not provide any rate enhancement. Including 2.2 mol % $NaBAr^F_4$ and 78 mm Et_2O on the other hand, led to a 3-fold rate enhancement (TOF=5.4 h^{-1}) relative to salt-free conditions, reaching completion after about 100 h. The three ether donors in samples of $LiBAr^F_4$•$3Et_2O$ provide full solubility in CD_2Cl_2, whereas $NaBAr^F_4$ requires > 12 equivalents Et_2O, and $KBAr^F_4$ needs > 60 equivalents Et_2O. Lithium salts foster remarkable increases in catalytic activity: Upon injection of allylbenzene into an NMR tube containing 1 mol % **2** and 0.8 mol % $LiBAr^F_4$ in CD_2Cl_2, complete isomerization occurred within

10 min. The selective response of catalyst **2** to Li^+ is striking, given that Na^+ and Li^+ have similar binding affinity with 12-crown-4.[117]

Scheme 4.2

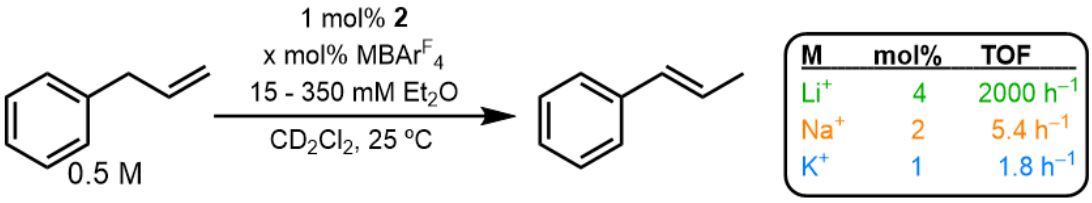

Rapid olefin isomerization is not confined to allylbenzene. The phenylpropenoid 4-methoxyallylbenzene is isomerized by the **2**/Li^+ system in less than 10 min, forming the fragrance additive anethole[118] in 98% yield and with 97.3% selectivity for the *trans* isomer. Isomerization of 0.5 M 1-hexene by 1 mol% **2** (and no added salt) reached 97% conversion after 40 h ($t_{1/2}$ = 487 min) with a distribution of isomers favoring *trans*-2-hexene (81% yield). In the presence of 1.3 mol% $LiBAr^F_4$•$3Et_2O$, it took only 2 min to reach a similar distribution ($^0t_{1/2}$ = 0.59 min), indicating an 825-fold rate enhancement. The **2**/Li^+ system is among the fastest isomerization catalysts at room temperature.[112,118–121]

Mechanistic Studies of Cation Effects

Detailed kinetic studies were carried out to provide insight into the mechanism of cation-tuned catalysis. The concentration vs. time data from each allylbenzene isomerization reaction was monitored by ^{1}H NMR spectroscopy. The reaction was analyzed to determine the appropriate kinetic model. Each data set was plotted as: (a) allylbenzene concentration vs time, (b) natural log of allylbenzene concentration vs time, and (c) the inverse of the concentration of allylbenzene vs time. The plot with the best linear fit indicates the order in allylbenzene and is used to obtain rate constants for the reaction. Turnover frequency (TOF) values were determined

by a linear fit of the concentration vs time data at less than 10% conversion. All reactions displayed zero order behavior, or first order behavior, and were treated by the procedures below.

Zero-Order Reactions. For reactions displaying zero-order behavior, the zero-order observed rate constant, ${}^{0}k_{obs}$, was determined by a linear fit of the data (slope = ${}^{0}k_{obs}$). The concentration at t=0 was estimated based on the sum of reactant and product concentrations, which was approximately constant during the reaction. The zero-order half-life, ${}^{0}t_{1/2}$, was determined from ${}^{0}t_{1/2} = 0.5\ M / (2 \times {}^{0}k_{obs})$. For convenience, units of time are given in minutes for all rate constants and half-lives.

First-Order Reactions. For data that exhibited the best linear fit for a plot of Ln[allylbenzene] vs time, a linear fit provides a slope = $-{}^{1}k_{obs}$. From the slope the first order half-life would be determined from ${}^{1}t_{1/2} = Ln(2)/{}^{1}k_{obs}$ in units of min.

With catalyst **2** (without alkali metal salts), the concentration of allylbenzene decreased exponentially (Figure 4.1), indicating that the reaction is first-order in olefin. In the absence of salts, the observed rate constant was $k_{obs} = 3.83 \times 10^{-4}\ min^{-1}$, and the half-life was $t_{1/2} = 1810$ min based on a first-order kinetic analysis (Figure 4.2). The reaction is also first-order in **2**, on the basis of k_{obs} increasing linearly with increasing catalyst concentration (Figure 4.3).

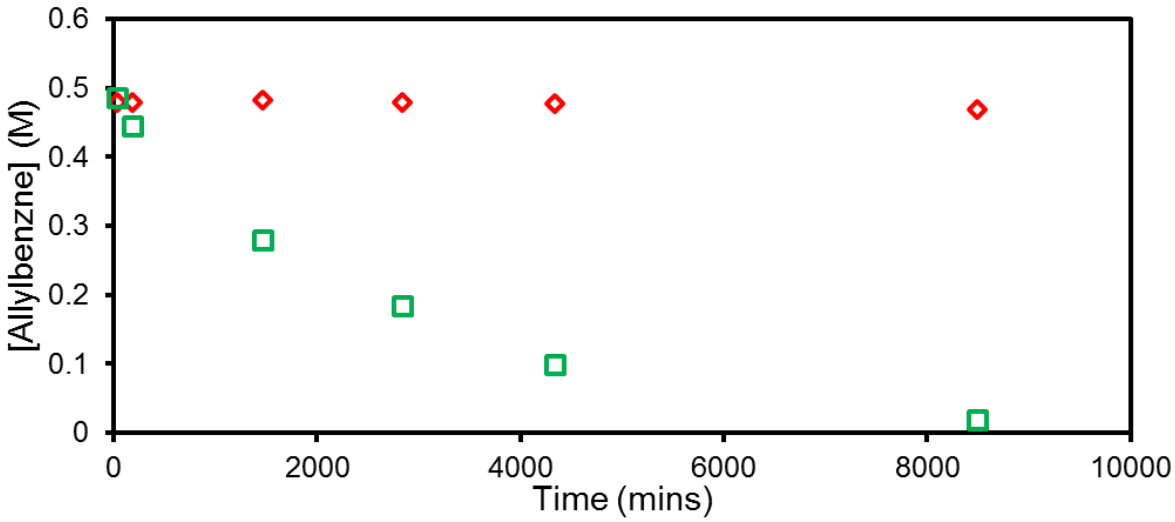

Figure 4.1: Conversion of 0.5 M allylbenzene over time by complex **1** (red diamonds) and complex **2** (green squares). Complex **2** initially isomerizes allylbenzene with TOF = 1.8 h^{-1}.

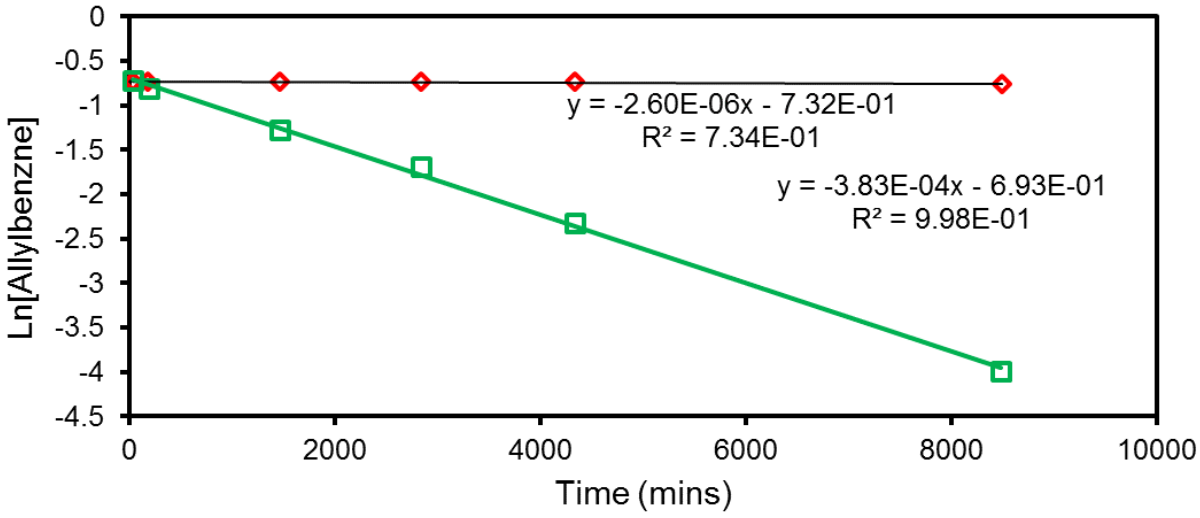

Figure 4.2: Conversion of 0.5 M allylbenzene over time by complex **1** (red diamonds) and complex **2** (green squares) plotted as Ln(allylbenzene) vs time.

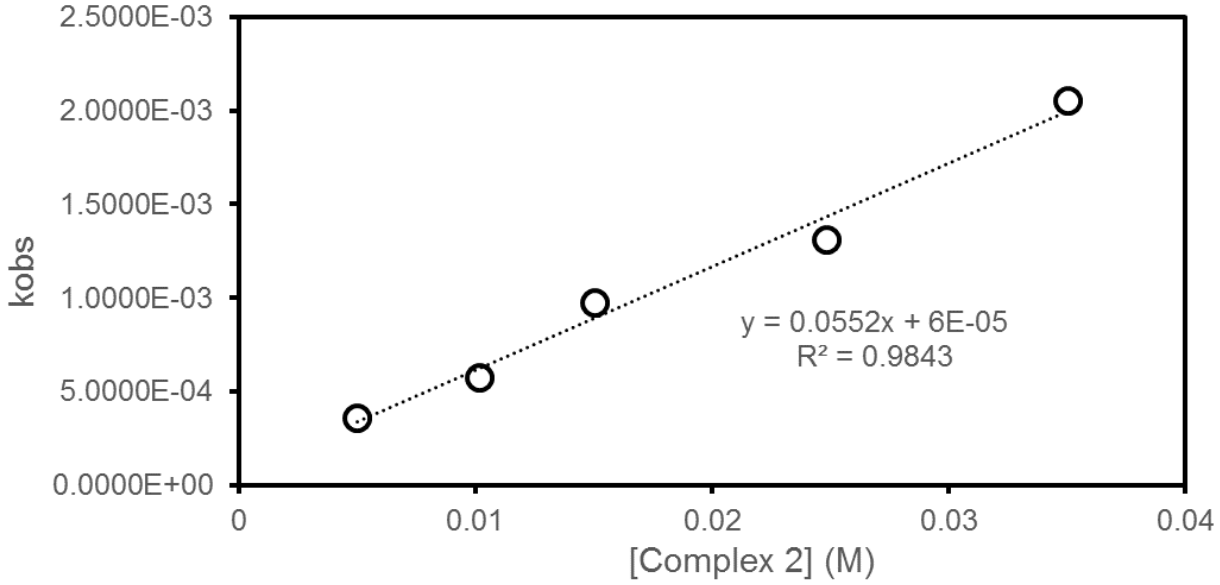

Figure 4.3: Plot of pseudo first order k_{obs} against concentration of complex **2** for the isomerization of 0.5 M allylbenzene to determine first order behavior of complex **2**.

The broad mechanistic features do not change in the presence of Na^+. The rate of isomerization increases linearly as the Na^+/**2** ratio increases from 1.1 to 7.5 (constant 0.5 M Et_2O), with each plot exhibiting exponential decay of allylbenzene (Figure 4.4). A plot of k_{obs} vs $[Na^+]$ is linear (Figure 4.5) with a non-zero intercept (3.06×10^{-4} min^{-1}) close to the experimentally observed value for cation-free isomerization in comparable conditions (Figure 4.2). An empirical rate-law for the sodium-promoted reactions is shown in equation 4.1 (where allylbenzene is written simply as *AB*). The presence of an additional Na^+-dependent term in the rate law is consistent with a cation-crown binding equilibrium. NMR spectroscopy confirms that **2** is the resting state in each case.

$$\frac{-d[A]}{dt} = k_1 K_{eq}[AB][2][Na^+] + k_2[A][2] \qquad \text{(equation 4.1)}$$

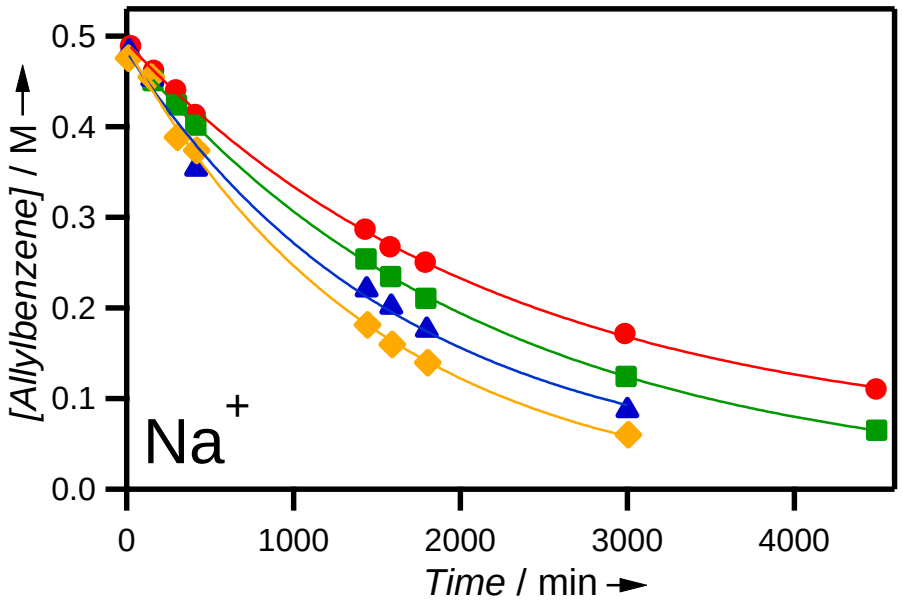

Figure 4.4: Allylbenzene isomerization by 5 mM **2** with 1.1 (red circles), 2.5 (green squares), 5.0 (blue triangles), and 7.4 (yellow diamonds) equiv $NaBAr^{F}_{4}$.

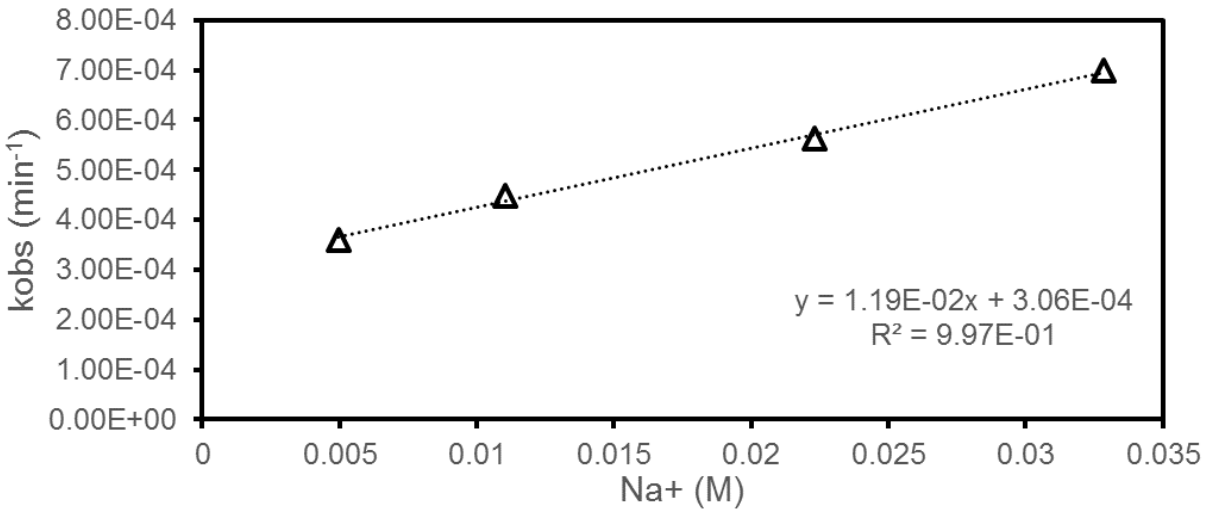

Figure 4.5: First order k_{obs} plotted against increasing $NaBAr^{F}_{4}$ concentration with linear regression for allylbenzene isomerization using 5 mM **2** and 100 equivalents allylbenzene.

The dramatic Li^+-promoted rate enhancement is accompanied by a striking change in kinetic profile. In the presence of Li^+, the concentration of allylbenzene decreases *linearly* over time (Figure 4.6), indicating a shift to a regime that is zero-order in olefin. As the Li^+/**2** ratio increases, the rate of isomerization increases dramatically before eventually leveling off (Figure 4.7). The fastest Li^+-accelerated trial (TOF = 1870 h^{-1} and zero-order half-life, ${}^{0}t_{1/2}$ = 1.6 min) features 1100-fold enhancement compared to the standard conditions (TOF = 1.8 h^{-1} and $t_{1/2}$ = 1810 min).

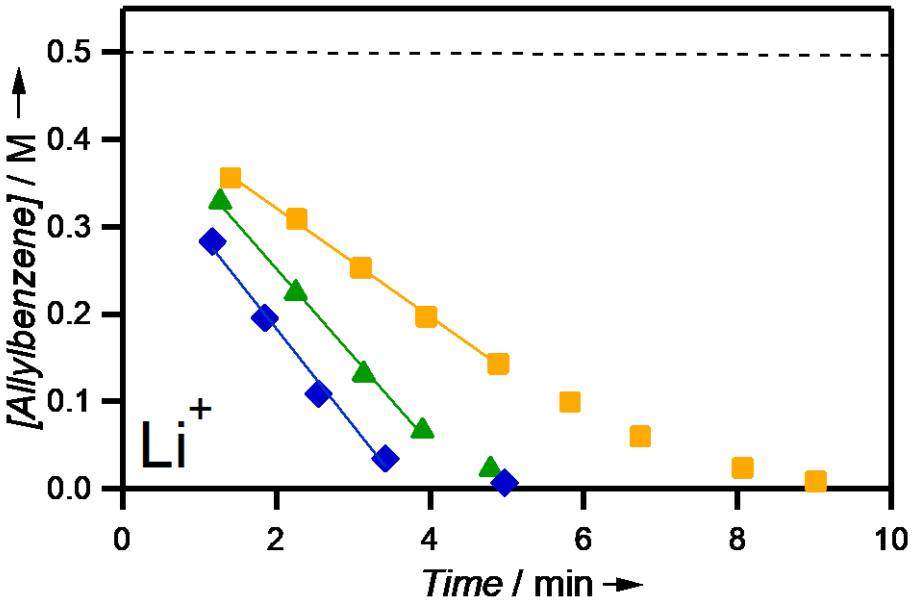

Figure 4.6: Allylbenzene isomerization by 5 mM **2** with 0.8 (orange squares), 2.0 (green triangles), 4.2 (blue diamonds) equiv $LiBAr^F{}_4$•$3Et_2O$, and without salt (dashed line).

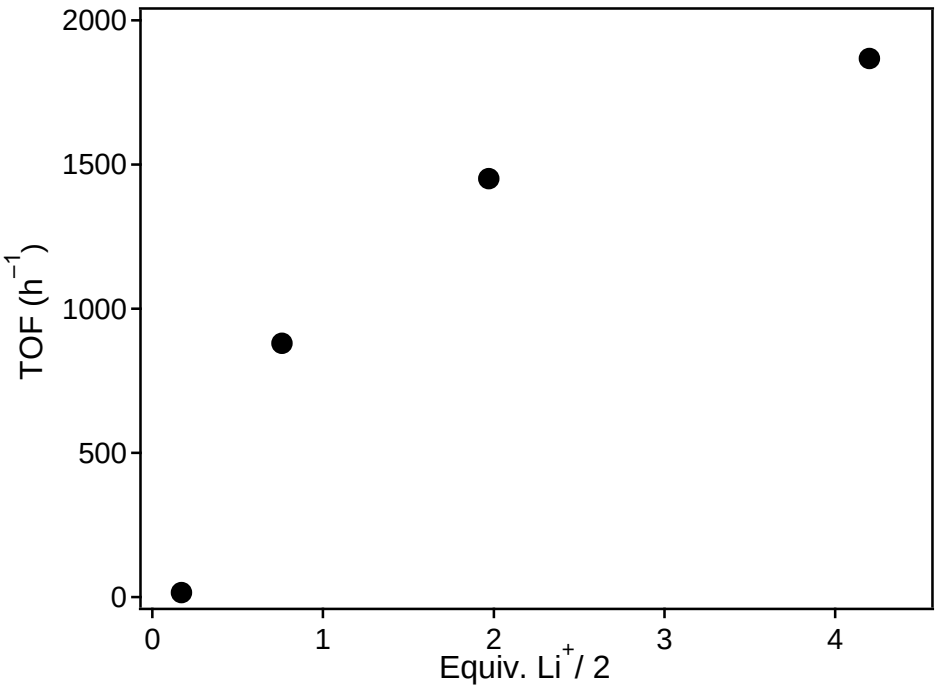

Figure 4.7: Li^+ influence on TOF

A mechanism consistent with the data is shown in scheme 4.3. In the absence of cations, the reaction is first-order in catalyst and allylbenzene, consistent with pre-equilibrium displacement of crown ether by allylbenzene ($K_{eq,1}$) influencing the observed rate. The rate accelerates as the alkali metal salt concentration increases, indicating a parallel catalytic cycle in which cation-crown interactions stabilize proposed olefin adduct **A** ($K_{eq,2}$). Li^+ salts shift $K_{eq,2}$ further towards **A**, reaching a regime that is zero-order in allylbenzene and eventually zero-order in Li^+, with turnover-limiting insertion or elimination at Ir. Accordingly, the hydride resonance of **2** diminishes and other spectral features broaden as the concentration of Li^+ increases.

Scheme 4.3

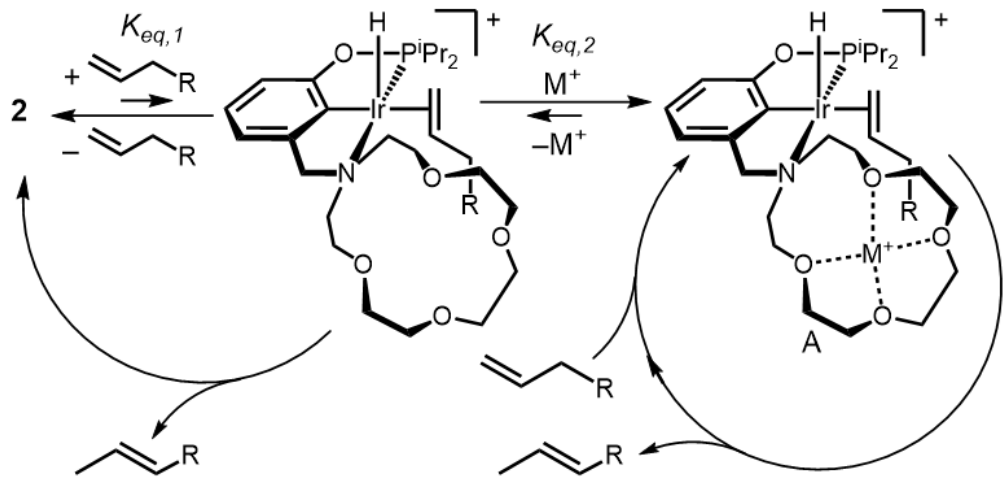

We hypothesize that **A** is the predominant resting state when the reaction becomes Li^+-independent, at which point the maximum rate is achieved. A simple kinetic model based on Scheme 4.3 provides excellent fits to the experimental data (Experimental section Figure 4.27), suggesting that Li^+ binding generates a new catalyst state that is highly active because it is *not limited by substrate binding*.

The dramatic increase in activity with lithium salts enables a reduction in the required amount of precious metal catalyst. At 0.1 mol% (0.5 mM) **2** in the presence of 10 equiv $LiBAr^F{}_4 \bullet 3Et_2O$, full conversion of allylbenzene to *β*-methylstyrene (>99% *trans*) was observed in 24 min ($^0t_{1/2}$ = 11.6 min, TOF = 2750 h^{-1}). Isomerization by **2** alone, even at 5 mol% loading, proceeded with $^1t_{1/2}$ = 530 min. The cation tuning approach thus enabled a 50-fold reduction in Ir loading while still producing *trans-β*-methylstyrene 46 times faster than 5 mol% **2**!

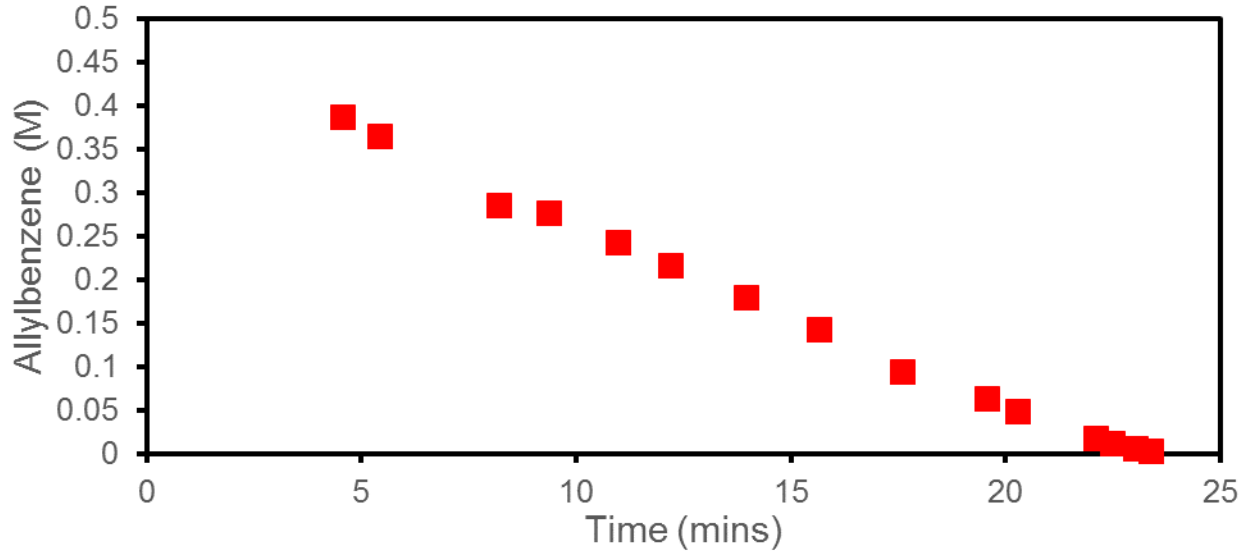

Figure 4.8: Consumption of 0.5 M allylbenzene by 0.5 mM **2** and 10 equiv $LiBAr^{F}_{4}$•$3Et_2O$ (red squares, TOF = 2750 h^{-1}, $^{0}t_{1/2}$ = 11.6 min, k_{obs} = 2.16 x 10^{-2} M min^{-1})

Fine Tuning by Diethyl Ether

We next sought to reverse the effects of cation modulation to provide full control over catalytic activity. The impact of Li^+ salts is readily dampened by donor ligands. The effect of Et_2O on Li^+-enhanced allylbenzene isomerization with **2** was quantified by monitoring **2**-catalyzed isomerization of allylbenzene with 1 mol% $LiBAr^{F}_{4}$•$3Et_2O$ and 0-23 equiv Et_2O. By varying the ratio of Et_2O/Li^+, the isomerization rate can be tuned across two orders of magnitude (Figure 4.9). In the presence of extra ether, allylbenzene decays exponentially, indicating pre-equilibrium steps involving hemilability. The Et_2O likely ligates Li^+, reducing its Lewis acidity and disrupting the cation-crown interactions ($K_{eq,2}$) that enable rate enhancement.

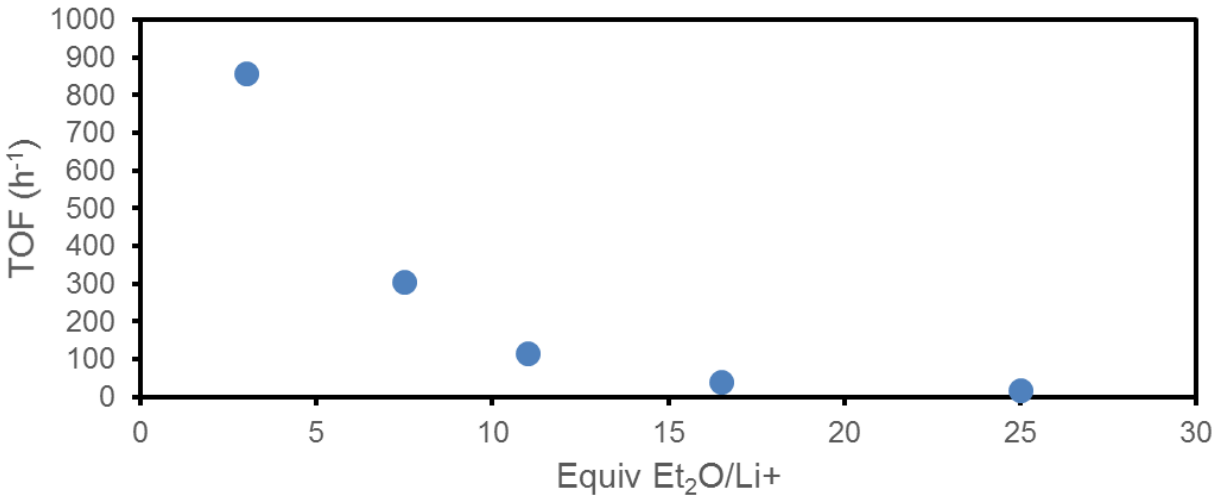

Figure 4.9: Effect of altering the equiv. Et_2O/Li^+ on allylbenzene isomerization catalyzed by 5 mM **2** and accelerated by 5 mM $LiBAr^F{}_4 \bullet 3Et_2O$.

Ether dampening helps explain why the readily available salt $LiBPh_4 \bullet 3(MeOCH_2CH_2OMe)$, with six ether donors per Li^+, does not produce dramatic enhancements. On the other end of the spectrum are soluble, donor free salts, such as $LiAl(OC(CF_3)_3)_4$.[122] Catalysis under standard conditions with 1.6 mol% $LiAl(OC(CF_3)_3)_4$ proceeded rapidly (TOF = 2010 h^{-1}) and with a zero-order half-life ($^0t_{1/2}$ = 1.62 min), achieving the same maximum rate reached with $LiBAr^F{}_4 \bullet 3Et_2O$.

4.3 Switchable Isomerization Catalysis

Chloride salts can stop catalytic activity entirely. If there are Na^+ or Li^+ ions in solution, addition of Cl^- promotes NaCl or LiCl precipitation and restores activity to the level of **2** alone. Additional Cl^- binds the Ir center, converting **2** to the catalytically inactive hydridochloride complex **1**, as shown in Scheme 4.1 above.

Recognizing that $NaBAr^F{}_4$ is capable of converting an inactive catalyst state (chloride **1**) to an active catalyst state (cation **2**), we targeted *in situ* switchable catalysis using Na^+ salts and

chloride salts as external stimuli. Figure 4.10 shows that the initial mixture of **1** and allylbenzene in CD_2Cl_2 did not isomerize over 1 hour of *in situ* NMR spectroscopic monitoring. Addition of 2 equiv $NaBAr^F{}_4$ initiated catalysis. After 1 h, addition of 2 equiv PPNCl (PPN is bis(triphenylphosphine)iminium) prompted precipitation of NaCl, and formation of **1**, halting catalysis. The catalyst was switched on and off in this fashion three times successfully. This is a rare example of switchable olefin isomerization,[123,124] with excellent rate differentiation between the on and off states attributed to direct control over substrate binding.[125,34]

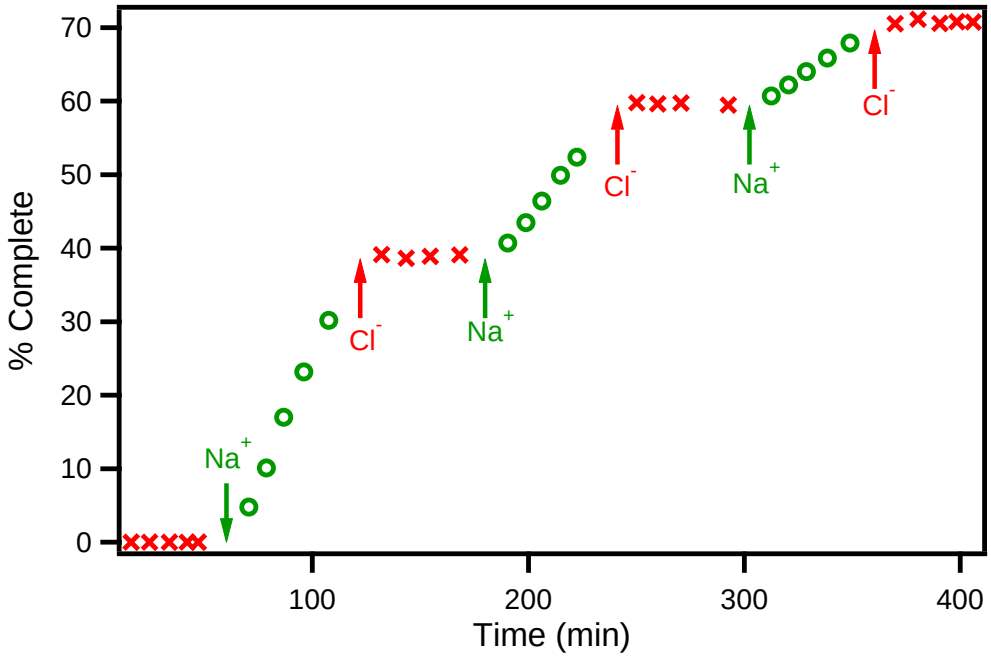

Figure 4.10: Switchable allylbenzene isomerization catalysis monitored by ^{1}H NMR spectroscopy in CD_2Cl_2 (5 mM catalyst, 0.5 M allylbenzene). Starting from chloride complex **1**, green arrows marked 'Na^+' indicate point at which 2 equiv $NaBAr^F{}_4$ was added, and red arrows marked 'Cl^-' indicate point at which 2 equiv PPNCl was added.

Although $NaBAr^F{}_4$ successfully switched on the two-state system of Scheme 4.1, the isomerization rate of the "switched on" catalyst was surprisingly fast (k_{obs} = 8.46 x 10^{-3} min^{-1}, $t_{1/2}$ = 82 min^{-1}) compared to isolated samples of **2** containing excess Na^+ ($t_{1/2}$ = 992 min). Evidence for an unexpected intermediate along the path of halide abstraction was obtained in the absence

of olefin. Upon injection of ~2 equiv $NaBAr^F_4$ to a solution of **1** (Scheme 4.4), the color changed from yellow to burnt orange and ^{1}H NMR spectroscopy revealed one hydride resonance for **2** (δ –29.8), and a second, previously unobserved resonance for **B** (δ –32.5). Only **2** was present after 50 min (Figure 4.11). Similar behavior is apparent during catalysis (Figure 4.11 inset), with the reaction progressing rapidly at early times when substantial amounts of intermediate **B** are present. After 50 min, complete dehalogenation leaves only **2** in solution and catalysis slows considerably. We propose that an intermediate with Na^+ bridging the crown ether and the Ir–Cl, [κ^3-(^{15c5}NCOP^{iPr})Ir(H)(NaCl)]$^+$ (**B**), facilitates chloride substitution.

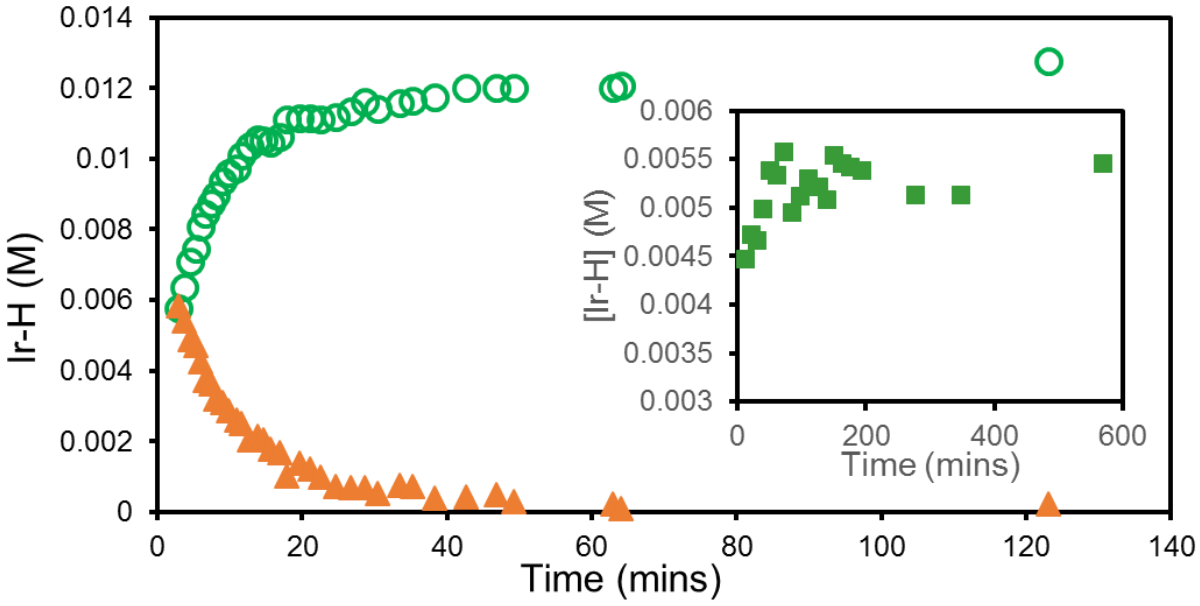

Figure 4.11: *In situ* ^{1}H NMR monitoring for the dehalogenation of **1** with 1.7 equiv Na^+ to form a previously unobserved hydride species (orange triangles), as it converts to complex **2** (green circles). Inset: concentration of complex **2** over time during dehalogenation initiated isomerization reaction.

Scheme 4.4

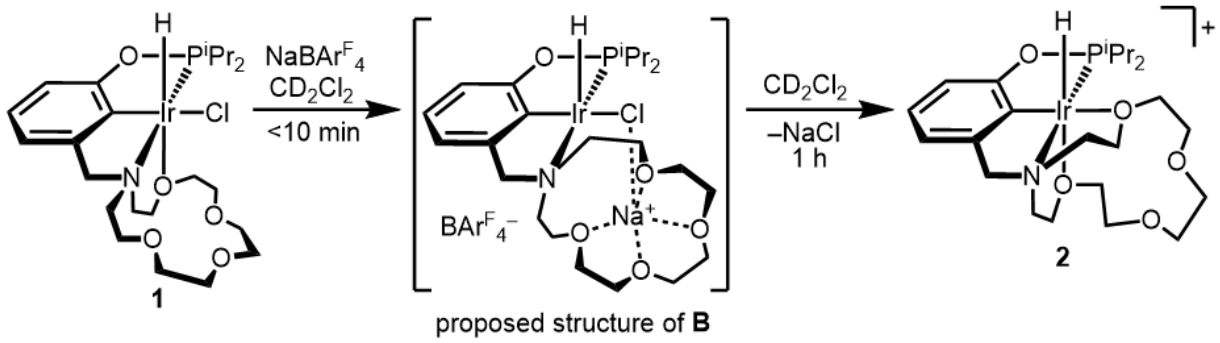

Multi Stage Catalysis

Each of the four activity regimes can be toggled *in situ*, illustrating comprehensive control over activity using simple ions as switches and tuning agents (Figure 4.12). Allylbenzene isomerization is initiated by addition of complex **2**, a slow "on" state. After 355 min (11% yield *β*-methylstyrene), $LiBAr^F_4 \bullet 3Et_2O$ was added and the mixture was allowed to react for 1 min before 2.5 equiv PPNCl was added to precipitate LiCl and bind Ir; in just 1 min of cation-enhanced catalysis, the yield increased to 70%. Chloride complex **1** is the "off" state, and the reaction progress was halted entirely for 73 min when Ir was present in the form of **1**. Addition of excess $NaBAr^F_4$ restarts isomerization at the intermediate rate of metastable species **B**.

This small organometallic example is complementary to supramolecular approaches that have made great strides in two-state switchable catalysts.[56,126,127] Recently, a unique three-state supramolecular system, capable of generating racemic mixtures or the desired enantiomer by switchable encapsulation of chiral organocatalysts, was reported.[128] Catalyst systems with three or more well-defined states with different activity levels are extremely rare, and facile *in situ* modulation of such a catalyst system may be unprecedented.

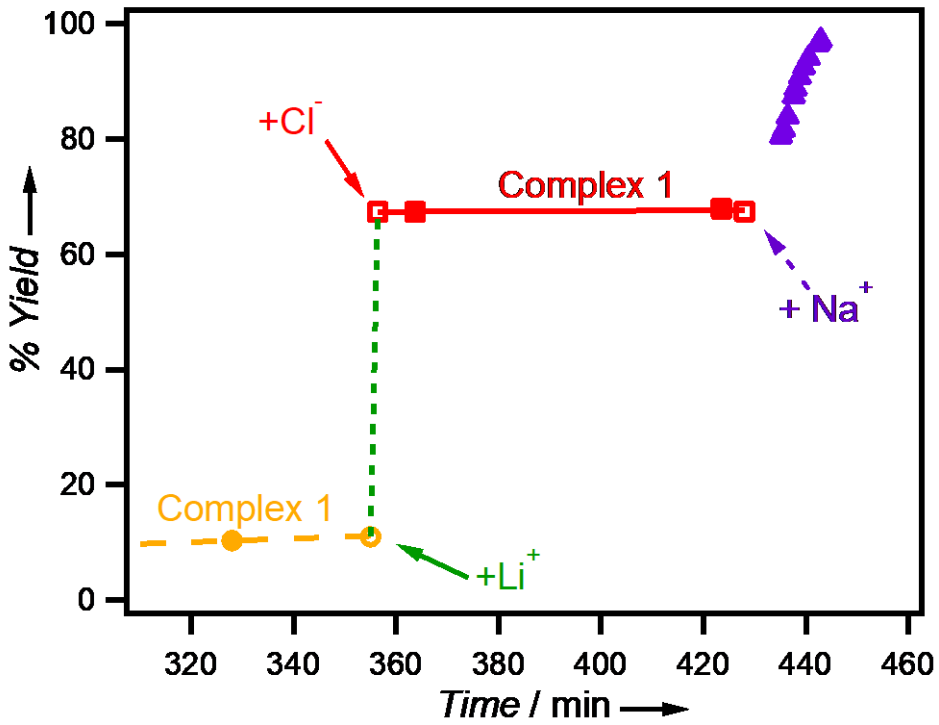

Figure 4.12: Switchable allylbenzene isomerization catalysis monitored by ^{1}H NMR spectroscopy in CD_2Cl_2 (5 mM catalyst, 0.5 M allylbenzene). Multi-state *in situ* switching starting from cationic complex 2; green arrow indicates addition of 1.0 equiv $LiBAr^F_4$, red arrow indicates addition of 2.5 equiv PPNCl, purple arrow indicates addition of 6.3 equiv $NaBAr^F_4$.

4.4 Regioselectivity in Catalysis

With an in depth understanding for how to use ions to control the rate of catalytic alkene isomerization using **2**, we wanted to investigate how cations affect regioselectivity in the isomerization of alkenes with multiple possible isomerization products. Controlled rearrangement of double bonds along long-chain alkenes remains a major challenge in isomerization catalysis. The Grotjahn lab has done considerable work studying how to perform multiple isomerizations on a substrate,[119] or selectively stop after one isomerization.[129,130] They were able to design catalysts that could distinguish the substrate approach pathway based on sterics, and thus achieve high positional control. A catalyst with the proper steric environment

about the metal center could selectively bind the terminal alkene over the disubstituted. This selectivity based on sterics ensures that only monoisomerization occurs.

We imagined that the regioselectivity in long chain alkene isomerization by catalyst **2** might be tuned by added cations. Two scenarios were imagined:

- Steric Control: The Ir–O bond in catalyst **2** is difficult to displace and can only bind terminal alkenes for isomerization when no cations are present. Li^+ addition helps relieve this steric congestion so that disubstituted alkenes can bind, and isomerize futher.
- Rate Control: Catalyst **2** is a slow isomerization catalyst, so a single isomerization takes considerable time. Addition of Li^+ accelerates the rate so that multiple isomerizations can be done in the same time period as one isomerization with no cations.

We first imagined the above possibilities after performing the isomerization of 1-hexene with and without cations. In the isomerization of 0.5 M 1-hexene by 1 mol% **2**, 94% conversion of starting material to 2-hexene isomers was achieved after 2400 min ($t_{1/2}$ = 487 min). The major product was *trans*-2-hexene (78% yield), with 16% yield of *cis*-2-hexene, and 3% yield of 3-hexene isomers. When the same reaction was carried out in the presence of 1.3 mol% $LiBAr^F{}_4 \bullet 3Et_2O$, it took only 2 min to reach a similar distribution favoring 2-hexene isomers ($^0t_{1/2}$ = 0.59 min). Allowing the Li^+-containing mixture to react further, however, led to ~17% yield of 3-hexenes after 190 min.

To better understand the influence of cations on regioselectivity, we studied the isomerization of 4-phenyl-1-butene. Single isomerization produces 1-phenyl-2-butene, a disubstituted alkene. Double isomerization produces 1-phenyl-1-butene, an disubstituted alkene that is thermodynamically favored due to a conjugated phenyl group.

Using the standard reaction conditions depicted in scheme 4.5, 0.5 M 4-phenyl-1-butene was treated with 1 mol% **2** in CD_2Cl_2. After 143 hours (8580 min), 94% conversion to 1-phenyl-2-butene was observed, with the 94% selectivity for the *E* isomer resulting from migration of the double-bond by one position. The kinetics followed pseudo-first-order behavior, with exponential decay of 4-phenyl-1-butene as shown in Figure 4.13 (k_{obs} = 3.74 x 10^{-4} min^{-1}, $t_{1/2}$ = 1860 min).

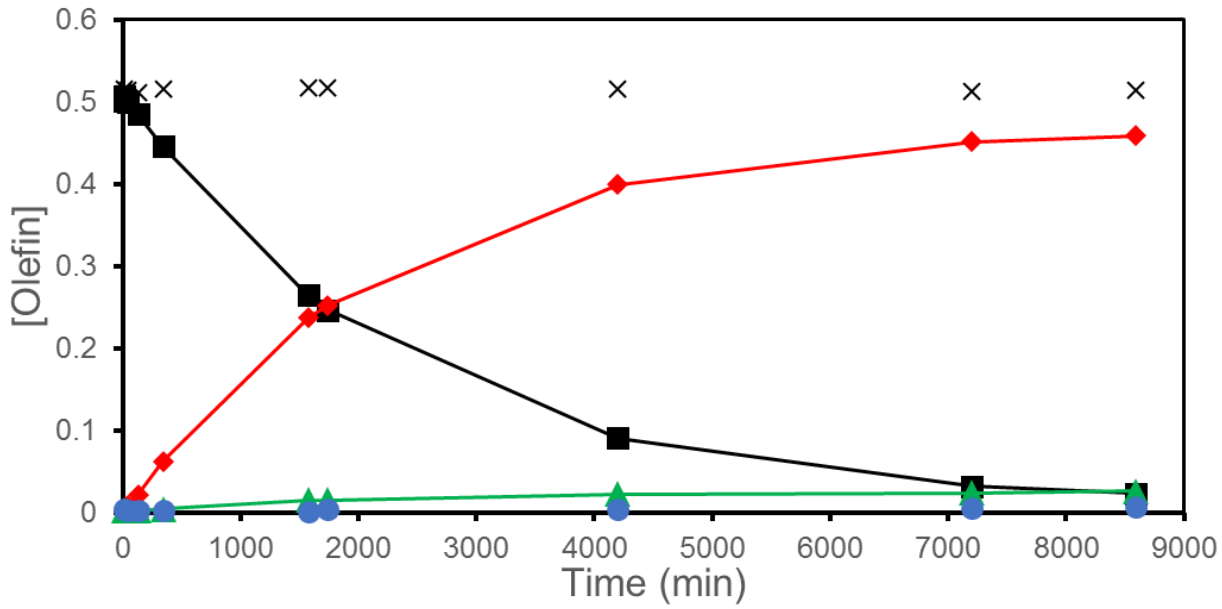

Figure 4.13: Isomerization of 0.5 M 4-phenyl-1-butene (black squares) by 1 mol% 2 to form (E)-1-phenyl-2-butene (red diamonds), (Z)-1-phenyl-2-butene (green triangles), and nominal amounts of 1-phenyl-1-butene (blue circles).

Scheme 4.5

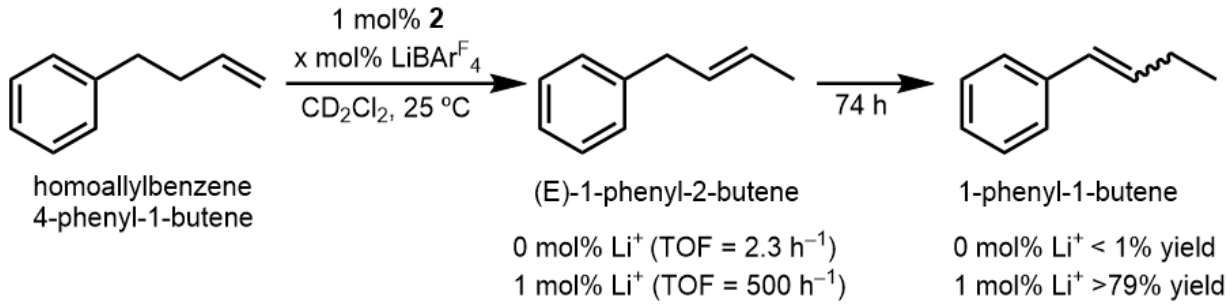

Consistent with previous substrates using the **2**/Li^+ system, rapid isomerization of 0.5 M 4-phenyl-1-butene was achieved at a rate 230x faster than **2** alone by including 1 mol% $LiBAr^F{}_4$. After 27 minutes, 80% conversion to 1-phenyl-2-butene was observed with 77% selectivity for the *E* isomer (Figure 4.14). After 112 minutes, the ~0.4 M 1-phenyl-2-butene in solution began isomerization to 1-phenyl-1-butene (Figure 4.15). After 74 hours, 79% yield of 1-phenyl-1-butene was observed. Comparing these results with Li^+ free catalysis, <1% conversion to 1-phenyl-1-butene, and 83% conversion to 1-phenyl-2-butene isomers had been observed by 74 hours.

The isomerization results from 4-phenyl-1-butene are much easier to interpret than the data for 1-hexene. The data shows that isomerization of terminal olefin 4-phenyl-1-butene with **2**/Li^+ is about 240x faster than disubstituted olefin 1-phenyl-2-butene, possibly due to steric control discussed above. If the reaction was not limited by sterics, one might expect that the first isomerization rate would be roughly equal to the second isomerization event. One would also expect that after the first isomerization to form 1-phenyl-2-butene, the olefin might remain bound to the metal center and isomerize to the thermodynamically favored 1-phenyl-1butene. Instead, we observed a large spike of 1-phenyl-2-butene (~80% yield) within 120 minutes for the Li^+ containing reaction, and <4% yield for the 1-phenyl-1-butene. These results suggest that binding of bulkier olefins is more difficult, and results in slower rates. Additional studies need to be performed to give further evidence for regioselectivity based on steric control of binding.

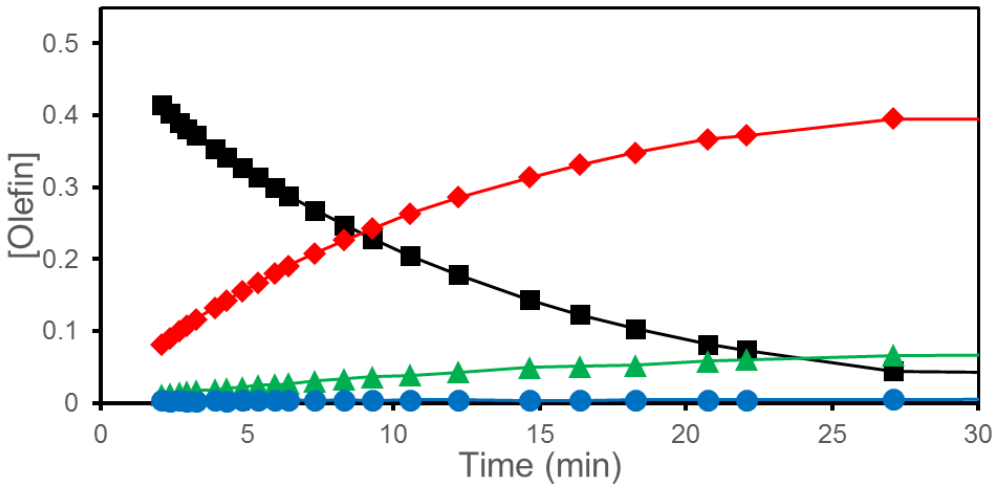

Figure 4.14: Isomerization of 0.5 M 4-phenyl-1-butene (black squares) by 1 mol% **2** to form E-2-phenyl-1-butene (red diamonds), Z-2-phenyl-1-butene (green triangles), and 1-phenyl-1-butene (blue circles). Data shown for the first 30 minutes of reactivity.

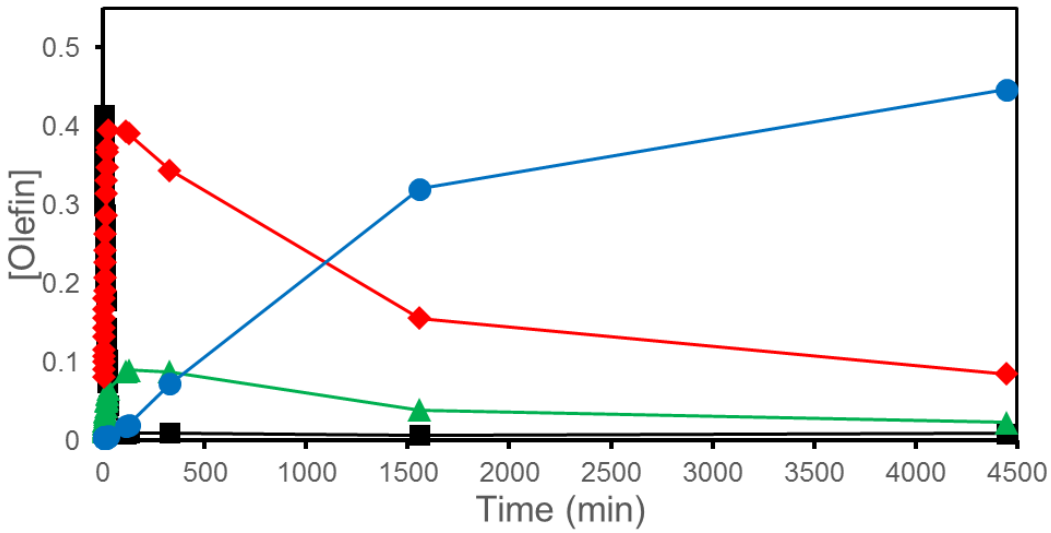

Figure 4.15: Isomerization over long times of 0.5 M 4-phenyl-1-butene (black squares) by 1 mol% **2** to form E-2-phenyl-1-butene (red diamonds), Z-2-phenyl-1-butene (green triangles), and 1-phenyl-1-butene (blue circles)

4.5 Conclusions

The ability to precisely control substrate binding by tuning ligand hemilability has sparked the development of a catalyst whose activity can be tuned between no activity and high activity. Simple alkali metal cations and chloride anions act as *in situ* switches to tune activity in

the isomerization of olefins, with a massive span in turnover frequency ranging from inactive to more than 2000 h^{-1}. This range of activity can also be used to dictate the regioselectivity of isomerization presumably based on steric control over olefin binding.

The approach introduced here could be applicable to many catalytic reactions that are limited by substrate binding or involve ligand hemilability. The results of chapters 3 and 4 lead to several general principles of cation-tunable reactivity with iridium pincer-crown ether complexes.

1. The reversible binding of a hemilabile chelate must be possible. The pentadentate pincer-crown ether ligand in complex **2** dissociates at least one Ir–O bond before binding H_2, $NCCH_3$, or an olefin substrate.
2. A slow or "off" state is achieved when the substrate does not displace the hemilable ligand from the metal center in the absence of salts. In the H_2 exchange studies, and olefin isomerization studies, no substrate binding was observed by NMR. The slow rates of bond activation and catalysis imply that ligand binding was accessible to a small degree, with the pincer-crown ether ligand effectively acting as a gate to substrate binding.
3. Cations should interact strongly with the complex featuring bound to the metal, but weakly with the substrate-free complex. In the $NCCH_3$ binding studies of **2**, excess $NCCH_3$ rapidly displaced the Ir–O bond *cis* to the hydride forming **5** [κ^4-$^{15c5}NCOP^{iPr}Ir(H)(NCCH_3)]^+$, but only produced equilibrium mixtures of **6** [κ^3-$^{15c5}NCOP^{iPr}Ir(H)(NCCH_3)_2]^+$. Cations did not bind the ligand when Ir–O bonds were present (eg κ^4 and κ^5), but rapidly bound the hemilabile macrocycle when all oxygen atoms had dissociated.

4. Cation-specific rates are achieved when the catalyst has different binding equilibria for various cations. Studies by Jacob Smith show that square planar nickel complexes of κ^3-(^{15c5}NCOP^{iPr})NiX (X = Br, Cl) show high affinity for Li^+, moderate affinity for Na^+, and virtually no affinity for K^+. These studies follow the same trend as the cation accelerated isomerization rates. These varying affinities allow for careful tuning based on cation-crown ether equilibria.

Looking forward, the iridium complexes containing ^{18c6}NCOP^{iPr} should be expected to show similar reactivity to their ^{15c5}NCOP^{iPr} siblings, with different cation affinity. Preliminary studies suggest that complexes containing ^{18c6}NCOP^{iPr} will have very high affinities for Na^+. More broadly, we expect that pincer-crown ether complexes containing M–O bonds will display cation tunable reactivity as long as the M–O bond acts as a gate for substrate binding. The above principles can now serve as a basis for synthesizing new transition metal pincer-crown ether complexes and understanding their reactivity.

4.6 Experimental Details

General Considerations

All compounds were manipulated using standard vacuum line or Schlenk techniques or in a glovebox under a nitrogen atmosphere. NMR-scale reactions were prepared under nitrogen in a glovebox and kept in Teflon-sealed or septum sealed tubes. Under standard glovebox operating conditions, pentane, diethyl ether, benzene, toluene, and tetrahydrofuran were used without purging, such that traces of those solvents were present in the atmosphere and in the solvent bottles. ^{1}H, ^{31}P, and ^{13}C NMR spectra were recorded on 400, 500, or 600 MHz spectrometers at 298 K. All NMR solvents and isotopically labeled reagents were purchased from Cambridge Isotope Laboratories, Inc. Methylene chloride-d_2 (CD_2Cl_2) was freeze−pump−thaw degassed

three times before drying by passage through a small column of activated alumina. Chemical shifts for ^{1}H and ^{13}C NMR spectra are reported in ppm relative to residual protio solvent impurity, ^{31}P resonances are reported relative to 85% H_3PO_4 external standard (0 ppm), and ^{19}F resonances are reported relative to $CFCl_3$. $NaBAr^{F}_{4}$,[92] $LiBAr^{F}_{4}$•$3Et_2O$,[109] $LiAl(OC(CF_3)_3)_4$,[131] and benzyl potassium,[132] were synthesized according to literature procedures. Allylbenzene, 4-allylanisole, and 1-hexene were freeze−pump−thaw degassed three times before drying by passage through a small column of activated alumina. All other reagents were commercially available and were used without further purification.

General Procedure for Catalytic Olefin Isomerization

In the nitrogen atmosphere of a glovebox, a solution of **2** (typically 5 mM) in CD_2Cl_2 containing HMDSO (hexamethyldisiloxane) as an internal standard was prepared. Small amounts of diethyl ether were added by syringe as needed to ensure full solubility of the salts. The solution was transferred to an NMR tube (sealed with a septum, threaded screw-cap, or Teflon stopper). Allylbenzene (typically 0.5 M) was then added via syringe to initiate the reaction. Reaction progress was monitored via NMR spectroscopy. The concertation of allylbenzene was determined based on integration of the olefinic protons relative to HMDSO and the concentration of methyl styrene was determined based on integration the methyl protons relative to HMDSO.

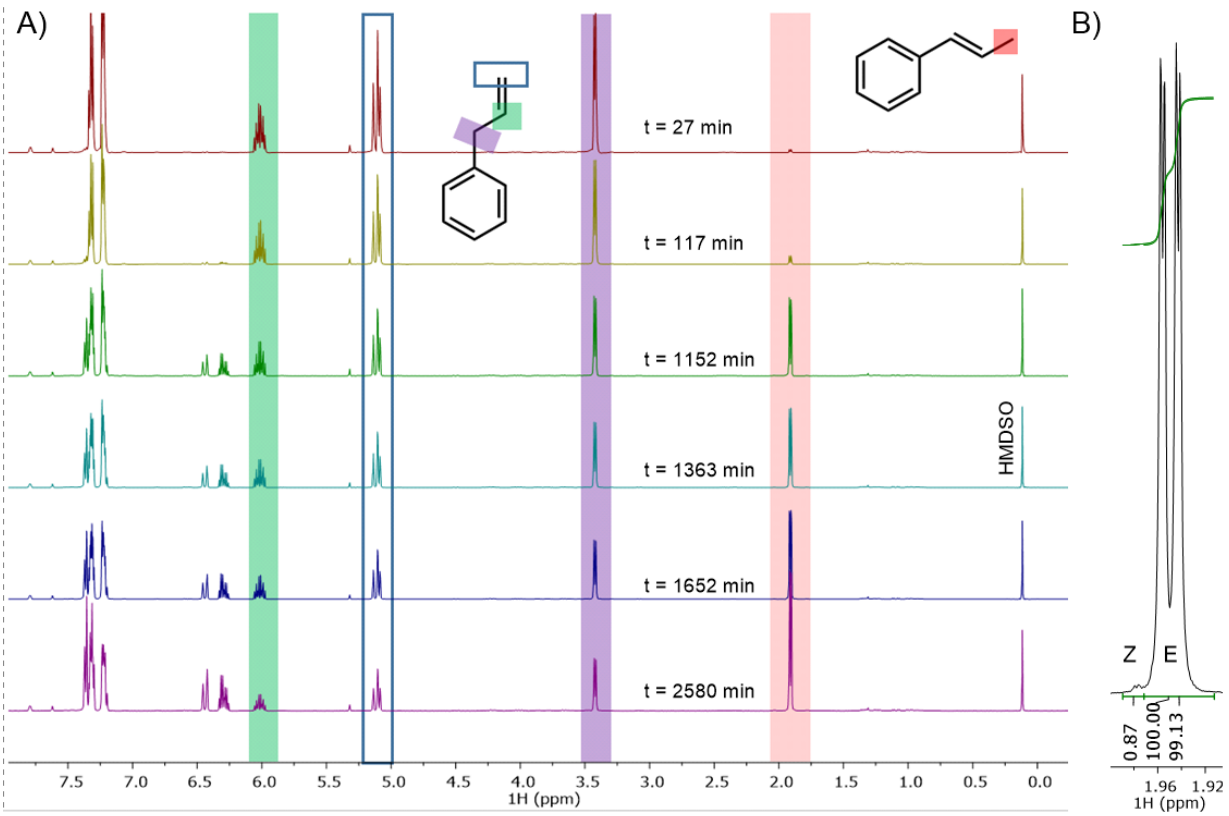

Figure 4.16: A) Example NMR stack showing relevant peaks used to determine the concentration of allylbenzene and methylstyrene during catalysis relative to HMDSO. B) Inset showing the relative concentrations of the E and Z isomers of β-methylstyrene.

Iridium Concentration Dependence on Allylbenzene Isomerization

A scintillation vial was charged with 0.0723 g (0.0483 mmol) **2**, and dissolved in 1380 μL CD_2Cl_2 along with 10 μL HMDSO to make a 35.0 mM solution of **2**. Aliquots (145-500 μL) were transferred to Teflon-stoppered NMR tubes containing the appropriate amount of CD_2Cl_2 to prepare 500 μL solutions ranging in concentration from 10 mM **2** to 35 mM **2**. For example, the trial containing 15 mM **2** was prepared by mixing 215 μL of the stock solution with 285 μL CD_2Cl_2. Allylbenzene (33 μL, 0.249 mmol) was injected to each (0.5 M allylbenzene), and the reaction progress was monitored by NMR spectroscopy.

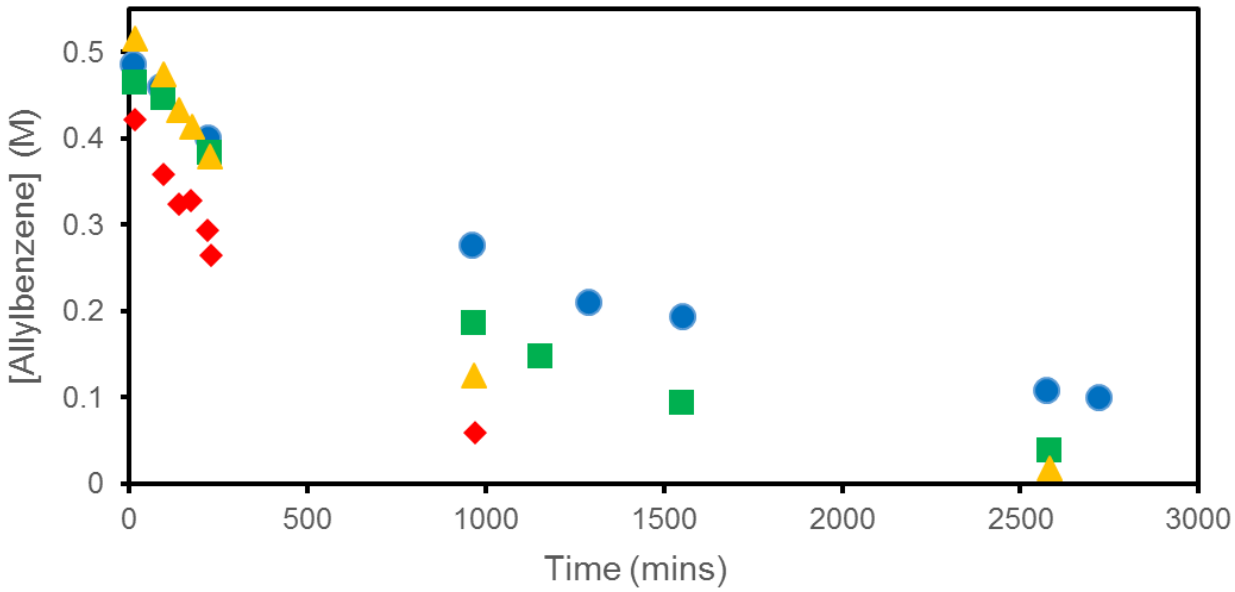

Figure 4.17: Conversion of 0.5 M allylbenzene to methyl styrene by **2** at concentrations ranging from 10 mM (blue circles, TOF = 2.4 h^{-1}), 15 mM (green squares, TOF = 2.4 h^{-1}), 25 mM (yellow triangles, TOF = 3.3 h^{-1}), 35 mM (red diamonds, TOF = 2.8 h^{-1}).

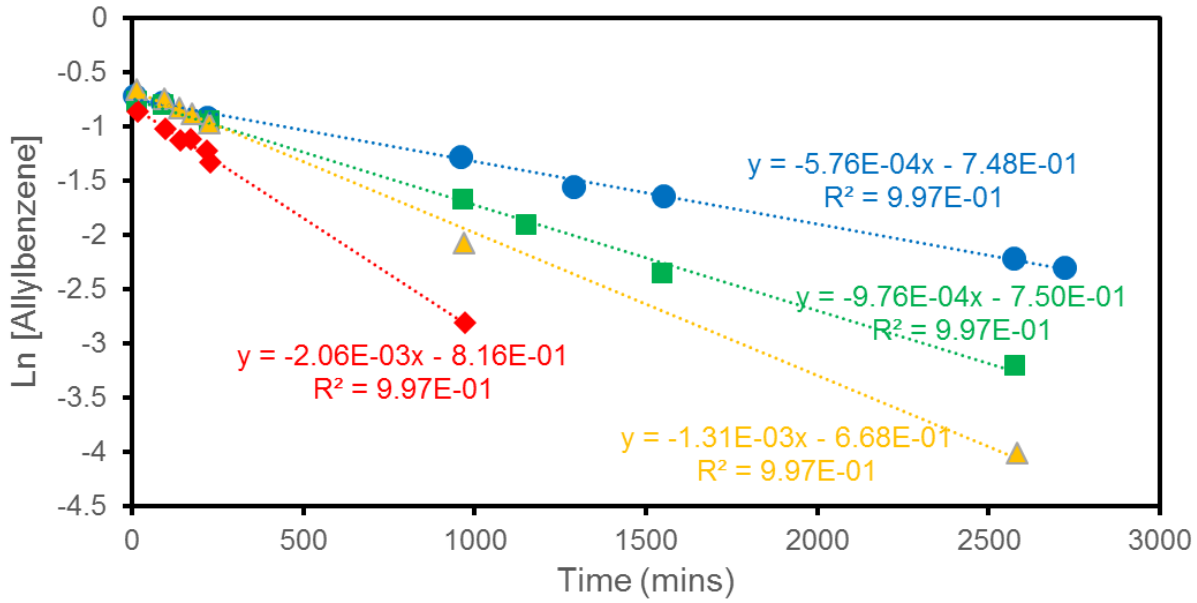

Figure 4.18: Conversion of 0.5 M allylbenzene to methyl styrene by **2** at concentrations ranging from 10 mM (blue circles, $t_{1/2}$ = 1200 min), 15 mM (green squares, $t_{1/2}$ = 710 min), 25 mM (yellow triangles, $t_{1/2}$ = 528 min), 35 mM (red diamonds, $t_{1/2}$ = 359 min).

Effect of Et_2O on Isomerization.

A scintillation vial was charged with 0.0092 g (0.00615 mmol) **2**, 10 μL HMDSO, 82 μL (0.619 mmol) allylbenzene, and 1230 μL CD_2Cl_2 to make a 5.00 mM solution of **2**. Two 500 μL aliquots were transferred to Teflon sealed NMR tubes, and 16 μL Et_2O was added to one of the tubes. The reaction progress was monitored by ^1H NMR spectroscopy.

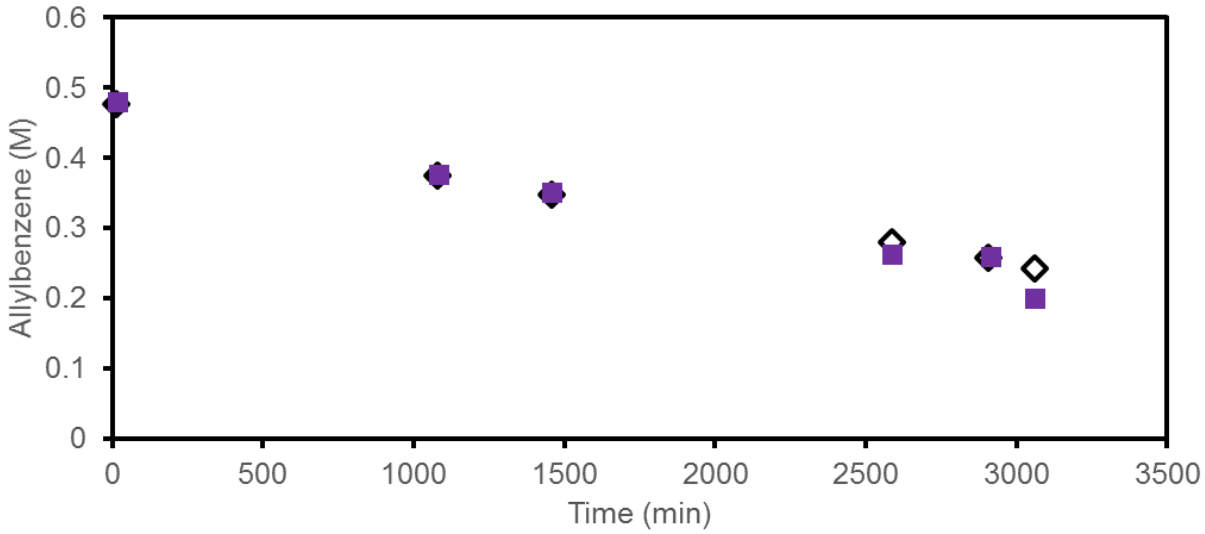

Figure 4.19: Consumption of 0.5 M allylbenzene by 5 mM **2** with no added Et_2O (hollow black diamonds), and 300 mM Et_2O (filled purple squares).

Effect of $KBAr^F_4$ on Allylbenzene Isomerization

A scintillation vial was charged with 0.0172 g (0.0115 mmol) **2**, 2.30 mL CD_2Cl_2, 5 μL HMDSO, and 153 μL (1.1155 mmol) allylbenzene. The solution was transferred in 500 μL aliquots to Teflon sealed NMR tubes containing, no additive, 0.0022 g (0.0244 mmol) $KBAr^F_4$ with 8 μL (0.0770 mmol) Et_2O, 0.0022 g (0.0244 mmol) $KBAr^F_4$ with 18 μL (0.173 mmol) Et_2O, and 0.0031 g (0.00343 mmol) $KBAr^F_4$. The reaction progress was then monitored by ^1H NMR spectroscopy.

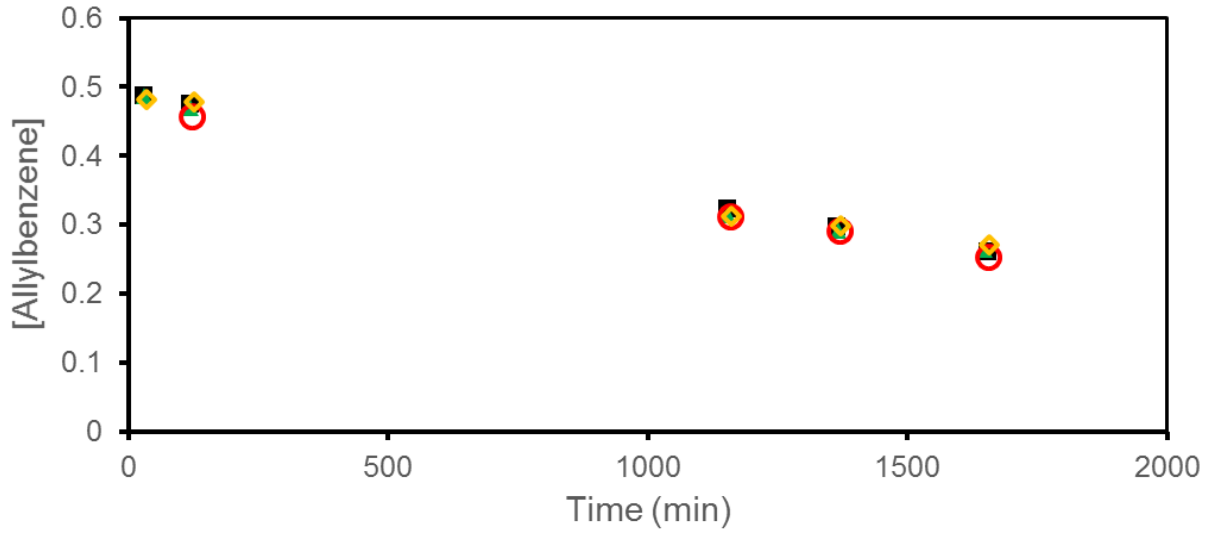

Figure 4.20: Isomerization of 0.5 M allylbenzene by 5 mM **2** with no additive (black squares), heterogeneous $KBAr^{F}_{4}$ (red circles), 1 equiv $KBAr^{F}_{4}$ with 32 equiv Et_2O (green triangles), and 1 equiv $KBAr^{F}_{4}$ with 69 equiv Et_2O (yellow diamonds).

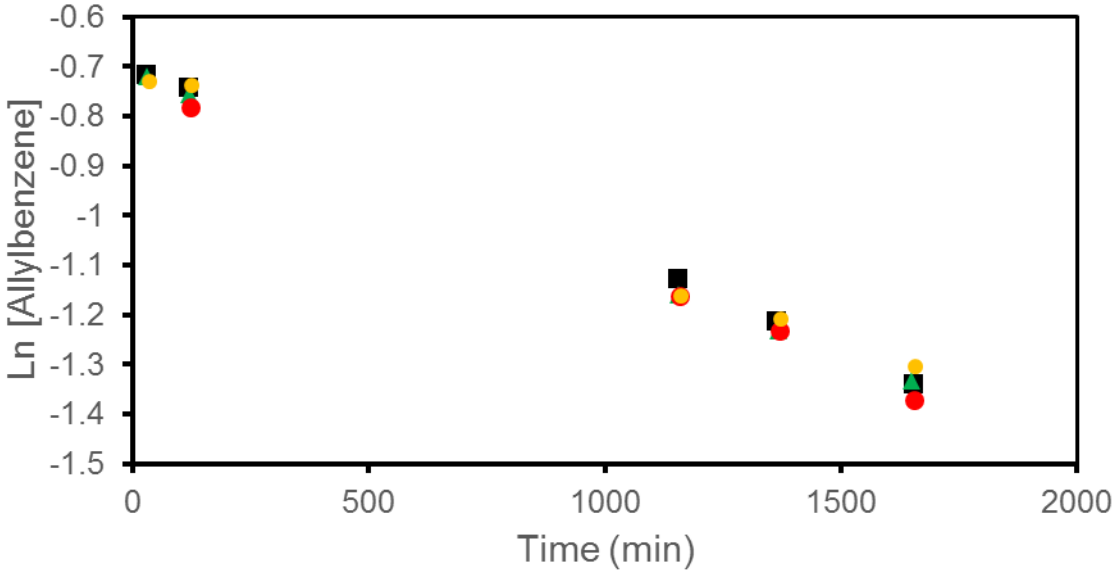

Figure 4.21: Isomerization of 0.5 M allylbenzene by 5 mM **2** with no additive (black squares), heterogeneous $KBAr^{F}_{4}$ (red circles), 1 equiv $KBAr^{F}_{4}$ with 32 equiv Et_2O (green triangles), and 1 equiv $KBAr^{F}_{4}$ with 69 equiv Et_2O (yellow diamonds).

Effect of $NaBAr^F_4$ on Allylbenzene Isomerization

Trial 1. A scintillation vial was charged with 0.0173 g (0.0115 mmol) **2**, 10 μL HMDSO, 153 μL (1.115 mmol) allylbenzene, and 2.310 mL CD_2Cl_2 to make a solution of 5 mM **2** with 0.5 M allylbenzene. The solution was transferred to Teflon sealed NMR tubes containing: 0.0049 g (0.0055 mmol) $NaBAr^F_4$, and 4 μL (0.039 mmol) Et_2O. The reaction progress was then monitored by ^1H NMR spectroscopy.

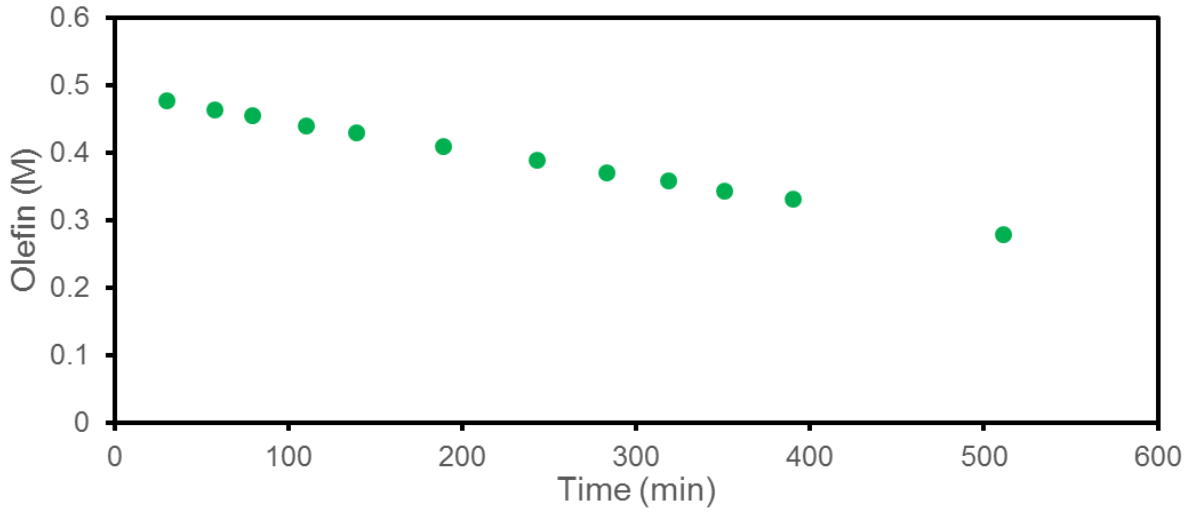

Figure 4.22: Consumption of 0.5 M allylbenzene by **2** and 2.2 equiv. Na^+/2 and 7.5 equiv. Et_2O/Na^+ (green circles, TOF = 5.4 h^{-1}).

Trial 2. A scintillation vial was charged with 0.0173 g (0.0116 mmol) **2**,11 μL HMDSO, 153 μL (1.155 mmol) allylbenzene, 120 μL (1.155 mmol) Et_2O, and 2.310 mL CD_2Cl_2. The solution was transferred in 500 μL aliquots to Teflon sealed NMR tubes containing 0.0022 g (0.0025 mmol) $NaBAr^F_4$, 0.0049 g (0.0055 mmol) $NaBAr^F_4$, 0.0099 g (0.0112 mmol) $NaBAr^F_4$, and 0.0160 g (0.0181 mmol) $NaBAr^F_4$. The reaction was then monitored by ^1H NMR spectroscopy.

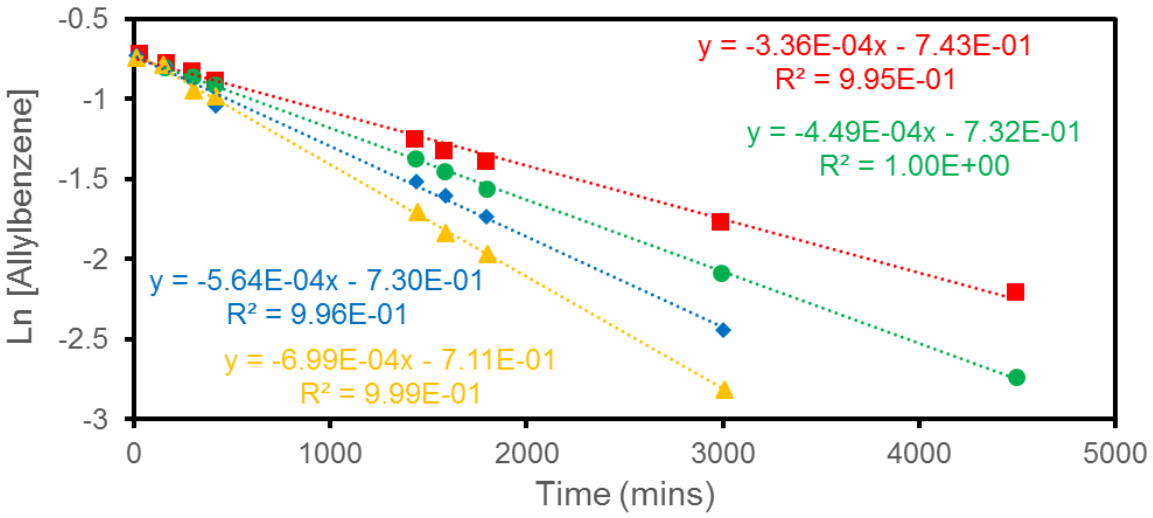

Figure 4.23: Ln[Allylbenzene] vs time plot for the consumption of 0.5 M allylbenzene by 5 mM **2** in CD_2Cl_2 with 0.5 M Et_2O and 1.1 equiv. $NaBAr^F{}_4$ (red squares), 2.5 equiv. $NaBAr^F{}_4$ (green circles), 5.0 equiv. $NaBAr^F{}_4$ (blue diamonds), and 7.4 equiv. $NaBAr^F{}_4$ (yellow triangles).

Effect of $LiBAr^F{}_4$•$3Et_2O$ on Allylbenzene Isomerization

A scintillation vial was charged with 0.0177 g (0.01182 mmol) **2**, 10 uL HMDSO, and 2365 µL CD_2Cl_2 to make a 4.98 mM solution of **2** in CD_2Cl_2. From this solution 500 µL aliquots were transferred into septa sealed screw cap NMR tubes containing, 0.0011 g (0.0010 mmol) $LiBAr^F{}_4$•$3Et_2O$, 0.0030 g (0.00275 mmol) $LiBAr^F{}_4$•$3Et_2O$, 0.0056 g (0.00513 mmol) $LiBAr^F{}_4$•$3Et_2O$, and 0.0112 g (0.0103 mmol) $LiBAr^F{}_4$•$3Et_2O$. To each tube was added 33 µL (0.249 mmol) allylbenzene via syringe. Conversion was monitored by ^1H NMR spectroscopy.

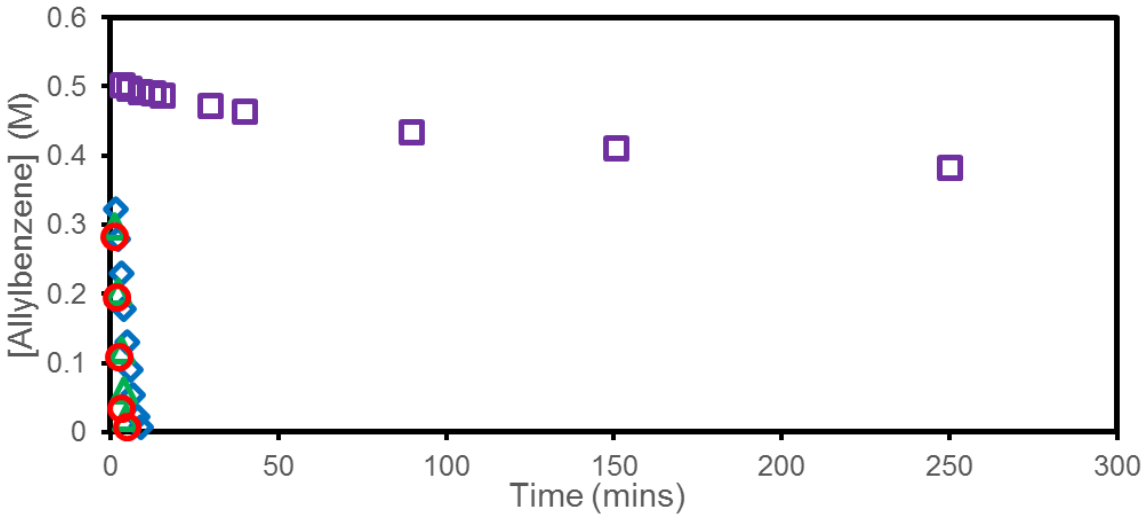

Figure 4.24: Concentration vs time plot for the isomerization of 0.5 M allylbenzene by 4.98 mM **2**, and increasing $LiBAr^{F}_{4}$•$3Et_2O$ from 0.2 equiv. Li^{+}/**2** (purple square), 0.8 equiv. Li^{+}/**2** (blue diamond), 2.0 equiv. Li^{+}/**2** (green triangle), and 4.2 equiv. Li^{+}/**2** (red circle).

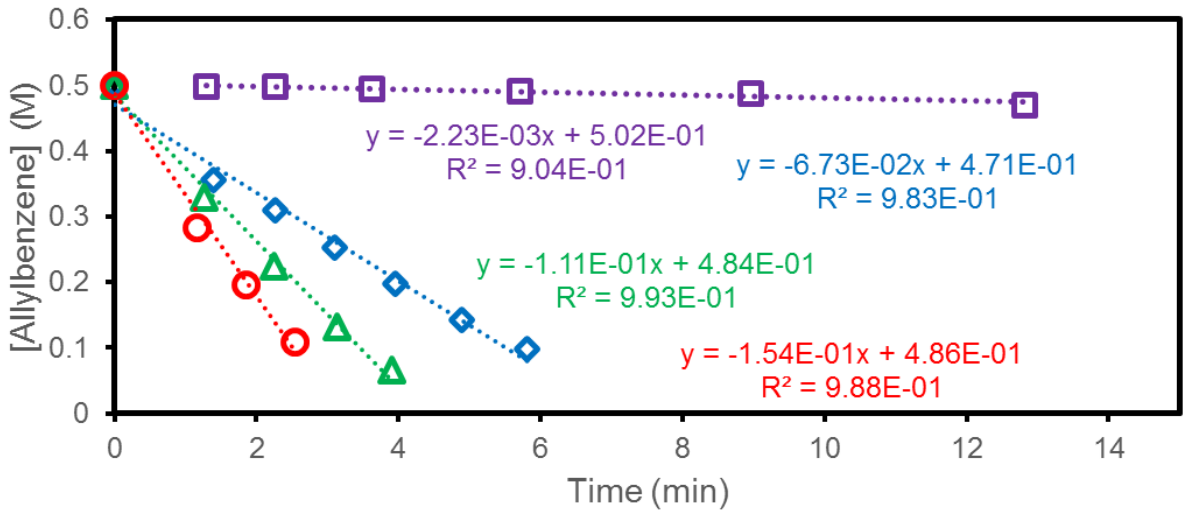

Figure 4.25: Concentration vs time plot for the isomerization of 0.5 M allylbenzene by 4.98 mM **2**, and increasing $LiBAr^{F}_{4}$•$3Et_2O$ from 0.2 equiv. Li^{+}/**2** (purple square), 0.8 equiv. Li^{+}/**2** (blue diamond), 2.0 equiv. Li^{+}/**2** (green triangle), and 4.2 equiv. Li^{+}/**2** (red circle).

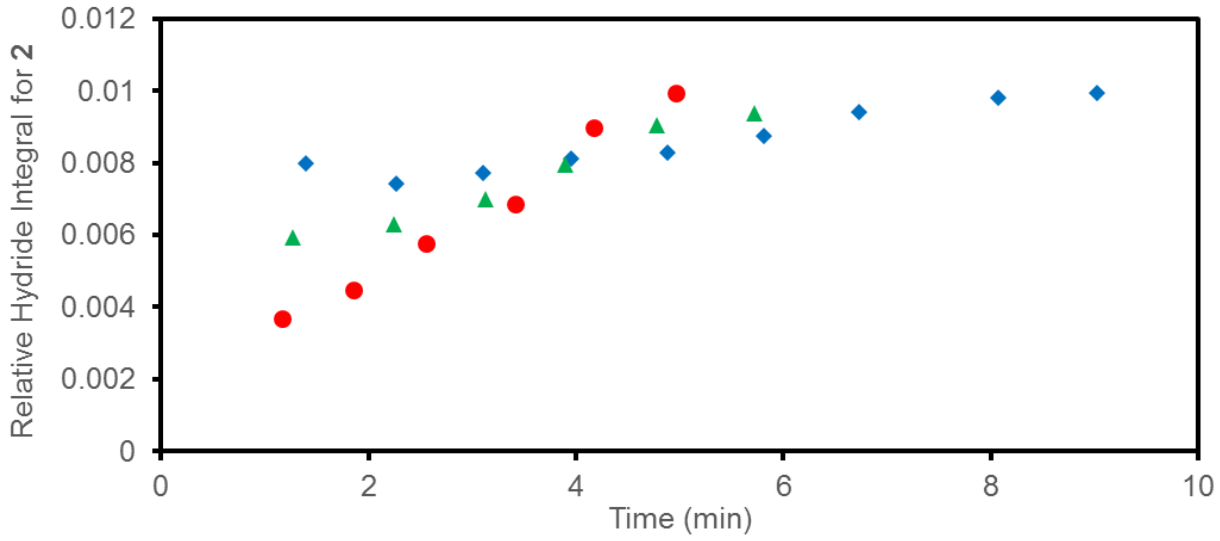

Figure 4.26: Relative hydride region integration relative to HMDSO during isomerization reactions containing increasing $LiBAr^{F}_{4}$•$3Et_2O$ from 0.8 equiv. Li^+/**2** (blue diamond), 2.0 equiv. Li^+/**2** (green triangle), and 4.2 equiv. Li^+/**2** (red circle).

Kinetic Modeling

The kinetic modeling software Copasi was used to assess the viability of the mechanism proposed in Scheme 2 of the main text. In order to limit the number of kinetic parameters in the fit, a simplified model featuring only four chemical steps was used. Equilibrium olefin (**AB**) binding by complex **2** (equation 4.2) forms an intermediate (**I**) that can either undergo irreversible catalysis to form the product (P) (equation 4.3) or enter a second equilibrium binding an alkali metal cation ($\mathbf{M^+}$) to form another intermediate **I2** (equation 4.4) before entering a parallel irreversible catalytic cycle (equation 5).

$$\mathbf{2} + \mathbf{AB} \rightleftharpoons \mathbf{I} \qquad \text{(equation 4.2)}$$

$$\mathbf{I} \rightarrow \mathbf{2} + \mathbf{P} \qquad \text{(equation 4.3)}$$

$$\mathbf{I} + \mathbf{M^+} \rightleftharpoons \mathbf{I2} \qquad \text{(equation 4.4)}$$

$$\mathbf{I2} \rightarrow \mathbf{2} + \mathbf{M^+} + \mathbf{P} \qquad \text{(equation 4.5)}$$

Experimental data at four different concentrations of $LiBAr^{F}_{4}$•$3OEt_2$ (data from Figure 4.24, along with a salt-free experiment Figure 4.1) was fit simultaneously using Copasi. As can be seen in Figure 4.24, the model provides excellent fits to all four data sets using a conserved set of rate constants. There is not enough data to provide exact values for the rate constants, but the parameters required to achieve good fits are consistent with unfavorable olefin binding, extremely favorable lithium binding, and faster catalysis by **I2**. (A model that more directly mimics Scheme 4.2 gave equally good fits, but is disfavored for modeling purposes because it involves more chemical equations.)

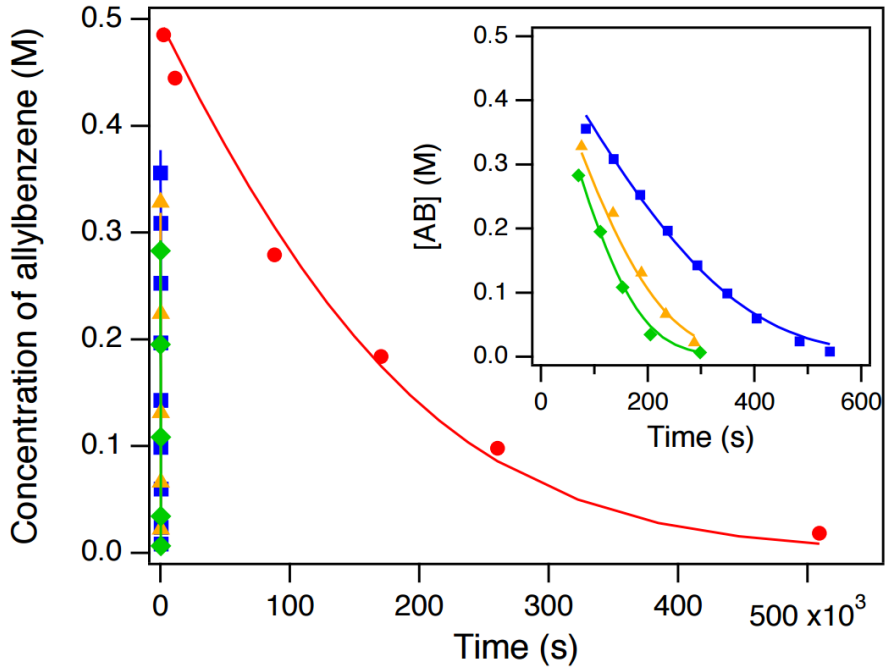

Figure 4.27: Fits of experimental data using the kinetic model of equations 4.2-4.5. Isomerization of 0.5 M allylbenzene by 5 mM **2** (red circles), and with 0.8 equiv. Li^+ (blue squares), 2.0 equiv. Li^+ (yellow triangles), and 4.2 equiv. Li^+ (green diamonds). The experimental data is plotted as markers and the fit is shown in solid lines. Inset is same data shown at short times.

Isomerization at Low Catalyst Loading

A scintillation vial was charged with 0.0016 g (0.00107 mmol) **2**, 0.0112 g (0.0103 mmol) $LiBAr^F_4$•$3OEt_2$, 5 μL HMDSO, and 2.140 mL CD_2Cl_2. The solution was transferred in 500 μL portions to two Teflon sealed NMR tubes. To the first tube 33 μL (0.249 mmol) allylbenzene was injected and the reaction was monitored via ^{1}H NMR.

Isomerization of 1-hexene

A scintillation vial was charged with 0.0220 g (0.0147 mmol) **2**, 2.940 mL CD_2Cl_2, and 10 μL HMDSO. A 500 μL aliquot was transferred to a Teflon sealed NMR tube, with 31 μL (0.248 mmol) 1-hexene. Reaction was monitored by ^{1}H NMR spectroscopy.

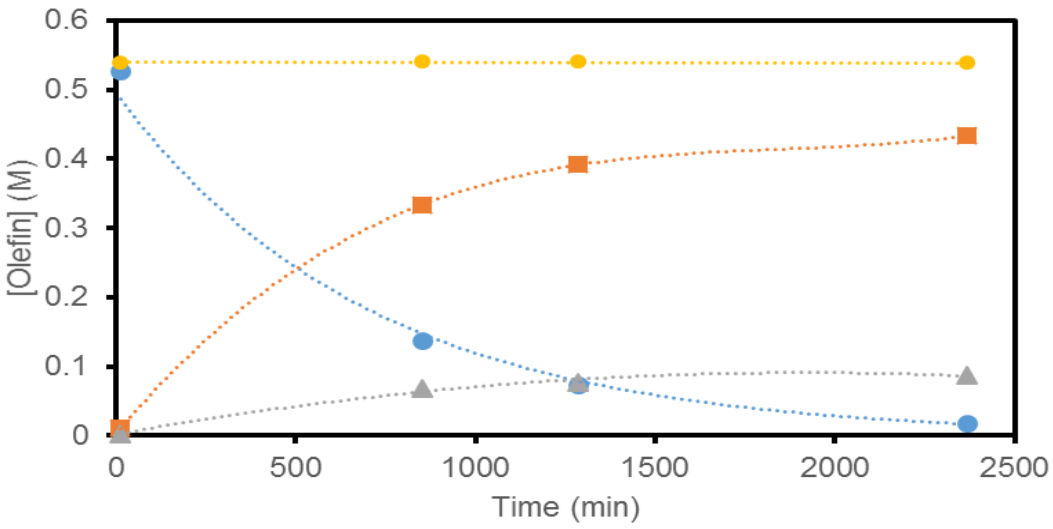

Figure 4.28: Isomerization of 0.5 M 1-hexene (blue circles) by 5 mM complex **2**, to form cis-2-hexene (grey triangles), and trans-2-hexene (orange squares)

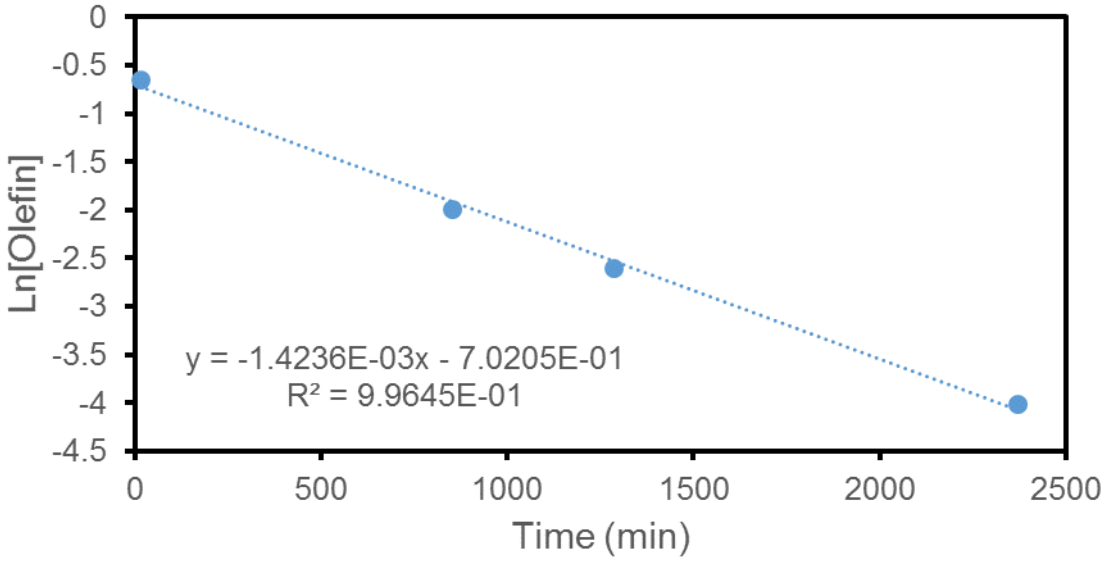

Figure 4.29: Isomerization of 0.5 M 1-hexene (blue circles) by 5 mM complex **2** plotted as Ln[Allylbenzene] vs time with half life $t_{1/2}$ = 487 min.

Effect of LiBAr$^{F}_{4}$•3Et$_2$O on 1-hexene Isomerization

A 20 mL scintillation vial was charged with 0.0177 g (0.0118 mmol) **2**, 1.420 mL CD_2Cl_2, and 5 µL HMDSO to make an 8.33 mM solution of **2**. A scintillation vial was charged with 0.0127 g (0.0116 mmol) LiBAr$^{F}_{4}$•3Et$_2$O, and 500 µL CD_2Cl_2. The solution of **2** was transferred

to septa sealed NMR tubes in 300 µL aliquots. The Li^+ solution was transferred to the tubes in aliquots of 0, 50, 100, 200 µL. Next, $CD_2Cl_2$was added to the tubes to make the total volume 500 µL. Next 31 µL (0.248 mmol) 1-hexene was injected to the tubes and reaction progress was monitored by ^1H NMR spectroscopy.

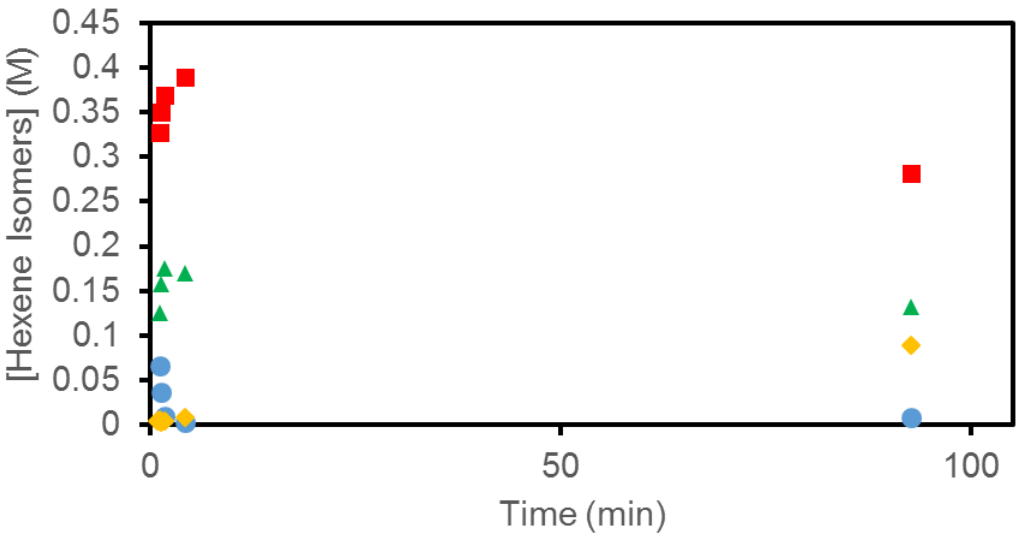

Figure 4.30: Isomerization of 0.5 M 1-hexene (blue circles) by 5 mM **2**, to form trans-2-hexene (red squares), and cis-2-hexene (green triangles).

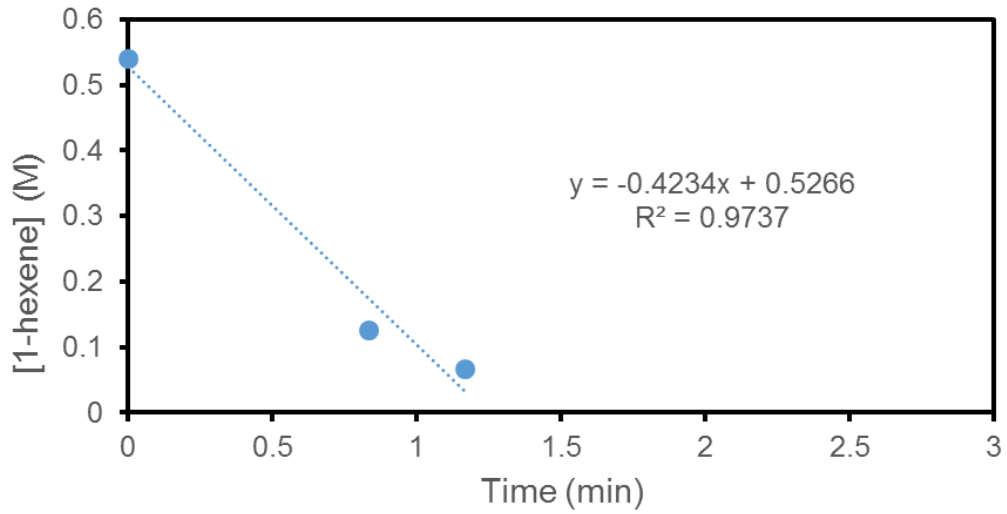

Figure 4.31: Isomerization of 0.5 M 1-hexene (blue circles) by 5 mM **2**. Initial 1-hexene concentration was artificially placed at 0 min and a linear fit was added to determine the zero-order half life $t_{1/2}$ = 0.59 min or 825x faster than without Li^+.

Cation Free 4-Methoxyallylbenzene (estragole) Isomerization

A scintillation vial was charged with 0.0062 g (0.00414 mmol) **2**, 0.830 mL CD_2Cl_2, and 10 µL HMDSO to make a 4.99 mM solution of **2**. A 500 µL aliquot of the solution (0.00250 mmol **2**) was transferred to a Teflon sealed NMR tube, and charged with 38 µL (0.247 mmol) 4-methoxyallylbenzene. The reaction was monitored by ^{1}H NMR spectroscopy.

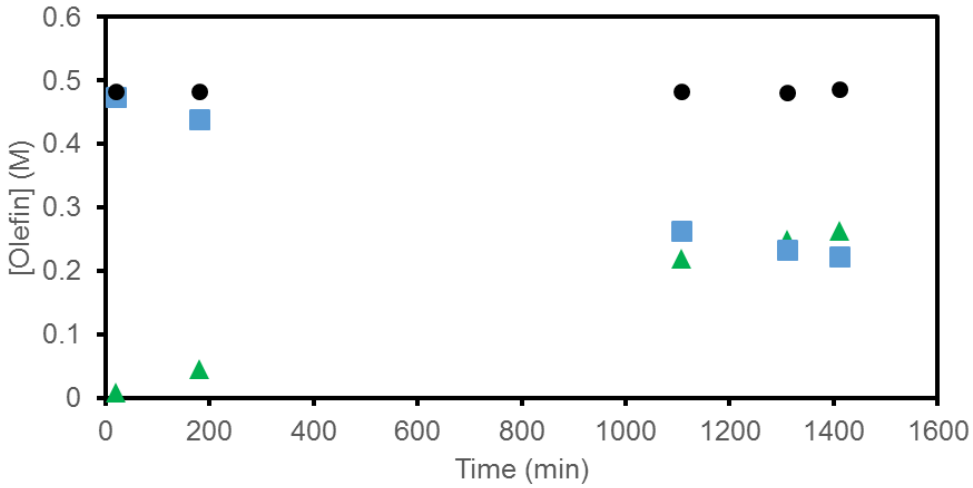

Figure 4.32: Conversion of 0.5 M 4-methoxyallylbenzene over time by complex **2** (blue squares) to form 4-methoxy-β-methylstyrene (green triangles).

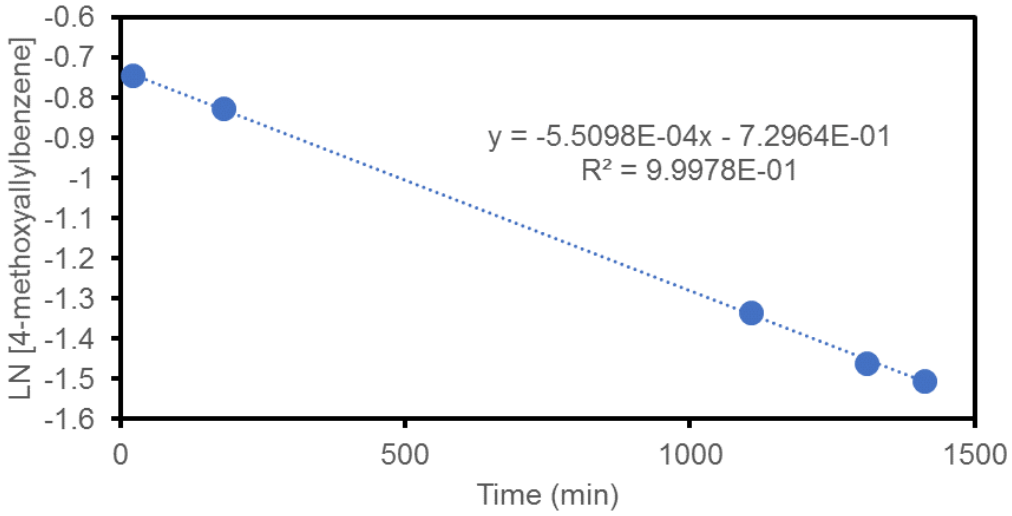

Figure 4.33: Conversion of 0.5 M 4-methoxyallylbenzene over time by complex **2** (blue circles) $t_{1/2}$ = 1260 min.

Effect of $LiBAr^F_4$•$3Et_2O$ on 4-methoxyallylbenzene isomerization

A scintillation vial was charged with 0.0142 g (0.00949 mmol) **2**, 1.90 mL CD_2Cl_2, and 11 µL HMDSO to make a 4.99 mM solution of **2**. A 1.250 mL aliquot of the solution was transferred to a vial charged with 0.0164 g (0.0150 mmol) $LiBAr^F_4$•$3Et_2O$. A 500 µL aliquot was transferred to a septa sealed NMR tube. Via injection, 38 µL (0.247 mmol) 4-methoxyallylbenzene was added and the reaction was monitored by ^1H NMR spectroscopy.

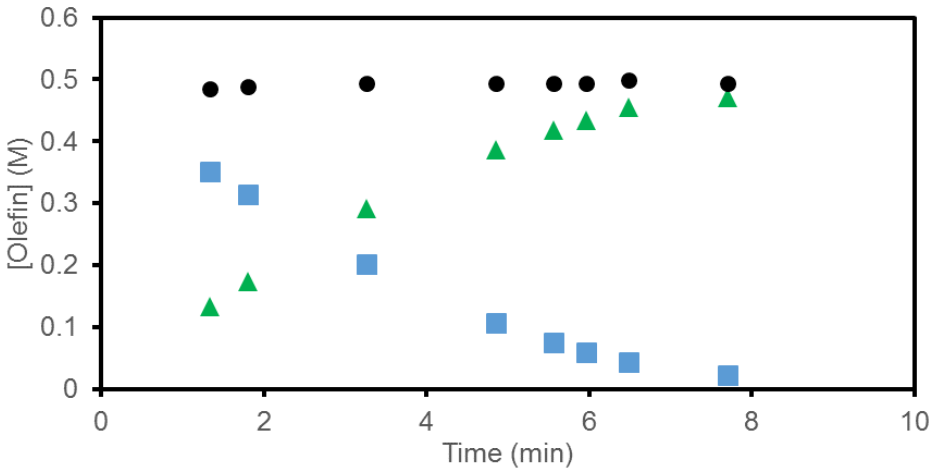

Figure 4.34: Conversion of 0.5 M 4-methoxyallylbenzene over time by complex **2** (blue squares) to form 4-methoxy-β-methylstyrene (green triangles).

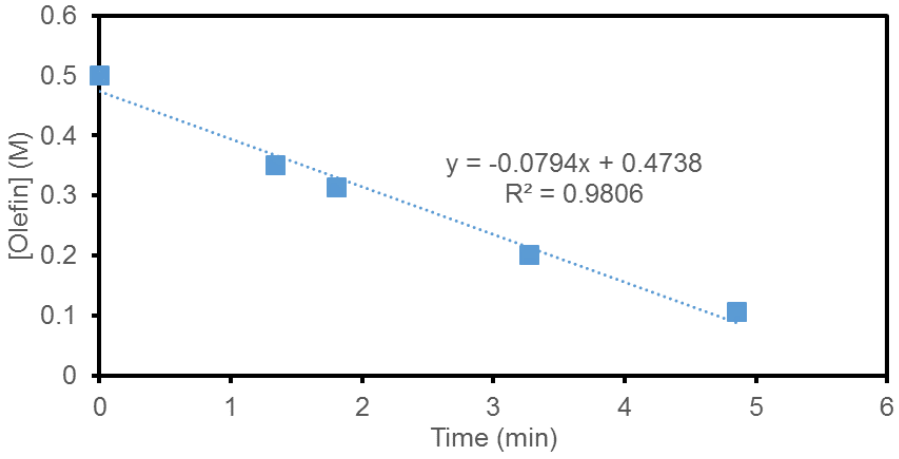

Figure 4.35: Conversion of 0.5 M 4-methoxyallylbenzene over time by complex **2** (blue squares) fit for a zero order half life $^0t_{1/2}$ = 3.15 min.

Effect of Et_2O on Lithium-Accelerated Allylbenzene Isomerization

A 20 mL scintillation vial was charged with 0.0246 g (0.01643 mmol) **2**, 0.0179 g (0.01638 mmol) $LiBAr^F{}_4 \bullet 3Et_2O$, 10 µL (0.04705 mmol) HMDSO, and 3.290 mL deuterated methylene chloride to create a 5 mM solution of **2**, and 5 mM $LiBAr^F{}_4 \bullet 3Et_2O$. The solution was transferred to screw cap NMR tubes in 500 µL aliquots. Diethyl ether was added to adjust the ratio of Et_2O/Li+ from 3 equiv – 25 equiv. Allylbenzene 33 µL (0.249 mmol) was injected to each tube and the conversion was monitored by ^1H NMR spectroscopy.

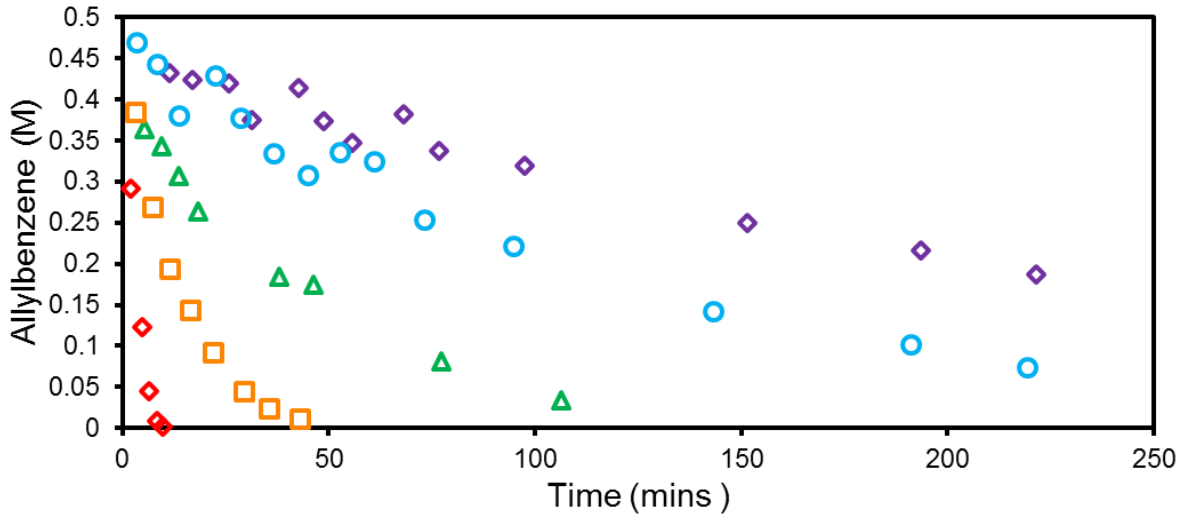

Figure 4.36: Consumption of 0.5 M allylbenzene by 5 mM **2**, 5 mM $LiBAr^F{}_4 \bullet 3Et_2O$, and increasing equiv. Et_2O/Li^+ from 3 equiv. (red diamonds, TOF = 858 h^{-1}), 7.5 equiv. (orange square, TOF = 304 h^{-1}), 11 equiv. (green triangle, TOF = 117 h^{-1}), 16.5 equiv. (blue circle, TOF = 41 h^{-1}), and 25 equiv. (purple diamond, 17.3 h^{-1}).

Allylbenzene Isomerization with $LiAl(OC(CF_3)_3)_4$ and $LiBPh_4 \bullet 3(MeOCH_2CH_2OMe)$.

A scintillation vial was charged with 0.0138 g (0.00922 mmol) **2**, and 1.850 mL CD_2Cl_2 to make a 5.00 mM solution of **2**. Using a syringe, 500 µL aliquots were transferred to 3 septa sealed NMR tubes containing, 0.0028 g (0.0067 mmol) $LiBPh_4 \bullet 3(MeOCH_2CH_2OMe)$, and

0.0038 g (0.0039 mmol) $LiAl(OC(CF_3)_3)_4$. Via syringe, 33 µl (0.249 mmol) allylbenzene were injected and the reaction was monitored.

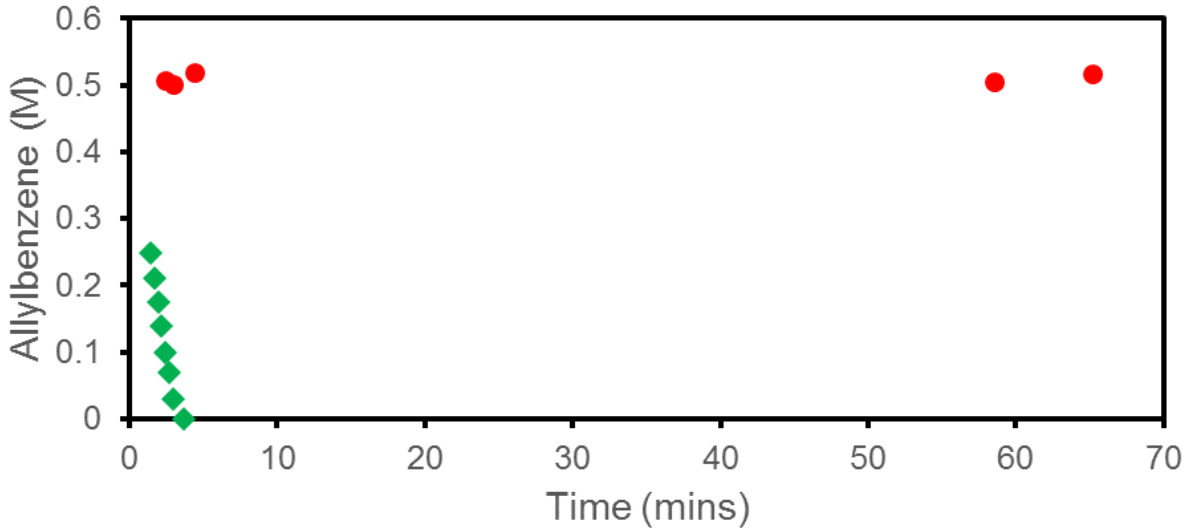

Figure 4.37: Conversion vs time plot for 5 mM **2** with 100 equiv allylbenzene with added $LiBPh_4 \bullet 3(MeOCH_2CH_2OMe)$ (red circles), and $LiAl(OC(CF_3)_3)_4$ (green diamonds).

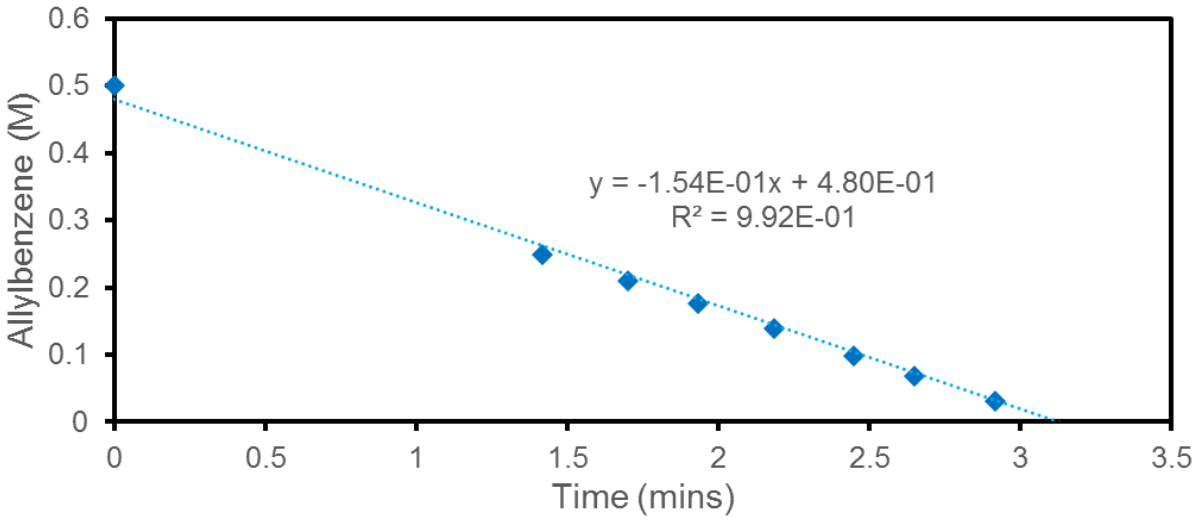

Figure 4.38: Conversion vs time plot for $LiAl(OC(CF_3)_3)_4$ data with an added point for 500 mM allylbenzene at time zero. Data was fit with linear trend.

Switchable Catalysis

A scintillation vial was charged with 0.0076 g (0.01136 mmol) **1**, 2260 μL CD_2Cl_2, and 10 μL HMDSO to make a 5.00 mM solution of **1**. A 500 μL aliquot (0.0025 mmol 1) was transferred to a Teflon sealed NMR tube, followed by injection of 34 μL (0.2566 mmol) allylbenzene. A separate scintillation vial was charged with 0.0850 g (0.09591 mmol) $NaBAr^F{}_4$, 810 μL CD_2Cl_2, and 150 μL diethyl ether to make a 99.91 mM $NaBAr^F{}_4$ solution. A third vial was charged with 0.0647 g (0.1135 mmol) PPNCl (PPNCl = Bis(triphenylphosphine)iminium chloride), and 1130 μL CD_2Cl_2 to make a 100.42 mM solution of PPNCl. The isomerization reaction was monitored for 1 h via ^1H NMR spectroscopy and pumped back into the glovebox. To start the reaction, a 50 μL of the 99.91 mM $NaBAr^F{}_4$ solution (0.00500 mmol Na^+ or 2 equiv Na^+/**1**) was added to the reaction tube. The reaction was monitored for another hour before pumping the tube back into the glovebox, and injecting 50 μL of the 100 mM PPNCl solution (0.005 mmol Cl^- or 2 equiv Cl^-/**2**) to stop the reaction. This process was repeated three times. During this process the initially 0.500 mM allylbenzene solution becomes diluted as Na^+ and Cl^- are added. To best represent the start-stop activity, reactions are plotted as conversion.

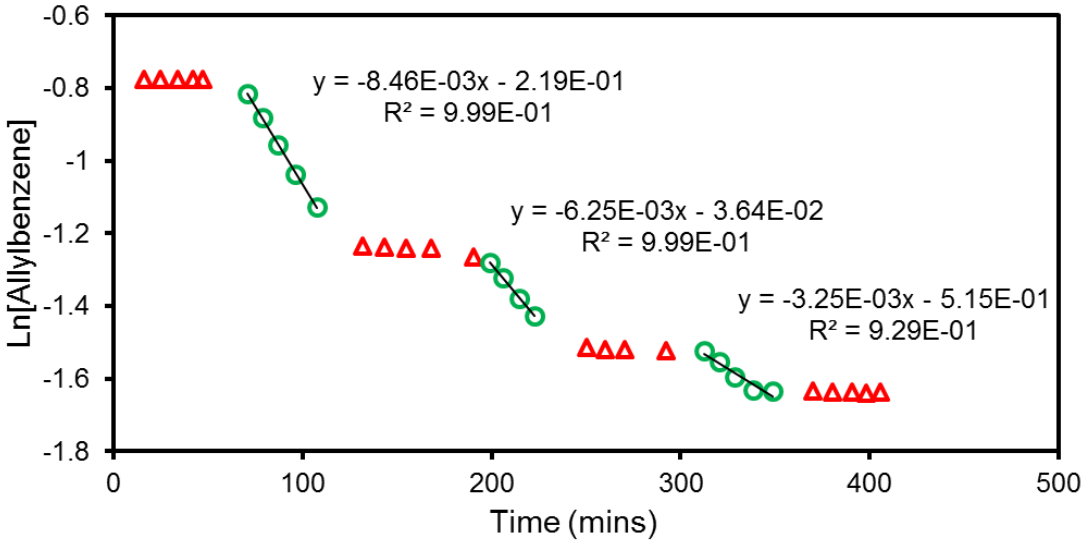

Figure 4.39: Consumption of allylbenzene during the start stop experiment plotted as Ln[allylbenzene] vs time.

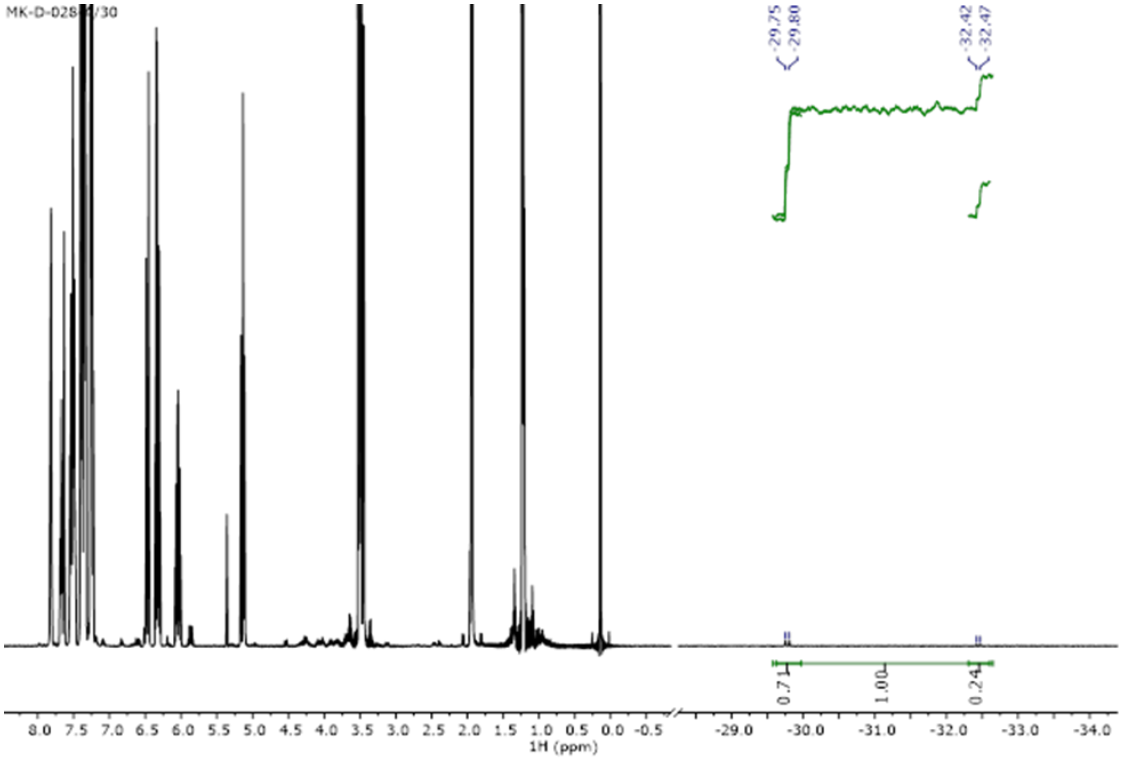

Figure 4.40: ^{1}H NMR spectrum showing formation of [(^{15c5}NCOP^{iPr})Ir(H)(OH_2)][BAr^F_4] at -32.43 ppm after multiple on/off cycles.

Monitoring Chloride Abstraction from 1

A scintillation vial was charged with 0.0093 g (0.01399 mmol) **1**, 5 µL HMDSO, and 556 µL CD_2Cl_2. A syringe was used to transfer 525 µL to a septa sealed screw cap NMR. In a separate scintillation vial, 0.0237 g (0.02674 mmol) $NaBAr^F{}_4$, 42 µL (0.4042 mmol) Et_2O, and 535 µL CD_2Cl_2 were combined to make a 46 mM $NaBAr^F{}_4$ solution. The Na^+ solution was transferred to a syringe and removed from the glove box. Spectra were acquired before injection. Then 500 µL of the Na^+ solution was injected into the screw cap tube and the conversion was monitored via ^1H NMR spectroscopy.

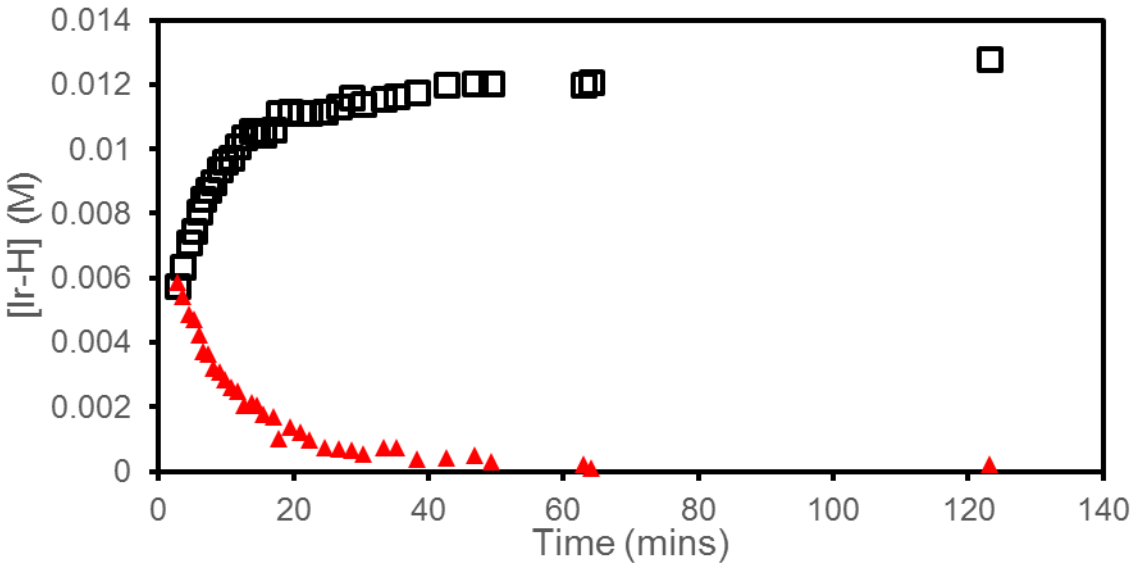

Figure 4.41: In situ ^1H NMR monitoring for the dehalogenation of **1** with 1.7 equiv Na^+ to form a previously unobserved hydride species (red diamonds), as it converts to complex **2** (hollow black squares).

Monitoring Allybenzene Isomerization after Chloride Abstaction.

A scintillation vial was charged with 0.0051 g (0.00762 mmol) 1, 0.0178 g (0.02008 mmol) $NaBAr^F{}_4$, 1525 µL CD_2Cl_2, 5 µL HMDSO, 15 µL diethyl ether, and 101 µL allylbenzene with stirring. Following the addition of CD_2Cl_2 the reaction turned brick orange and was allowed

to stir for 3 minutes. A 500 μL aliquot was transferred unfettered to a Teflon sealed NMR tube. The rest of the solution was filtered through a glass frit into a separate Teflon sealed NMR tube. Reaction progress for both tubes was monitored via ^{1}H NMR spectroscopy.

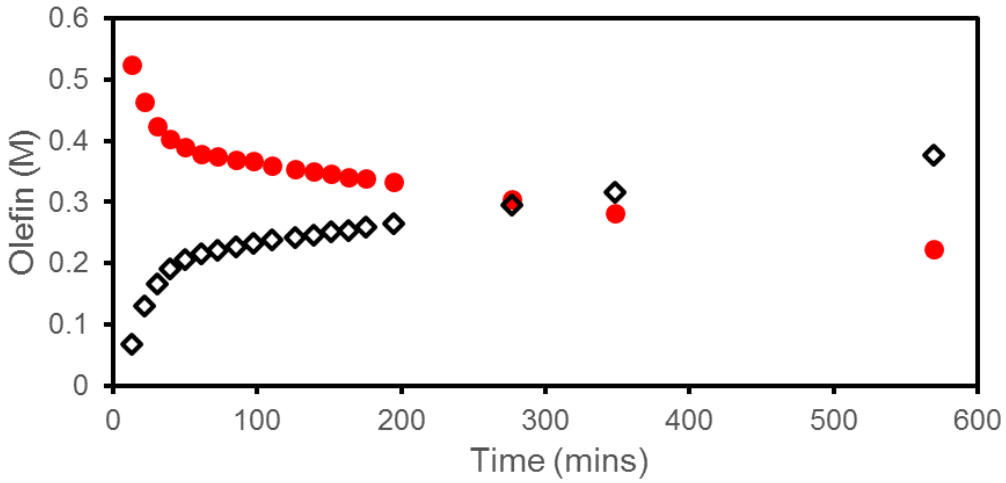

Figure 4.42: Concentration vs time plot for allylbenzene (red circles) isomerization to β-methylstyrene (black diamonds) initiated by adding $NaBAr^{F}_{4}$ to 1.

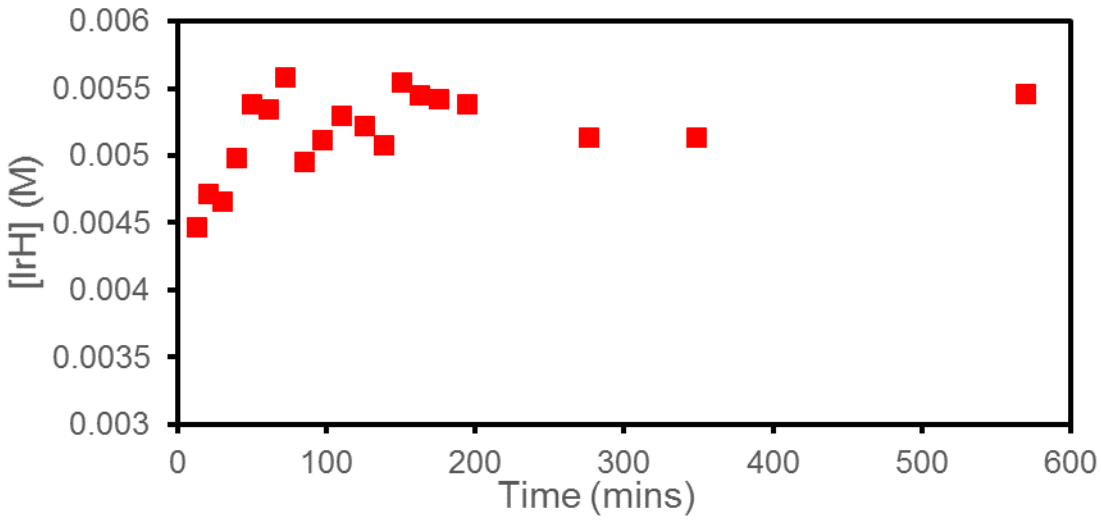

Figure 4.43: Concentration of complex **2** over time during dehalogenation initiated isomerization reaction

***In-Situ* Catalyst Cycling Experiment**

In a nitrogen atmosphere glove box, a scintillation vial was charged with 0.0135 (0.00902 mmol) **2**, 1.800 mL CD_2Cl_2, and 5 µL HMDSO to make a 5.01 mM solution of **2**. Next 120 µL (0.9057 mmol) allylbenzene was injected to the vial to yield a 0.5 M solution allylbenzene. A 500 µL aliquot was transferred to a Teflon sealed NMR tube, the tube was removed from the glovebox, and the reaction was monitored for 340 minutes by ^{1}H NMR spectroscopy. The tube was pumped back into the glove box and 0.0028 g (0.00256 mmol) $LiBAr^F_4$•$3Et_2O$ was added to the tube. The solution was mixed for 75 seconds before adding 0.0036 g (0.00627 mmol) PPNCl. The tube was removed from the glove box and monitored by ^{1}H NMR spectroscopy for 72 minutes. The tube was brought back into the glove box and 0.0140 g (0.0158 mmol) $NaBAr^F_4$ was added to the tube. The reaction was removed from the glovebox and monitored by ^{1}H NMR spectroscopy for 15 minutes.

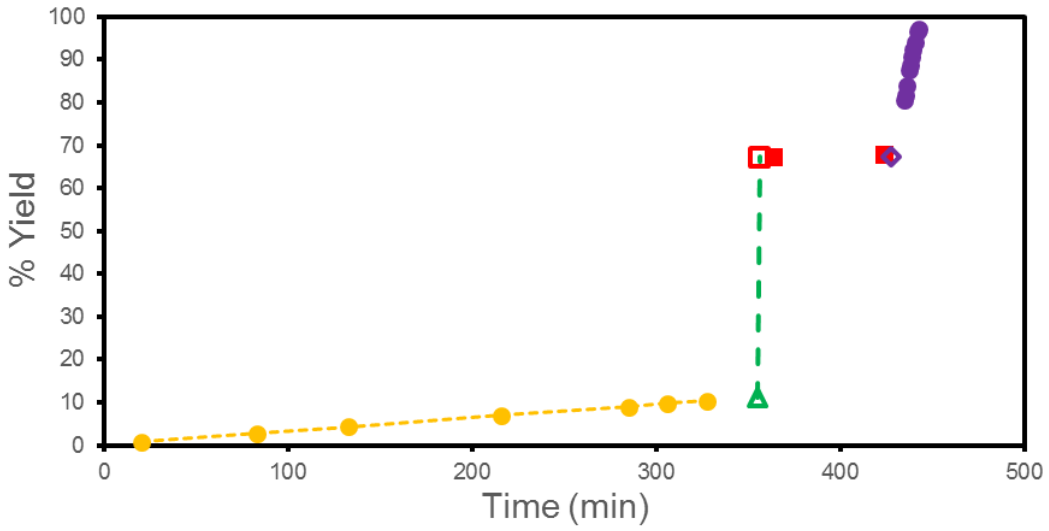

Figure 4.44: Plot of % conversion vs time for the isomerization of 0.5 M allylbenzene by 5 mM (1 mol%) **2** (closed yellow circles) before the addition of 1 equiv $LiBAr^F_4$•$3Et_2O$ (open green triangle, % conversion estimated), followed by 2.5 equiv PPNCl (open red square, % conversion estimated). Reaction was monitored (red squares) until 6 equiv $NaBAr^F_4$ (open purple diamond) was added to monitor the reaction to completion (purple circles).

Table 8. Compilation of allylbenzene isomerization data. All reactions carried out in dichloromethane with 0.5 M allylbenzene at ambient temperature. The salts used were $KB(C_6F_5)_4$, $NaBAr^F{}_4$, and $LiBAr^F{}_4 \bullet 3Et_2O$.

Cat.	Catalyst Loading (mM)	Cation	Cation Loading (mM)	Et_2O/Cation Ratio	TOF (h^{-1})	$t_{1/2}$ (min)	${}^1k_{obs}$ (min^{-1})	${}^0t_{1/2}$ (min)	${}^0k_{obs}$ (M/min)
1	5	–	–	–	0	N/A			
2	5	–	–	–	1.8	1810	3.83×10^{-4}		
2	10	–	–	–	2.4	1200	5.80×10^{-4}		
2	15	–	–	–	2.4	710	9.76×10^{-4}		
2	25	–	–	–	3.3	528	1.31×10^{-3}		
2	35	–	–	–	2.8	359	2.06×10^{-3}		
2	5	K^+	5	69	1.8	1720	4.02×10^{-4}		
2	5		11	0	3.70	987	7.02×10^{-4}		
2	5	Na^+	11	7.5	5.38	652	1.06×10^{-3}		
2	5		12	15	2.93	1240	5.58×10^{-3}		
2	5		5.5	91	2.5	1930	3.59×10^{-4}		
2	5	Na^+	12.5	40	2.2	1550	4.49×10^{-4}		
2	5		25	20	2.8	1230	5.64×10^{-4}		
2	5		37	14	3.3	992	6.99×10^{-4}		
2	5		1	3	15.2			112	2.23×10^{-3}
2	5	Li^+	4	3	880			3.71	6.69×10^{-2}
2	5		10	3	1450			2.25	1.11×10^{-1}
2	5		21	3	1870			1.62	1.54×10^{-1}
2	0.5	Li^+	10	3	2750			11.60	2.16×10^{-2}
2	5		5	25	17			197	1.27×10^{-3}
2	5		5	17	41			98.0	2.55×10^{-3}
2	5	Li^+	5	11	117			33.0	7.69×10^{-3}
2	5		5	7.5	304			13.9	1.80×10^{-2}
2	5		5	3	858			4.4	5.66×10^{-2}
2	5		1	3	278			12.4	2.02×10^{-2}
2	5	Li^+	2	3	600			5.67	4.41×10^{-2}
2	5		2.9	3	912			3.83	6.53×10^{-2}
2	5		4	3	1190			2.74	9.11×10^{-2}
2	5	Li^+ [a]	8	0	2010			1.6	1.54×10^{-1}

[a] $LiAl(OC(CF_3)_3)_4$.

Synthesis of $KBAr^{F}_{4}$

A scintillation vial was charged with 0.1120 g (0.1106 mmol) $HBAr^{F}_{4}$•$2Et_2O$, and 5 mL Et_2O. A second vial was charged with 0.0125 g (0.0960 mmol) benzylpotassium and 5 mL Et_2O. The benzylpotassium was only slightly soluble. Both vials were placed in a cold well chilled using liquid nitrogen. The solutions were allowed to freeze. A stir bar was then placed on top of the frozen benzylpotassium solution. The $HBAr^{F}_{4}$•$2Et_2O$ solution was removed from the cold well and allowed to thaw. Once thawed, the $HBAr^{F}_{4}$•$2Et_2O$ solution was transferred to the benzylpotassium vial and the entire mixture was allowed to thaw while stirring. The initially red heterogenous mixture began to lose color as the solution warmed turning orange, yellow, and finally clear. The mixture was then pumped to a solid. The solids were rinsed with DCM to remove excess $HBAr^{F}_{4}$•$2Et_2O$, and then pumped to solid. The solids were rinsed with 2 x 2 mL portions of n-pentane, 3 x 2 mL benzene, then pumped to solid to yield 0.081 g (0.0897 mmol) 93% yield. Characterization[133] consistent with previous procedures ^{1}H NMR (400 MHz, Methylene Chloride-d_2) δ 7.72 (s, 8H), 7.56 (s, 4H). ^{19}F NMR (376 MHz, Methylene Chloride-d_2) δ -62.4 (s).

Chapter 5 : CO_2 REDUCTION WITH PINCER-CROWN ETHER IRIDIUM COMPLEXES

5.1 Introduction to CO_2 Reduction with Iridium Pincer Complexes

Since the industrial revolution began over 200 years ago, emissions of carbon dioxide (CO_2) into the atmosphere have increased dramatically. Considering the threat of climate change from increased CO_2 levels, chemists have sought ways to convert CO_2 into useful chemicals. The catalytic conversion of CO_2 into other chemicals represents a significant challenge, considering the highly-oxidized nature of CO_2 which requires multiple reduction events ($+e^-$), and proton transfers ($+H^+$) to yield useful products. The UNC Energy Frontier Research Center for Solar Fuels has set out to develop new catalysts for CO_2 reduction in the context of light-driven fuel generation. Two major goals of the Center are to understand the origins of selectivity in CO_2 reduction and to reduce the overpotential required for CO_2 reduction.

The two most commonly observed products of two-electron reduction of CO_2 are carbon monoxide (CO) and formic acid (HCOOH). These two products are distinct in physical properties and represent a branch point in envisioned sequences to reach liquid fuels. Formic acid, the product of net hydrogen addition across a single CO_2 molecule, will be the focus of this chapter. In the gas phase, the reaction of CO_2 and H_2 to form formic acid is slightly uphill (~7 kcal•mol^{-1}), but in aqueous solution added base to convert formic acid to formate $HCOO^-$, makes the reaction favorable.[134]

Catalytic CO_2 reduction to formate with homogeneous transition metal catalysts has typically been achieved chemically via hydrogenation of CO_2 with H_2 in basic media at high temperatures and pressures.[135,136] Stoichiometric amounts of base are typically required in these hydrogenation reactions, and many systems use organic solvents.[137,138] Catalysts that operate in aqueous solvent with inexpensive bases like carbonate or hydroxide would be industrially preferred. Nozaki recently reported[139] the use of iridium pincer complexes for CO_2 hydrogenation in 1M KOH, 50-60 bar of CO_2/H_2, and temperatures up to 200˚C. These systems achieved turnover numbers up to 3.5 million with yields of 94%.

For a solar fuels device that stores the energy of the sun in chemical bonds, CO_2 reduction to formate would be ideally achieved electrochemically, via $2e^-/ 1H^+$ reduction. This electrochemical transformation is less common because H^+ reduction to generate H_2 can compete with CO_2 reduction to HCO_2H, leading to mixtures of H_2 and formate.[140–143]

Kang, Meyer, and Brookhart recently reported the selective electrocatalytic reduction of CO_2 to formate by the organometallic pincer complex (^{tBu}POCOP)Ir$(H)_2$.[72] In THF solution, the iridium dihydride (^{tBu}POCOP)Ir$(H)_2$ rapidly inserts CO_2 to form a κ^2-formate species (^{tBu}POCOP)Ir(H)(κ^2-OOCH). Adding >2 equivalents $NCCH_3$ to the κ^2-formate species forms [(^{tBu}POCOP)Ir(H)$(NCCH_3)_2]^+$ after release of the formate ligand. Reformation of an active dihydride species [(^{tBu}POCOP)Ir$(H)_2(NCCH_3)]^+$ can be accomplished by electrochemical reduction at –1.2 V vs NHE (–1.83 V vs Fc/Fc^+, Fc = ferrocene)[144] in $NCCH_3$ solutions with 5% H_2O. During this process, the iridium species undergoes a $2e^-$, $1H^+$ event to lose the $NCCH_3$ ligand *trans* to the hydride, and form a second hydride via protonation of the iridium center with H_2O in solution acting as the acid. Based on these steps a catalytic cycle was realized similar as shown in Scheme 5.1.

The system was moved out of $NCCH_3$ solvent, and into H_2O by making the catalyst water soluble by attaching a quaternary amine to the arene backbone of the catalyst.[145] In neutral pH solutions the dihydride complex is stable to proton reduction, showing excellent selectivity for CO_2 giving 93% Faradaic yield. In a different study, the arene backbone of the catalyst was substituted with a pyrene group, and immobilized on a carbon nanotube surface for use in flow cells.[146] In the immobilized architecture high turnover numbers were achieved (>54,000), with good catalyst activity (~15 s^{-1}).

Scheme 5.1

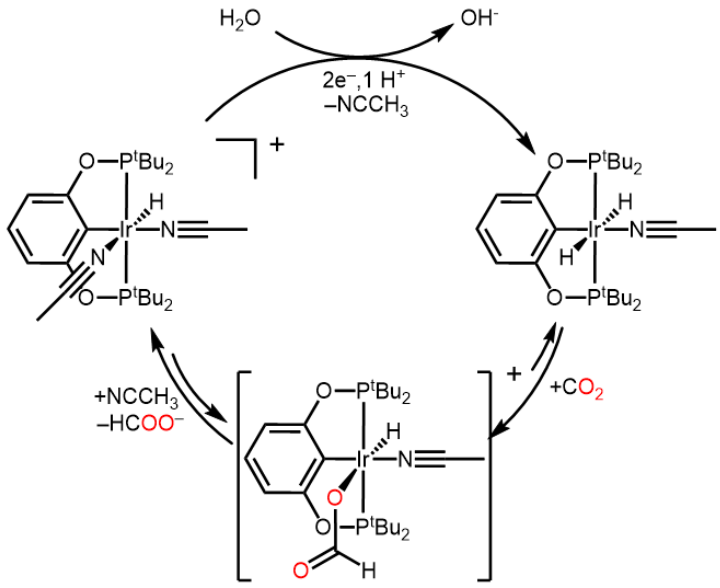

The cationic catalytic intermediate $[(^{tBu}POCOP)Ir(H)(NCCH_3)_2]^+$ above is isoelectronic to many of the pincer-crown ether complexes described in Chapter 2, as shown in scheme 5.2. We hypothesized that analogous pincer-crown ether complexes might be viable CO_2 reduction catalysts with properties tunable by installation of Lewis acidic cations in the pendent macrocycle. In previous CO_2 reduction studies, Lewis acids were shown to improve reactivity.[137,147] We imagined that cations held in close proximity to the iridium center might

interact with formate, assisting with product formation and release. Studies to synthesize iridium pincer-crown ether CO_2 reduction catalyst to generate formate were undertaken.

Scheme 5.2

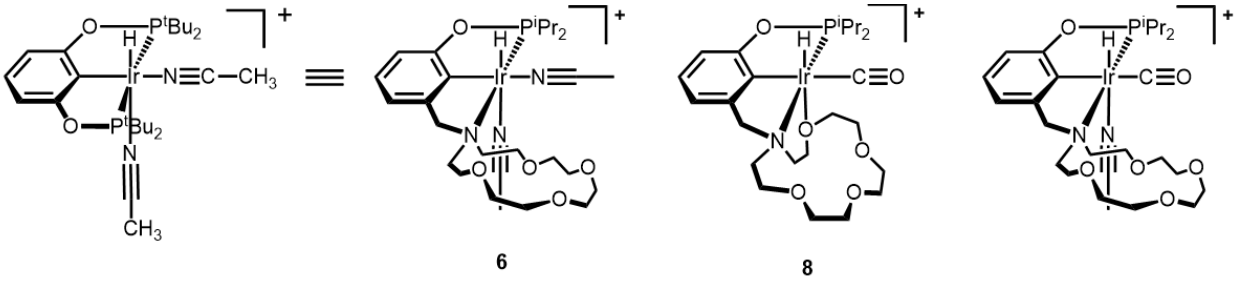

5.2 Results and Discussion

Attempted Synthesis of Dihydride Complexes

Dihydride (^{tBu}POCOP)Ir(H)$_2$ was used as the precatalyst in previous reports of CO_2 electroreduction to formate, with well-defined insertion of CO_2 into a Ir–H bond.[72] Thus, we wanted to convert existing pincer-crown ether iridium complexes into dihydrides. The first method we attempted was hydrodehalogenation[148] of (^{15c5}NCOP^{iPr})IrHCl **(1)** under an atmosphere of hydrogen according to Scheme 5.3. Solids of **1** and KO^{t}Bu were placed under a hydrogen atmosphere, then dissolved in hydrogen saturated toluene. The initially yellow solution quickly turned dark orange upon stirring, and eventually turned dark brown. Upon removing the solvent, a crude ^{1}H NMR spectra revealed considerable decomposition, disappearance of **1**, and no hydride signals indicative of dihydride formation. Repeating this method at –78˚C did not improve the reaction. We also attempted other bases like DBU (1,8-Diazabicyclo[5.4.0]undec-7-ene) in hydrogen saturated solutions of **1** in toluene at –78˚C, and hydride donors like super hydride (lithium triethyl borohydride), but observed similar decomposition upon workup.

Scheme 5.3

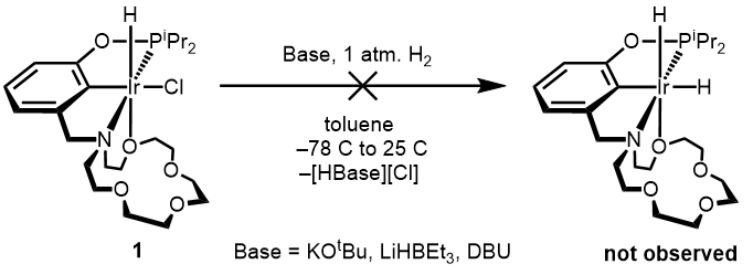

Hypothesizing that a *trans*-dihydride geometry might be stabilized by a carbonyl ligand, we targeted the hydrogenation of (^{15c5}NCOP^{iPr})Ir(CO) (**10**) to produce (^{15c5}NCOP^{iPr})Ir(H)$_2$(CO) according to Scheme 5.4. Literature precedent shows that the formation of such *trans*-dihydride species is possible via H_2 oxidative addition to form a *cis*-dihydride, followed by isomerization to form a more stable *trans* geometry.[149,150] No reaction was observed upon treating C_6D_6 solutions of **10** with 1 atm of H_2. Unfortunately, heating these mixtures under H_2 to reflux lead to decomposition of the ligand.

Scheme 5.4

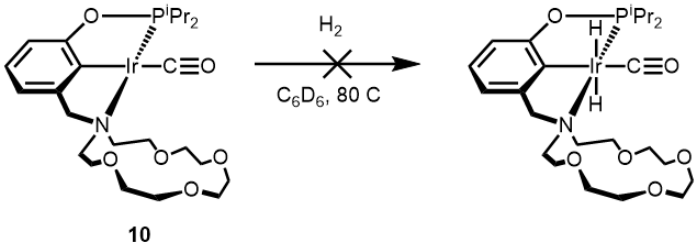

Electrochemical Studies

Without synthetic access to a dihydride, we shifted our focus to other precatalysts that could generate the dihydride in situ. Dissolving complex **2** in $NCCH_3$ fully forms (κ^3-[^{15c5}NCOP^{iPr})Ir(H)($NCCH_3$)$_2$]$^+$ **(6)**, which is isoelectronic to [(^{tBu}POCOP)Ir(H)($NCCH_3$)$_2$]$^+$ but contains a crown ether for possible cations effects. We theorized that the amine arm donor in **(6)**

would be less donating than the second $^{t}Bu_2P$ group, resulting in an anodic reduction potential anodically from –1.83 V vs Fc/Fc^+. If additional anodic shifting was needed incorporation of a good backbonding ligand such as the carbonyl in $[(\kappa^4\text{-}\,^{15c5}NCOP^{iPr})Ir(H)(CO)]^+$ **(8)** or $NCCH_3$ adduct form[86] $[(\kappa^3\text{-}^{15c5}NCOP^{iPr})Ir(H)(CO)(NCCH_3)]^+$ could provide additional electronic tuning to favor CO_2 reduction at more positive potentials. In this context, we set out to explore the electrochemical CO_2 reduction abilities of iridium pincer-crown ether complexes, and observe any potential cation effects.

We first looked at complex **6** by cyclic voltammetry (CV) by dissolving **2** in dry acetonitrile with 100 mM tetrabutylammonium hexafluorophoshate ($TBAPF_6$). Using glassy carbon as the working electrode with Ag/Ag^+ as the reference electrode, reductive scans were performed under a N_2 atmosphere on complex **6**. The reductive scans showed no reduction waves before the solvent window was reached, consistent with the behavior of $[(^{tBu}POCOP)Ir(H)(NCCH_3)_2]^+$ in dry acetonitrile. A proton-coupled electron transfer (PCET) involving a $2e^-/1H^+$ event has been proposed, for the reduction, so 5% H_2O was included as a proton source in solution. Surprisingly, reductive scans still revealed no reduction process.

To observe a reduction of **2**, CV was performed in tetrahydrofuran (THF) (Figure 5.1). Reductive scans of 0.3 mM **2** in THF revealed a reduction wave at –2.52 V vs Fc/Fc^+. Rather than the expected anodic shift relative to the $[(^{tBu}POCOP)Ir(H)(NCCH_3)_2]^+$, the reduction is actually *more cathodic* by ~700 mV than the value for $[(^{tBu}POCOP)Ir(H)(NCCH_3)_2]^+$ in $NCCH_3$! At such negative potentials, the background reaction for H^+ reduction to H_2 would become highly competitive, almost certainly eroding selectivity towards formate. Complex **2** was abandoned at this point as a poor candidate for CO_2 reduction. We hypothesize that the reason

for the cathodic shift is related to the PCET process, and that perhaps the acidity of the dihydride changed sufficiently that water was not able to protonate the metal center.

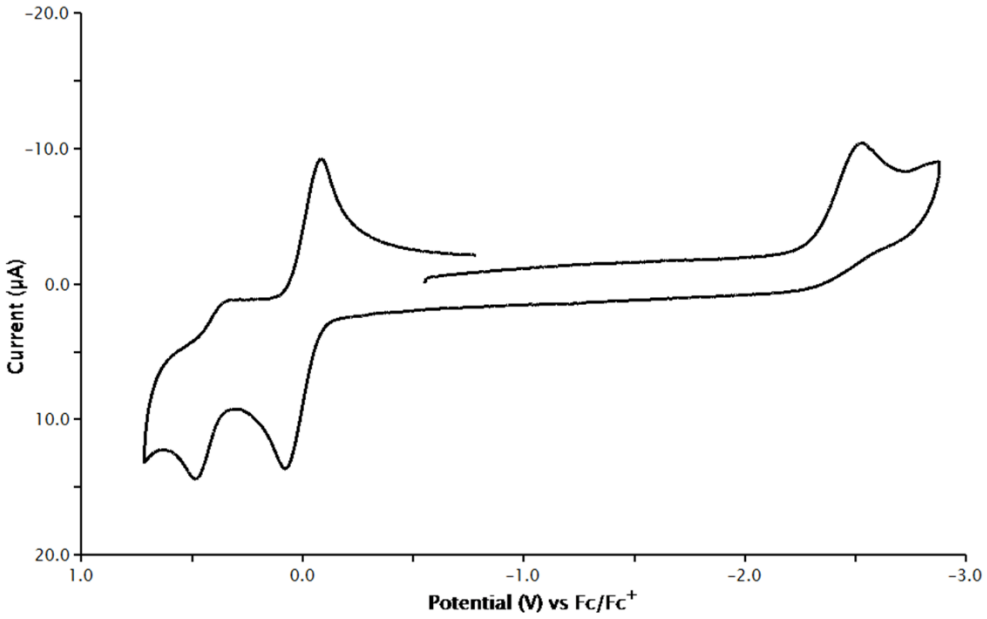

Figure 5.1: Cyclic voltammogram at 250 mV•s^{-1} of 0.3 mM complex **2** in THF with 0.1 M TBA PF_6 and 1 mM H_2O under a nitrogen atmosphere. Reduction of the complex appears at –2.52 V. Glassy carbon working electrode, silver wire pseudo-reference electrode, and platinum counter electrode, with added ferrocene as an internal reference (0 V).

To help shift the reduction potential more positive, 1 mM complex **8** was investigated by CV in acetonitrile solutions with 5% water. A reductive scan under CO_2 revealed a reduction peak at –2.53 V vs Fc/Fc^+, which is again extremely negative relative to the $[(^{tBu}POCOP)Ir(H)(NCCH_3)_2]^+$ complexes, and very close to the $NCCH_3$ solvent window. Considering the extremely negative reduction potentials required to reduce the complex, we stopped exploring the complexes as candidates for CO_2 reduction electrocatalysts, and began exploring their activity as hydrogenation catalysts.

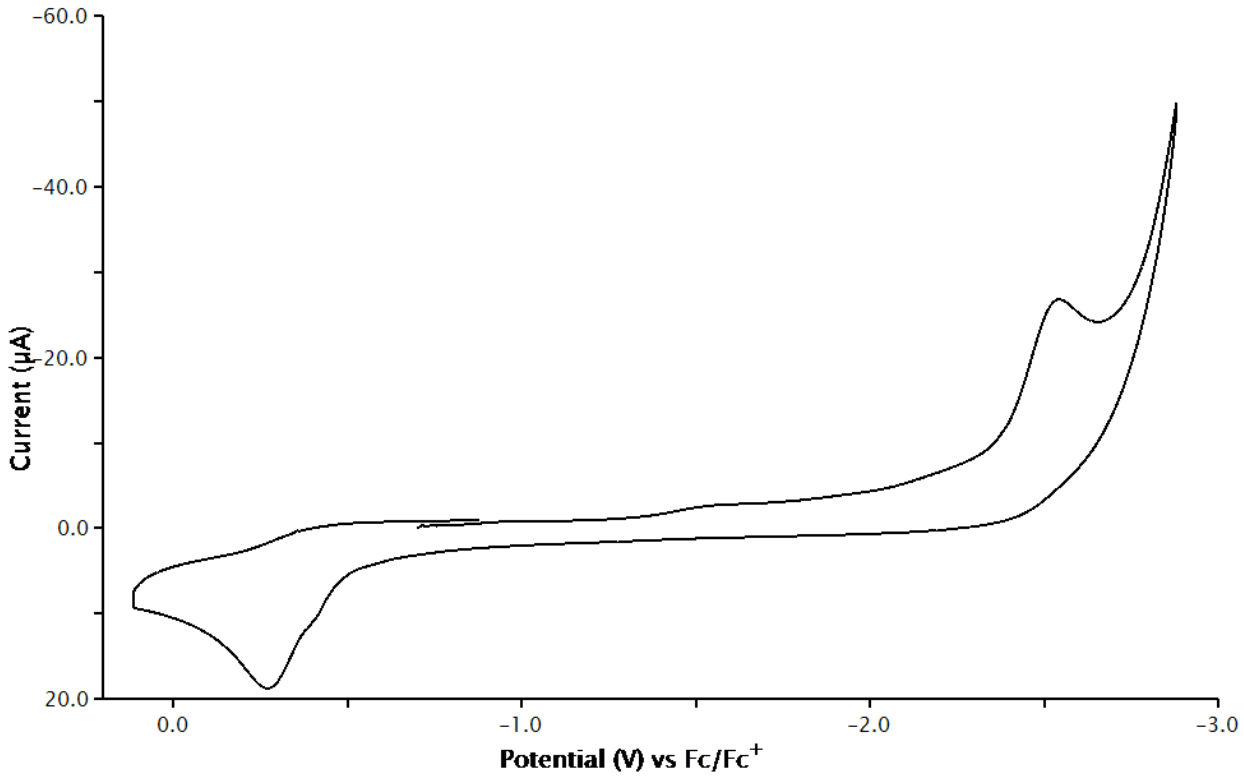

Figure 5.2: CV of 1 mM **8** in 5% H_2O acetonitrile solution with 100 mM $TBAPF_6$ and 1 atmosphere CO_2. Glassy carbon working electrode, platinum wire counter electrode, Ag^0/Ag^+ reference electrode.

High Pressure High Temperature Studies

To assess the activity of iridium pincer-crown ether complexes in CO_2 hydrogenation, we first needed to determine a suitable complex, solvent, and base. After noticing that complexes **1** and **2**, decompose when treated with base, we decided to look at complex **10** for CO_2 hydrogenation activity since it is stable to excess KO^tBu used during synthesis. We chose bicarbonate HCO_3^- for the base because it is cheap, abundant, applicable to electrochemical reactions, and much less corrosive than hydroxide salts. The solvent system used in the reaction needed to solubilize the catalyst and the bicarbonate salts, so we tested THF/H_2O and $NCCH_3/H_2O$ at ratios of 10/90, 25/75, and 50/50. In these solvent trials, 0.5 mM **10** was used

with 1M $NaHCO_3$ (assuming full solubility). The reactions were pressurized with 50:50 H_2:CO_2 to 24 bar, and heated to 100˚C for 3 hours. After cooling the reaction and depressurizing the vessels, the formate concentration was determined by ^1H NMR spectroscopy using 150 mM sodium *p*-toluenesulfonate (NaOTs). Overall the $NCCH_3$ trials performed better than the THF trials (Figure 5.3), producing up to 2x more formate. Of the $NCCH_3$ trials, the 50/50 $NCCH_3/H_2O$ trial, achieved a TON = 320, but suffered from poor $NaHCO_3$ solubility. On the other hand, the 10/90 $NCCH_3/H_2O$ trial had full $NaHCO_3$ solubility, achieved a TON = 173, but seemed to not offer full catalyst solubility.

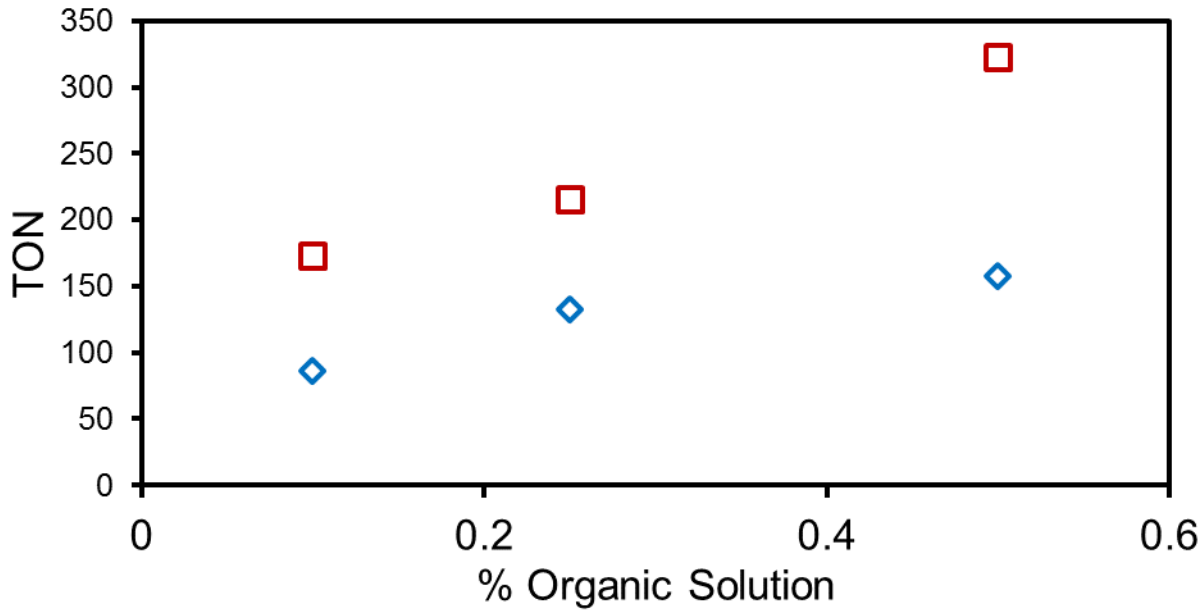

Figure 5.3: TON for sodium formate using 0.5 mM **10**, 1M NaHCO3 overall, and varying solvent percentages of $NCCH_3$ (red squares), and THF (blue diamonds) mixed with H_2O for a total volume of 5 mL. Vessels pressurized to 24±0.2 bar, heated for 3 hours at 100˚C. Formate determined using 150mM NaOTs in D_2O.

In order to determine what $NCCH_3/H_2O$ ratio to use, 10/90 vs 50/50, reactions were run at varying catalyst concentrations at both ratios. The catalyst concentration of **10** was varied from 0.5-1000 μM in reactions containing 50/50 $NCCH_3/H_2O$, saturated $NaHCO_3$ (1M assuming full solubility), and 24 bar 50:50 H_2 CO_2. The reactions were heated to 100˚C for 3 hours and

formate concentration was determined by injection of ^{t}BuOH as a standard. In these trials at 50/50 $NCCH_3/H_2O$, lower catalyst loadings produced higher TON, with 0.5 μM producing TON = 225.

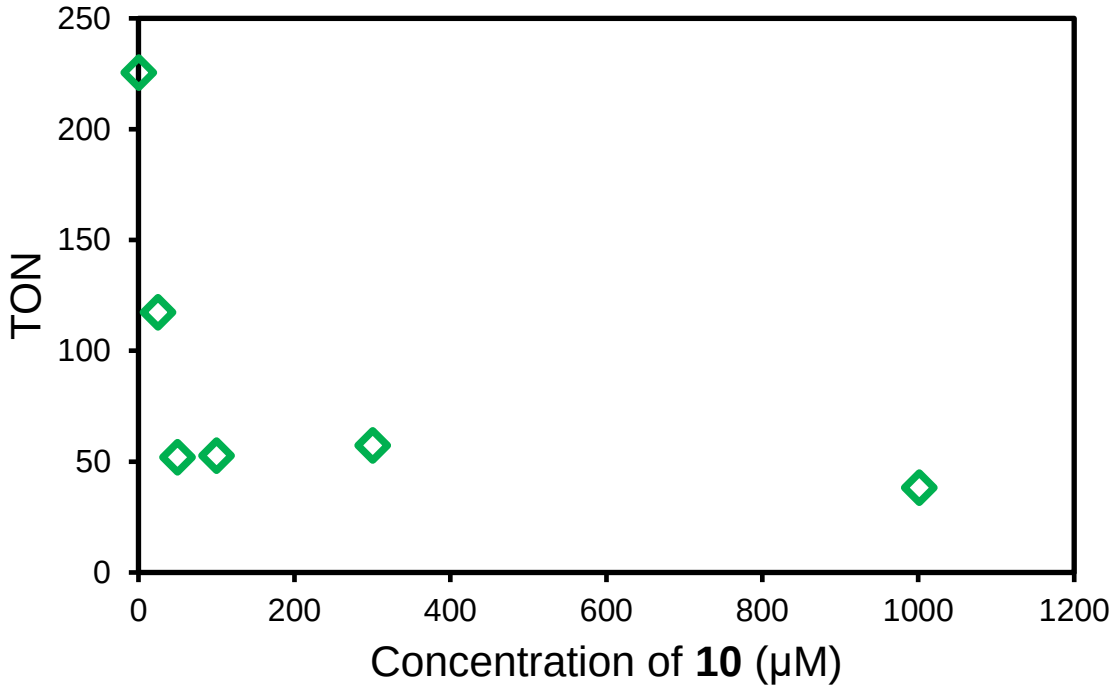

Figure 5.4: TON for formate production in 50/50 $NCCH_3/H_2O$ with 1 M $NaHCO_3$, varying amounts of complex **10**, and 24 bar 50:50 H_2:CO_2. Reactions heated to 100˚C for 3 hours. Formate concentration determined by ^{1}H NMR using ^{t}BuOH as a standard.

The catalyst concentration study on the 10/90 $NCCH_3/H_2O$ system produced higher TON overall. The catalyst concentration of **10** was varied from 1.5-150 μM in reactions containing 10/90 $NCCH_3/H_2O$, 1M $NaHCO_3$, and 24 bar 55/0:50 H_2 CO_2. The reactions were heated to 100˚C for 3 hours and formate concentration was determined by injection of ^{t}BuOH as a standard. In these trials, the best TON was also achieved at low catalyst loading, with 1.5 μM **10** yielding TON = 1000.

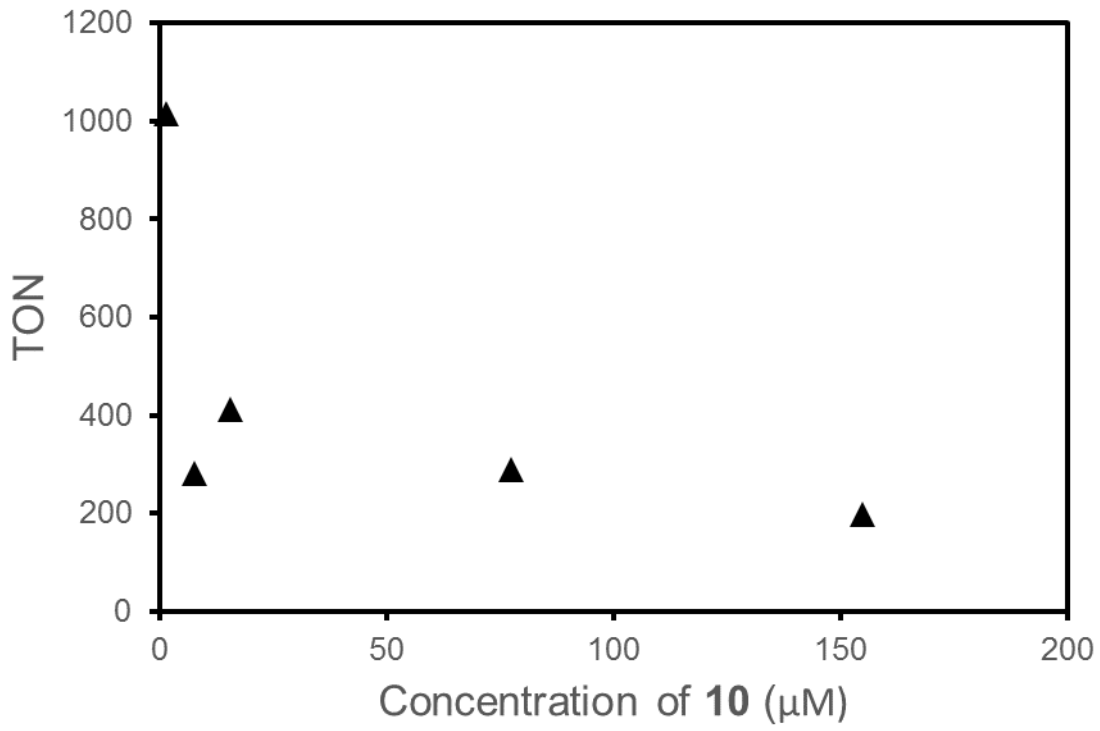

Figure 5.5: TON for formate production in 10% $NCCH_3$ with 1 M $NaHCO_3$, varying amounts of complex **10**, and 24 bar 50:50 H_2:CO_2. Reactions heated to 100˚C for 3 hours. Formate concentration determined by ^{1}H NMR using ^{t}BuOH as a standard.

Cation Effects is CO_2 Hydrogenation

From the data above, we determined conditions for the hydrogenation of CO_2 to formate using complex **10**. It was found that lower catalyst loadings ~1 μM, and a 10/90 $NCCH_3/H_2O$ solvent system, were best for achieving high TON. From the work in Chapters 3 and 4, we know that the reactivity of pincer-crown ether complexes containing an aza-15-crown-5 moiety are highly effected by Li^+, moderately effected by Na^+, and show no effects with K^+. Therefore, we wanted to see if the CO_2 hydrogenation results with **10** show any cation effects. We expected that cations held in close proximity might assist with formate production and release by forming

formate–cation interactions like that shown in Scheme 5.5. To do so we ran reactivity studies containing 0.1 μM complex **10** and different cations.

Scheme 5.5

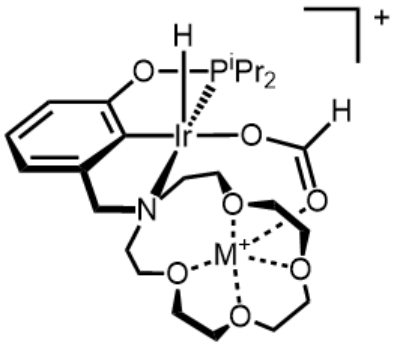

To determine cation effects between K^+, Na^+, and Li^+ three trials were run containing a) 1 M $KHCO_3$ as the base, b) 1 M $NaHCO_3$ as the base, and c) 1 M $KHCO_3$ with 140 mM LiOTf. Reactions were carried out in triplicate in 10/90 $NCCH_3/H_2O$ under 24 bar 50:50 H_2:CO_2 for 3 hours at 100˚C. The influence of the alkali metal cation is negligible, as shown in Figure 5.6.

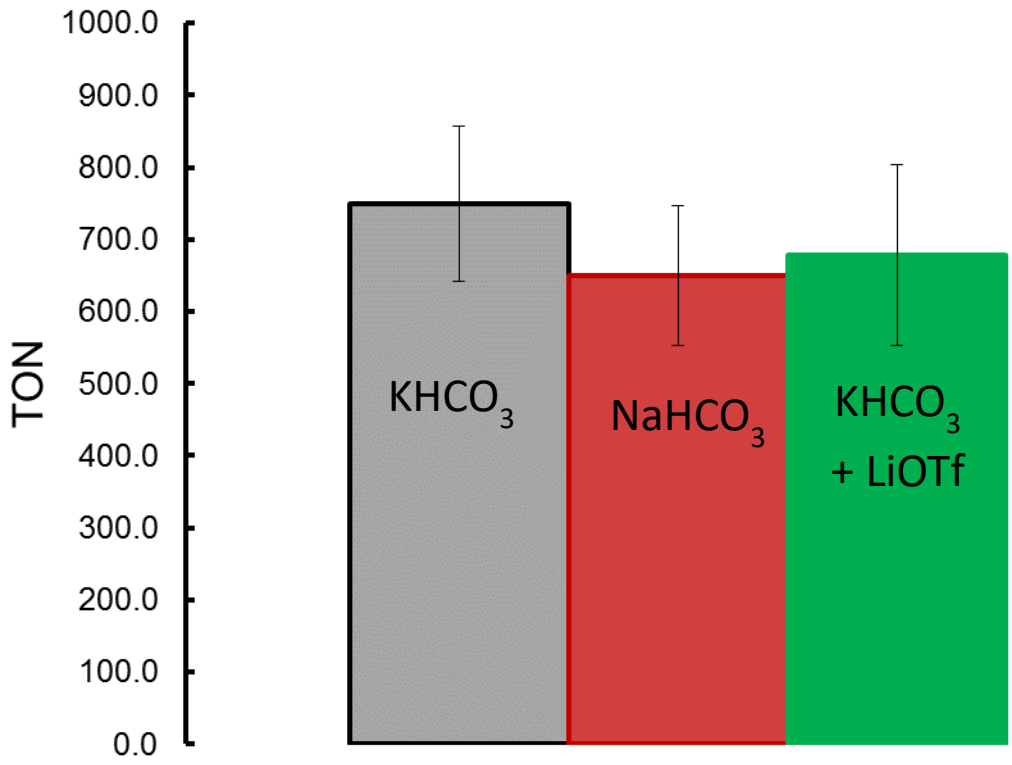

Figure 5.6: **Conditions, 0.1 μM complex** 10**, 10% $NCCH_3$, with 90% H_2O and 10% $MHCO_3$ according to the chart. Vessels pressurized to 24 bar and heated to 100˚C for 3 hours. Formate concentration determing by NMR using ^{t}BuOH internal standard.**

5.3 Conclusions

Taken together, our studies show that iridium pincer-crown ether complexes are not promising candidates for CO_2 reduction catalysis under the explored conditions. What seemed to be a minimal structural change, replacing a di-tert-butylphosphine donor with an aza-crown ether amine donor, turned out to change the chemical properties of the iridium complexes dramatically. Iridium dihydride species are stable with the POCOP ligand, but could not be isolated with the NCOP ligand. The reduction potential of the NCOP complexes were >600 mV

more negative than the best iridium POCOP complexes used in electrocatalytic formate production. The iridium pincer-crown ether complexes do show modest activity for CO_2 hydrogenation (TON ~ 750), but did not show any effects when different cations were added to the solution.

5.3 Experimental Information

All compounds were manipulated using standard vacuum line or Schlenk techniques or in a glovebox under a nitrogen atmosphere. NMR-scale reactions were prepared under nitrogen in a glovebox and kept in Teflon-sealed or septum sealed tubes. Under standard glovebox operating conditions, pentane, diethyl ether, benzene, toluene, tetrahydrofuran, and water were used without purging, such that traces of those solvents were present in the atmosphere and in the solvent bottles. ^{1}H, ^{31}P, and ^{13}C NMR spectra were recorded on 400, 500, or 600 MHz spectrometers at 298 K. All NMR solvents and isotopically labeled reagents were purchased from Cambridge Isotope Laboratories, Inc. All reagents used were commercially available and were used without further purification.

All electrochemical experiments were done using a Pine WaveNow potentiostat or Pine WaveDriver bipotentiostat ran using Aftermath software. All experiments were performed in 20 mL scintillation vials equipped with a cap containing holes for a glassy carbon working electrode (3 mm disc), a silver reference wire, a platinum wire counter electrode, a gas line with flowing N_2 or CO_2, and a hole for venting. All electrochemical experiments were done using a polished glassy carbon working electrode. Between scans mixtures were stirred.

All high pressure, high temperature CO_2 hydrogenation studies were performed using a Parr 5000 multi reactor system equipped with snug fitting PTFE teflon liners inserted into the

reactor vessels. The reactor vessels were oven warmed to 110˚C, while the reactor heads were gently warmed on top of a warming oven. The reactors were pumped into a glovebox using standard techniques. All reactor runs were done at a total volume of 10 mL. Carbonate salts were massed out and transferred to the reactor vessel such that 1 M concentration would be achieved by dissolving the solids. Water, acetonitrile, and THF were added to the vessel as needed to achieve the desired solvent mixture. Complex **10** was added to reactors via Hamilton syringe as a 100 mM stock solution in THF or $NCCH_3$. After adding the appropriate solids, solvents, and catalyst, the reactor heads were attached to the reactor vessels, and tightened using an allen key. The reactors were removed from the glovebox, and placed on the Parr 5000 multireactor system. The nitrogen atmosphere of the vessels was removed by charging the reactors with 10 bar H_2/CO_2 and releasing the pressure three times. After removing N_2, the reactors were then pressurized to 24 bar, and heated to 100˚C for 3 hours. After the reactors were cooled, the reactors were opened in a hood, and ^{t}BuOH or NaOTs was added as an internal standard. The formate concentration was then determined by ^{1}H NMR spectroscopy.

REFERENCES

(1) Crabtree, R. H. *The Organometallic Chemistry of the Transition Metals*, Fifth Edit.; John Wiley & Sons, Inc.: Hoboken, New Jersey, 2009.

(2) Hartwig, J. F. *Organotransition Metal Chemistry*; Murdzek, J., Ed.; University Science Books: Mill Valley, California, 2010.

(3) Tolman, C. A. *J. Am. Chem. Soc.* **1970**, *92* (10), 2953–2956.

(4) Tolman, C. A. *Chem. Rev.* **1977**, *77* (3), 313–348.

(5) Golovin, M. N.; Rahman, M. M.; Belmonte, J. E.; Giering, W. P. *Organometallics* **1985**, *4* (11), 1981–1991.

(6) Rahman, M. M.; Liu, H. Y.; Prock, A.; Giering, W. P. *Organometallics* **1987**, *6* (3), 650–658.

(7) Jover, J.; Fey, N.; Harvey, J. N.; Lloyd-Jones, G. C.; Orpen, A. G.; Owen-Smith, G. J. J.; Murray, P.; Hose, D. R. J.; Osborne, R.; Purdie, M. *Organometallics* **2010**, *29* (23), 6245–6258.

(8) Lever, A. B. P. *Inorg. Chem.* **1991**, *30* (9), 1980–1985.

(9) Kuhl, O. *Coordination Chemistry Reviews*. 2005, pp 693–704.

(10) Howell, J. A. S.; Burkinshaw, P. M. *Chem. Rev.* **1983**, *83* (5), 557–599.

(11) Wovkulich, M. J.; Feinberg, S. J.; Atwood, J. D. *Inorg. Chem.* **1980**, *19* (9), 2608–2611.

(12) Wovkulich, M. J.; Atwood, J. D. *J. Organomet. Chem.* **1979**, *184*, 77–89.

(13) Lohan, M.; Milde, B.; Heider, S.; Speck, J. M.; Krauße, S.; Schaarschmidt, D.; Rüffer, T.; Lang, H. *Organometallics* **2012**, *31* (6), 2310–2326.

(14) Lin, H.-J.; Siretanu, D.; Dickie, D. A.; Subedi, D.; Scepaniak, J. J.; Mitcov, D.; Clérac, R.; Smith, J. M. *J. Am. Chem. Soc.* **2014**, *136* (38), 13326–13332.

(15) Surry, D. S.; Buchwald, S. L. *Chem. Sci.* **2011**, *2* (1), 27–50.

(16) Niemeyer, Z. L.; Milo, A.; Hickey, D. P.; Sigman, M. S. *Nat. Chem.* **2016**, *8* (6), 610–617.

(17) Trnka, T. M.; Grubbs, R. H. *Acc. Chem. Res.* **2001**, *34* (1), 18–29.

(18) Vougioukalakis, G. C.; Grubbs, R. H. *Chem. Rev.* **2010**, *110* (3), 1746–1787.

(19) Chung, C. K.; Grubbs, R. H. *Org. Lett.* **2008**, *10* (13), 2693–2696.

(20) Scholl, M.; Trnka, T. M.; Morgan, J. P.; Grubbs, R. H. *Tetrahedron Lett.* **1999**, *40* (12), 2247–2250.

(21) Lappert, M. F. *J. Organomet. Chem.* **1975**, *100* (1), 139–159.

(22) Sandford, M. S.; Love, J. A.; Grubbs, R. H. *J. Am. Chem. Soc.* **2001**, *123* (27), 6543–6554.

(23) McGuinness, D. S.; Cavell, K. J.; Skelton, B. W.; White, A. H. *Organometallics* **1999**, *18* (9), 1596–1605.

(24) Love, J. A.; Morgan, J. P.; Trnka, T. M.; Grubbs, R. H. *Angew. Chem. Int. Ed.* **2002**, *41* (21), 4035–4037.

(25) Choi, T. L.; Grubbs, R. H. *Angew. Chem. Int. Ed.* **2003**, *42* (15), 1743–1746.

(26) Leitgeb, A.; Wappel, J.; Slugovc, C. *Polymer (Guildf).* **2010**, *51*, 2927–2946.

(27) Kingsbury, J. S.; Harrity, J. P. A.; Bonitatebus, P. J.; Hoveyda, A. H. *J. Am. Chem. Soc.* **1999**, *121* (4), 791–799.

(28) Gunanathan, C.; Milstein, D. *Acc. Chem. Res.* **2011**, *44* (8), 588–602.

(29) Grützmacher, H. *Angewandte Chemie - International Edition*. 2008, pp 1814–1818.

(30) Crabtree, R. H. *New J. Chem.* **2011**, *35* (1), 18–23.

(31) Khusnutdinova, J. R.; Milstein, D. *Angew. Chem. Int. Ed.* **2015**, *54* (42), 12236–12273.

(32) Clapham, S. E.; Hadzovic, A.; Morris, R. H. *Coordination Chemistry Reviews*. 2004, pp 2201–2237.

(33) Blanco, V.; Leigh, D. A.; Marcos, V. *Chem. Soc. Rev.* **2015**, *44* (44), 5341–5370.

(34) Teator, A. J.; Lastovickova, D. N.; Bielawski, C. W. *Chem. Rev.* **2016**, *116* (4), 1969–1992.

(35) Lüning, U. *Angew. Chem. Int. Ed.* **2012**, *51* (33), 8163–8165.

(36) Bader, A.; Lindner, E. *Coord. Chem. Rev.* **1991**, *108* (1), 27–110.

(37) Jeffrey, J. C.; Rauchfuss, T. B. *Inorg. Chem.* **1979**, *18* (10), 2658–2666.

(38) Braunstein, P.; Naud, F. *Angewandte Chemie - International Edition*. February 16, 2001, pp 680–699.

(39) Slone, C. S.; Weinberger, D. A.; Mirkin, C. A. *Prog. Inorg. Chem.* **1999**, *48*, 233–350.

(40) Bassetti, M. *European Journal of Inorganic Chemistry*. November 2006, pp 4473–4482.

(41) Zaja, M.; Connon, S. J.; Dunne, A. M.; Rivard, M.; Buschmann, N.; Jiricek, J.; Blechert, S. *Tetrahedron* **2003**, *59* (34), 6545–6558.

(42) Dunne, A. M.; Mix, S.; Blechert, S. *Tetrahedron Lett.* **2003**, *44* (13), 2733–2736.

(43) Wakamatsu, H.; Blechert, S. *Angew. Chem. Int. Ed.* **2002**, *41* (13), 2403–2405.

(44) Frank, N.; Hanau, K.; Langer, R. *Inorg. Chem.* **2014**, *53* (20), 11335–11343.

(45) Poverenov, E.; Gandelman, M.; Shimon, L. J. W.; Rozenberg, H.; Ben-David, Y.; Milstein, D. *Chem. Eur. J.* **2004**, *10* (19), 4673–4684.

(46) Poverenov, E.; Gandelman, M.; Shimon, L. J. W.; Rozenberg, H.; Ben-David, Y.; Milstein, D. *Organometallics* **2005**, *24* (6), 1082–1090.

(47) Lindner, R.; van den Bosch, B.; Lutz, M.; Reek, J. N. H.; van der Vlugt, J. I.; Ivar Van Der Vlugt, J. *Organometallics* **2011**, *30* (3), 499–510.

(48) Balof, S. L.; P'Pool, S. J.; Berger, N. J.; Valente, E. J.; Shiller, A. M.; Schanz, H.-J. *Dalt. Trans.* **2008**, 5791–5799.

(49) Balof, S. L.; Yu, B.; Lowe, A. B.; Ling, Y.; Zhang, Y.; Schanz, H. J. *Eur. J. Inorg. Chem.* **2009**, *2009* (13), 1717–1722.

(50) Arumugam, K.; Varnado, C. D.; Sproules, S.; Lynch, V. M.; Bielawski, C. W. *Chem. Eur. J.* **2013**, *19* (33), 10866–10875.

(51) Baerends, E. J.; Rosa, A. *Coord. Chem. Rev* **1998**, *177*, 97–125.

(52) Salassa, L.; Garino, C.; Salassa, G.; Gobetto, R.; Nervi, C. *J. Am. Chem. Soc.* **2008**, *130* (29), 9590–9597.

(53) Neilson, B. M.; Bielawski, C. W. *Organometallics* **2013**, *32* (10), 3121–3128.

(54) McConnell, A. J.; Wood, C. S.; Neelakandan, P. P.; Nitschke, J. R. *Chem. Rev.* **2015**, *115* (15), 7729–7793.

(55) Lifschitz, A. M.; Rosen, M. S.; McGuirk, C. M.; Mirkin, C. A. *J. Am. Chem. Soc.* **2015**, *137* (23), 7252–7261.

(56) Yoon, H. J.; Kuwabara, J.; Kim, J.-H.; Mirkin, C. A. *Science* **2010**, *330* (6000).

(57) Oliveri, C. G.; Ulmann, P. A.; Wiester, M. J.; Mirkin, C. A. *Acc. Chem. Res.* **2008**, *41* (12), 1618–1629.

(58) Izatt, R. M. R.; Bradshaw, J. J. S.; Nielsen, S. S. A.; Lamb, J. D.; Christensen, J. J.; Sen, D. *Chem. Rev* **1985**, *85*, 271–339.

(59) Izatt, R. M.; Pawlak, K.; Bradshaw, J. S.; Bruening, R. L. *Chem. Rev.* **1991**, *91* (8), 1721–2085.

(60) Izatt, R. M.; Pawlak, K.; Bradshaw, J. S.; Bruening, R. L. *Chem. Rev.* **1995**, *95* (7), 2529–2586.

(61) Hyde, E. M.; Shaw, B. L.; Shepherd, I. *J. Chem. Soc., Dalt. Trans.* **1978**, No. 12, 1696–1705.

(62) Carroy, A.; Lehn, J.-M. *J. Chem. Soc., Chem. Commun.* **1986**, 1232–1234.

(63) Van Veggel, F. C. J. M.; Verboom, W.; Reinhoudt ', D. N.; Vi, V.; Veggel, F. C. J. M. van; Verboom, W.; Reinhoudt, D. N. *Chem. Rev.* **1994**, *94* (2), 279–299.

(64) Hazari, A.; Labinger, J. A.; Bercaw, J. E. *Angew. Chem. Int. Ed.* **2012**, *51* (33), 8268–8271.

(65) Przybilla, K. J.; Vögtle, F. *Chem. Ber.* **1989**, *122* (2), 347–355.

(66) Zhang, X.; Huang, D.; Chen, Y.-S.; Holm, R. H. *Inorg. Chem.* **2012**, *51* (20), 11017–11029.

(67) Spasyuk, D. M.; Zargarian, D.; van der Est, A. *Organometallics* **2009**, *28* (22), 6531–6540.

(68) Spasyuk, D. M.; Zargarian, D. *Inorg. Chem.* **2010**, *49* (13), 6203–6213.

(69) Spasyuk, D. M.; Gorelsky, S. I.; van der Est, A.; Zargarian, D. *Inorg. Chem.* **2011**, *50* (6), 2661–2674.

(70) Gregor, L. C.; Grajeda, J.; Kita, M. R.; White, P. S.; Vetter, A. J.; Miller, A. J. M. .

(71) Göttker-Schnetmann, I.; White, P.; Brookhart, M. *J. Am. Chem. Soc.* **2004**, *126* (6), 1804–1811.

(72) Kang, P.; Cheng, C.; Chen, Z.; Schauer, C. K.; Meyer, T. J.; Brookhart, M. *J. Am. Chem. Soc.* **2012**, *134* (12), 5500–5503.

(73) Iglesias, M.; Pérez-Nicolás, M.; Miguel, P. J. S.; Polo, V.; Fernández-Alvarez, F. J.; Pérez-Torrente, J. J.; Oro, L. A. *Chem. Commun.* **2012**, *48* (76), 9480.

(74) Camp, A. M.; Kita, M. R.; Grajeda, J.; White P. S.; Miller, A. J. M. *Inorg. Chem.*

(75) Lindner, E.; Gierling, K.; Fawzi, R.; Steinmann, M. *Inorg. Chim. Acta.* **1998**, *269* (1), 13–22.

(76) Yamamoto, Y.; Kawasaki, K.; Nishimura, S. *J. Organomet. Chem.* **1999**, *587* (1), 49–57.

(77) Dorta, R.; Broggini, D.; Kissner, R.; Togni, A. *Chem. Eur. J.* **2004**, *10* (18), 4546–4555.

(78) Álvarez, E.; Paneque, M.; Petronilho, A. G.; Poveda, M. L.; Santos, L. L.; Carmona, E.; Mereiter, K. *Organometallics* **2007**, *26* (5), 1231–1240.

(79) Werner, H.; Schulz, M.; Windmueller, B. *Organometallics* **1995**, *14* (8), 3659–3668.

(80) Gray, G. M. *Comments Inorg. Chem.* **1995**, *17* (2), 95–114.

(81) Lehn, J.-M. *Pure Appi. Chem* **1980**, *52*, 2441–2459.

(82) Yang, J.; Brookhart, M. *Adv. Synth. Catal.* **2009**, *351* (1–2), 175–187.

(83) Camp, A. M.; Kita, M. R.; Grajeda, J.; Miller, A. J. M. *Inorg. Chem. Front.* **2017**, submitted.

(84) Adams, J. J.; Lau, A.; Arulsamy, N.; Roddick, D. M. *Organometallics* **2011**, *30* (4), 689–696.

(85) Shi, Y.; Suguri, T.; Dohi, C.; Yamada, H.; Kojima, S.; Yamamoto, Y. *Chem. Eur. J.* **2013**, *19* (32), 10672–10689.

(86) Grajeda, J.; Kita, M. R.; Gregor, L. C.; White, P. S.; Miller, A. J. M. *Organometallics* **2016**, *35* (3), 306–316.

(87) Haynes, A.; Maitlis, P. M.; Morris, G. E.; Sunley, G. J.; Adams, H.; Badger, P. W.; Bowers, C. M.; Cook, D. B.; Elliott, P. I. P.; Ghaffar, T.; Green, H.; Griffin, T. R.; Payne, M.; Pearson, J. M.; Taylor, M. J.; Vickers, P. W.; Watt, R. J. *J. Am. Chem. Soc.* **2004**, *126*, 2847–2861.

(88) Haynes, A. In *Advances in Catalysis*; 2010; Vol. 53, pp 1–45.

(89) Elliott, P. I. P.; Haak, S.; Meijer, A. J. H. M.; Sunley, G. J.; Haynes, A. *Dalt. Trans.* **2013**, *42* (47), 16538.

(90) Izatt, R. M.; Bradshaw, J. S.; Pawlak, K.; Bruening, R. L.; Tarbet, B. J. *Chem. Rev.* **1992**, *92* (6), 1261–1354.

(91) Fulmer, G. R.; Miller, A. J. M.; Sherden, N. H.; Gottlieb, H. E.; Nudelman, A.; Stoltz, B. M.; Bercaw, J. E.; Goldberg, K. I. *Organometallics* **2010**, *29* (9), 2176–2179.

(92) Yakelis, N. A.; Bergman, R. G. *Organometallics* **2005**, *24* (14), 3579–3581.

(93) Brookhart, M.; Grant, B.; Volpe Jr., a. F. *Organometallics* **1992**, *11* (11), 3920–3922.

(94) Dolomanov, O. V.; Bourhis, L. J.; Gildea, R. J.; Howard, J. A. K.; Puschmann, H. *J. Appl. Crystallogr.* **2009**, *42* (2), 339–341.

(95) Vuzman, D.; Poverenov, E.; Shimon, L. J. W.; Diskin-Posner, Y.; Milstein, D. *Organometallics* **2008**, *27* (11), 2627–2634.

(96) De Boer, J. A. A.; Reinhoudt, D. N.; Harkema, S.; Van Hummekt, G. J.; De Jongs, F. *J. Am. Chem. Soc.* **1982**, *104*, 4073–4076.

(97) Grootenhuis, P. D. J.; Kollman, P. A. *J. Am. Chem. Soc.* **1989**, *111* (11), 4046–4051.

(98) Li, D.; Keresztes, I.; Hopson, R.; Williard, P. G. *Acc. Chem. Res.* **2009**, *42* (2), 270–280.

(99) Fernanndez, I.; Martinnez-Viviente, E. S.; Breher, F.; Pregosin, P. S. *Chem. Eur. J.* **2005**, *11* (5), 1495–1506.

(100) Gibson, H. W.; Yamaguchi, N.; Hamilton, L.; Jones, J. W. *J. Am. Chem. Soc.* **2001**, *124* (4653–4665).

(101) Heinekey, D. M.; Oldham Jr, W. J. *Chem. Rev.* **1993**, *93*, 913–928.

(102) Kubas, G. J. *Chemical Reviews*. American Chemical Society 2007, pp 4152–4205.

(103) Findlater, M.; Schultz, K. M.; Bernskoetter, W. H.; Cartwright-Sykes, A.; Heinekey, D. M.; Brookhart, M. *Inorg. Chem.* **2012**, *51* (8), 4672–4678.

(104) Wallingford Ct 2009.

(105) Perdew, J. P.; Burke, K.; Ernzerhof, M. *Phys. Rev. Lett.* **1996**, *77* (18), 3865–3868.

(106) Hay, P. J.; Wadt, W. R. *J. Chem. Phys.* **1985**, *82* (1), 270.

(107) McLean, A. D.; Chandler, G. S. *J. Chem. Phys.* **1980**, *72* (10), 5639.

(108) Krishnan, R.; Binkley, J. S.; Seeger, R.; Pople, J. A. *J. Chem. Phys.* **1980**, *72* (1), 650–654.

(109) Kita, M. R.; Miller, A. J. M. *J. Am. Chem. Soc.* **2014**, *136* (41), 14519–14529.

(110) Gregor, L. C.; Grajeda, J.; Kita, M. R.; White, P. S.; Vetter, A. J.; Miller, A. J. M. *Organometallics* **2016**, *35* (17), 3074–3086.

(111) Smith, J. B.; Miller, A. J. M. *Organometallics* **2015**, *34* (19), 4669–4677.

(112) Hassam, M.; Taher, A.; Arnott, G. E.; Green, I. R.; van Otterlo, W. a. L. *Chem. Rev.* **2015**, 5462.

(113) Dinger, M. B.; Mol, J. C. *Eur. J. Inorg. Chem.* **2003**, *2003* (15), 2827–2833.

(114) Scarso, A.; Colladon, M.; Sgarbossa, P.; Santo, C.; Michelin, R. A.; Strukul, G. *Organometallics* **2010**, *29* (6), 1487–1497.

(115) Krompiec, S.; Kuźnik, N.; Krompiec, M.; Penczek, R.; Mrzigod, J.; Tórz, A. *J. Mol. Catal. A Chem.* **2006**, *253* (1–2), 132–146.

(116) Taskinen, E.; Lindholm, N. *J. Phys. Org. Chem.* **1994**, *7* (5), 256–258.

(117) Arnaud-Neu, F.; Delgado, R.; Chaves, S. *Pure Appl. Chem.* **2003**, *75* (1), 71–102.

(118) Larsen, C.; Paulson, E.; Erdogan, G.; Grotjahn, D. *Synlett* **2015**, *26* (17), 2462–2466.

(119) Grotjahn, D. B.; Larsen, C. R.; Gustafson, J. L.; Nair, R.; Sharma, A. *J. Am. Chem. Soc.* **2007**, *129* (31), 9592–9593.

(120) Larsen, C. R.; Erdogan, G.; Grotjahn, D. B. *J. Am. Chem. Soc.* **2014**, *136* (4), 1226–1229.

(121) Albéniz, A. C.; Espinet, P.; López-Fernández, R.; Sen, A. *J. Am. Chem. Soc.* **2002**, *124* (38), 11278–11279.

(122) Ivanova, S. M.; Nolan, B. G.; Kobayashi, Y.; Miller, S. M.; Anderson, O. P.; Strauss, S. H. *Chem. Eur. J.* **2001**, *7* (2), 503–510.

(123) Slone, C. S.; Mirkin, C. A.; Yap, G. P. A.; Guzei, I. A.; Rheingold, A. L. *J. Am. Chem. Soc.* **1997**, *119* (44), 10743–10753.

(124) Neumann, P.; Dib, H.; Caminade, A.-M.; Hey-Hawkins, E. *Angew. Chem. Int. Ed.* **2015**, *54* (1), 311–314.

(125) Blanco, V.; Leigh, D. A.; Marcos, V. *Chem. Soc. Rev.* **2015**, *44*, 5341–5370.

(126) Mendez-Arroyo, J.; Barroso-Flores, J.; Lifschitz, A. M.; Sarjeant, A. A.; Stern, C. L.; Mirkin, C. A. *J. Am. Chem. Soc.* **2014**, *136* (29), 10340–10348.

(127) Beswick, J.; Blanco, V.; De Bo, G.; Leigh, D. A.; Lewandowska, U.; Lewandowski, B.; Mishiro, K. *Chem. Sci.* **2015**, *6* (1), 140–143.

(128) Wang, J.; Feringa, B. L. *Science* **2011**, *331* (6023).

(129) Larsen, C. R.; Erdogan, G.; Grotjahn, D. B. *J. Am. Chem. Soc.* **2014**, *136* (4), 1226–1229.

(130) Grotjahn, D. B.; Larsen, C. R.; Erdogan, G. *Top. Catal.* **2014**, *57* (17–20), 1483–1489.

(131) Ivanova, S. M.; Nolan, B. G.; Kobayashi, Y.; Miller, S. M.; Anderson, O. P.; Strauss, S. H. *Chem. Eur. J.* **2001**, *7* (2), 503–510.

(132) Bailey, P. J.; Coxall, R. A.; Dick, C. M.; Fabre, S.; Henderson, L. C.; Herber, C.; Liddle, S. T.; Loroño-González, D.; Parkin, A.; Parsons, S. *Chem. Eur. J.* **2003**, *9* (19), 4820–

4828.

(133) Buschmann, W. E., Miller, J. S., Bowman-James, C. N., Miller, C. N. *Inorg. Synth.* **2002**, *33*, 83–91.

(134) Jessop, P. G.; Joó, F.; Tai, C. C. *Coordination Chemistry Reviews*. 2004, pp 2425–2442.

(135) Jessop, P. G.; Ikariya, T.; Noyori, R. *Chem. Rev.* **1995**, *95* (2), 259–272.

(136) Leitner, W. *Angewandte Chemie - International Edition*. Hüthig & Wepf Verlag November 3, 1995, pp 2207–2221.

(137) Zhang, Y.; MacIntosh, A. D.; Wong, J. L.; Bielinski, E. A.; Williard, P. G.; Mercado, B. Q.; Hazari, N.; Bernskoetter, W. H. *Chem. Sci.* **2015**, *6* (7), 4291–4299.

(138) Jeletic, M. S.; Mock, M. T.; Appel, A. M.; Linehan, J. C. *J. Am. Chem. Soc.* **2013**, *135* (31), 11533–11536.

(139) Tanaka, R.; Tanaka, R.; Yamashita, M.; Yamashita, M.; Nozaki, K.; Nozaki, K. *J. Am. Chem. Soc.* **2009**, *131* (40), 14168–14169.

(140) Diego Rail, M.; Berben, L. A. *J. Am. Chem. Soc.* **2011**, *133* (46), 18577–18579.

(141) Slater, S.; Wagenknecht, J. H. *J. Am. Chem. Soc.* **1984**, *106* (6), 5367–5368.

(142) Keshavarz-k, M.; Potts, K. T.; Abruila, H. D. *Inorg. Chem.* **1992**, *31* (13), 3680–3682.

(143) Bolinger, C. M.; Story, N.; Sullivan, B. P.; Meyer, T. J. *Inorg. Chem.* **1988**, *27* (25), 4582–4587.

(144) Pavlishchuk, V. V; Addison, A. W. *Inorg. Chim. Acta.* **2000**, *298* (1), 97–102.

(145) Kang, P.; Meyer, T. J.; Brookhart, M. *Chem. Sci.* **2013**, *4* (9), 3497–3502.

(146) Kang, P.; Zhang, S.; Meyer, T. J.; Brookhart, M. *Angew. Chem. Int. Ed.* **2014**, *53* (33), 8709–8713.

(147) Bhugun, I.; Lexa, D.; Save, J.; Savéant, J.-M. *J. Phys. Chem.* **1996**, *100* (51), 19981–19985.

(148) Gupta, M.; Hagen, C.; Flesher, R. J.; Kaska, W. C.; Jensen, C. M. *Chem. Commun.* **1996**, *36*, 2083–2084.

(149) Rybtchinski, B.; Ben-David, Y.; Milstein, D. *Organometallics* **1997**, *16* (8), 3786–3793.

(150) Goldberg, J. M.; Wong, G. W.; Brastow, K. E.; Kaminsky, W.; Goldberg, K. I.; Heinekey, D. M. *Organometallics* **2015**, *34*, 753–762.